Experimental Investigation, Modeling, Simulation and Optimization of Molded Interconnect Devices (MID) Based on Laser Direct Structuring (LDS)

Mechanical Department
The Faculty of Engineering
Friedrich-Alexander-University
Erlangen-Nuremberg
To Obtaining
Doctoral Degree Dr. Engineer

Submitted by
Bassim Shaheen Bachy
2017

Experimentelle Untersuchung, Modellierung, Simulation und Optimierung von Molded Interconnect Devices (MID) basierend auf Laser Direktstrukturierung (LDS)

Der Technischen Fakultät der
Friedrich-Alexander-Universität
Erlangen-Nürnberg
zur
Erlangung des Doktorgrades Dr.-Ingenieur

vorgelegt von
Bassim Shaheen Bachy
2017

Als Dissertation genehmigt von
der Technischen Fakultät der
Friedrich-Alexander-Universität
Erlangen-Nürnberg

Tag der mündlichen Prüfung:

Vorsitzender des Promotionsorgans:	Prof. Dr.-Ing. K. Feldmann
Gutachter:	Prof. Dr.-Ing. J. Franke
	Prof. Dr.-Ing. A. Zimmermann

This Dissertation is dedicated to my

Mom, my Wife and my Children

Acknowledgment

First of all, I would like to thank the Ministry of Higher Education and Scientific Research in Iraq for giving me the opportunity to complete my Ph.D. study.

I would like to thank professor *Jörg Franke* for giving me the opportunity to work with him at the Institute for Factory Automation and Production Systems (FAPS) and for supporting and advising me throughout my studies.

Great thank for the members of *Bordnetze group* for the support that came in many ways and forms.

I would like to express my gratitude to my family for their encouragement, and for supporting me in many ways during my academic study.

And, a very special thanks to my wife, *Luma*, who has been with me every step of the way, for her love, support, and patience.

Bassim Sh. Bachy, 2017

Table of Contents

List of Symbols and Abbreviations

$\dot{q}_{LASER}$	Volumetric Laser Heat Source Per Unit Volume (W/ m^3)
z_r	The Rayleigh Length $z_r = \pi R^2 . \lambda^{-1}$
a	Distance Between Two Successive Laser Passes (µm)
ANN	Artificial Neural Networks
APDL	ANSYS Parametric Design Language
b_i	The Linear Terms
b_{ii}	The Quadratic Terms
b_{ij}	The Interaction Terms
b_o	Constant of the Regression Equation
Cp	The Specific Heat Capacity (J/Kg.°C)
Cu_2O	The Additive of the Copper Oxide
CW	Continuous Wave Lasers
D	The Focused Laser Beam Diameter (µm)
Dc	The Characteristic Length (µm)
Do	The Entrance Beam Diameter (µm)
DoE	Design Of Experiments
E	The Pulse Energy (J)
ESP	Electronic Stability Program
f	Pulse Frequency (Hz)
FEM	Finite Element Method
FL	The Focal Length of the Focus Lens (mm)
GMDH	Group Method of Data Handling
H	The Enthalpy (J/Kg)
H%	Hatching Percentage
HAZ	Heat Affected Zone
h_c	The Convection Heat Transfer Coefficient ($W.m^{-2}.C^{-1}$)
H_f	Heat Of Fusion (J/G)
K_x, K_y, K_z	The Thermal Conductivity (W/(m.°C))
L	Characteristic Length (µm)
LDS	Laser Direct Structuring
LS	The Lines Structuring Type
LSM	Laser Surface Modification
LSS	Laser Subtractive Structuring
LTW	Laser Transmission Welding
MA	The Mixed Ablation Type
MID	Molded Interconnect Devices
MS	The Mixed Structuring Type
MZ	The Mixed Zone
n	The Numbers Of Neurons In The Hidden Layer
n	The Number of Investigated Parameters
Nd:YAG	Neodymium-Doped Yttrium Aluminum Garnet-Laser Type

Nu	Nusselt Number
PO	Pulses Overlap %
PA	The Puffing Ablation Type
PEEK	Poly Ether Ether Ketone
P_{Mean}	The Average Power (W)
PMMA	Poly-Methyl-Methacrylate
PN	The Pulses Number
PPA	Polyphthalamide
P_{Peak}	The Maximum Power (W)
Pr	Prandtl Number
PW	Average Power for the Pulsed Wave Laser
PZ	The Puffing and Resolidification Zone
q_c	Convection Heat Transfer (W/m^2)
q_r	Radiation Heat Transfer (W/m^2)
R	Radius of the Focused Laser Beam (µm)
Ra	Surface Roughness (µm)
RA	The Removing Ablation Type
Re	Reynolds Number
RFID	Radio-Frequency Identification Devices
RS	The Random Structuring Type
RSM	Response Surface Methodology
Rz	Surface Roughness
RZ	The Removing Zone
SIR	Surface Insulation Resistance
t	Time Between Two Pulses (s)
T	The Temperature (°C)
T_a	Ambience Temperature In (°C)
T_g	Glass Transition Temperature In (°C)
T_L	Liquids Temperature (°C)
T_m	Melting Temperature (°C)
$T_{o(x,y,z)}$	Initial Temperature (27°C)
T_S	Sintering Temperature(°C)
T_{Sur}	Temperature of the Work-Piece Surface (°C)
v	Laser Scanning Speed in Term of (m/s)
V	The Air Velocity (1,2218 m/s)
W_d	The Designed Conductor Width (µm)
W_e	The Experimental Measured Conductor Width (µm)
W_{xy}	The Weight From The Input Layer To Hidden Layer
W_{yz}	The Weight From The Hidden Layer To Output Layer
x, y and z	The Axis Coordinate (m)
X_o	The Bias For The Input Layer
y_o	The Bias For The Hidden Layer
Y_p	The Five Highest Peaks (µm)

Y_v	The Lowest Valleys (µm)
α	The Thermal Diffusivity In (m^2/s)
β	The Incidence Angle (°)
δ	Stefan-Boltzmann Constant 5.67×10^{-8} $W.m^{-2}.K^{-4}$
ε	The Material Emissivity
ἐ	The Residual Errors
λ	The Wavelength (nm)
µ	The Dynamic Viscosity Of The Air ($N.s/m^2$)
ρ	The Density Of The Material (Kg/m^3)
ρ_a	Density Of Amorphous Phase (Kg/m^3)
ρ_c	Density Of Crystalline Phase (Kg/m^3)
v	The Kinematic Viscosity Of The Air ($153.5*10^{-7}$ m^2 /s At T 20 °C)

1. Introduction and Outline of the Thesis

1.1. Introduction

Molded Interconnect Devices (MID) comprise of injection-molded plastic parts with conductive circuit patterns, mechanical and electrical functions integrated on a single device. It is an important technology with enormous potential for industrial applications. The process chain for the manufacturing of MID can be divided into four steps which include molding, structuring, metallization and finally placement of electronic components or assembly. The MID technology has many manufacturing processes; the most important process is the Laser Direct Structuring (LDS), which is under investigation in this work. This technology offers the best combination of design freedom, economic potential, and the possibility of high quantities, process chain simplification and reduction of components, cost and weights. As a result, it shows great applications especially in automotive industry, medical technology, information technology (IT), and telecommunications.

MID-LDS technology is influenced by many complex parameters, some of these parameters are controllable and the others are uncontrollable. The work of this thesis focuses on MID-LDS technology. Consequently, it focuses on the effect of LDS parameters, which are classified into two groups. The first are working parameters, which include laser power, speed, frequency, wavelength, and the laser beam diameter. The second are defined as the design parameters, which include focal distance, the incidence angle of the laser beam and overlapping or the hatching between laser lines. During the sophistication of MID-LDS process, many challenges have appeared. Some of these challenges concern on the necessity to use new materials, which can be utilized for further MID applications. Another is based on the implementation of 3D and micro MID products which need special requirements. Further challenges were raised regarding the lack of available industry standards and information, which can be used to cover the influence of all process parameters. These drive to consider this process under investigation to fulfill various objectives. They are achieved by using: experimental investigation, computer simulation, mathematical modeling and finally optimization tools.

A computer simulation is also employed in this thesis. Such a tool helps to reduce the required effort, cost, and time-consumption forecast. It is used to successfully predict process performance with easy-to-modify computer models. This simulation utilizes a mathematical heat transfer model based on Finite Element Method (FEM). It can be used to calculate the temperature at each point of the substrate material and estimate the temperature distribution during LDS processes. It also has the capability of handling 2D and 3D processes, nonlinear material properties, the heat source of the laser beam profile, and the phase transformation during the LDS process. The final simulation results, which show a good agreement with the experimental data,

provide deep explanations for the relationship between the adopted parameters and the process responses.

The experimental investigation includes series of experiments to realize the influence of process parameters including, laser incidence angle, focal length, hatching, laser power, laser velocity, and laser frequency on the process responses, namely the groove dimensions, profile and its edge factor, characteristics of structured area, accuracy, quality, and reliability of the final MID product. The experimental investigations conclude important descriptions for the correlation between adopted parameters and corresponding responses.

Mathematical tools were also employed in this thesis employing the Artificial Neural Networks (ANN) and the Response Surface Methodology (RSM) to correlate the process parameter and their respective response, to find the importance of each process parameters as well as the interaction between them and finally they can be used for process optimization. These modeling approaches show good and vital results regarding the accuracy of the models, the influence, the interaction and the importance of the adopted parameters.

1.2. Outline of the Thesis

This thesis presents 3 years of research work. The organization of this thesis will be described in this chapter as follows:

Chapter 1 presents an outline of the thesis and shows a full description of each chapter.

Chapter 2 presents an introduction to MID technology. Further details, which encompass the process definition, the important applications, the potentials and advantages of MID technology are given. The classification and definition of process parameters are also described in this chapter. Finally, motivations and main objectives of this thesis are given.

Chapter 3 reviews the state of the art of MID-LDS- technology. This literature review focuses on different fields of research which include the experimental investigations of process parameters, the quality inspections and the extensive experimental measurements of the quality and the reliability. Further exploration for the important researches which covers the use of the computer simulation, the mathematical modeling, and the optimization of this technique are also presented.

Chapter 4 defines and outlines the concept of thermal simulation of LDS processes as it relates to analyze, understand and optimize the LDS process parameters. It also describes how computer simulation can be used to caring out the thermal analysis of LDS processes. This chapter presents further details about the proposed mathematical model of heat transfer processes during the laser direct

structuring process, the boundary conditions, the laser source models, the calculation of heat transfer coefficient, the thermal and the physical material properties. Additional information regarding the simulation procedures is also given to explain how this simulation method is used to perform simulation tests of 2D and 3D LDS processes. This chapter presents a new classification of the process parameters to explain the relationship between the adopted parameters and the process responses. This helps to explain and describe the final results, which are presented in the last part of this chapter. Finally, this chapter shows how the simulation tool is used to suggest the suitable parameters that support the LDS quality.

Chapter 5 describes all the details of the experimental works that are employed to investigate the LDS-MID technology. It presents a full description of the investigated materials, the characteristics of laser machine, the required experimental measurements, the instruments or devices and the design or layout of the conductor shape used in this work. Further details regarding the design of the experiments (DoE) used in this experimental investigation are also presented in this chapter. These details include determination of the adopted parameters, the levels of these parameters, the types of responses and the form of the used design of experiments (DoE). The experimental investigation focuses on the process parameters including laser power, velocity, frequency, hatching, focal length and incidence angle, whereas the experimental measurements of process responses are groove dimensions (width and depth), groove edge dimensions (width and height), surface roughness, the structuring ablation types, structuring accuracy, structuring quality and the metallization quality and reliability.

Chapter 6 and 7 presents the results and the discussion of the experimental work. In this section, the relationship between the adopted process parameters and the final process responses have been shown, analyzed and discussed deeply. In addition, the interaction between these adopted parameters is also explored and discussed for all process responses, which helps to understand the influence of the adopted parameters in this investigation. The experimental investigations are implemented in this chapter in order to determine the impact of process parameters on the LDS and metallization quality. The quality of LDS process has a great significant concerning the final quality of MID structure, which is clearly observed in this chapter in conjunction with the important relationship between the adopted process parameters and the process responses.

Chapter 8 is about the modeling and the optimization. It presents the reasons behind using modeling tools in engineering fields in general and in LDS-MID processes by describing the advantages and the potential of modeling. Further details about the Artificial Neural Networks (ANN) and Response Surface Methodology (RSM) approaches are also described, as important kinds of modeling approaches that

are proposed to use in this work. These details include the modeling requirements, the modeling structure, steps and procedures of the modeling. The results and discussion of these models are presented in another part of this chapter. They include empirical equations of all process responses, which can be used to correlate these responses with all the process parameters, to analyze the impact of each parameter on the responses and to analyze the interaction between parameters and their impact on the responses. The results of these models are compared with experimental work as validation procedure of the model's accuracy. The comparison shows a good matching between them. The proposed models are used to determine the optimum parameters setting that can be used to support the quality, accuracy and reliability of the MID structure.

Chapter 9 and 10 presents and summarizes the most important conclusion of these researches. The chapter concludes with recommendations for future work.

2. Background of MID and LDS Processes

2.1 Introduction

Currently, the latest trend in the electronic industry is continuous miniaturization and increasing the functionality of the devices, which consume thus less space. It clearly means the printed circuit board (PCB) should contain numerous electronic functions and be able to face the steady reduction in product life cycles. Several industries in the automotive and the medical sector demand modern products and components, which ensure high quality. Consequently, to face these challenges and to enable three-dimensional shapes, the Molded Interconnect Devices (MID) are developed by the electronics industry.

Basically, an MID is a molded circuit board manufactured by injection molding combined with printing processes. It was introduced in the early 1980s by the companies in the United States [1]. The USA were the leader in MID field from the late 1980’s until the 1990's. Then the situation changed and the Germany emerged as the leader in this field and continues to be till date [2]. Initially, the development was focused on the possibility to utilize different materials and metallization processes. During the 1990s, the companies and the research institutes combined their projects to develop this process. The MID market is expanding vastly. From 2000 to 2008, it grossed from 7 to 50 million Euros respectively. Whereas in 2014, the MID market size grew to more than 183 million Euros [3]. Thus, the growing market and the increasing significance of important applications in automotive or health sectors use MID to improve their production processes and to achieve high product quality.

2.2 MID Definition

The Molded Interconnect Devices (MID) comprise of injection molded part with conductive circuit patterns, mechanical and electrical functions integrated on a single part. Figure 2.1 shows the sequence of MID technology. The process chain for manufacturing of MID can be divided into four steps including molding, structuring, metallization and placement of electronic components or the assembly. MID technology have many manufacturing processes. The most vital processes are the two-shot molding, the LDS (Additive Laser Direct Structuring), the LSS (Laser Subtractive Structuring), the mask structuring, the hot embossing, the film insert molding, the printing technologies, the plasma structuring, and the primer technology [4][5][6].

Figure 2.1: The principle of MID technology [1].

2.3 Application Fields of MID

The MID applications show a big spectrum in terms of the industrial applications and products. As an outcome, MID applications are successfully served in all markets for conventional circuit boards and electronic modules. The high-profile of MIDs regarding functionality and reliability make it suitable to serve in different fields and applications, especially in the automotive and medical technology. Furthermore, Asian manufacturers utilize MID technology for antenna applications and IT and telecommunication industry, which are applied in the aerospace field, the military technology and in the consumer goods.

2.3.1 Automotive

In the automotive industry, the manufacturers require a modern technology for communications and information, which guarantees a high safety and security with higher ecological awareness. The above mentioned traits necessitate the increase in the number of electronic systems and devices in cars. The sensors and the electronic control units such as engine control are an example of this application [7][8][9]. In addition, a higher degree of miniaturization and functionality are enabled by increasing knowledge of MID and process control. Furthermore, materials for MID are developed to resist extreme situations such as elevated temperature applications. Therefore high demands of reliability should be fulfilled for such important applications [10]. Further applications of MID in the automotive fields are shown in figure 2.2.

2.3.2 Medical Technology

The medical industry requires innovative and cost efficient products. Moreover, special characteristics are required for medical applications, which can be achieved using the MID technology. As an example, audiological devices, which extremely need the alignment of microphones in the smallest spaces or the accurate locating of sounds and tones [1] [11]. Other important applications are presented in figure 2.3.

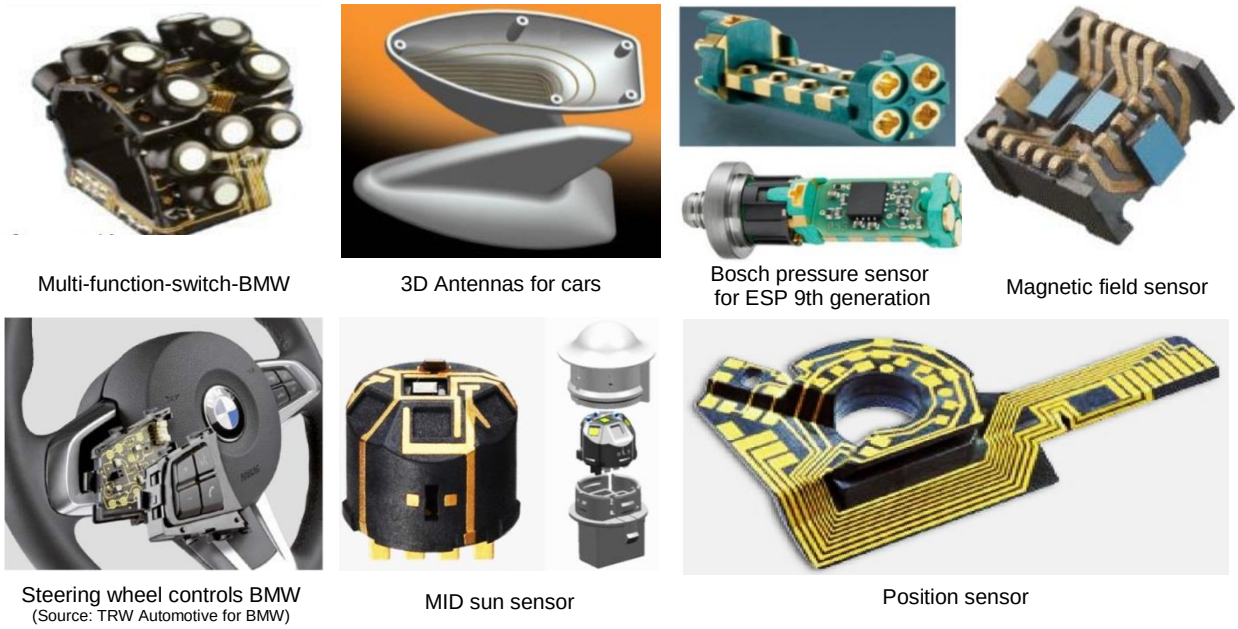

Figure 2.2: MID applications in automotive industry [7][8][9][10].

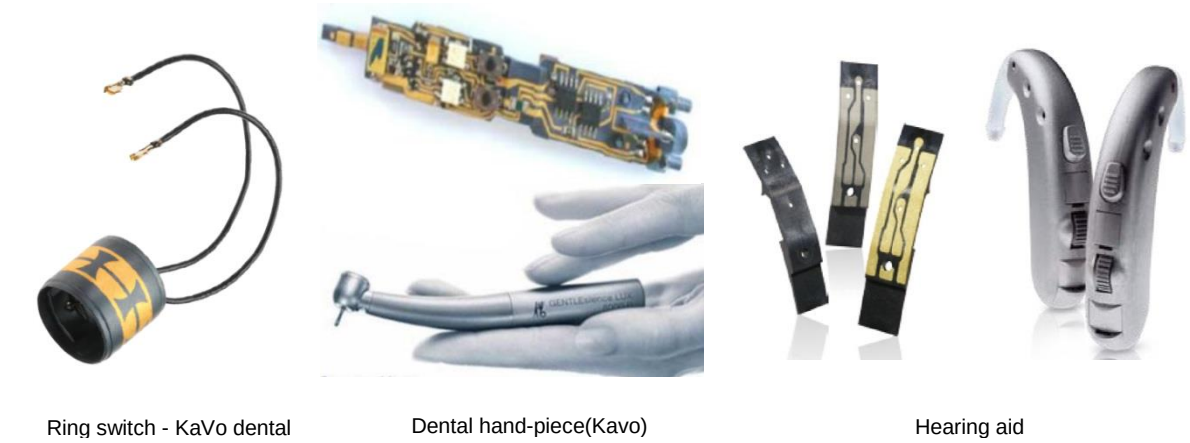

Figure 2.3: MID applications in medical technology [1][11].

2.3.3 IT and Telecommunications

The telecommunication industry based in Asia has a high demand for MID. Because of the advantages of MID, it has wide applications in this field. The most important applications include antennas for smartphones, wireless fidelity (Wi-Fi), Bluetooth, and universal mobile telecommunications system (UMTS). LDS antennas spanning 300 mm are integrated into the chassis of mobile computers which demand a thinner and lighter system, see figure 2.4.[1] [12].

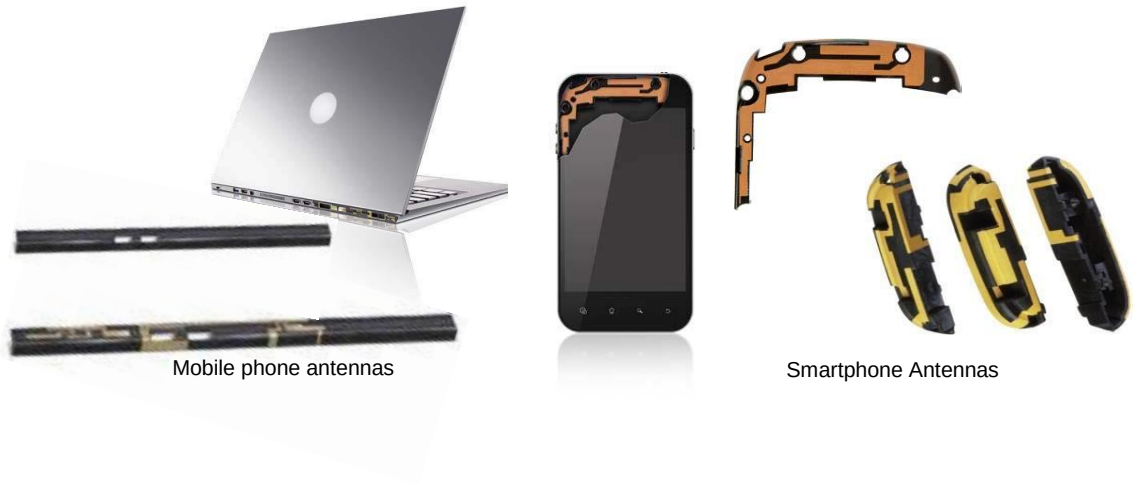

Figure 2.4: MID applications in IT and telecommunications [1][12].

2.3.4 Automation

MID are successfully used in the automation field, which require a high flexibility, availability, and profitability that can be achieved by MID. This makes the MID suitable for different applications such as intelligent sensor concepts, which are based on the arrangement of light emitting diodes (LED) or sensor chips and the radio-frequency identification devices (RFID) [7].

2.4 Potentials and Advantages of MID

In general, the introduction of MID provides many potentials and advantages. They are summarized in the following points: [1][13].

- ***Freedom of design*:** The MID technology offers new functions and better miniaturization of products by its ability to introduce three-dimensional design. This helps to integrate the electronics and the mechanics in one device and increase the flexibility to design random shapes. Miniaturization is vital to meet the strict demands of integration into small devices and spaces. Therefore, the designers must consider the installation space of mechanical-electrical assemblies while designing circuit boards. Furthermore, the flexibility of design allows the optimization of the available space by minimizing the necessary space and improving the position and shape of the three-dimensional devices [8] [13].
- ***Economization*:** MID are intended to provide economic objectives through the reduction of parts, shorter process chains, minor material consumption, and higher reliability. Thus, MID are perfectly designed to be suitable for keeping the energy and the resource conservation. In general, with MID technology, the construction methods and processes, the number of interfaces and

assembly steps can significantly be reduced. Additionally, the administration and logistics of the necessary parts are less costly, due to economized process chains [1] [13].

- ***Environmental sustainability*:** MID are also helpful to conserve the environment and save resources. Through the introduction of MID-related production systems and process chains, the material diversity and the consumption can be reduced extremely. Furthermore, it is easier to handle the material recycling and disposal of the old MID [1] [13].

2.5 Laser Direct Structuring (LDS) for MID

As mentioned previously, the structuring can be performed using many ways. The most important and conventional methods are based on the laser as a structuring tool such as laser direct structuring (LDS) [1] [14]. The LDS technology has been developed by LPKF since 1997, as a production tool of MID products [7] [15]. By using the MID-LDS it is possible to produce high resolution circuits on complex 3D MID. It is suitable for a wide range of materials. Currently, the MID-LDS is a commercially available industrial process and has successful applications. This method uses a modified thermoplastic polymer, which is processed by mixing with special additive fillers. Nano powder particles of copper oxide-chromite with a density of 5.30 g/cm^3 are the commercial LDS additive. These additives can be activated by laser radiation. This activation process induces by physical-chemical and thermal reaction under the focal point of the laser beam. Due to the laser effect, the polymer bonds are broken and the chemical connections of the metal oxide molecules are released. This will act as the base for the next step, namely the metallization. In general, the production sequence for the additive LPKF-LDS technology includes three steps, as shown in figure 2.5 [1] [15]. These process chains include:

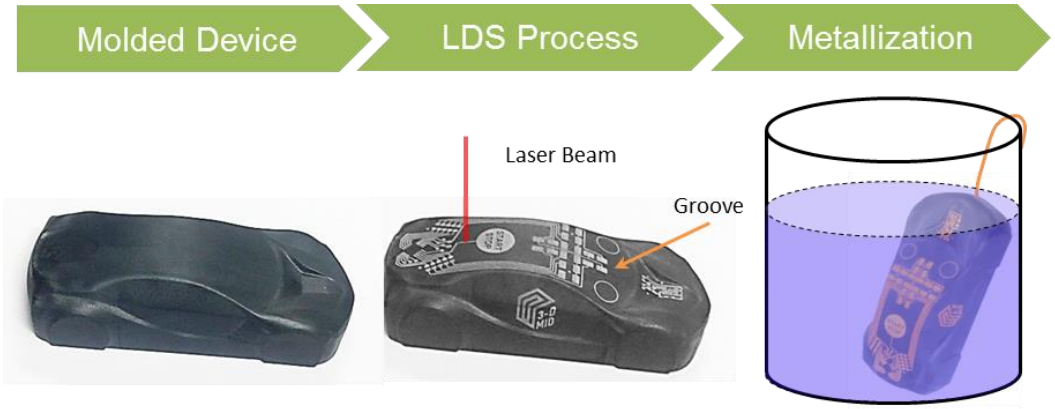

Figure 2.5: The production sequence of LDS-MID process [1].

2.5.1 Plastic Component Injection Molding

The first and the primary step is forming the designated shape in accordance with the one designed in a CAD/CAM-system. As mentioned earlier, the special additive fillers are mixed with the thermoplastic granules. For the LPKF-LDS® process, one-shot molding is sufficient and a huge variety of plastics can be chosen.

2.5.2 Laser Direct Structuring

The second step is the structuring of the circuit lines by the laser radiation. Generally, LDS is based on the principle of the ablation and activation of the nucleus by a laser beam. It draws a certain pattern of circuit lines on the surface through material removal, while the additive gets activated simultaneously. Thus, a micro-rough surface emerges. Figure 2.6 illustrates the ablation principle or the laser surface treatment during the LDS step. The new surface contains activated nuclei of the additive which enables a good adherence between the metal layer and the polymer.

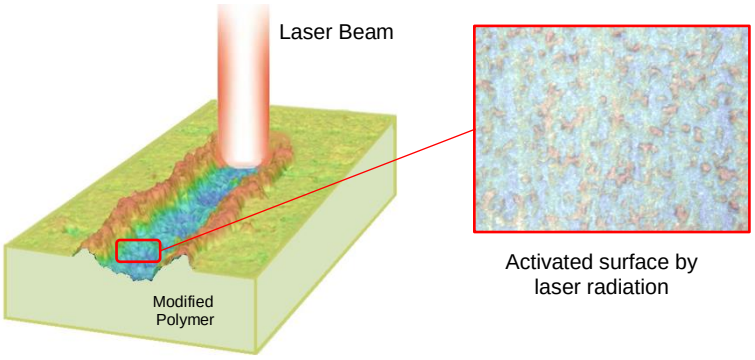

Figure 2.6: The laser surface treatment during the LDS step.

2.5.3 Metallization (Cu–Ni-Au)

After the activation in the structuring step, the electro-less copper plating bath is used for the metallization process. Afterwards, nickel and gold are added on top of the copper layer again by the electro-less plating. Before proceeding with the copper plating, a cleaning step is necessary to guarantee the quality of the conductor paths. This can possibly be done by an aqueous supersonic bath mixed with a surface-active agent, CO_2 snow jet cleaning, and water jet cleaning. The overall objective of the cleaning is removing the residues formed during the laser process. The thicknesses of the three layers are shown in Table 2.1, which shows the minimum, typical, maximum thickness and tolerance for those three layers [16].

Table 2.1: Thicknesses of the Cu-Ni-Au layers [16]

Layer thickness	Unit	Min.	Typical	Max.	Tolerance ± µm
Cu	µm	3	7	15	3
Ni	µm	3	7	20	3
Au	µm	0.05	0.1	0.15	0.05

2.6 LDS Process Parameterization

In the MID-LDS process, there are several and complex parameters which influence the quality. MID-LDS as the technology of interest in this thesis is influenced by many complexe parameters, specified in figure 2.7, which shows the 5 Ms diagram i.e. the fish bone diagram for these parameters. In each MID-LDS step, there are a lot of parameters, which affect the output quality of this step, moreover, some of these parameters are controllable and the others are uncontrollable. There are several research works, which investigate how the process parameters affect the quality of the MID using experimental analysis [17] [18]. All these studies explored the effect of only three traditional parameters including laser power, laser speed, and laser frequency. As mentioned in the previous chapter, the work of this thesis focuses on the LDS process as a main tool for the MID technology. Consequently, it will concentrate on the effect of the laser parameters namely the laser beam source and guidance and the structuring process groups which are shown in figure 2.7. Those parameters can be classified into two groups. The first is: ***working parameters***, which includes the laser power, velocity, frequency, and beam diameter. The second is defined as the ***design parameters,*** it includes the focal distance or focal length, incidence angle of the laser and overlapping or hatching between the laser lines. The focal length and incidence angle pose a threat for complex 3D shapes produced by LDS. The following sections define the most important parameters.

2.6.1 Laser Power

The optical output power of the laser beam is referring to the power of the laser. It is measured in Watts, and often mentioned in terms of nW, mW, W etc. The laser power can be defined as continuous output power of the continuous wave lasers (CW) or the average power for the pulsed wave laser (PW). This parameter has a significant effect on the LDS response.

2.6.2 Laser Frequency

The laser frequency refers to the number of pulses per second. It is measured in (Hz). Each pulse has a thermal impact on the incidence surface and any change in the laser frequency induces a change in laser energy, which depends on the laser power and frequency, see equation 2.1 [15] [19].

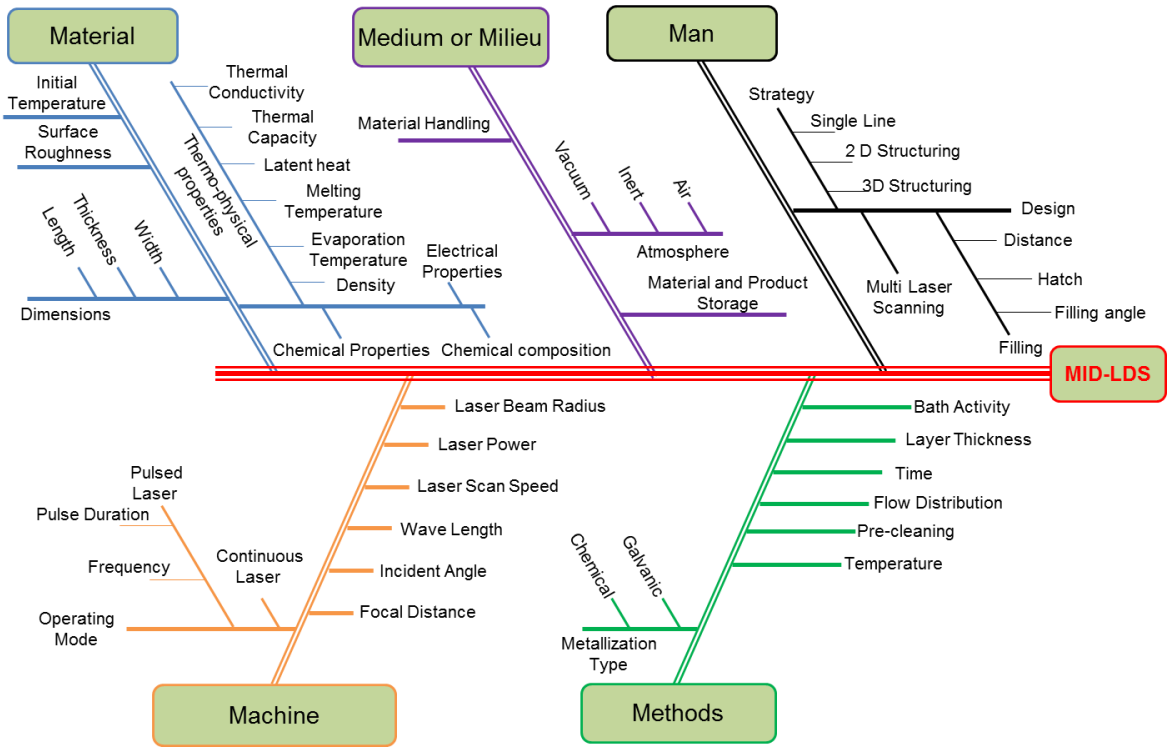

Figure 2.7: The 5 Ms-diagram, the influencing MID-LDS parameters.

$$Pulse\ Energy\ (E) = P_{Mean} \times t = \frac{P_{Mean}}{f} \quad or \quad P_{Peak} \times Pulseduration \qquad 2.1$$

Where, E is the pulse energy, P_{Mean} is the average power (W), P_{Peak} is the maximum power (W), f is the pulse frequency (Hz), and t is the time between two pulses (s), (see figure 2.8).

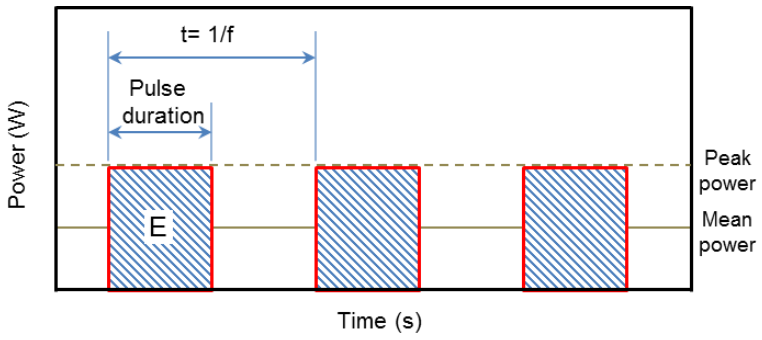

Figure 2.8: Pulsed laser description [15] [19].

2.6.3 Laser Scan Speed or Velocity

Laser scan speed is the speed of the laser beam which follows the path of the circuit layout. It is measured in (m/s). The laser speed is a controllable parameter that can be selected or defined directly on the laser machine.

2.6.4 Focused laser beam diameter and focal distance or focal length

The diameter of the laser beam is defined as the diameter focused by the used lenses. Moreover, this diameter contains 86 % of the focused energy. In the principle of the laser, the focus head receives the laser energy from the fiber optic cable. In the focus head, there is a set of leans by which the emitted laser light is focus on to the material being structured. There is a very important relationship between the spot diameter and the focal length of the lenses (see figure 2.9). Longer focal length produces larger spot diameter while the shorter focal length produces smaller spot diameter. Equation 2.2 describes the relation between the focal length, the entrance beam diameter, and the wavelength [20] [21].

$$D = \frac{2.\mathrm{FL}.\lambda}{\mathrm{Do}} \qquad 2.2$$

Where D is the focused laser beam diameter, FL is the focal length of the focus lens, Do is the entrance beam diameter, and λ is the wavelength, (see figure 2.9).

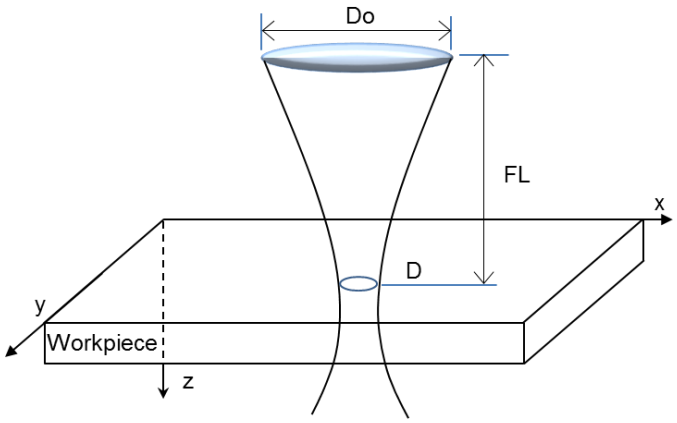

Figure 2.9: Focusing of laser beam.

2.6.5 Pulses and Passes Overlapping

There are two types of overlapping in the laser structuring process, namely the pulse overlapping and the laser passes overlapping or the hatching percentage [22]. Figure 2.10 illustrates the schematic representation of laser overlapping of the two laser passes. The overlapping between two subsequent laser pulses can be defined as a pulse overlapping (O_P). It depends on the laser parameters like the laser speed, the laser frequency, and the laser beam diameter. Equation 2.3 can be used to calculate this overlapping [23].

$$O_P = \left(1 - \frac{\mathrm{v}}{f.\mathrm{D}}\right) \times 100 \qquad 2.3$$

Where O_P is the pulses overlap, v is the scanning speed (in term of m/s), and D is the spot diameter (in μm). According to this equation the pulses overlapping increases with laser frequency or when the laser speed decreases at fixed spot diameter. The second overlapping is the hatching percentage. It is related to the distance between two successive laser passes (a). It can be calculated by using equation 2.4 [22] [23].

$$\mathrm{H} = \left(1 - \frac{\mathrm{a}}{\mathrm{D}}\right) \times 100 \qquad 2.4$$

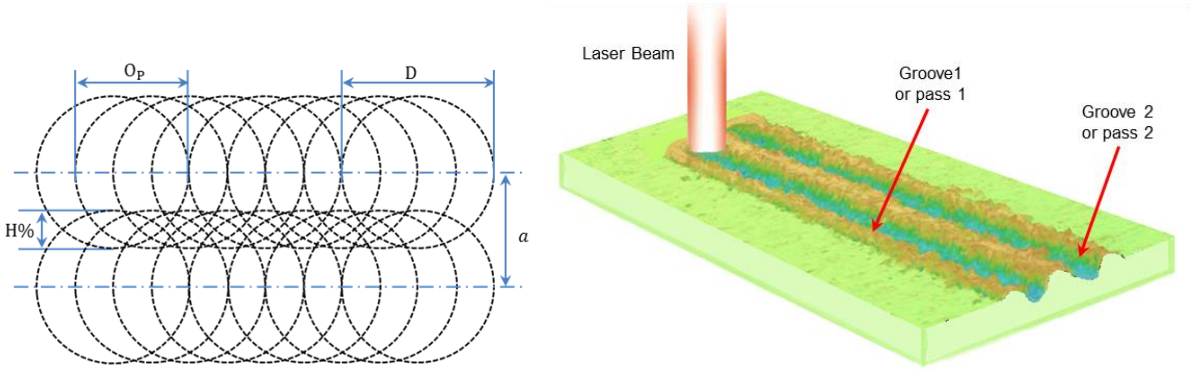

Figure 2.10: Schematic illustration of the laser overlapping

2.6.6 Incidence Angle of the Laser Beam

The angle of incidence refers to the angle between the laser irradiation and a line perpendicular to the surface of the substrate. According to the industry standard, there are limitations for this angle. It is possible to structure the surface of the substrate with angles of incidence less than 70 degrees, other ways the angle should be reduced by using the rotation of the component during the LDS process [24].

2.7 Motivations

The project focuses on the molded interconnect devices (MID) produced by the laser direct structuring process (LDS) and selective metallization. The main motivations of the current thesis can be summarized as follows:

- The available information from the industry standards and scientific researches doesn't cover all the LDS process parameters and their effect on the dimensional precision, quality, and reliability of the MID-LDS products.
- The relationship between the LDS process parameters is not completely clear. Moreover, the influence of these parameters on the process response is not thoroughly investigated.
- Further knowledge is needed in terms of implementation of three-dimensional and micro MID products, which need special process requirements. Due to this lack of available industry standards and information, further deep investigations are needed regarding the effective parameters in such micro MID applications.
- Real challenges appeared in the MID-LDS process to use new materials, which in turn can be utilized for further important MID applications. This required to find out the typical and the optimal process parameters, which can be employed to handle these new materials.
- The structuring quality and accuracy are affected by the heat accumulation and the temperature distribution of the structured surface. From another side, the heat accumulation and the surface temperature distribution are related to the effective process parameters which include working and design parameters. However, a need for the thorough investigation by using a computer simulation to explore the interaction between the laser as a heat source and the surface of the substrate at different process parameters is at stake.
- Modeling and optimization of the process parameters are extremely required to enhance the process efficiency.

2.8 Objectives

The main objectives of the research in this thesis are summarized as follows:

- Employ a computer simulation which utilizes a mathematical heat transfer model based on Finite Element Method (FEM) to calculate the temperature at each point of the substrate material and to estimate the temperature distribution during the LDS process. It has the capability of handling the 2D and the 3D applications, the nonlinear material properties, the heat source of the laser beam profile and the phase transformation during the LDS process. This helps to examine and analyze the effect of the LDS process parameters on the temperature distribution induced by the laser irradiation. Also, it helps to understand the complex relationship

between these parameters, the temperature distribution and the characteristics of the structured area.

- Experimental investigations based on the design of the experiment (DoE) are carried out to analyze the complex relationship between the LDS parameters which include:
    - Laser power
    - Laser scanning speed
    - Pulse repetition rate (frequency)
    - Hatching percentage
    - Focal length
    - Incidence angle

And the process responses which include:

- Groove dimensions (width and depth)
- Groove edge dimensions (Height and width)
- Groove profile
- Minimum circuit line width and pitch
- Surface roughness of the structured area (Ra and Rz)
- Structuring-ablation type
- Structuring accuracy and quality
- Metallization quality and reliability

For different substrate materials which include

- Polymers
- New innovative ceramic based materials

- Propose a mathematical model for the LDS process based on Artificial Neural Networks (ANN) and Response Surface Methodology (RSM) to correlate the process parameters and their respective responses.
- Explain the relation between the process parameters and determine their important factors.
- Perform a process optimization to define the process strategy regarding the proposed parameters setting that can be used to achieve the highest accuracy, quality, and reliability.

.

3. State of the Art

In the literature of the laser process and its applications, some studies focused on using the experimental investigations found by utilizing the design of experiment (DoE) to find the relationship between the process parameters and their response and then to suggest the optimum parameters. However, in many cases, experimental investigations are time and costly consuming especially for the processes, which have a numerous input factors. Therefore, modeling of the laser process and its numerical or computer simulation serve as a tool for other researchers for cost reduction and to decrease repeatability. The DoE can be used as a base to develop a mathematical model for any process, which can also be used to define the optimal process parameters. The simulation is mostly devoted to building up thermal heat transfer models to find the temperature distribution which is in turn used to predict the ablation dimensions and characteristics under the laser irradiated domain. So far, no experimental investigations, mathematical modeling, and numerical simulation have been employed to cover all the important process parameters. Approximately, all the previous studies focused on the classical process parameters including laser power, laser speed, and laser frequency. Anyways, the literature of the laser process and its applications can be classified into three groups. They will be explained in the following sections.

3.1. Experimental Investigation

There are numerous applications for laser technology in engineering especially in material processing, which include laser machining, drilling, cutting, welding, and surface treatments. All these applications are mainly based on the conversion of laser radiation energy into local heat. The main difference between these applications and the laser direct structuring is in the parameter setup. According to the parameter set up, the substrate surface obtains different heat input under the effect of the laser source. Therefore, various effects occur in the material like heating, melting, vaporization or plasma shielding [25][26].

In the previous works, the researchers described the principles and steps for the additive LPKF-LDS technology [10][27]. The LDS process was presented as one of the important methods to produce fine circuit lines with a high degree of flexibility in the circuit layout compared to conventional methods. Moreover, these works defines the requirement to qualify the LDS-MID technology as it designates several applications from this process. With the increase in implementation of the LDS process to produce MID products in various applications, the ability of the LDS process to produce fine circuit lines with high quality and reliability is at stake. This is the main reason behind the various aspects of much research in this field.

The adhesion strength between the metallization and the thermoplastic substrate is one of the most important requirements for the quality of MID products. T. Kuhn [28] investigated the factors influencing the adhesion strength. The work employs various tests methods for measuring the adhesion strength including traditional methods like the pull-off test, peel test and shear force measurement test. Also, a new method called the hot pin pull test is used to measure the adhesion strength of the substrate. The investigation was carried out on two different materials which include the LCP Vectra E840i LDS and PA6T/X Vestamid HTplus TGP 3586. It was found that the micro-rough surface produced by laser structuring is essential for increasing the adhesion strength. This result was assured by all the above mentioned measuring tests.

Another study performed in [29] utilized the hot pin pull method to examine the adhesion strength of MID structures, which was governed by the laser process parameters like the laser power, laser frequency, and laser velocity. It was performed on polymer based material of LCP Vectra E840i LDS and PA6T/X Vestamid HTplus TGP 3586. The researchers investigated the variables of the test which includes the influence of the size of test pads, the temperature profile and the wetting of test structures. As a summary, increasing peak temperatures and the pad diameter had a negative effect on the adhesion of the metallization structure. Moreover, for reliable results, the tested area should be covered completely by the solder material.

All previous publications and literature approximately assumed that a U-shaped groove was created due to the laser irradiation, but this hypothesis unrealistic. Actually, the groove form is completely different. Therefore, a further inspection was essentially carried out to realize the relation between the LDS process parameters and the groove characteristics. Consequently, a deep understanding is obtained for the impact of grooves on the metallization structure [17]. Experimental investigations and optimization of the LDS process were conducted in [17]. In this study, the researchers employed the design of experiment method (DoE) to investigate the influence of the laser power, the laser speed, and laser frequency on the groove dimensions (width and depth), groove profile and quality of the LDS process. These experiments were performed on a polymer plate of PA6T/X Vestamid HT plus TGP 3586 which was structured using an Nd:YAG laser machine. The researchers concluded that the effect of laser speed and laser power on the groove profile and dimensions are greater than the effect of laser frequency. Moreover, the metallization profile depends on the groove profile which again depends on the LDS parameters. It was also found that the dimensions of the resolidification groove edge including width and height must be reduced to its lowest possible value, in order to increase the LDS quality.

An experimental study was performed in [30] to examine the influence of LDS parameters on the MID quality. The study was employed to optimize the laser

parameters which govern the roughness and adhesion of the metallization structure (Cu-Ni-Au) layers. In this work, the researchers discuss the impact of three classical parameters, namely laser power, laser speed, and laser frequency. The investigation was performed for different polymers substrates made of LCP Vectra E840i LDS, PA6/6T Ultramid T4381 LDS and PET+PBT Pocan DPT 7140. Moreover, after optimization of the laser activation process, two different leveling tactics were used to improve the bonding between the aluminum wedge-wedge wire bonding and the metallization structure. These leveling processes utilize a stamping with a heated tool and CO_2 snow jet processing. It was concluded that the leveling process is required after laser activation and before electro-less plating to increase the bonding between aluminum wedge-wedge wire bonding and the metallization structure.

The LDS-MID process was introduced as an important and accurate method to produce 3-dimensional (3D) electronic parts in [31]. The researchers in this work give an overview of the advantages of galvanic and chemical plating (metallization) for 3D-MID as well as the differences in the plating processes between the galvanic and chemical precipitation. The requirements which should be considered for the development of the galvanic process are also discussed in this work.

A further study focused on the metallization process as an important step in the MID process [16]. This study focused on the chemical plating of MID parts that are made of thermoplastic substrates. The low conductivity of the thermoplastic materials makes them unsuitable for galvanic metallization. The chemical reactions during the metallization process, the process sequence for chemical plating, the layer thicknesses of the standard (Cu-Ni-Au) coating system and the important requirements to enhance the metallization quality are described in this study. It was mentioned that the high adhesion strength of the metallization structure can be accomplished by the rough surface. On the other hand, a smooth surface is required for supporting the adhesion of the wire bonding on the metallization structure. Therefore, a leveling by means of CO_2 snow jet cleaning and the stamping are proposed for the implements of their adhesion strength [30].

The traditional plastic based materials that are used in MID applications have limited properties such as low thermal stability. This drives to propose new inventive materials, which can be used in further MID applications or to realize different objectives. In this respect, different directions were taken for the purpose of development. One is regarded use an alternative base material such as ceramics. Another focused on proposing substitution of additives or even using a substrate material free of additives [32].

A new material based on high-performance ceramics has been proposed in [32]. They used alumina ceramics (AL_2O_3) as a base material without any additive. This ceramic substrate can be activated by using the laser process to make it suitable for the metallization by electro-less plating. The impact of the process parameters

including laser power, laser speed and laser frequency on the structure characteristics was investigated in this study. The researchers concluded that metal line pitches of less than 200 µm are feasible. They found also that the metallization thickness of ceramics is less than that for polymer base materials.

Experimental analysis on Nd:YAG laser micro-turning of alumina ceramics was carried out by G. Kibria [33]. The study designed to explore the impact of the laser parameters such as lamp current, laser frequency and laser beam scanning speed on the output responses such as surface roughness. The laser direct structuring was also used to produce printed circuit boards (PCB). B. Zhang [34] investigated the quality and reliability of the fine circuit lines on PCB fabricated by using LDS processes. The researchers employed open/short, surface insulation resistance (SIR) and peel tests to define the quality and the reliability of PCB products. The effect of the width of circuit lines/spaces and the etching time were only considered in this study. In another study [35], B. Zhang investigated the feasibility of using excimer laser in laser structuring instead of Nd:YAG lasers in the production of fine circuit lines on the PCB. In this work, the impact of the laser parameters such as laser power, laser frequency, and number of repetitions on the laser structuring was investigated. It was found that the groove depth increased with laser power while it decreased with laser frequency.

Due to of lasers advantages namely the flexibility, accuracy, high production rate, and quality, they can also be used in micromachining, cutting and drilling processes. There are a lot of commonalities between the LDS process and these applications. Therefore, it is very important to explore the trend of related researches.

By S. Genna [36], experimental work was performed to explore the mechanisms of the surface formation during the laser grooving of commercial poly-methyl-methacrylate (PMMA). A CO_2 laser source working in continuous wave and pulsed wave mode has been employed in the experiments. The study examines the impact of the process setup including released energy, laser wave mode (CW or PW) and scan speed on the process responses namely depth and surface roughness. Also, a semi-empirical model based on energy considerations was developed by the researchers to estimate the depth of the created groove and the roughness as a function of the related process setup. It was concluded that the groove depth and width increase with laser energy or when laser speed is reduced for both of the continuous and pulsed wave mode, also high scan speed and CW mode are desirable for a smooth surface.

L. Romoli [37] carried out experimental and theoretical studies to examine the vaporization of PMMA during the manufacturing of 3D cavities by CO_2 laser machining. A theoretical model was proposed to investigate the impact of the laser radiant flux, laser scanning speed, and number of passes on the created groove profile (depth and width). The main results of this study were: the groove depth and

width are directly proportional to the laser power and number of passes and inversely proportional to the scanning speed.

An experimental work for the laser micromachining of the MEH–PPV polymer was taken by C.R. Mendonca, et al [38]. In this study, the effect of some laser parameters such as pulse energy and laser scan speed on depth of the laser groove and surface roughness of the micro-machined area was investigated. The researchers conclude that the surface roughness and the groove depth increase with laser energy. The relevance among laser fluence, ablation depth and rate for different materials has been studied by G. Raciukaitis et al [39] and G. Spyratou et al [40]. These experimental works carried out to study the effect of the laser fluence on the depth and metal removal rate.

3.2. Simulation of Laser Process

In laser-material processing, the computer simulation is used as a powerful tool to investigate the impact of the laser on the work-piece in terms of process parameters and process responses. Some of these works are restricted to certain process parameters like the laser power, laser speed, and the laser frequency. Other studies are based on a limited model regarding the physical meaning of the laser process.

A simulation for the LDS system by three-dimensional mathematical heat transfer model is implemented in [41]. In this study, a three-dimensional numerical heat transfer model has been employed to describe the thermal behavior during the laser structuring process of the polymer substrate material. This model provides a full description of the temperature distribution, as well as it calculates the depth and the width of the groove upon material removal at a different set of laser parameters. This simulation employed the finite element methods (FEM) to solve the transient thermal heat transfer model by using APDL (ANSYS Parametric Design Language). The effect of the mixed boundary conditions which consist of convection and radiation heat transfer is also considered in this simulation, while the effect of latent heat of fusion and the variations in the thermal material properties with temperature are not considered. In order to verify the simulation results, experimental works were conducted to study the effect of the laser parameters including laser power and laser speed on the depth and width of the created groove.

In [42] a new simulation procedure based on a three-dimensional finite element model was developed. The effect of the latent heat of fusion, the temperature on the material properties as well as the 3D Gaussian heat source for the laser beam are considered in this work. The used material was a polymer plate of Poly-Ether-Ether-Ketone (PEEK). The effect of the process parameters including laser power, laser speed, laser frequency, hatching percentage or overlap between the laser lines, laser incidence angle, and focal length are experimentally and theoretically investigated. This simulation can be used to predict the temperature distribution, maximum

temperature, groove dimensions and groove profile for different process parameters. The theoretical and experimental results showed a good accordance.

A 2D model was developed by [43] [44] to simulate the laser drilling process of aluminum substrates and tungsten alloys. The effect of phase change in both melting and vaporization are considered in this model. The researchers utilize a mathematical model based on the thermal energy equation to determine the temperature distribution which in turn predicts the heat affected zone (HAZ), dimensions and shape of the holes formed and the process quality. It was found that the groove depth and width tend to increase as the power density amplifies. An experiment was performed to verify the validity of the simulation results and to analyze the laser drilling process.

By M. Moncayo [45] [46] a computer simulation in conjunction with experimental investigations has been performed. These studies focused on the laser surface modification (LSM) process as an important tool to generate a specific surface topography for the alumina surface. A 2D mathematical heat transfer model was used in this simulation. This model takes into account the effect of the complex boundary conditions as well as the phase change during the LSM process. The researchers employed COMSOL Multiphysics software to find the final solutions for the proposed model. The study in [45] explores the effect of laser power on the surface temperature and the cooling rate, consequently the influence of these results on the variation in the surface characteristics. It is found that the density of the laser energy increases the surface temperature, the width, and depth of the melting and the vaporization. The impact of laser scanning speed and fill space or the hatching is investigated in [46]. This study is designed to discuss the multi-track laser surface modification (LSM) process for alumina also.

A. Joshi [47] proposed a mathematical thermal model in conjunction with experimental investigations for the laser assisted machining of ceramics silicon nitride materials. A finite element method has been used to find the final solution for the moving Gaussian heat source of the laser beam by employing the APDL. In this study, the effect of the laser process parameters including laser power, speed and beam radius on the temperature distributions in both the FEM simulation and the experimental were considered. It is concluded that the temperature of the work-piece is directly proportional to the laser power and inversely to laser speed and beam radius.

3.3. Modeling of Laser Process

The numerical methods and their applications such as artificial neural networks (ANN), response surface methodology (RSM), multi-regression, genetic algorithms, etc. have been sophisticatedly used in the last decades. These methods service as an important tool to develop a mathematical model for any process, by establishing mathematical relationships between the controllable process parameters and the desired responses.

A study has been performed in [18] to model and optimize the laser structuring process using the artificial neural networks (ANN) and response surface methodology (RSM). The proposed models are base on experimental work, which utilize the DoE data of the LDS processes. These DoE data examined the effect of the process parameters including the laser power, laser speed, and the laser frequency. The proposed models are used to study and analyze the influence of these process parameters on the groove dimensions (width and depth), lap dimensions (lap width and height) and the interaction width or the laser track width. These are vital to determine the line width/space in MID products and the longitudinal surface roughness which is crucial for the adhesion strength of MID structures. Moreover these models are capable to find the optimum LDS parameters that provide the required micro-channel dimensions with the suitable surface roughness.

The ANN approach was developed to predict the CO_2 laser cutting process of stainless steel by M. Madic [48]. This model was used to study the effect of process parameters such as specific laser energy, focus position and the assist gas. The optimum cutting conditions were identified through the proposal ANN model. [49] study the same laser cutting process with the kerf taper angle obtained in CO_2 laser cutting. The researchers used ANN method for proposing a model to study the relationship among the laser cutting parameters such as laser power, cutting speed, assist gas pressure and the focus position.

M. Ismail [50] and K. Kalaiselvan [51] proposed ANN in the laser micro-welding of thin steel sheets to describe the impact of the process parameters including laser power, laser scan speed and the laser beam diameter on the weld bead (depth and width) and pool geometry. The ANN approach is also used to predict the weld bead geometry with a wide range of process parameters. The researchers tested the accuracy of the proposed ANN model by comparing it with the experimental data of the laser micro-welding.

X. Wang [52] carried out a mathematical modeling using RSM method for the laser transmission welding (LTW). The proposed model was devoted to explore the influence of the process parameters namely the laser power, laser velocity and the stand-off distance or the focal length on process quality. These input process parameters were correlated with the process response namely the characteristics of

the molten pool geometric (width and depth of the e pool) and the ratio of the molten pool depth to the welding material thickness (D/T).

ANN and multi-regression approaches have been used in the laser heat-treatment of 4340 steel to make surface modifications [53]. The authors proposed a model based on the above mentioned methods to predict the hardness profile and depth. These models are also used to study the effect of process parameters and material properties on the surface hardness. The researchers concluded that the ANN and Multi Regression model could be used to propose a model for this process due to the good agreement with the experimental data.

A study presented in [54], discussed the application of the artificial neural network numerical methods in the laser milling tests of poly-methyl-methacrylate (PMMA) plates. The proposed model is used to correlate the adopted input process parameters like laser power, laser wave mode (CW and PW), and the laser scan speed with the responses like the depth and the surface roughness.

4. Thermal Simulation of LDS Processes

Simulation has been used in the last decade as an alternative tool complementary to the traditional prototyping and testing. Such a process is helpful to reduce the required effort, cost, time-consumption and helps to successfully predict product or process performance with easy-to-modify computer models. This chapter defines and outlines the concept of thermal simulation for the LDS process as it relates to analyze, understand and optimize the LDS process parameters. It will also describe method and procedures to perform significant LDS simulation; specifically, how can computer simulation be utilized to perform thermal analysis of LDS processes.

Laser processes, in general, are characterized by highly concentrated beam energy. This makes it difficult to use an accurate measurement of temperature and its distributions at different points of substrate surfaces or inside the based material. Therefore, the computer simulation acts as an important and powerful tool to perform this investigation. Theoretically, this will help to examine and analyze the effect of the LDS process parameters including working parameters, design parameters and material parameters on the temperature distribution which is induced by laser irradiation. Furthermore, it is necessary to understand the relationship between these parameters and their influence on the temperature distribution, groove dimensions, and groove profile. In order to build up the thermal simulation, the following requirements should be defined.

4.1 Proposed Model

The proposed mathematical heat transfer model which is used in this simulation is shown in equation (1) [42][55][56]. This model employs the governing equation for the non-linear 3D transient heat conduction undergoing moving heat source.

$$\frac{\partial}{\partial x}\left(k_x \frac{\partial T}{\partial x}\right) + \frac{\partial}{\partial y}\left(k_y \frac{\partial T}{\partial y}\right) + \frac{\partial}{\partial z}\left(k_z \frac{\partial T}{\partial z}\right) - \rho C_p v \frac{\partial T}{\partial x} + \dot{q}_{LASER}(x, y, z, t) = \rho C_p \frac{\partial T}{\partial t} \qquad 4.1$$

Where T is the temperature (in °C), it is a function of x, y, z and the time t in seconds (s), *v* is the velocity of the laser beam (m/s), ρ is the density of the material (kg.m^{-3}), k_x , k_y and k_z are the thermal conductivity (W.m^{-1}.C^{-1}) in the three dimensions, C_p is the specific heat capacity (J. kg^{-3}.C^{-1}) and $\dot{\mathrm{q}}_{\mathrm{LASER}}$ is the volumetric laser heat source per unit volume (W.m^{-3}).

This proposed model, in equation 1, can be used to define the temperature distribution within the body, based on the energy conservation law. In this model, the first three terms on the left-hand side represent the energy conduction across the work-piece. The fourth and the fifth terms represent the required energy for the

phase change during the LDS process and the input heat flux from the laser source respectively. Finally, the term on the right-hand side represents the change of the internal energy with time. Figure 4.1 shows this energy and the boundary conditions.

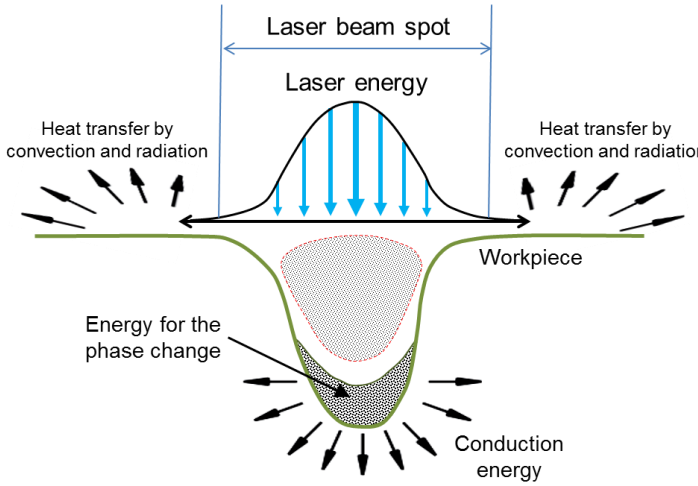

Figure 4.1: The energy and the boundary conditions.

4.2 Initial and Boundary Conditions

In order to complete the mathematical description of the thermal problem, the initial and boundary conditions should be specified as follows:

4.2.1 Initial Conditions

At a time of 0 (s), the workplace is at its initial condition. Equation 4.2 can be used to define the initial conditions in the thermal model.

$$T(x, y, z, t = 0) = T_o(x, y, z) \qquad 4.2$$

Where $T_o(x, y, z)$ is the initial temperature which is closed to be $27\ ^\circ C$.

4.2.2 Boundary Conditions

When the heat is conducted inside the material, this leads to increase the material temperature. This increase depends on the material properties such as thermal properties, physical properties and the amount of the heat flux from the laser beam, which depends on process parameters. Consequently, heat losses from the surface of the substrate will take place by natural convection and radiation [41][55][57].

Thus, the boundary conditions are divided into two types which include radiation and convection. They can be defined as

$$-k_n \frac{\partial T}{\partial n} = q_c + q_r \qquad 4.3$$

The radiation heat transfer formula is

$$q_r = \delta\varepsilon(T_{Sur}^4 - T_a^4). \quad 4.4$$

And the convection heat transfer formula is

$$q_c = h_c(T_{Sur} - T_a). \quad 4.5$$

Where: h_c is the convection heat transfer coefficient ($W.m^{-2}.C^{-1}$), T_{Sur} is the temperature of the work-piece surface, T_a is ambience temperature, ε the emissivity and δ is the Stefan-Boltzmann constant (5.67×10^{-8} $W.m^{-2}.K^{-4}$).

4.2.3 Convection Heat Transfer Coefficient Calculation

The heat transfer coefficient calculation is a very important step, which should be considered in this thermal simulation. The methods below have been used for calculation of the heat transfer coefficient [57][58].

Calculate the Reynolds number.

$$Re = \frac{\rho V L}{\mu} \quad or \quad \frac{V L}{v} \quad 4.6$$

Where ρ is the density kg/m^3, V the air velocity (1.2218 m/s) [59], μ is the dynamic viscosity of the air (N·s/m^2), v is the kinematic viscosity of the air (153.5*10^{-7} m^2/s at temperature of 20 °C) and L a characteristic length (0.04 m).

Calculate the Prandtl number.

$$Pr = \frac{v}{a} = \frac{C_p \mu}{k} \quad 4.7$$

Where α is thermal diffusivity, α =k/(ρ C_p) in (m2/s) which is about 20*10^{-6} m^2 /s at 20°C), C_p is the heat capacity (J/kg°C) and k the thermal conductivity of the air (0.0262 W/m°C).

Calculate the Nusselt number.

For turbulent flow which has been defined according to the Re number Nu can be calculated by equation

$$Nu = \frac{0.037 Re^{0.8} Pr}{1+2.443 Re^{-0.1}(Pr^{0.667}-1)} \quad 4.8$$

Then the heat transfer coefficient h can be calculated by using equation 4.9

$$Nu = \frac{h\, Dc}{k} \quad 4.9$$

Where: Dc is the characteristic length (0.1 m). According to the above equations 4.6 to 4.9 the heat transfer coefficient has been calculated. It is found to be about 5.73 W/m^2°C.

4.3 Laser Source Models

The physical phenomena of the heat source of laser beam profile in the LDS process can be modeled by using the most popular two profiles: they are the hot top and the 3D-Gaussian profile. Figure 4.2 shows these profiles and the differences between them. The Gaussian profile distribution shows that the maximum heat flux or the laser power density is located at the center of the laser beam spot, while the minimum value sets at the boundary of the beam spot. On the other hand, a constant laser density over the laser beam spot can be noted for the hot top profile. In general, the laser heat flux is affected by different laser parameters including the laser power, the laser beam diameter, the radial distance from the laser beam spot center, focal distance or z position, the laser incidence angle and the focal length [60][61].

In the present work, a 3D Gaussian heat source will be used due to its higher reliability for simulating the heat distribution. Equation 4.10 can be used to calculate the distribution of laser intensity under the laser beam spot [62][63].

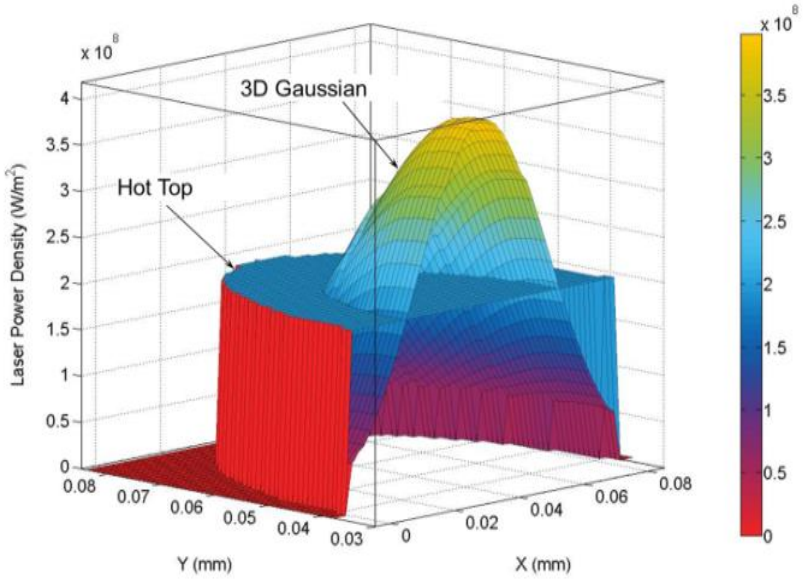

Figure 4.2: The hot top and the 3D Gaussian profile

$$\dot{q}_{LASER}(x,y,z) = \frac{2\,P}{\pi R(z)^2}\exp\left(-\frac{2\,(x^2+y^2)}{R(z)^2}\right) \qquad 4.10$$

Where P is the laser power (W), R is the radius of the focused laser beam (40µm), and x, y are the coordinates for the Gaussian curve at the surface of the work-piece (at z=0). In 3D LDS applications, the focal length changes with z value according to the shape of the 3D product, therefore, the focus radius (spot size) will be also changed. It is very important to consider this changing in the 3D LDS simulation to

calculate the new spot size. Equation 4.11 can be used to calculate it as a function of z [62][64].

$$R(z) = R\sqrt{1 + (\frac{z}{z_r})^2} \qquad 4.11$$

Where z_r is the Rayleigh length ($z_r = \pi R^2/\lambda$), and λ is the wave length.

4.4 Thermal and Physical Materials Properties

For the proposed model in equation 6.1, the material properties including thermal and physical properties should be defined in order to find the final solution for this model. In fact, these material properties are depending on temperature. Therefore, the effect of temperature on these properties should be considered in this simulation. In the next steps, the material properties of the PEEK material, which has been employed in the simulation, will be defined as follows:

The thermal properties, including the thermal conductivity and the specific heat capacity of PEEK polymer at different temperatures, are shown in table 4.1 and 4.2 respectively [65][66]. Whereas, the other important thermal and physical properties of the PEEK material are shown in table 4.3 [67][68].

Table 4.1: Thermal conductivity of PEEK at different temperatures.

T °C	25	50	100	150	200	250	300	343
K $W.m^{-1}.K^{-1}$	0,25	0,2538	0,259	0,265	0,271	0,278	0,2848	0,29

Table 4.2: Specific heat capacity of PEEK at different temperatures.

T °C	25	50	100	150	200	250	300	350	380	400	450	500	550
Cp $(J.kg^{-1}K^{-1})$	2160	2217	2294	2371	2448	2525	2602	2679	2725	2756	2833	2910	2987

Table 4.3: Thermal and physical properties of PEEK.

The properties	**value**	**Units**
Density		(g/cm3)
ρ_a (density of amorphous phase)	12.62	
ρ_c (density of crystalline phase)	14.00	
T_g (Glass transition temperature)	143	°C
T_m (Melting temperature)	343	°C
H_f (Heat of fusion)	130	J/g

Under the effect of the laser beam, a phase transformation occurs from solid to liquid for the PEEK material. This transformation and the latent heat of fusion should be considered in the thermal analysis of the LDS process, due to their importance. This can be carried out in this simulation by increasing the specific heat in the temperature range between the solidus (T_S) and liquids temperature (T_L). As mentioned in the proposed model in equation 4.1 is considered the effect of temperature on the enthalpy. This effect can be defined by using equation 4.12, which can be used to describe the temperature-dependent enthalpy (H) during the process [69]-[71].

$$H = \int_{T_o}^{T} \rho(T) C_p(T) dT \qquad (T < T_m)$$

$$H = \int_{T_o}^{T} \rho(T) C_p(T) dT + Hf_{melt} \quad (T \geq T_m) \tag{4.12}$$

Where H is enthalpy (J/m^3),T_o is the initial temperature, T_m is melting point of the PEEK material (°C) and Hf_{melt} is latent heat of fusion (J/kg^1). According to the equation 4.12, the three states of PEEK material including solid (H_s), mushy (H_m) and liquid (H_L), with respect to temperature can be calculated as follows:

$$H_s = \rho\, C_{p(S)}(T_S - T_o) \tag{4.13}$$

$$H_m = \rho\, C_{p(mz)}(T_L - T_S) + H_S \tag{4.14}$$

$$H_l = \rho\, C_{p(L)}(T - T_L) + H_m \tag{4.15}$$

Where $C_{p(mz)}$ is defined by using equation 4.16.

$$C_{p(mz)} = C_{p(m)} + \frac{Hf_{melt}}{T_L - T_S} \tag{4.16}$$

Where T_S is the solidus temperature (°C), T_L is the liquidus temperature (°C).

4.5 Simulation Procedures

As it is described in the previous chapter, the laser which is under investigation is a Nd:YAG pulsed laser. If the laser parameters are assigned to be: laser power of 1 W, laser speed of 0.75 m/s, laser frequency of 60 kHz and hatching percentage of 0 for the normal 2D structuring. Under these parameter set and according to the Nd:YAG laser characteristics, the first pulse for this laser will be in contact with the material surface for a period equal to the pulse duration which is about 23,7 ns, this is according to data of the laser source [72]. The laser intensity for this pulse, under a laser beam spot of 80 µm can be calculated by using equations 4.10 and 4.11. This is the first heat load of the laser beam source. Under this heat load of the first step (first pulse), the temperature of the substrate surface will be increased. The second pulse will contact the substrate surface after the time of 1/f, after 16.67 µs, at a distance of (v/f), which is 12.5 µm. This means the pulses overlap is about 84.4 %

[42]. According to this laser beam movement and pulses overlapping, there is an interaction between the pulses which leads to further increase in temperature of the substrate surface [42]. To describe the effect of the other pulses during the laser process, these pulses should be defined in the simulation steps be setting time, position and laser intensity, for all these pulses. Equations 4.18 can be used to define the pulse time and pulse position for each pulse, during the process respectively. Equations 4.10 and 4.11 can be used to calculate the laser intensity which is constant for each pulse. Figure 4.3 shows the interaction between pulses including the pulse overlapping, the matching between the laser intensity of the pulses, the groove formation, and the laser beam movement.

In the case of three-dimensional LDS applications, there is a variation in the focal length and incidence angle, which represents a serious problem in such applications. So that, it is very important to investigate, explain and then control these effects in the process. As it is expanded in the previous section, when the focal length is increasing or decreasing, the radius of the focal laser beam will be also increased, see equation 4.11. Consequently, the laser intensity, under the laser beam spot, will be reduced, according to equation 4.10. Due to the effect of laser incidence angle, there is a distortion in the spot of the laser beam at the substrate surface, as shown in figure 4.4. Equation 4.17 can be used to calculate the new spot area under the effect of incidence angle.

$$\text{Spot Area} = \frac{\pi D^2}{\cos \beta} \qquad 4.17$$

In this case, the laser beam spot should be recalculated by considering the effect of the laser incidence angle and focal length. Then the laser beam intensity or the 3D Gaussian heat source must be recalculated [24][73].

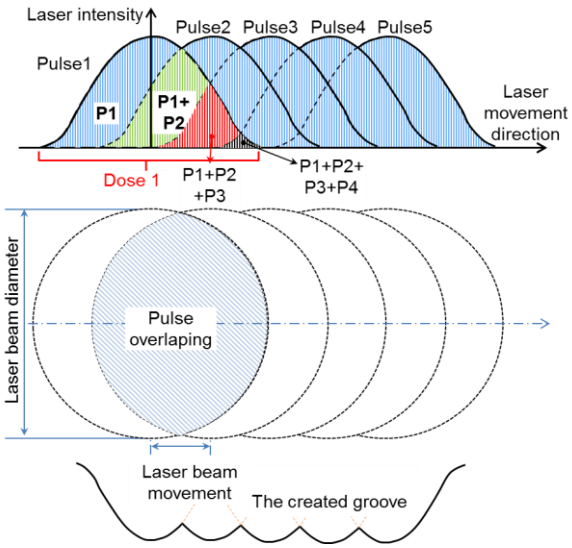

Figure 4.3: The interaction between pulses, the matching between the laser intensity and groove formation.

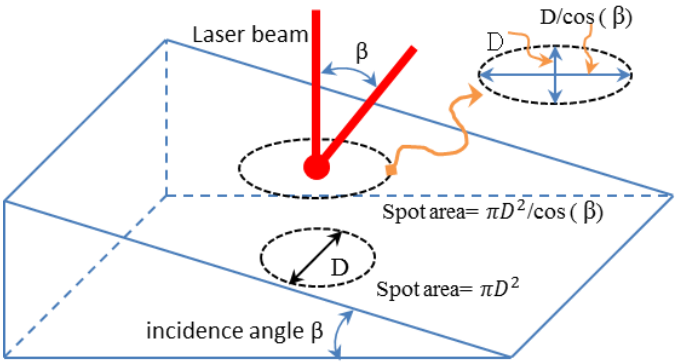

Figure 4.4: The effect of the incidence angle on the spot area.

The simulation task in this work includes a set of procedures and steps which are described below.

1. In the first step, the process parameters including the working parameters (power, speed, frequency) and the overlap between the laser lines or hatching will be defined.
2. In this step, the process will be checked, whether it is two-dimensional (2D) or three-dimensional (3D). If the process is 3D then it goes to the next 3D steps. If it is 2D then it goes to the 2D steps.
3. 3D steps: This step consists of different sub-steps. In the 3D case, the radius of the focused laser beam is changed at each point on the substrate surface. In this step, the 3D Gaussian heat source must be recalculated. By considering the effect of the focal length and the incidence angle on: first the spot area, second on the laser intensity.
   3.1 Calculate the new spot radius as a function of the focal length by using the MATLAB programming for equation 4.11. Export the results data to the ANSYS APDL to create the CAD system.
   3.2 Calculate the effect of the incidence angle on the area spot by using the MATLAB programming for equation 4.17. Export the result data to the ANSYS APDL to create the CAD system.
   3.3 Calculate the 3D Gaussian laser heat source by using the MATLAB programming for equation 4.10. Export the results data to the ANSYS Workbench to define it as a heat load.

The other simulation steps and procedures are shown in the flowchart in figure 4.5, which also shows the overall steps for the LDS process simulation.

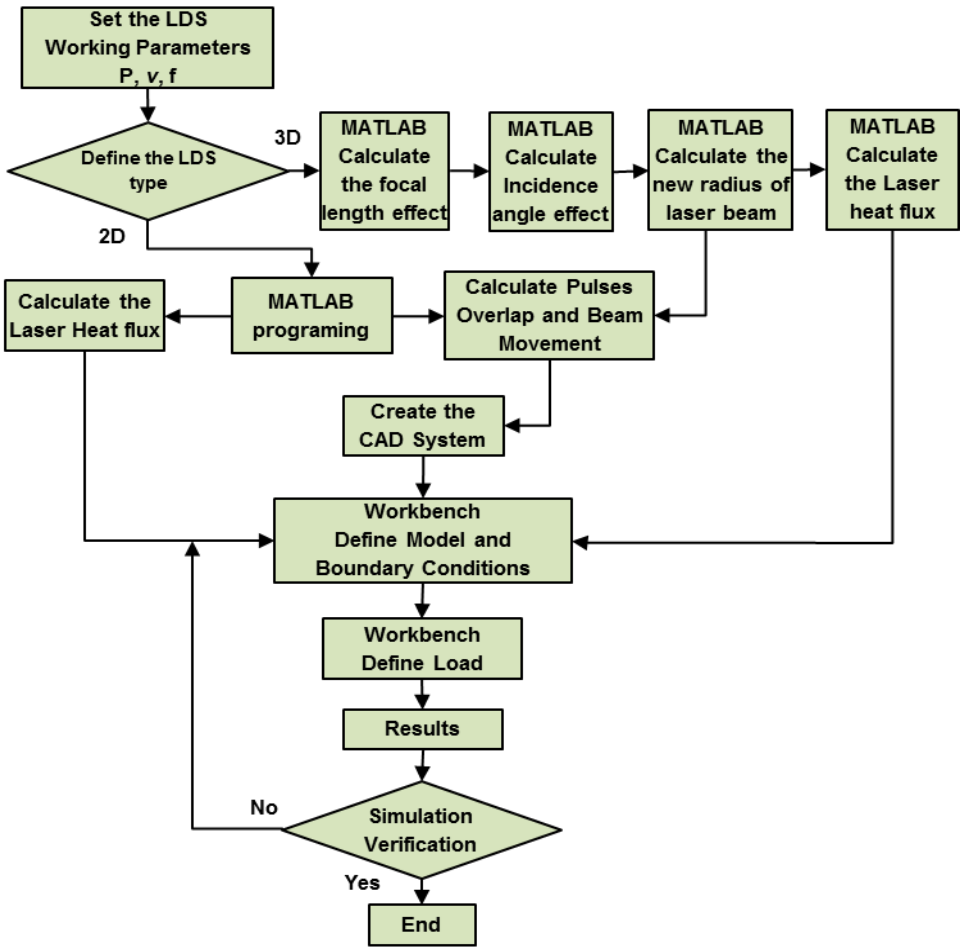

Figure 4.5: Flow chart for the simulation procedures.

4.6 Simulation Results and Discussion

As it was described previously, the simulation is necessary in order to understand the phenomenon of the structured area on the substrate surface or the groove formation, during the LDS process. Moreover, the interlaced relationship among the adopted laser parameters and their impact on the structured area will be understood. Because of the fact that the LDS process is predominantly a heat problem, the thermal simulation has been employed in this work. The temperature distributions for the material during the process at different parameter setups are the main results of this simulation. This means for each process setup, there is a different temperature distribution; consequently, there are different characteristics for the laser structured area.

4.6.1 Analysis of the LDS Parameters by Simulation

In order to clarify the relationship among all the LDS process parameters and the temperature distribution. The current simulation for the 2D/3D LDS process, which is based on a 3D heat transfer model, will be used to study, explain and analyze the

process parameters and their effects on the temperature distribution. Afterwards the outputs of the process, namely the groove profiles and dimensions, can be predicted as a function of the process setup. The theoretical investigations for the process parameters by using the computer simulation tool are designed to cover all the effective parameters, as it shown in Table 4.4. This table shows the total number of the adopted simulation tests, as well as the typical process parameters including working and design groups.

Table 4.4: The adopted study in the simulation.

Simulation Test No.	Focal length (mm)	Incidence angle (°)	Hatching (%)	Power (W)	Frequency (kHz)	Speed (m/s)	Max. fluence J/mm^2	PN per spot	Max. irradiation dose J/mm^2
1	0	0	0	1	60	0.75	3315.7	6.4	21220.6
2	0	0	0	1	60	1.5	3315.7	3.2	10610.3
3	0	0	0	1	100	1.5	1989.4	5.33	10610.3
4	0	0	0	1	140	1.5	1421	7.46	10610.3
5	0	0	0	1	60	2.25	3315.7	2.13	7073.5
6	0	0	0	5	60	2.25	16578.6	2.13	35367.6
7	0	0	50	1	60	1.5	3315.7	3.2	10610.3
8	3	0	0	1	60	0.75	3315.7	6.4	21220.6
9	3	0	0	5	60	0.75	16578.6	6.4	106103
10	0	20	0	1	60	0.75	3315.7	6.4	21220.6
11	0	20	0	5	60	0.75	16578.6	6.4	106103
12	0	0	0	5	60	0.75	16578.6	6.4	106103

For the simulation test number 1 in table 4.4, the corresponding laser working parameters are laser power of 1 W, a speed of 0.75 m/s, and a frequency of 60 kHz. According to these parameters, the interval time between two pulses is 1/60000 sec [15][19], during this time the laser beam moves a distance of (v/f) 0.0125 mm. The behavior of the material under the effect of the laser irradiation should be understood. In this work, a new classification for the three traditional process parameters including laser power, velocity and frequency will be employed to explain the interaction between these parameters and their influence on the structured area. Figure 4.6 shows the interaction between these parameters and the new classification.

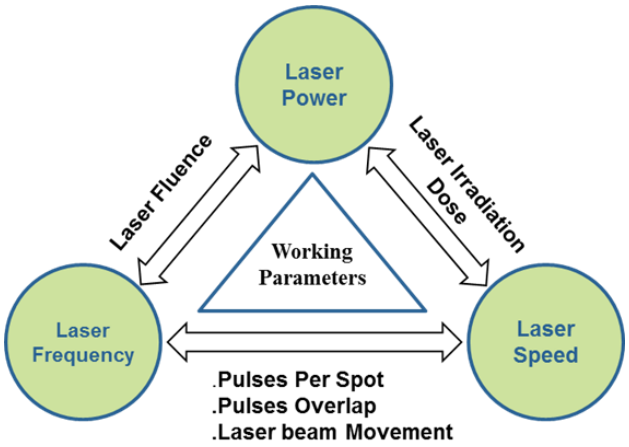

Figure 4.6: The new classification for the laser parameters.

An appointed area under the laser irradiation will be selected. Therefore the term (per spot diameter), which refers to the area under the laser spot diameter, will be used to describe the pulses number, fluence and the dose for the laser irradiation [42][74], they can be calculated by using equation 4.18 to 4.20, [75][76] as below

$$\text{Pulse Number (per spot)} = \frac{\text{f.D}}{\text{v}} \text{(Pulses)} \qquad 4.18$$

$$Fluence = \frac{P}{f\pi R^2} \ (\text{J/mm}^2) \qquad 4.19$$

$$Dose\ (per\ spot) = Fluence.PN = \frac{P.D}{v\pi R^2} (\text{J/mm}^2) \qquad 4.20$$

Where D is the laser beam diameter of 80 (µm).

According to equation 4.18 the total number of the pulses per spot diameter, for the first dose, is 6.4 (7) pulses. Whereas the maximum fluence per spot diameters is 3315.7 J.mm^{-2}, and dose per spot diameters is 21220.6 J.mm^{-2}. This means the first dose (area under the spot diameter) is effected by 6.4 laser pulses. These pulses have a total fluence of 3315.7 J.mm^{-2}, and total dose of 21220.6 J.mm^{-2}. In fact, the temperature distribution under the laser irradiation depends on the interaction between these pulses. One of the most important advantages in this simulation is the ability of this simulation to investigate the interactions between the pulses and their effects on the temperature distribution for different doses [42]. This will be helpful to increase the simulation reliability and the accuracy of the results in comparison with previous work [41].

Figure 4.7 shows the variation in the temperature over time, for three different points under the laser beam. These points are selected at three different distances from the center of the first pulse. The first point is at a distance of 40 µm while the other two points are at distances of 152.5 µm and 302.5 µm respectively. It is clear to note that, at the first point, the temperature increases until it reaches the maximum value of

about 1000 °C. Afterward it goes down again to room temperature. The other two points are showing the same behavior except the maximum temperature which is representing an important difference. It was about 1050 °C and 950 °C for point 2 and point 3 respectively. The variation in the maximum temperature for these three points is due to the difference in the number of pulses. Deep investigation of the interaction between laser pulses and their thermal effect on the substrate surface is required for a specific area not only for points. Therefore, the impact of laser pulses per spot diameters for different doses should be investigated as it is described in the next figures.

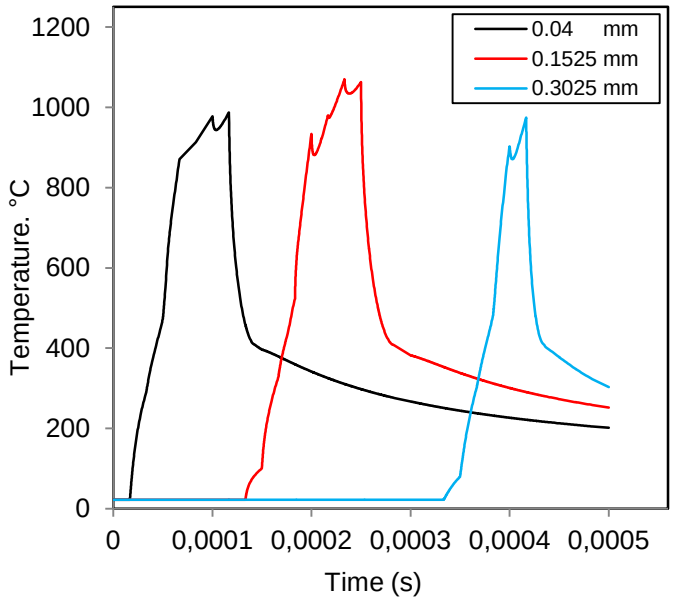

Figure 4.7: The variation in temperature with time for three selected points at the line of the laser beam movement of the simulation test No.1.

Figure 4.8 (a), shows the influence of the laser pulses on the temperature distribution, maximum temperature and its location for the dose 1 which is located at the beginning of the laser process. This dose is under the action of about 7 pulses, each pulse has a thermal effect on the substrate surface. This figure describes the effect of pulses 1 to 7 on the temperature distribution. It is clear to see that maximum temperature is increased due to the thermal influence of the interaction between the pulses. Figure 4.8 (b) shows the behavior of another selected area namely dose 2. To understand the accumulative effect of the laser on the substrate surface, a second dose (dose 2) is directly located (or starts) at the end of the first dose 1 has selected. This dose is under the action of 13 pulses. Here the impact of the pulses from 1 to 13 on the temperatures distribution can be seen. Moreover, the thermal effect of these pulses is completely different than the effect of dose 1 in terms of temperature distribution, maximum temperature, and its location.

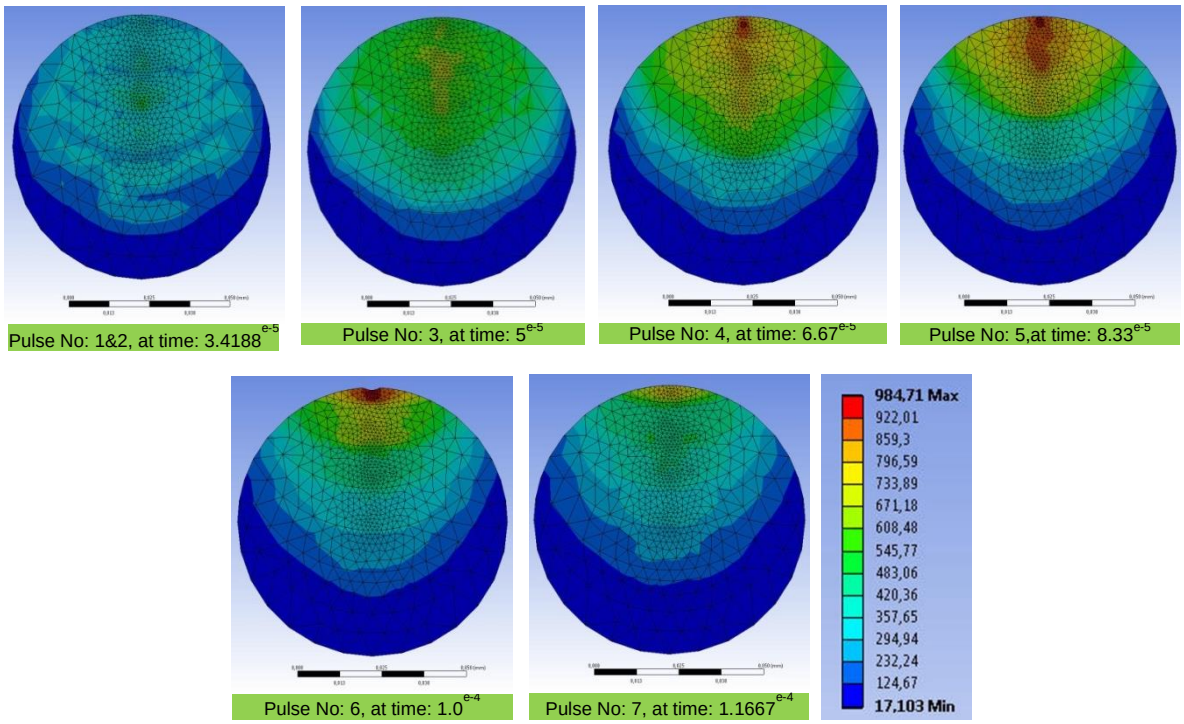

(a)

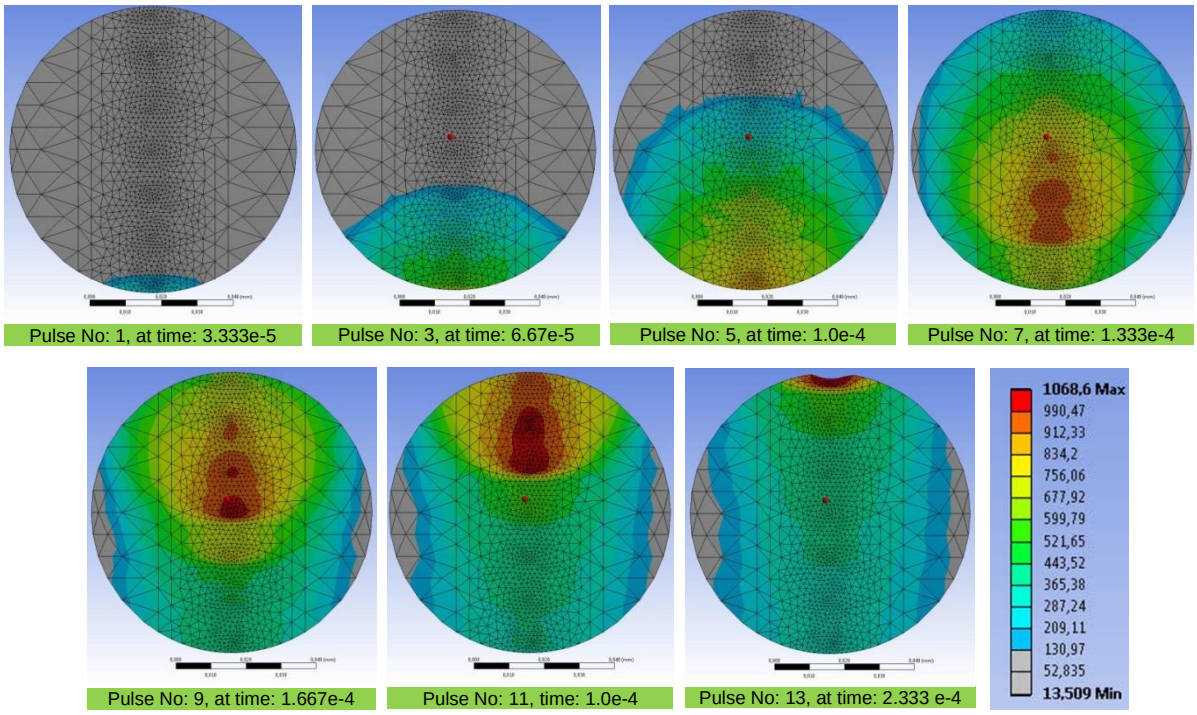

(b)

Figure 4.8: The effect of the laser pulses on temperature distribution, of simulation test No.1, for (a) Dose number 1 (b). Dose number 2.

Due to the difference in the previously described behaviors, for the same structured line, there is a difference between the groove characteristics along the axis of the

laser direction. The groove properties at the points of the end and the start of the structured track are different than within the internal points of the structured area. This difference is affected by the laser beam movement and pulse overlapping, which depend on the speed of the laser beam and laser frequency, at constant laser beam diameters. This variation can be reduced by setting smaller pulse overlapping or by increasing the beam movement. Experimentally this can be achieved by increasing the laser speed or by decreasing the laser frequency. On the other hand, any changing in these two technical laser parameters has effects on the laser fluence and laser irradiation dose shown in equations 4.18 to 4.20. According to these equations, at constant laser power, the fluence decreases with the frequency and the laser irradiation dose decreases with the laser speed, consequently, the maximum temperature will decrease.

Figure 4.9 shows the change in the maximum temperature with time for the above two doses. From this figure, it can be concluded that the maximum temperature for the two doses increases cumulatively with the number of pulses till it reaches saturation at the maximum value. As well, the maximum temperature of dose 1 is lower than dose 2. As discussed previously, this is based on the differences in the pulse number between the two doses.

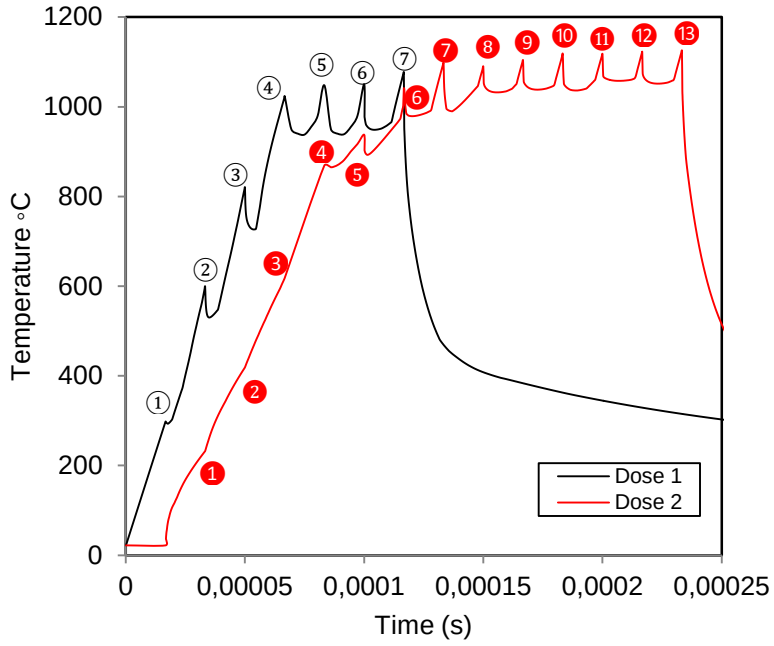

Figure 4.9: The maximum temperature against the process time for two doses.

For dose 1, which is located at the beginning of the laser track, the spot diameter is under the effect 7 laser pulses (or 6.4 pulses according to equation 4.18); this is corresponding with the [76]. After the laser beam moves a distance of more than the beam diameter, the dose 2 starts with its first pulse. The total pulse number for

dose 2 is 13 pulses (or 12.8 pulses according to equation 4.18). In this work, it was found that the pulse number per beam diameter in the beginning and the end of the laser track (to structure one line) can be calculated by equation 4.18. But in the internal areas (distance between the beginning and the ending) the pulse are more than that at the boundary. This pulse number is starting with 7 pulses at the process beginning. Then by a linear and cumulative increment, it reaches up to 13 pulses. At the end of the structured line, it decreases again from 13 to 7. Figure 4.10 shows the relation between the laser frequency, speed and pulse number at different points along the axis of the laser direction for different simulation tests. It can be seen from this figure that the pulse number increases with the overlapping between pulses or when laser beam movement decreases. On the other hand, the pulse overlapping and the laser beam movements depend on the laser frequency and speed. When the frequency increases the pulses overlapping increases while the laser beam movement reduces, consequently the pulse number per spot diameter will increase. The same behavior occurs when the laser speed is reduced. It can be concluded that equation 4.21 can be used to calculate the pulse numbers at the center of the structured line.

$$\mathrm{PN(per\ spot)} = \frac{2f.D}{v}\ \text{(Pulses)} \qquad 4.21$$

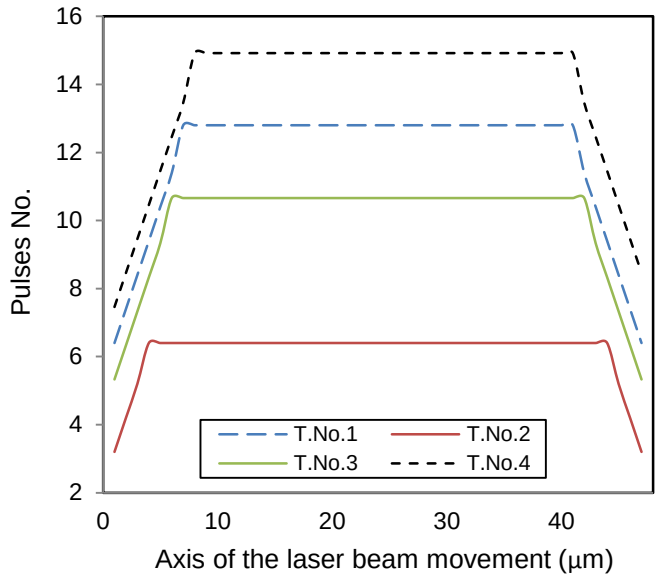

Figure 4.10: The variation in the pulse number along the X axis for different simulation tests.

The above discussion focuses on the variation in the thermal behavior for different points in the structured area under the action of laser irradiation. And it was found that the characteristic of the structured or activated area at its boundaries is different than within its center. Now, if the LDS process is carried out by using other parameter

setting, the thermal behavior will be completely changed, as it will be described in the next sections.

Figure 4.11 shows the thermal behavior in terms of the maximum temperature, against the process time for three different simulation tests including test number 1, 2 and 5 (see Table 4.4). The corresponding technical laser parameters, at which these simulation tests are implemented, are laser power of 1 W and frequency of 60 kHz, while the laser speeds are 0.75 m/s, 1.5 m/s and 2.25m/s for test numbers 1, 2 and 5 respectively. According to equations 6.18 to 6.20, the laser fluence is dependent on the laser power and frequency and the laser irradiation dose is dependent on the laser power and speed while the pulse number is affected by laser speed and frequency. Therefore, for these tests, the pulse numbers are 6.4, 3.2 and 2.1, and the maximum irradiation doses for these tests are 21220.6, 10610.3 and 7073.5 $\mathrm{J.mm^{-2}}$ for these simulations respectively. Whereas the maximum laser fluence for these simulations is constant, it is about 3315.7 $\mathrm{J.mm^{-2}}$. It can be seen from this figure that the maximum temperature during process goes up with irradiation dose at constant laser fluence. Moreover, the variation in the maximum temperature is rising when the irradiation dose is decreased. In fact, this variation is related to the action of pulse number.

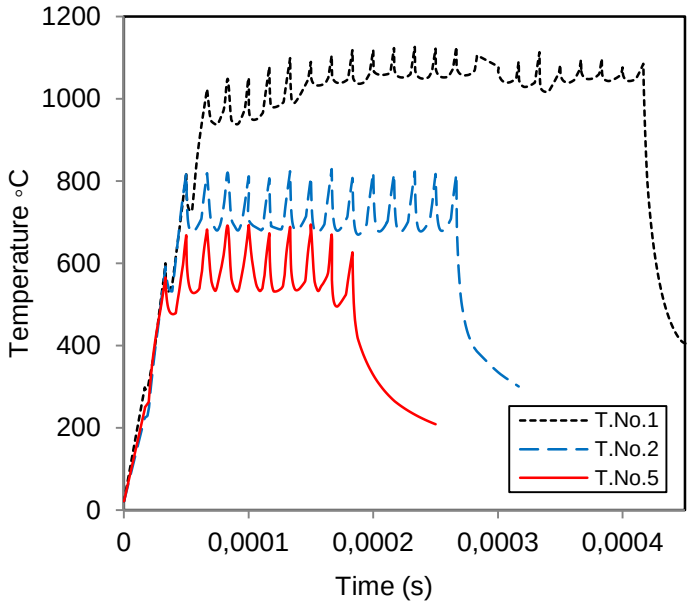

Figure 4.11: The effect of laser irradiation dose on the maximum temperature at constant laser fluence.

The other simulations are shown in figure 4.12 to investigate the effect of the laser fluence on the maximum temperature. Here the maximum temperature is plotted against the process time for test numbers 2, 3 and 4. The corresponding technical laser parameters are laser power of 1 W and laser speed of 1.5 m/s while the frequencies are 60 kHz, 100 kHz, and 140 kHz respectively for these tests. From this

figure, it can be seen that the maximum temperature and its variation are increasing with the laser fluence at constant irradiation dose. As a comparison between figure 4.11 and figure 4.12, it can be seen that the variation of the maximum temperature in the two figures above is not affected by the pulse numbers. It depends on the interval time between the pulses and the laser beam movement. The interval time is equal to 1/f, therefore the interval time between pulses is 1.667 10^{-5}, 1.0 10^{-5} and 7.14 10^{-6} (s) for the test numbers 2, 3 and 4 respectively, while for the test numbers 1, 2 and 5 they are constant. Consequently, the laser beam movement, which is depending on both of the laser frequency and speed, will be 12.5 µm, 25 µm, 15 µm, 10.7 µm and 37.5 µm for the tests numbers from 1 to 5 respectively. So that, the behavior observed in these two figures is completely different.

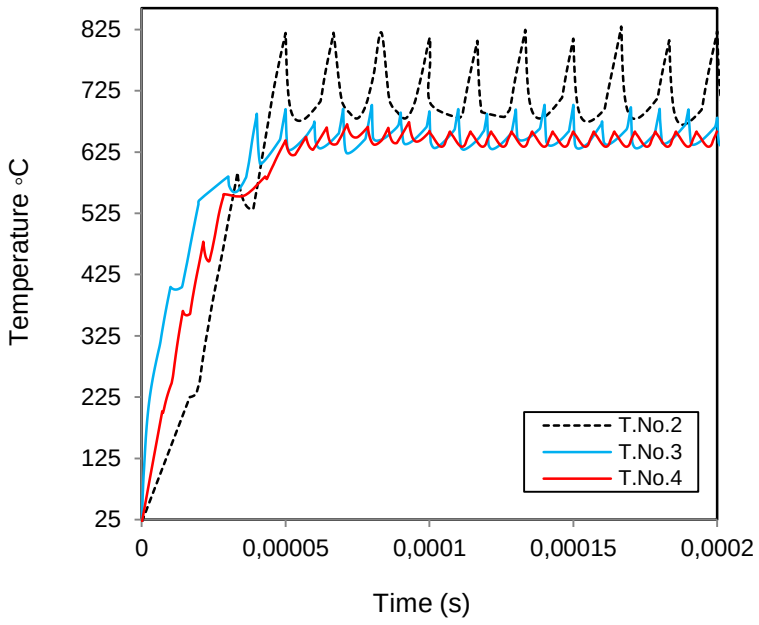

Figure 4.12: The effect of laser fluence on the maximum temperature, at constant laser irradiation dose.

Another important comparison between test number 5 and test 6 is shown in figure 4.13. For these simulations, the corresponding laser parameters are: laser speed of 2.25 m/s, laser frequency of 60 kHz, and the laser powers are 1 W and 5 W for these two tests respectively. As a comparison between those two tests, the laser beam movement and the overlapping between the pulses are constant because both investigated tests have the same values of laser speed and laser frequency. But, according to the parameters above, there is a high difference in both the laser fluence and the irradiation dose. Consequently, this leads to high differences in the maximum temperature as it is shown in figure 4.13. This figure shows the effect of the laser fluence and irradiation dose at constant pulse number on the maximum temperature and its fluctuation. From this figure, it can be seen that the effect of

those parameters is larger than for the pulse numbers as seen in the previous figures. These two different thermal behaviors lead to a variation in the characteristics of the structured area or the created groove which are depending on the temperature distribution.

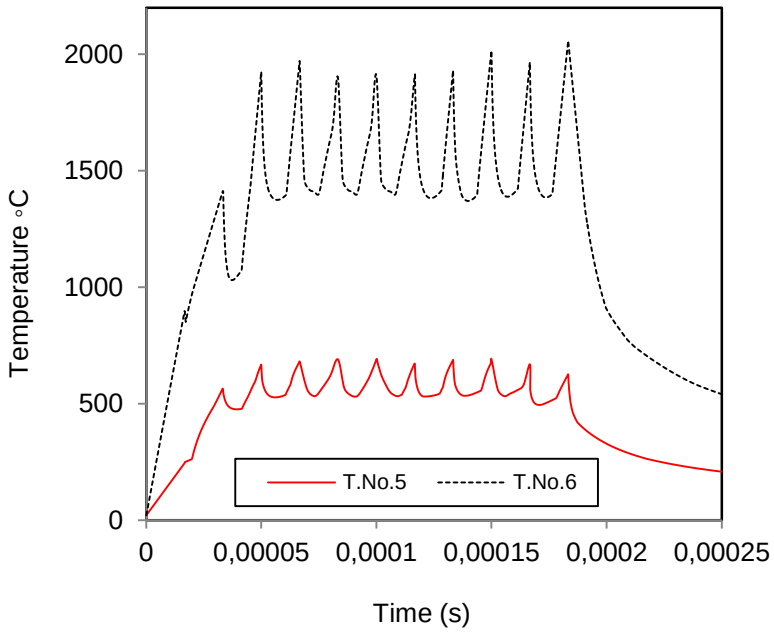

Figure 4.13: The effect of both irradiation dose and fluence on the maximum temperature at constant laser speed and laser frequency.

In the simulations, which are shown in table 4.4, the test number 7 is designed to investigate the effect of the hatching percentage on the thermal behavior under this process setup. The corresponding process parameters of this test are shown in table 4.4. In this test, the structured area contains three lines with hatching percentage of 50%. Due to this overlapping, the interaction between the pulses will be more complex in comparison with the previous cases. Figure 4.14 shows the temperature against time for dose number 1 for those three lines. Where, dose 1 is located exactly at the beginning of the structured line for each of those three lines. It can be seen from this figure that the dose 1 of line 1 is under the impact of the 4 pulses from the line 1 and 3 pulses from line 2 while there is no effect for the pulses of line 3. For this dose, there are two heating and cooling cycles as shown in figure 4.14. The dose 1 of line 2 is under the impact of the 4 pulses from line 2, and 3 pulses from each of line 1 and line 3. Consequently, there are three heating and cooling cycles for this dose. Finally, for the dose 1 line 3, this does under the effect of 4 pulses from line 3, and 3 pulses from line 2, while there is no effect for the pulses of line 1 on this dose. Therefore, there are only two heating and cooling cycles for this dose.

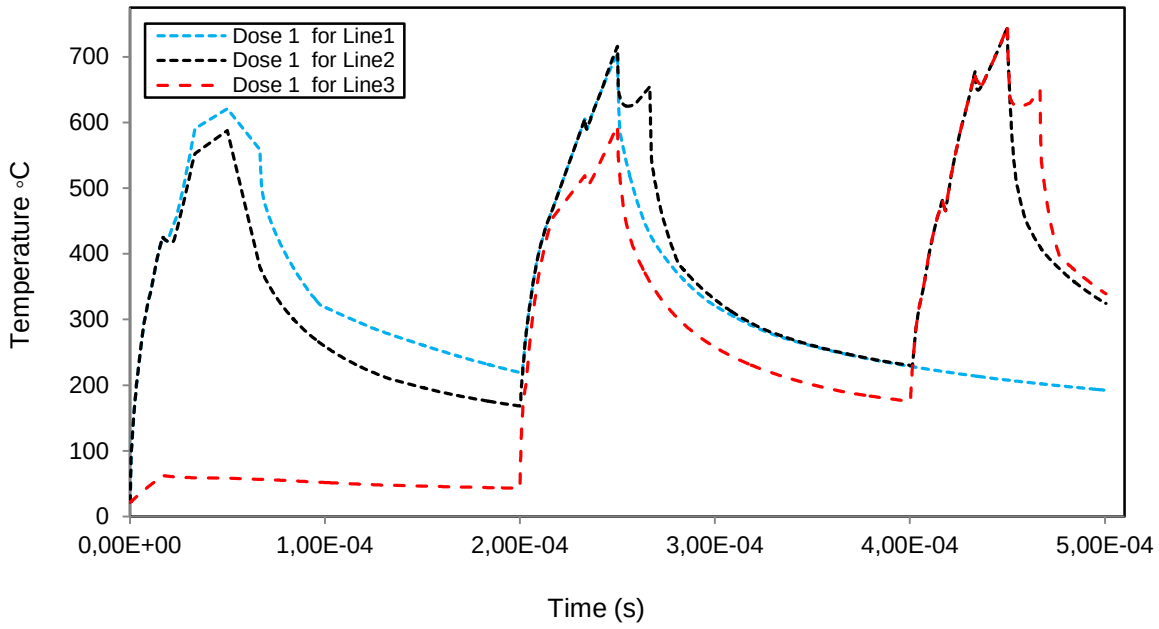

Figure 4.14: The maximum temperature against the process time for dose 1 of three different structural lines

As mentioned previously, the most complex and important parameters in the 3D LDS applications are laser incidence angle and focal length. In order to investigate the effect of these parameters more deeply, the effects of the other parameters including laser fluence, irradiation dose, and pulse numbers must be ignored by regarding them as constant. Although the 3D LDS process is affected by the incidence angle and the focal length at the same time, the effects of both must be investigated separately in the simulations. This can be achieved by changing one and fix another one. Consequently, a clear picture obtains about the effects of each parameter separately. The next important simulations of number 8 and 10 are designed for this purpose. These two simulation tests are carried out at constant laser parameters including laser power, speed, and frequency. The effect of focal length is investigated in the simulation number 8 while the simulation number 10 has been executed about the impact of the incidence angle.

Figure 4.15, shows the effect of the incidence angle and the focal length on the maximum temperature during the process. From this figure, we can see the difference in the maximum temperature for these simulations in comparison with simulation test number 1. In fact, both the incidence angle and the focal length have an effect on the spot area. The spot area increases with incidence angle and focal length, according to equation 4.11 and 4.17. Thereby, the laser density is reduced, according to equation 4.10. This effect leads to decrease the maximum temperature, as it is clear from figure 4.15. These effects of incidence angle and focal length can be reduced by elevating the laser fluence in order to offset the decline in laser

density which is absorbed by the substrate surface. Moreover, the effect of the focal length can be minimized by dividing the structured area to many smaller areas and defining or using different focal lengths for each area. In this case, the products are only under the effect of the incidence angle.

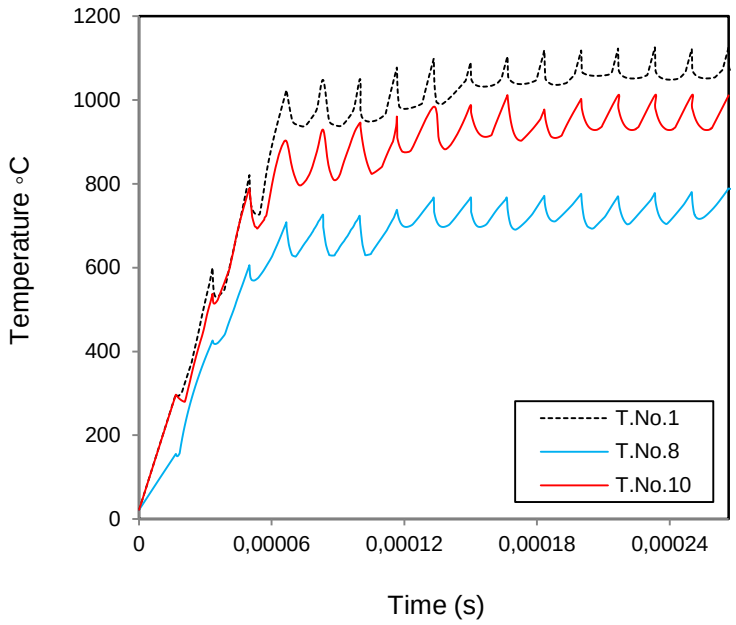

Figure 4.15: The effect of the incidence angle and the focal length on the maximum temperature at constant laser power, speed and frequency.

4.6.2 Experimental Verification for the Simulation Results

The groove shape and dimensions are the most important results that can be predicted in this simulation based on prediction of the temperature distributions. The structured area or the created groove occurs at a temperature of greater than the decomposition temperature of the substrate material (PEEK). According to the previous works the decomposition process for the PEEK starts at 575°C and reaches its maximum at 617 °C [65] [77]-[79]. Thereby, the groove formation will occur at temperatures over 575°C.

Figure 4.16 shows a comparison between the FEM simulation and the experimental results for the simulation number 5 (see table 4.4). The laser parameters for this simulation are a laser speed of 2.25 m/s, a laser frequency of 60 kHz, and a laser power of 1 W. The hatching percentage, the laser incidence angle and the focal length are set at 0. According to this parameter setting, the maximum laser fluence is 3315.7 J/mm^2, the pulse number is 2.13, and the maximum irradiation dose is 7073.5 J/mm^2. This figure shows the thermal behavior for the material with this certain parameter setting. The 3D laser microscope image for the substrate surface after the LDS process is also shown in this figure. It can be seen

that the groove formation or the structured area appears as a circular form. This is approximately the same result that is predicted in the simulation. The experimental measurement for the diameters of these circles are about 20 µm, while the simulation result is 18.5 µm, and the distance between the center of those circles is 35 µm to 39 µm. This agrees with the value of (*v*/f), or the movement of the laser beam under the corresponding laser parameters (*f,v*). According to these laser parameters, the theoretical laser beam movement is 37.5 µm. The structural area under these LDS parameters appears as a circle, because the amount of the laser fluence and the irradiation dose are not sufficient to produce a continuous structured area or continuous produced groove. Thereby, the structured area or the groove formation will appear in this form with puffiness or blowing surface [17][42]. This behavior can be prevented by increasing the laser fluence, irradiation dose, and the pulse numbers. Experimentally, this can be achieved by:

- First by raising the laser power. In this case, the irradiation dose and the laser fluence will be increased while the number of pulses is the same (see simulation test number 6 in table 4.4).
- Second by increasing the pulse number, this can be achieved by reducing the laser speed. In this case the irradiation dose will also be increased (simulation test number 1). This can be performed by increasing the laser frequency. In this case the laser fluence will be reduced. Generally, any reduction in laser speed leads to elevate pulse number and irradiation dose, while any reduction in laser frequency leads to increase laser fluence and decreases the pulse number.

Figure 4.17, illustrates another comparison between experimental result and simulation for test number 6, which is performed under the same process parameters of the previous test except the laser power. It is installed at 5 W. According to this change, the laser fluence increases to 16578.6 J/mm^2, and the irradiation dose to 35367.6 J/mm^2, whereas the pulse number is constant. This figure shows the experimental 3D laser microscope scan measurement for the groove and the simulation results namely the temperature distributions for the structural area at different process time. It can be seen from the experimental result that the groove after the LDS process shows a zigzag form at its boundaries with minimum width of 58 µm, and a maximum width of 70 µm. These values are comparable with the simulation results, where the minimum and the maximum width are 63 µm and 73 µm respectively. In fact, the zigzag forms of the groove under these parameters are caused by the high laser beam movement in comparison with laser beam diameter. In order to produce a uniform groove shape it is preferred to decrease the laser beam movement by decreasing the ratio of (v/f).

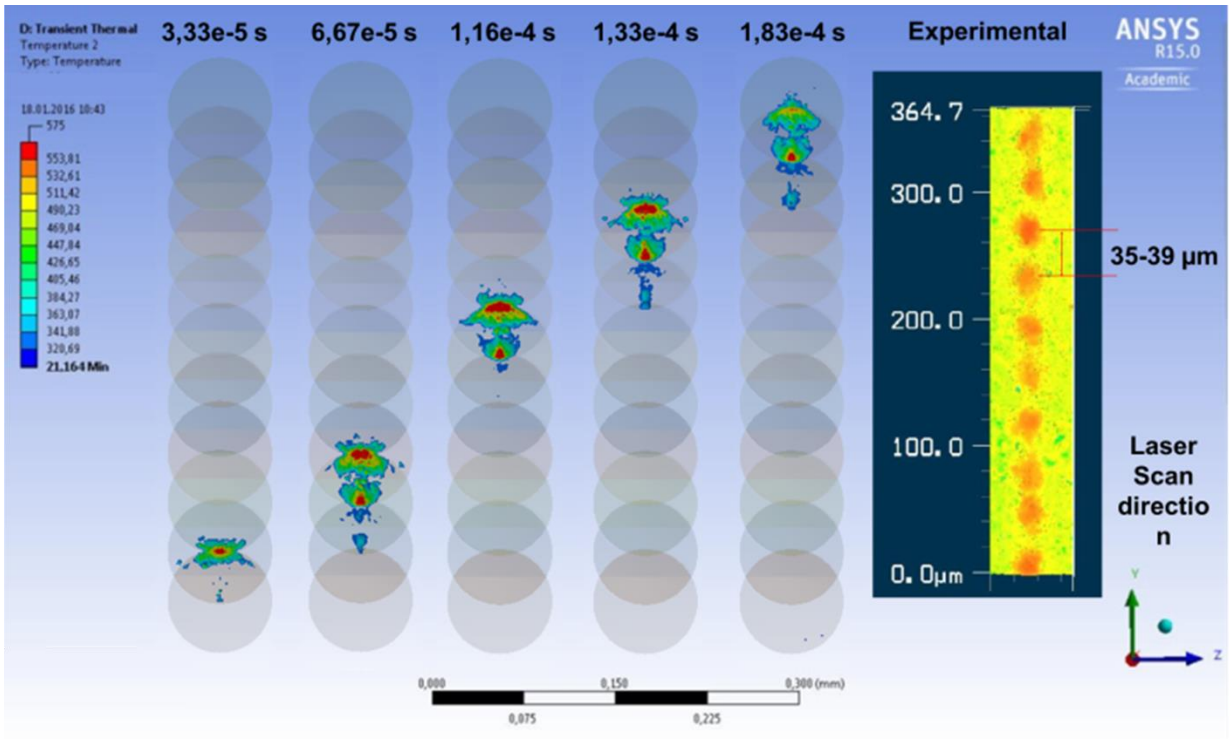

Figure 4.16: The structured area, comparison between the simulation and the experimental results for the simulation number 5.

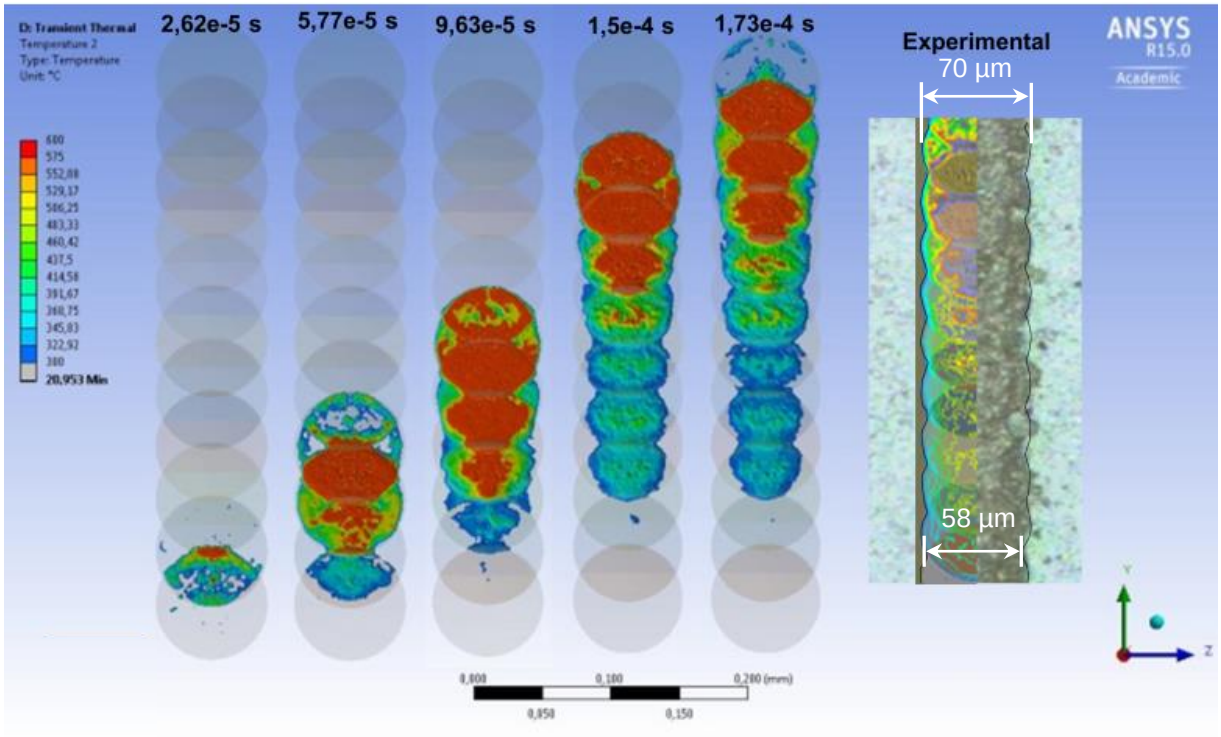

Figure 4.17: The groove shape comparison between the simulation and the experimental results for the simulation number 6.

Further verification for the simulation results are shown in figure 4.18 (a), (b). It shows the effect of both irradiation dose and the laser fluence on the width of the structured area. It can be seen that the width increases with the laser fluence at fixed irradiation dose, as shown in figure 4.18 (a), or when the irradiation dose increases at fixed laser fluence as shown in figure 4.18 (b). In general, the comparison between simulation and experimental investigation shows good agreement.

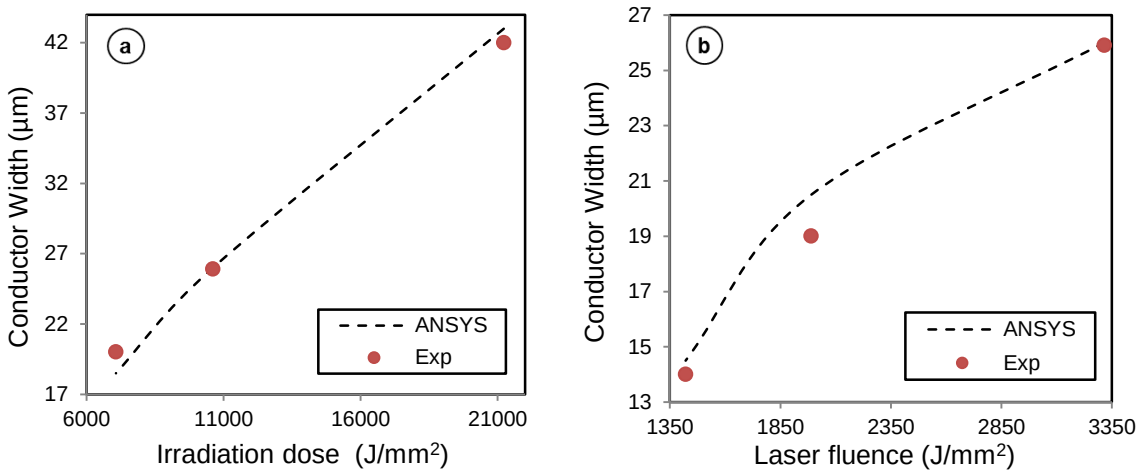

Figure 4.18: The comparison between experimental and simulation results for the conductor width for (a) different laser fluence (with an average error of 3.4%) and (b) different irradiation dose (with an average error of 3.9%).

Figure 4.19 illustrates the effect of the focal length, the incidence angle, and the hatching percentage on the conductor width. This figure shows the comparison between the experimental measurement and simulation result of simulation test number 1, 8 and 12. The corresponding process parameters for these tests are shown in the table 6.4. It can be seen from this figure that the conductor width decreases with the focal length and incidence angle, at low laser power. This is clear from the comparison among tests 1, 8 and 10, but it is increased with focal length and incidence angle, at high laser power, see the tests 9, 11, and 12.

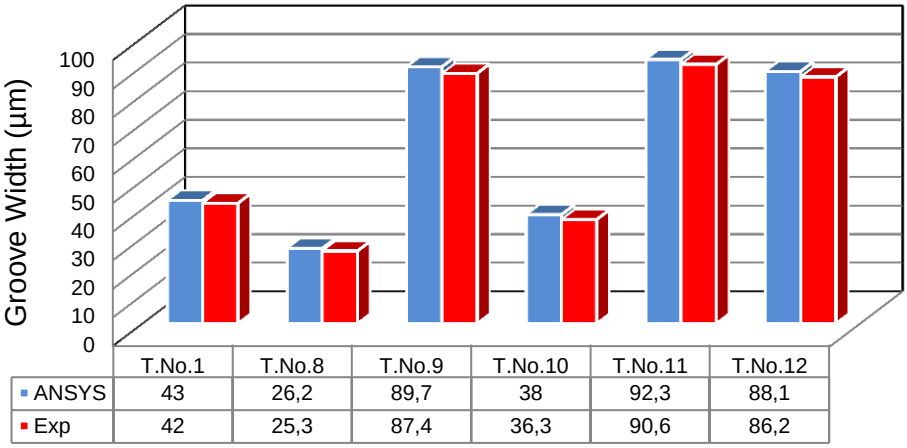

	T.No.1	T.No.8	T.No.9	T.No.10	T.No.11	T.No.12
ANSYS	43	26,2	89,7	38	92,3	88,1
Exp	42	25,3	87,4	36,3	90,6	86,2

Figure 4.19: The effect of the focal length and the incidence angle on the groove width, for the experimental and simulation results.

The groove profile, after the LDS process, can be predicted in this simulation. This can be carried out by analyzing the temperature distributions through the cross section for the structured area. Figure 4.20 (a) and (b), show the groove profile including the depth and the width at different points for two simulations in comparison with experimental measurements of these two profiles. Figure 4.20 (a) shows the comparison of the simulation number 9, and figure 4.20 (b) shows this of simulation number 11. The corresponding process parameters for these two tests are shown in table 4.4.

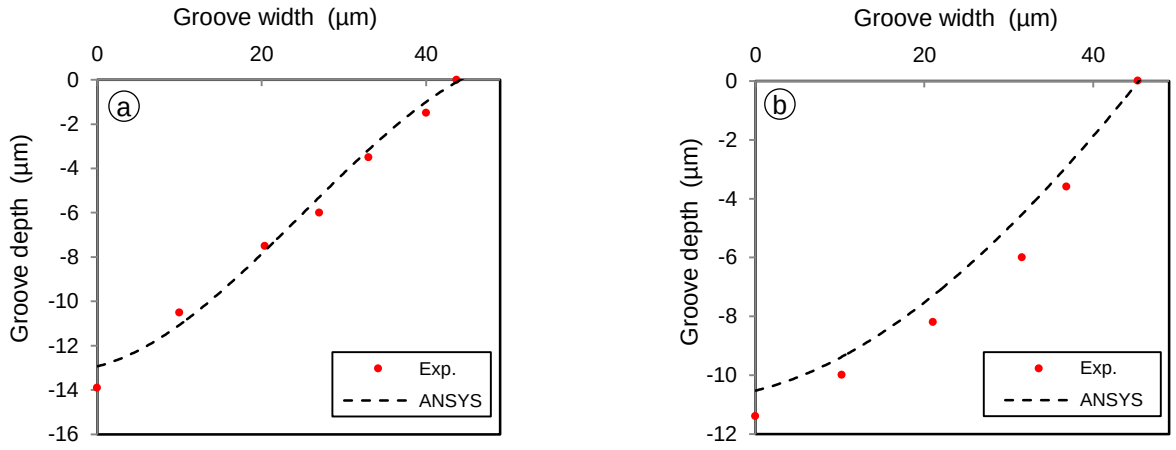

Figure 4.20: The comparison between the experimental and simulation results for the groove profiles for (a). Simulation number 9, (b) Simulation number

5. Experimental Set up, Procedures, Materials and Sample Preparation

5.1 Introduction

As mentioned in the previous chapters the LDS process is the key step for MID-LDS technology. Therefore, it is necessary to explore the change in the substrate surface under laser irradiation; this could be explained by studying the effect of adopted process parameters on the characteristics of the structured area. Under laser irradiation, there are two kinds of effect on the substrate surface. These are thermal and physical-chemical reactions. Due to these effects, the polymer bonds will break, chemical connections of the metal oxide molecules will be released and a groove will be created under the laser spot [10] [80]. These effects will act as a base for the next step, which is metallization.

Depending on the required design of the circuit, a certain pattern of circuit lines (only lines) or structure areas which consist of a set of lines will be created on the substrate surface through laser ablation. Figure 5.1 shows a 3D laser microscope scan of a groove profile and the dimensions at the surface of the polymer, after the LDS process. It also shows the 2D cross-sectional area of the groove as well as the important dimensions, which include the width of the laser track (effective or interactive zone), groove depth, groove width, groove edge width and height of the groove.

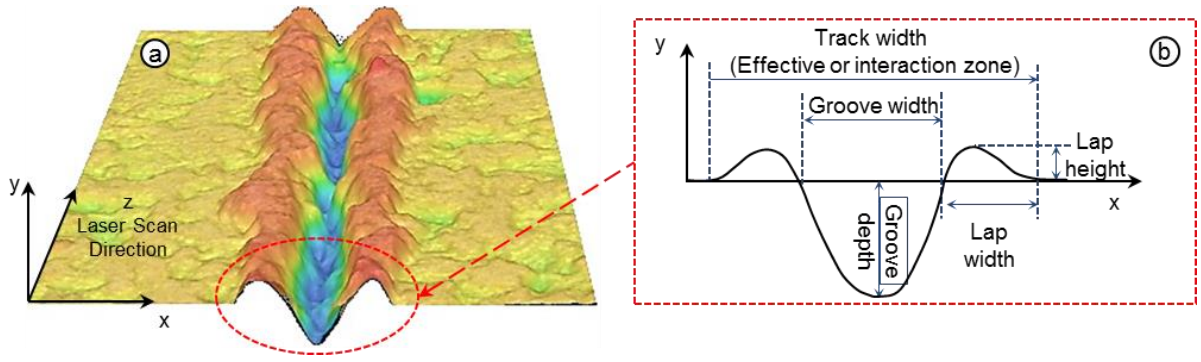

Figure 5.1: (a) 3D laser microscope scan of the groove profile after the LDS one line, (b) the 2D cross sectional area

These dimensions, as well as the surface topography of the structured area refer to the characteristics of this structured area (activated area). They play an important role in the accuracy, quality and reliability of the final MID products [17][18][81]. On the other hand, the characteristics of the structured area are related to parameter setting including working and design parameters or in other words, these characteristics refer to the process response of both the controllable and

uncontrollable input process parameters. Figure 5.2 displays the two important steps of MID-LDS process, namely LDS and metallization, as well as the relation between these two steps and various types of effective parameters. It is very significant to mention that in MID-LDS process, the responses of the LDS process should be regarded as an input to the metallization step in conjunction with the controllable and uncontrollable input parameters of this step. The characteristics of the metallization layer include the adhesion between the metallization layer and the substrate surface, thickness of the metallization layer (Cu-Ni-Au), surface roughness and the optical metallization quality can be denoted as the response of metallization step. The metallization is extremely depending on the LDS-responses and it has a great influence on the final MIDs quality and reliability. Therefore, the responses of metallization denote the final MIDs response.

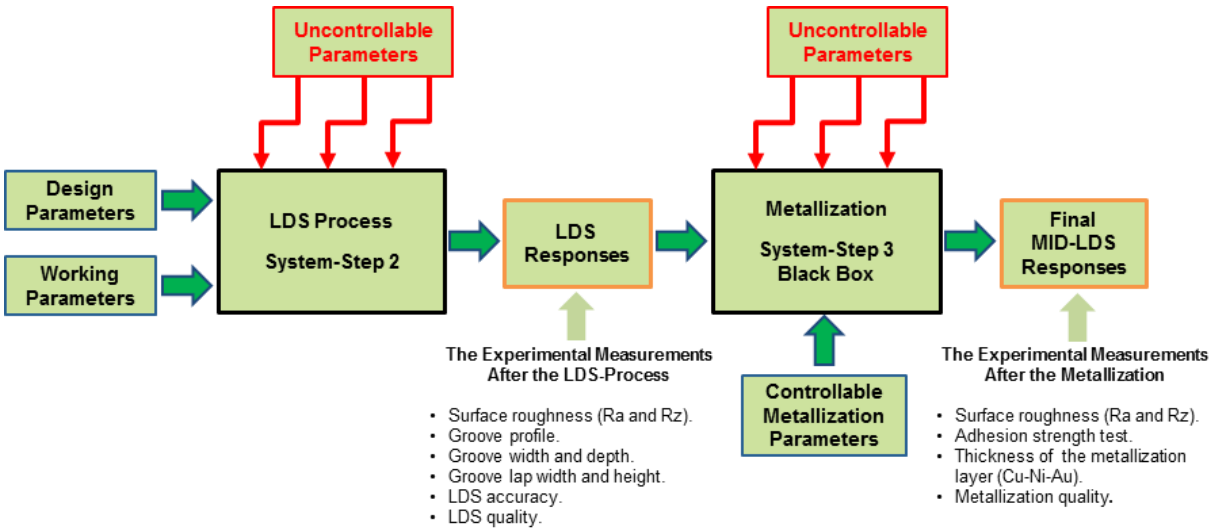

Figure 5.2: The controllable and uncontrollable parameters and the relationship between the LDS and the metallization steps.

The uncontrollable parameters during the LDS step can be defined as a combination of different parameters. They are: material properties including thermal, physical, chemical, and electrical properties, as well as, the discontinuity in these properties and the non-uniformity in the particle distribution of the additives. All those cannot be changed during the LDS process; therefore, they are regarded as uncontrollable parameters. On the other hand, the metallization step is affected by further uncontrollable parameters, which cannot be changed or which are hard to change during the metallization. They include particle size of the metallization layers, the concentration inside the used chemical metallization baths.

In the present chapter, experimental investigations based on the design of experiment (DoE) will be employed to reveal the relationship among the input process parameters and the process responses as shown in figure 5.2. These studies are designed to investigate the influence of the LDS process input

parameters, which include the laser power, speed, frequency, hatching percentage, focal length, and incidence angle of the laser beam on the LDS responses which include the surface roughness (Ra and Rz), groove profile, groove depth, dimensions of the groove lap (Width and Height), LDS accuracy, and LDS quality. On the other hand, the responses of the metallization step includes adhesion between the metallization layer and surface of the substrate, thickness of the metallization layer (Cu-Ni-Au), and surface roughness will be evaluated and analyzed with respect to the LDS responses in the experimental investigations of this chapter. In general, this chapter presents various experimental procedures, measurements, analysis, test equipment and materials used for a wide range of experimental investigations. In addition, the experiments of the current chapter are used as a reference throughout the thesis.

5.2 Laser System

An Nd-YAG pulsed laser machine, model “Fusion3D 1100” is used in the experiments, which are performed in this thesis. This machine is produced by LPKF Laser & Electronics AG Company, Germany [12] [82]. Depending on the laser material, there are different kinds of laser types namely solid, gas, and liquid lasers [83]. The Nd:YAG is a solid-state laser glass. It is most commonly used. Neodymium-Doped Yttrium Aluminum Garnet (Nd:YAG) has a combination of properties that makes it very suitable for laser applications. The hard host YAG has high thermal conductivity and good optical quality [84]. The specifications of the used laser machine are listed in table 5.1.

Table 5.1:The technical data of the laser machine - Fusion 3D 1100 [12]

Specifications	Units	Values
Laser Type		Nd:YAG
Nominal Average Output Power	W	17,66
Laser Pulse Frequency	kHz	10 – 200
Max. Structuring Speed	mm/s	4000
Max. Pulse Energy	mJ	0,174
Laser Beam Diameter	µm	80
Laser Wave Length	nm	1064
Pulse Duration Time	ns	23,7
Structuring Area (X x Y x Z)	mm x mm x mm	160 x 160 x 80
Software		LPKF CircuitPro3D

Figure 5.3 shows the influence of laser frequency on the maximum output power and pulse energy. According to the design of the used laser machine, the maximum output power increases with laser frequency until it reaches up to 100 kHz, thereafter it is almost constant in the range of 17.5 W to 17.66 W above the frequency of 100 kHz, see figure 4.3. From this figure, it can also be seen that the pulse energy is

nearly constant at 0.17 mJ over a frequency range from 50 kHz to 100 kHz. But at frequencies of more than 100 kHz, the pulse energy decreases.

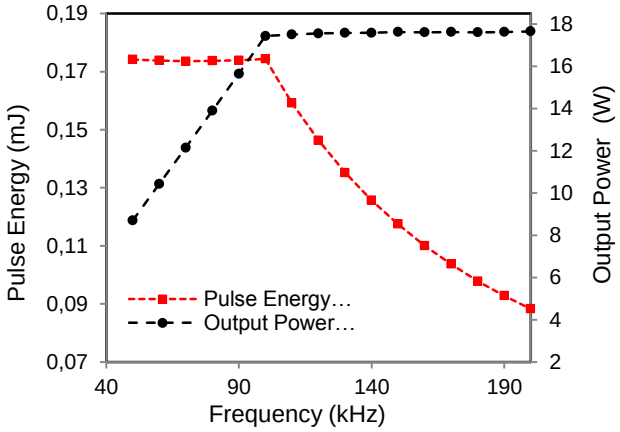

Figure 5.3: The maximum output power and pulse energy as a function of the frequency.

5.3 Investigated Materials

In this thesis, the experimental investigations are carried out using three different materials with different thermal and physical properties. In addition, several experimental investigations are performed on these materials to determine various objectives. Some materials are commonly used plastics of MID applications. Others are new innovative materials, which are high-performance ceramic based materials dealing with special MID applications. Table 5.2 lists the materials used in the experimental investigations.

Table 5.2: The materials used in the experimental investigations [72] [85].

No	Materials	Abbreviation	Trade name
1	Polyphthalamide (PPA) reinforced with glass fiber	PA6T/PPA	VESTAMID® HT plus LDS 3031 black
2	Polyetheretherketone	PEEK	TECACOMP® PEEK LDS black 3980
3	Alumina with Copper oxide	Al_2O_3+ Cu_2O	

The first two plastic materials are approved for laser direct structuring with LPKF LDS systems [72][85]. The third one is proposed in this work as a new innovative material based on high-performance ceramics. It is a mixture of alumina and copper oxide as an additive. These two oxides are responsible for the final physical and thermal properties of the produced phases, which depend on the interaction of the Cu-Al-O system [86]. The properties of these materials, which include excellent chemical, thermal and mechanical stability and lower thermal expansion, make it suitable for the use as circuit carrier at elevated temperatures. They can be used in important

applications such as medical technology, LEDs, aviation/aerospace and automotive industry. This new proposed material is manufactured by using the technology of powder metallurgy, where a powder of aluminum oxide Al_2O_3 and copper oxide are mixed together to produce the final material. The production process of the powder metal parts begins with the mixing of elemental or alloy powders and the compression of the mixture. Thereafter, the formed components are sintered in a controlled atmosphere furnace to bind the aluminum and copper oxides particles together. The sintering process is carried out at a certain temperature, which is defined as the sintering temperature. The final structure is influenced by the percentage of alumina, copper oxide and sintering temperature (T_S), therefore the effect of these two parameters as well as the LDS parameters including laser power, speed, and frequency on the responses are taken into account (see table 5.3). The three different materials are tested experimentally for different objectives as it will be presented in the next sections.

5.4 Experimental Details and Procedures

As mentioned in the previous chapter, there is a very important and complex relationship between input parameters and the main responses for both important MID-LDS steps involving the LDS and metallization. Therefore, it is very important to examine, analyze and then understand this relationship. This helps to control and optimize the MID-LDS process. In order to reveal this demanding relationship, experimental investigations based on design of experiment (DoE) are used for this purpose. The experimental investigations include all the investigated materials that are described in the previous section. It consists of two steps. The first is related to the LDS process and the second is about the metallization process. After each step, various experimental measurements and analysis are carried out to investigate the desired output responses. In general, the experimental work can be classified as follows.

5.4.1 LDS Process and its Measurements

The laser direct structuring involves a set of steps. First, in the CAD/CAM system is designed the required conductor or circuit layout. Then, this CAD system should be compatible with the software of the laser machine. The laser parameters will be defined for the laser structuring. In the present work, two different specific layouts for different purposes are created by using CAD/CAM software. These layouts cover the structure of double lines and areas as shown in figure 5.4. This figure shows the layout structure of two conductor shapes include double lines and areas, which are employed for the experiments of the PEEK and ceramic materials. The first type of structure (line structure) helps to explore the laser track width, groove profile, groove depth, groove edge dimensions (width and height) as a function of the adopted process parameters including laser power, speed, frequency, hatching percentage,

focal length, and incidence angle of the laser beam. Whereas, the second type of structure (area structure) helps to show the effect of the above parameters on the topography of the structure area, the surface roughness Ra and Rz, structuring-ablation type, structuring percentage and the minimum line/pitch. These give important indications about the accuracy, quality, and reliability of the final MID products.

Various materials are investigated for different objectives using several measurements and analysis methods. Table 5.3 shows the types of materials, patterns of the structure or circuit layout, the parameters being studied, the used measurements and the analysis that are carried out on those materials, as well as the objectives of this analysis.

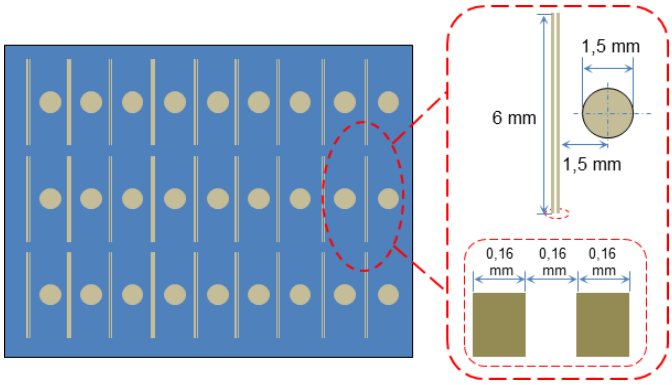

Figure 5.4: The structure shapes including two lines and area of the experimental investigation

Table 5.3: The implemented experiments on the used materials after the LDS process

No	Materials	Structure Layout	Investigated Parameters	Measurements & Analysis
1	VESTAMID	Line only	P, *v, f*	Groove profile and dimensions, lap dimensions, quality inspections
2	PEEK	Line and area	P, *v, f,* H, FL, β	Groove profile and dimensions, lap dimensions, Ra, Rz, accuracy and quality inspections.
3	Alumina	Line and area	P, *v, f,* T_S, Cu_2O	Groove profile and dimensions, lap dimensions, Ra, Rz, and quality inspections

For the first material, the polymer VESTAMID, the experiments are designed to investigate the influence of laser power, speed, and frequency on the groove profile, groove dimensions, and edge lap dimensions that are important for predicting the LDS quality. The second series of tests are performed on the plate of the polymer PEEK. PEEK is an attractive material for electrical and electronic applications due to

its excellent electrical properties as well as its ability to withstand high temperature [2]. This series of experiments is designed to explore a wide range of the most significant process parameters. They have a considerable influence on the accuracy and the quality of the LDS process. That can be proven by analyzing the relationship between these parameters and the process responses. In addition, these experiments are designed to meet the above-mentioned relationships for 2D as well as 3D MID, which refer to a serious challenge in the field of MID. The third series of experiments was performed on the ceramic based material. It focused on the effect of laser power, speed and frequency as well as the manufacturing conditions including additive percentage and sintering temperature. The groove profile, groove dimensions, lap dimensions, line/pitch, and surface roughness are measured as a function of the adopted parameters. This helps to qualify this new material and to find the optimum process parameters. All these measurements are carried out using a 3D laser scanning microscope (Keyence VK-9700), whereas the analysis is implemented using the VK Analyzer software, which is developed by the same company to analyze the Keyence measurements [87].

5.4.2 Metallization Process and its Measurements

Metallization is the next step in MID-LDS processes. It is generated for the activated area after the LDS step using electro-less metallization (chemical plating). As mentioned in the introduction, before the surface treatment another intermediate step of cleaning is necessary to guarantee the quality of the conductor paths. After cleaning, the circuit path can be installed. For this purpose, electro-less copper baths add a thin Cu layer of 3 µm to 15 µm onto the activated area of the substrate. Afterwards, another electro-less are application of a nickel layer of 3 µm to 20 µm and gold layer 0.05 µm to 0.15 µm applied on top of the Cu layer [16]. Figure 5.5 shows the typical chemical plating setup used for the electro-less metallization in the current work. The metallization process mainly depends on the responses of the LDS step, such as groove dimensions, groove profile and surface characteristics [17]. Moreover, the metallization structure is influenced by many process parameters, as shown in figure 2.7. The present work focuses on the effect of the LDS process parameters. Therefore, to neglect the effect of the metallization parameters, the experiments tests of this work are based on assumption that the metallization process is a black box, and it depends only on the LDS responses. This can experimentally be achieved by performing the chemical plating of all samples at the same time and under the same metallization conditions. This method helps to only consider the effect of LDS parameters and responses on the metallization responses. After the metallization step, which is performed for the three aforementioned materials, a set of measurements and analysis on the samples are performed as shown in table 5.4. This table also shows the measurements and the analysis of the materials under investigation.

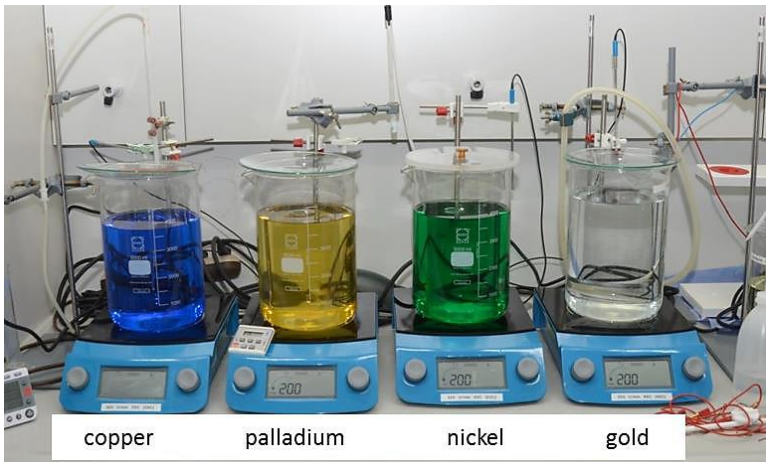

Figure 5.5: The typical chemical plating set-up for the laboratory.

Table 5.4: A measurements and analysis after the metallization.

No	Materials	Measurements & Analysis
1	VESTAMID	Keyence VK-9700K (metallization thickness measurements, quality)
2	PEEK	Fischer scope and Keyence VK-9700K (metallization thickness measurements), keyence vk-9700k (ra, rz, quality) and hot pin pull test-dage 4000plus (adhesion strength)
3	Alumina	Fischer scope and Keyence VK-9700K (metallization thickness measurements), keyence vk-9700k (ra, rz, quality) and hot pin pull test-dage 4000plus (adhesion strength)

Additionally, a Fischer scope machine is used to measure the thickness of (Cu-Ni-Au) metallization layers. The minimum measurement step for this machine is about 0.2 mm. Thus a groove width greater than 0.2 mm is optimal for this machine. In other words, it is not possible to use this machine for measuring the micro conductors with a width of less than 0.2 mm. A new innovative method is used to measure the overall metallization thickness of the (Cu–Ni-Au) layers. This method is based on using the 3D laser scanning microscope (Keyence VK-9700K), to measure the groove geometry (profile and dimensions) before and after metallization. Then, a comparison is made between the two measurements using the VK Analyzer software. This method can be used with measuring steps smaller than 0.01 mm. This process is beneficial for the comparison of the machine measuring steps discussed in the above methods.

5.5 Setup of the Design of Experiments (DoE)

Designed Experiments, **Experimental Design** and **Design of Experiments** (DOE). The first type of DoE was constituted in 1747 [88]. The term design and analysis of experiments can be defined as systematic experimental steps that can be carried out under various controlled conditions to discover an unknown effect, to examine or confirm a hypothesis, or to clarify a known influence. It is a statistical methodology employed to test and determine the impact of various process inputs (parameters) on different process outputs (responses). In the analysis of any process by the experimental investigation, the relevant questions are: **W*hich input parameters have an influence on the responses of the process***? ***What is the importance of each factor*** and ***which of these parameters has a great impact on the process responses?*** The experiments can be designed in many different ways to find the answers to these questions as shown in the next chapters. In general, the DoE includes the following steps [89] [90]:

5.5.1 Components of Experimental Design

In the DoE, there are three important terms that should be defined:

- **Factors**, **parameters** or **inputs** of the process all mean the same. They can be classified as controllable and uncontrollable variables. In this work, the controllable parameters for all the experiments are listed in table 5.5.
- **Levels** or **settings** of each parameter. These terms refer to the value used for each process parameter in the experiments. Depending on the parameter type, they can be divided into different values as shown in table 5.5.
- **Responses** or **outputs** of the process. In this work, the groove geometry (profile and dimensions), lap dimensions, line/pitch, surface roughness (Ra, Rz), accuracy and the quality are an examples refer to the responses of the LDS process (see table 5.3). Whereas the thickness of the metallization layers, surface roughness including Ra and Rz, quality and adhesion strength are the responses of the metallization process (see table 5.4). In the DoE, all the important responses are measured and analyzed to determine their attitudes and the corresponding parameters [91].

5.5.2 Experiment Design Procedures

In general, the experimental procedures are divided into eight steps as shown in figure 5.6. First, the initial situation must be defined or described. In this case, there is an experimental set-up for an MID-LDS process comprising of several steps. The most important steps are the LDS process and the subsequent metallization for the activated surface. The input for the laser machine, such as circuit line design, is done by programming with 3D-CAD software. Subsequently, the process parameters can be adjusted by using the software of the laser machine. The second step is to

determine the main objective for the experiments. In this case, the main objectives for the LDS and metallization are shown in table 5.3 and table 5.4. Thereafter, the input and output factors are defined in the third step. In this work, different input parameters are used for the different materials as shown in table 5.5. This table also shows the different levels of process parameters, which are important for the next DoE steps. The following steps are the execution of the experiment and the analysis through statistical methods. Last but not least, the final results must be interpreted and verified.

There are various types of the designs of experimental. The most common methods are:

- The full factorial DoE design [89]
- The rotatable central composite design [92]
- The group method of data handling (GMDH) [93]
- The split-plot design [94]

Figure 5.6: The procedure for the design of experiment.

In the present work, a full factorial and rotatable central composite design are used in the experimental investigations. In DoE, there is another important classification for the investigated input parameters that is based on the difficulties of changing the parameters. Thus, the parameters can be defined as parameters that are easy-to-change or parameters that are hard-to-change. The sequence of changing these parameters during the experiments is highly significant on the final results. The experiment should be started with the hard-to-change parameters and ended with easy-to-change parameters. This helps to achieve a more reliable experiment [95]. In this case, for the first material, the VESTAMID polymer, all investigated parameters are easy-to-change parameters (see table 5.5). It is very easy to change the laser

power, laser speed, and the laser frequency directly through the software of the laser machine. Therefore, there is no significance for the order of change of the parameters during the experiments. For the experiments of the second and third material, namely the PEEK and the ceramic, the investigated parameters are comprising of two types. Parameters such as focal length, the angle of incidence, sintering temperature and additive percentage are referred to hard-to-change parameters, while the parameters such as laser power, laser speed, laser frequency, and hatching percent are defined as easy-to-change parameters.

The total number of experiments depends on the number of parameters, levels of these parameters and the design of the DoE. For the cases in table 5.5, a full factorial DoE design requires a total number of experiments based on equation 5.1 as follows [90][96]:

$$\text{Total NO. of Experiment} = (\text{Levels})^{\text{Number of Parameters}} \qquad 5.1$$

Table 5.5: The controllable parameters and the corresponding.

No	Materials	Controllable Parameters	Levels	Units	Total No. of Exp.
1	VESTAMID	Power	4 Levels (3, 6, 9, 12)	W	80-Line
		Velocity	5 Levels (1.0, 1.3, 1.6, 1.9, 2.2)	m/s	
		Frequency	4 Levels (70, 90, 110, 130)	kHz	
2	PEEK	Power	3 Levels (1, 5, 9)	W	729-Line 729-Area
		Velocity	3 Levels (0.75, 1.5, 2.25)	m/s	
		Frequency	3 Levels (60, 100, 140)	kHz	
		Hatching	3 Levels (0, 50, 75)	%	
		Focal length	3 Levels (0, 3, 5)	mm	
		Incidence angle	3 Levels (0, 20, 40)	Degree	
3	Alumina	Power	3 Levels (4, 8, 12)	W	108-Line 108-Area
		Velocity	3 Levels (0.75, 1.5, 2.25)	m/s	
		Frequency	3 Levels (60, 90, 120)	kHz	
		Sintering Temperature	2 Levels (1200 , 1600)	°C	
		Additive percentage	2 Levels (5, 15)	%	

6. Experimental Results and Discussion of LDS process

6.1. Introduction

In this section, the relevance between the investigated process parameters and the final process responses will be shown, analyzed and discussed in detail for all materials under investigation. In general, the results and discussion can be divided into two groups. The first is concentrated on the results of the LDS process. This includes the influence of the adopted process parameters on the characteristics and topology of the structured area, as well as the effect of those process parameters on the LDS quality and accuracy.

The wide range of experiments showed an interconnected and complex behavior with regard to the correlation between the adopted process parameters and the numerous responses. Exploration of these complex relationships is one of the most important objectives of the present work, but it should be based on a theory or main hypothesis that could be used to explain the behavior of these experiments. In the simulation chapter, LDS processes were investigated theoretically using a physical model. This model and simulation procedures, which show a good matching with the experimental work, are employed to explore and analyze the effect of all the adopted LDS parameters for specific simulations and experiments. However, it was concluded that the LDS process is a heat transfer problem. The analysis of laser energy per unit area and its interaction with the substrate material is powerful to be considered as the main hypothesis. It considers the 3D-Gaussian distribution of laser density, which is more reliable for the laser source. Figure 6.1 shows the distribution of laser energy per unit area and its impact on the surface of the substrate for two different parameter settings (1 and 2). Since the parameter settings changes the distribution of laser energy will also be changed. The parameter settings used in this work include different factors. Therefore, their impact on the laser energy per unit area should be explained for all parameters as follows.

According to equation (4.19), the fluence increases as the laser power increases. As a result, the distributions of the laser energy will shift up, as shown in figure 6.1(a). It shows two different distributions, the first is at a low laser power (black line), while the red line refers to a high laser power. This change in energy distribution results in significant changes in the characteristics of the groove profile, including increments in groove width, groove depth, track width, and edge lap dimensions or edge factor (width and height). The setting of the laser frequency at lower values also increases the laser energy and results in a different distribution (see equation 4.19). The distribution of laser energy will show the same previous behavior. However, the groove profiles and its characteristics do not show the same prior behavior described for the impact of laser power. This is due to the fact that the laser frequency in conjunction with the laser velocity has a further important effect on laser beam

movement, pulse overlapping, and the number of pulses per spot diameters, see equations 6.1, 6.2 and 4.18 [97][98].

$$\text{Pulse Overlapping (P. O)} = 1 - \frac{v}{\text{f.D}} \qquad 6.1$$

$$\text{Laser Beam Movement} = \frac{v}{\text{f}} \qquad 6.2$$

According to the above equations, as the frequency decreases at a constant velocity, the number of pulses per spot diameter and pulses overlapping will also be decreased, whereas the laser beam movement increases. This leads to minimize the accumulative laser energy per unit area. The above relationship could also be used to describe the impact of laser velocity on the distributions of laser energy. A further influence for the laser velocity can be seen in terms of laser dose, see equation 4.20. Now, what about the impact of the other parameters such as hatching, focal length, and incidence angle? As hatching increases, the amount of accumulative laser energy per unit area is increased, without any impact on the laser energy and its distribution under the diameter of the laser spot. Any change in the focal length produces a corresponding variation in the spot area so that the laser energy shifts downwards, see equation 4.11 and figure 6.1 (b). According to equation 4.17 and figure 4.4, the spot diameter is also related to the incidence angle, any variations in this angle produce a distortion in the area of the laser spot. Therefore the distribution of the laser energy will be changed.

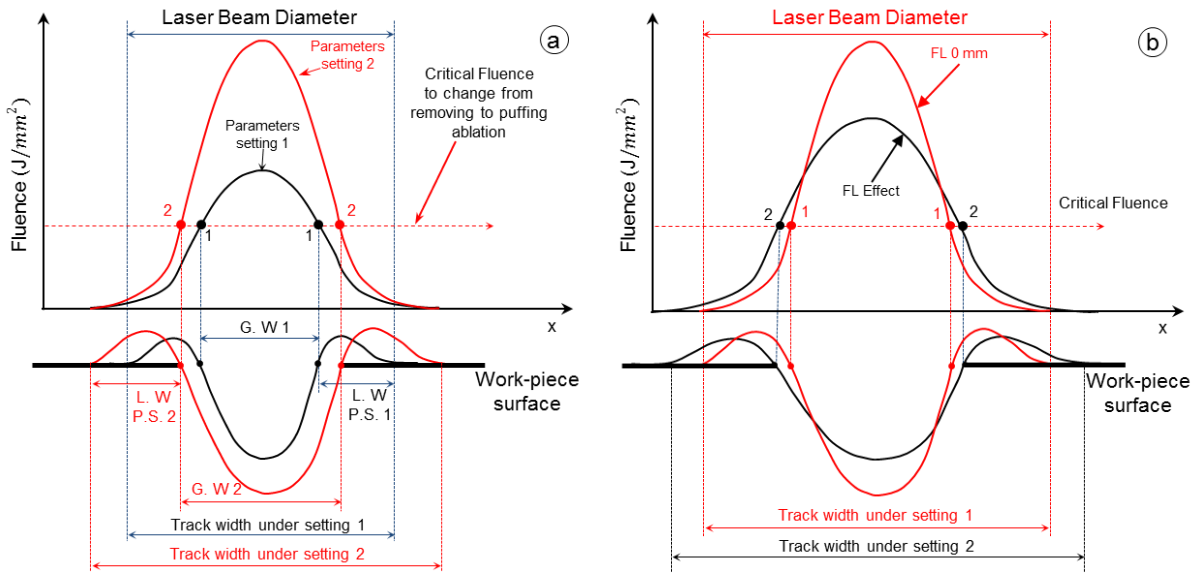

Figure 6.1: Laser energy distribution and the interaction with the substrate surface at different parameter settings.

6.2. Groove Dimensions

It was mentioned in the previous chapters that it is very important to analyze the relationship between the laser parameters and the groove configuration, due to its high importance for the LDS process output [17][18]. This is achieved by performing different LDS experimental tests at different parameters, for all the investigated materials. Afterwards, the groove characteristics which include, groove depth, the width of the laser track (interaction width) and groove edge dimensions (width and height), as well as the groove profile, are measured using a 3D laser microscope.

6.2.1. Groove Depth

A. PEEK Polymer Material

Figure 6.2 shows the effects of the laser power, laser speed and laser frequency on the groove depth of the PEEK material. In this figure, it can be observed that the groove depth increases with laser power or when laser velocity and frequency decrease. The increase in laser power or the decrease in laser speed or frequency leads to a rise of the heat input on the surface of the polymer. Then the amount of removed material from the polymer surface will be increased and as a result the groove depth will be growing. The same behavior is noted for the VESTAMID PA6T/X polymer. It can also be seen that at a low laser power of 1 W the depth is always 0, as shown in figure 6.2 (b). Moreover, the effect of laser frequency at low power is almost negligible in comparison with that effect at high laser power, see figure 6.2 (c). In general, it can be noted from the 3D figure, which is shown in figure 6.2 (d), that the effect of the laser power and velocity is more than that for the laser frequency. The above behavior or results did not consider the impact of other adopted parameters.

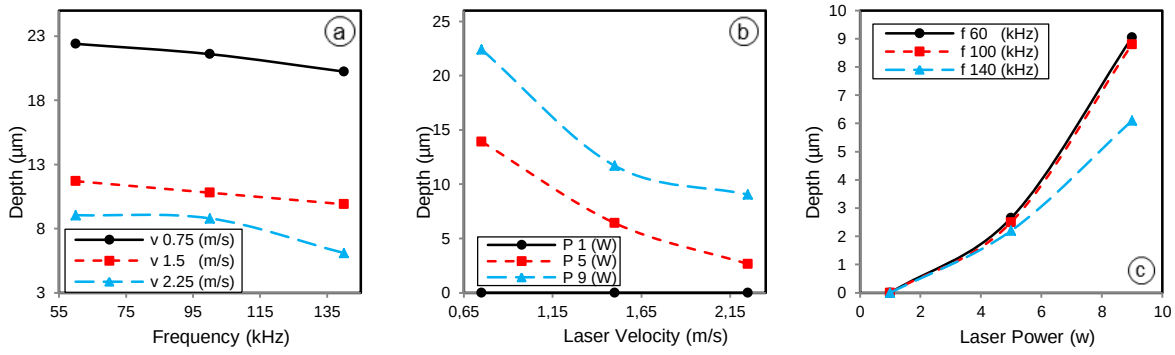

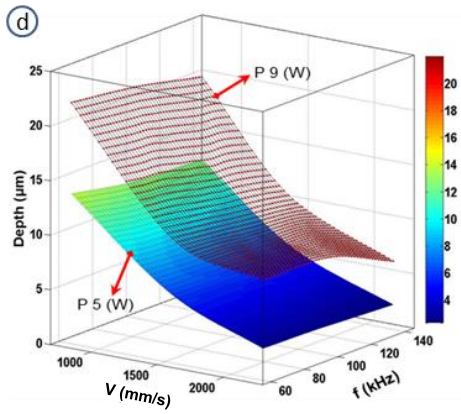

Figure 6.2: The effect of the laser power, laser speed and laser frequency on the groove depth for the PEEK material at (a) P 9 W. (b) f 60 kHz. (c) v 2.25 m/s. (d) 73D relation.

Figure 6.3 demonstrates the effect of hatching at different levels of laser powers, laser speeds and frequencies. It can be seen from this figure that there is an increment in the groove depth when the hatching is increased. But, this increment is also related to the other parameters such as laser power, speed, and frequency. For instance, there is low impact for the hatching on the groove depth at low laser power and high velocity, as shown in figure 6.3 (a) and (b). Furthermore, this effect is almost the same at different laser frequencies, see figure 6.3 (c). We can also see that at a high velocity, the depth is not affected by the increment of hatching from 0 % to 50 %. This effect is clearly shown in figure 6.3 (d), which shows the 3D relation between depth, frequency, velocity and hatching at a laser power of 9 W. This behavior does not exist at a low and a middle power and velocity. In general, the increase of hatching leads to a raise in the amount of the input laser energy to the surface of the substrate, therefore, the depth is increased.

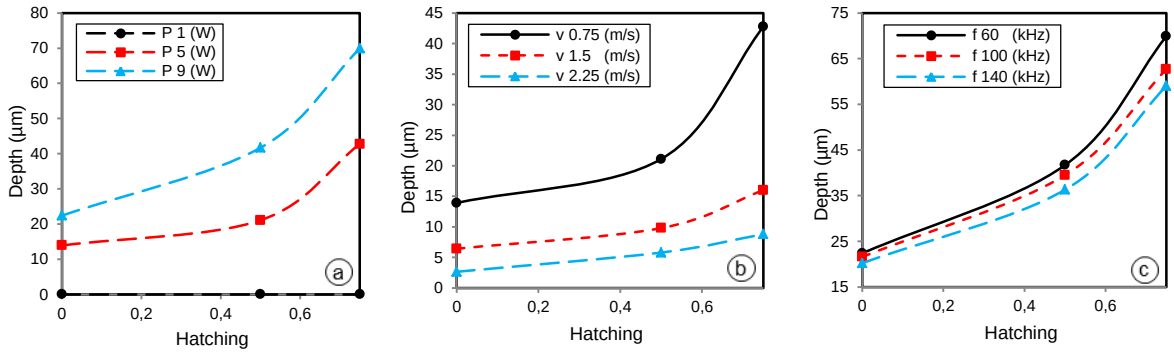

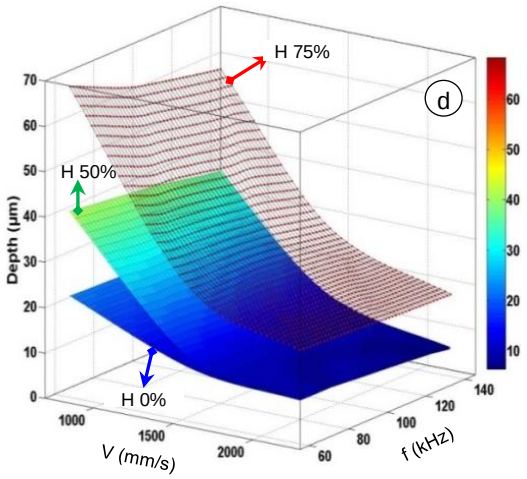

Figure 6.3: The effect of hatching on the depth at (a) v 0.75 m/s and f 60 kHz. (b) P 5 W and f 60 kHz. (c) P 5 W and v 0.75 m/s. (d) P 9 W 3D relation.

Previously, it was mentioned that the three-dimensional applications of MID or LDS are one of the most important challenges in this technology. In fact, according to the 3D shape of the product, the focal length and incidence angle of the laser beam are altered at different points on the substrate surface, or with the z-axis. Consequently, the focus radius (spot size) will also be changed. According to this variation, the laser intensity and its distribution under the laser beam spot will be altered [20][21]. As a conclusion, different focal lengths and incidence angles lead to a lot of variations in the characteristics of the structured area. In the previous section, this influence is described in detail. As long as the increase in the incidence angle, as well as the variation in the focal length results in equivalent variations in laser density, this divergence produces a decrease in groove depth. This trend in the groove depth depends on the other laser parameters such as laser power, velocity, and frequency. Figures 6.4 and 6.5 show the influence of focal length and incidence angle on the depth at different laser powers, velocities, and frequencies. Figures 6.4 (a) and 6.5 (a) illustrate the effect of the focal length and incidence angle at different laser powers respectively. It can be seen that at a low laser power of 1 W the groove depth is 0 µm. Furthermore, when the laser power increases the impact of focal length and incidence angle on the depth is also increased. Another attitude can be seen in figures 6.4 (b) and 6.5 (b), which show the effect of the laser velocity on the relation between the groove depth, incidence angle, and focal length. Where, at a low speed the effect of both of the incidence angle and focal length on the depth is higher than at a high speed. Figure 6.4 (c) shows the impact of the laser frequency on the relation between the depth and focal length. It is clear to see that there is no high impact for the frequency in this relation, while the relationship between the incidence angle and groove depth is extremely affected by the laser frequency, especially at high incidence angles. Elevated laser frequencies result in a high impact for the incidence angle on the groove depth, as shown in figure 6.5 (c). The 3D relation in figures 6.4(d) and 6.5(d) shows that the increase in the focal length and incidence

angle produces a reduction in the groove depth. Moreover, it is obvious that the shift in focal length from 0 to 3 mm does not reveal a strong impact on groove depth, in contrast to the effect of the increase to 5 mm. There is a distinct effect caused by this increment, especially at low speeds. Figure 6.5 (d) confirms that the increase in the incidence angle from 0 ° up to 20 ° and then to 40 ° respectively results in almost the same effect on the depth, except at low speeds or high frequencies, where the variation in depth is at highest value.

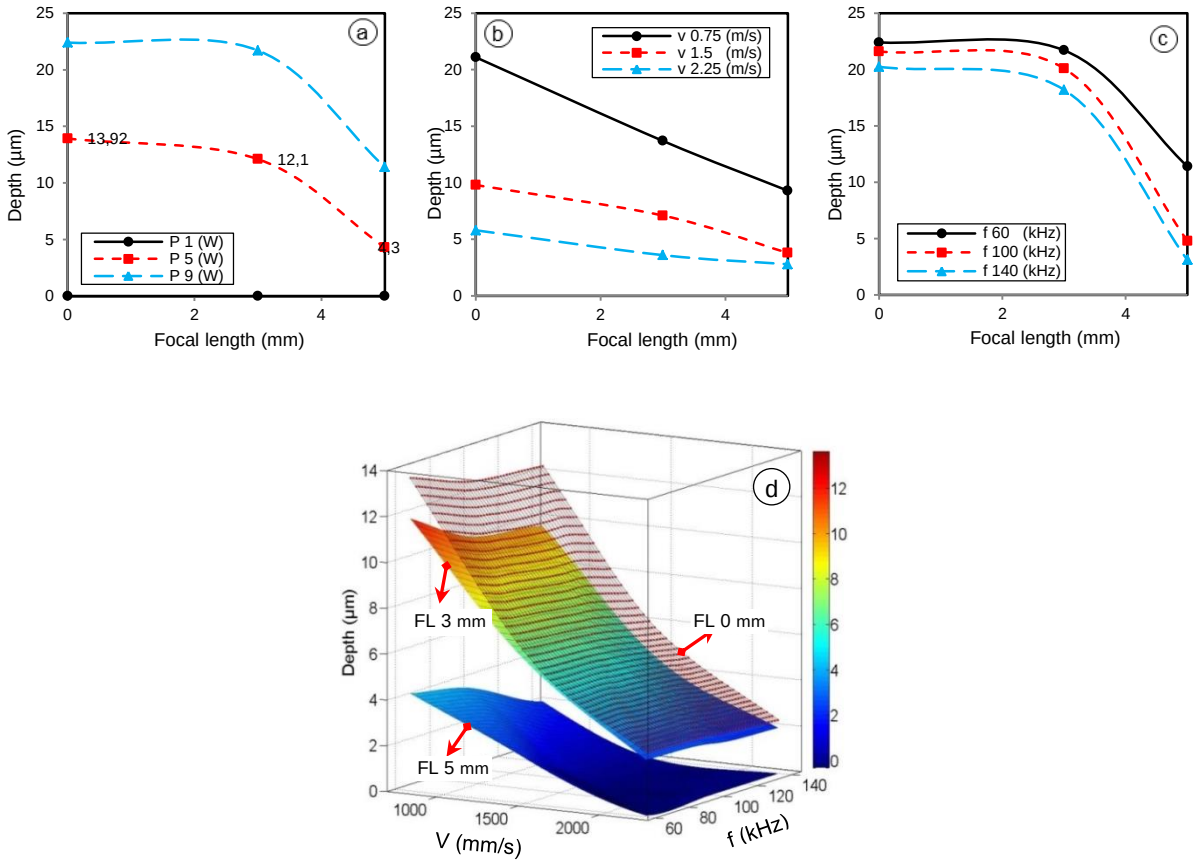

Figure 6.4: The effect of focal length on the depth at (a) v 0.75 m/s and f 60 kHz. (b) P 5W, H 50 % and f 60 kHz. (c) P 9 W and v 0.75 m/s. (d) 3D relation.

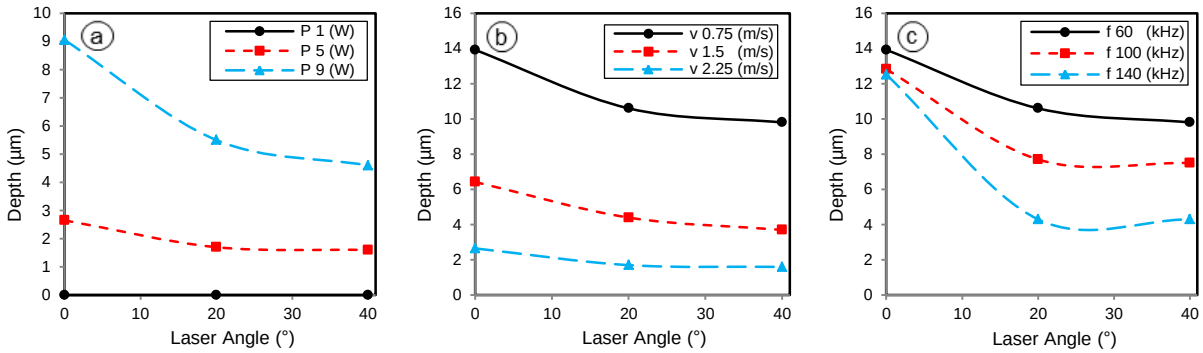

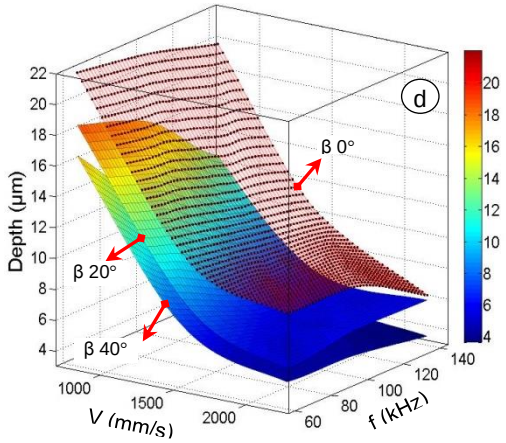

Figure 6.5: The effect of incidence angle on the depth at (a) v 2.25 m/s and f 60 kHz. (b) P 5 W and f 60 kHz. (c) P 5 W and v 0.75 m/s. (d) 3D relation.

The interaction between the three important process parameters including hatching, focal length, and incidence angle should also be explored regarding their effect on the groove depth. Figure 6.6 (a) shows the impact of focal length on depth at various hatching. It can be easily realized that the effect of the focal length is increased excessively when hatching rises from 0 % up to 50 % and then 75 %, respectively. The same behavior can be observed in figure 6.6 (b) which shows the interaction between hatching and incidence angle. It is significant to note that as the hatching increases the influence of the incidence angle is also increased.

At a focal length of 0 mm and a hatching of 0 %, the depth is about 13.92 µm. If the focal length increases to 5 mm or the incidence angle is set at 40 °, the depth is lowered to 4.3 µm and 9.8 µm respectively for the 5 mm focal length and 40 ° incidence angle (see figure 6.6(a) and (b)). By raising the hatching to 50 % or 75 % we can reduce the effect of focal length and incidence angle on the groove depth. At a focal length of 3 mm and an incidence angle of 20 °, it is possible to get a depth of 13.92 µm by increasing the hatching to 50 % only. However, at a focal length of 5 mm and the incidence angle of 40 °, the hatching should be set up in the range of between 50 % and 75 %. At a focal length of 5 mm, hatching should be even regulated to 63 % or 55 % if the incidence angle is 40 °. For 3D MID-LDS applications, the setup of the hatching should be selected according to the focal length and incidence angle. This means to reduce the effect of incidence angle and focal length on depth, it is preferred to increase the hatching. The offset in laser energy and its distribution, which results from the effect of focal length and incident angle, can be reduced by increasing the accumulative energy through using a high hatching value.

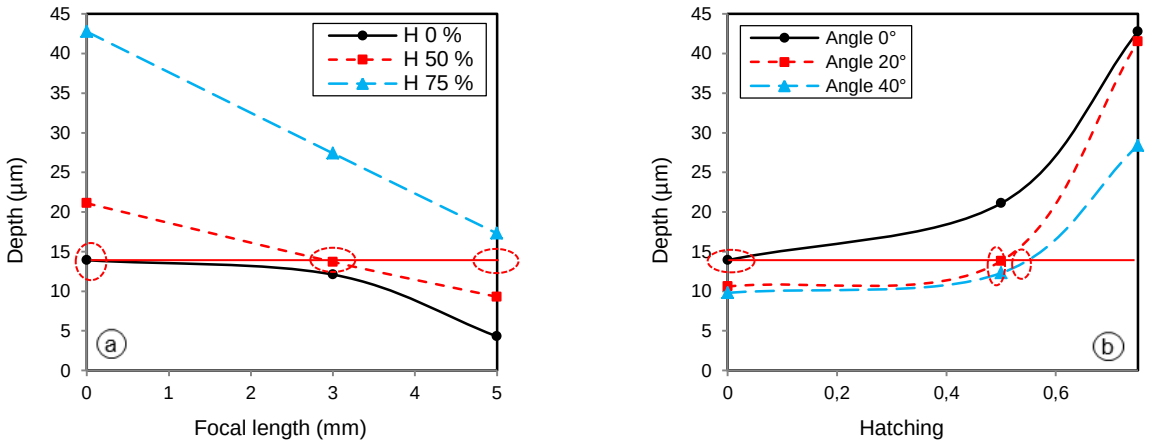

Figure 6.6: The interaction between process parameters and depth at P 5 W, v 0.75 m/s and f 60 kHz.(a). FL against H. (b). H against incidence angle.

B. Ceramic Based Material

The above shown results were belonging to the PEEK polymer. The impacts of the investigated parameters on the groove depth for the new innovative ceramic based material are presented in figure 6.7. We can see from figure 6.7(a) that the depth is raised when the laser power is increased or the velocity is reduced. The same behavior for the groove depth occurs at a low laser power of 4 W accompanied by decreasing the frequency, or at an elevated laser power of more than 8 W in conjunction with increasing the frequency. Figure 6.7(b) illustrates the influence of the percentage of additives on the relation between the groove depth, velocity and frequency at a laser power of 4 W. The complex relation is clearly visible. Under these corresponding process parameters, the effect of copper oxide can be classified into two types. In the first the depth is increased; this always under a low laser power of 4 W, laser velocities more than 1 m/s and different laser frequencies. While, other parameter settings of laser velocity and frequency lead to a decrease of the groove depth. In addition to that, the increasing in the sintering temperature leads always to an increase of the groove depth, as shown in figure 6.7 (c).

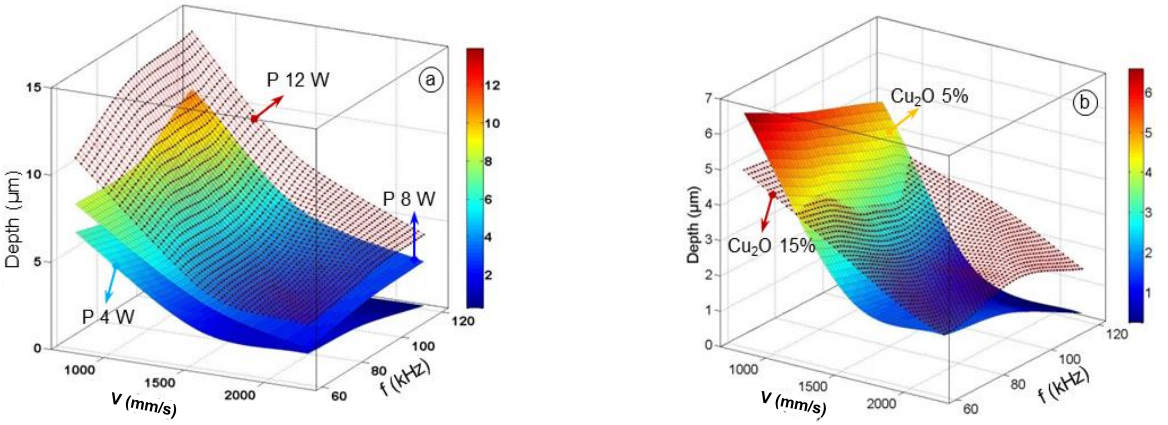

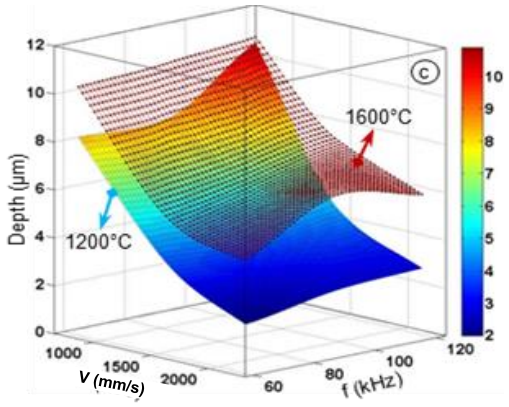

Figure 6.7: Groove depth against process parameters at (a) Cu_2O 5 %, T 1200 °C, P 4 W, 8 W and 12 W (b) T 1200 °C, P 4 W, Cu_2O 5 % and 15 % (c) Cu_2O 5 %, P 8 W, T 1200°C and 1600 °C.

6.2.2. Track or Conductor Width

A. PEEK Polymer Material

The laser beam creates a groove with dimensions (depth, width, edge height, and edge width) on the substrate surface. It was found in the previous work that the metallization structure covers the groove width as well as the width of two edges [17]. This refers to the track width or the interactive width (see figure 5.1 (b)). According to that, the next analysis is focused on the track width which is more important than the groove width.

Figure 6.8 shows the influence of the laser power, laser speed, and the frequency on the track width, where figure 6.8 (a) shows the impact of the laser frequency and speed on the track width at a laser power of 1 W. From this figure it can be seen that the track width is reduced with the laser speed and the frequency. Furthermore, as the laser speed increases, the influence of frequency on the track width is also increased. Another important effect for the laser speed is shown in figure 6.8 (b). It shows the effect of both the laser speed and the power on the track width at a laser frequency of 60 kHz. The inverse relationship between the laser speed and the width also appears here. It is in contrast to the behavior with the rise of the laser power. Figure 6.8 (c) clarifies the influence of the laser power and the frequency on the track width. It can be clearly stated that the impact of the laser power is bigger than the influence of the frequency. In general, there is an interfering relationship between the working parameters and track width. Their effect on the width is related to each other. This can be seen in figure 6.8 (d) which shows the 3D relation between those three parameters.

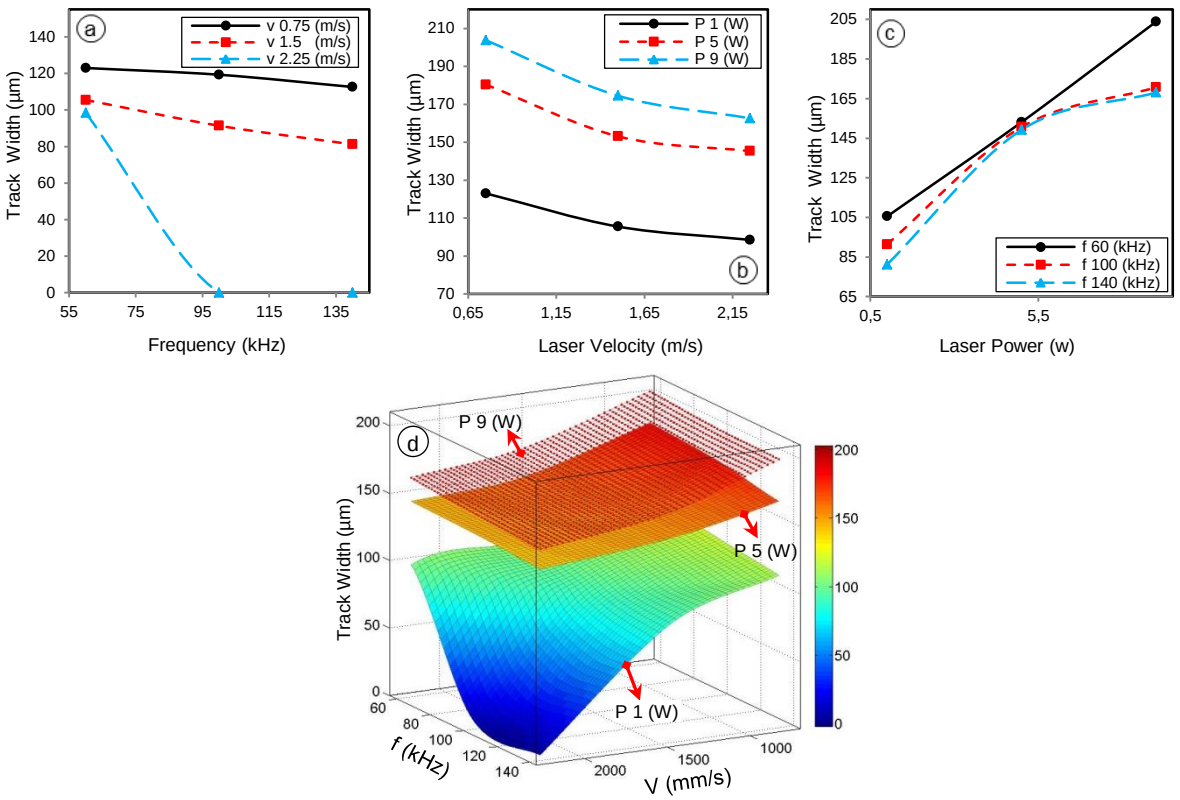

Figure 6.8: Track width against laser power, velocity and frequency, (a) at P 1 W. (b) at f 60 kHz. (c) at V 1.5 m/s. (d) 3D relation.

The influence of hatching on the track width at different working parameters is shown in figure 6.9. From this figure, it can be noted that the rise of in the hatching percantage increases the track width. Moreover, at elevated laser speeds or frequencies or at low laser powers, the hatching has a high impact on the track width in comparison to the impact of a low speed, a low frequency, and a high power. Although the increment in the hatching leads to an increase of the amount of laser energy, which is absorbed by the material through its surface, there is no strong influence for hatching on track width. It can be observed that the impact of the hatching on the groove depth is more than that on the track width. In fact, this is due to the way that is used, by the software, to change the number of the laser path lines in the structured area. According to the software, the number of laser path lines is increased at the interior area only to achieve the required hatching. Whereas the laser path lines at the boundary of the area are firmed at the same position and number. This helps to increase the laser energy in the interior area. Consequently, this leads to a bigger increase in the groove depth than the track width.

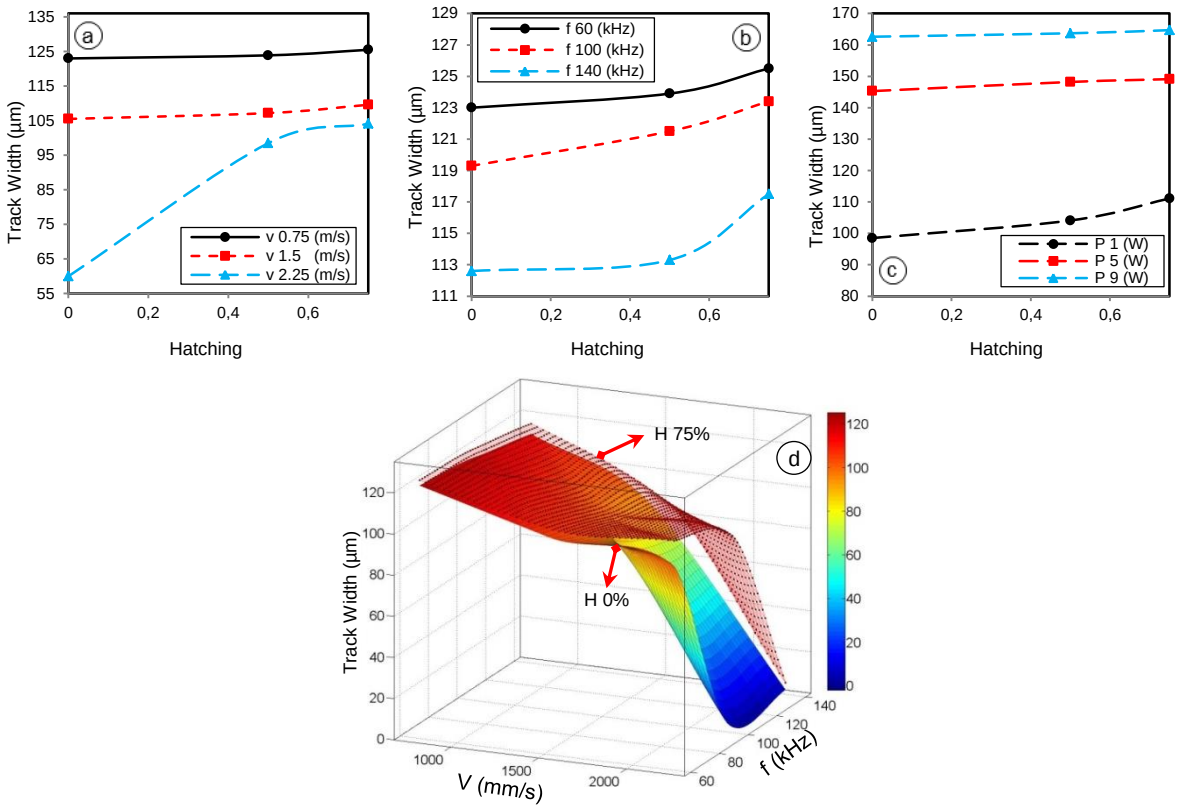

Figure 6.9: Track width against hatching at (a) P 1 W and f 60 kHz. (b) P 1 W and v 0.75 m/s. (c) v 2.25 m/s and f 60 kHz. (d) 3D relation.

It is already mentioned that the laser beam diameter is affected by the incidence angle and the focal length. Any variation in the focal length produces a broadening in the laser beam diameter and the area of the laser spot. Hence, the laser density and its distribution will be changed [42]. Figure 6.10 (a) illustrates the influence of the focal length on the track width at different levels of laser power. It can be noted that at low laser power the width is decreased with increase of focal length, unlike at high laser powers where the width increases with focal length. At high laser power, the laser energy is enough to structure the area under the laser spot even with decreasing the laser density, which is caused by the effect of focal length. Whereas at low laser power the reduction in laser density caused by the variation in focal length, leads to reduce the track width. It is very important to conclude that to reduce the effect of the focal length on track width. It is preferable to set up the laser power at high values. Figures 6.10 (b) and (c) demonstrate the effect of both, the laser speed and frequency on the relation between the track width and focal length respectively. It is clear to see that there is a direct relationship between width and focal length at different laser speeds and frequencies. Figure 6.10(d) shows the 3D relationship between the track width, laser speed, frequency and the focal length at a laser power of 9 W. At this laser power, the raising in the focal length results in an increase of the track width. As a conclusion, the focal length has a complex impact on the track width, because it is depended on the other process parameters. The

laser incidence angle has also a similar or even more complex impact on the width, like the focal length. This influence will be explored in the next section.

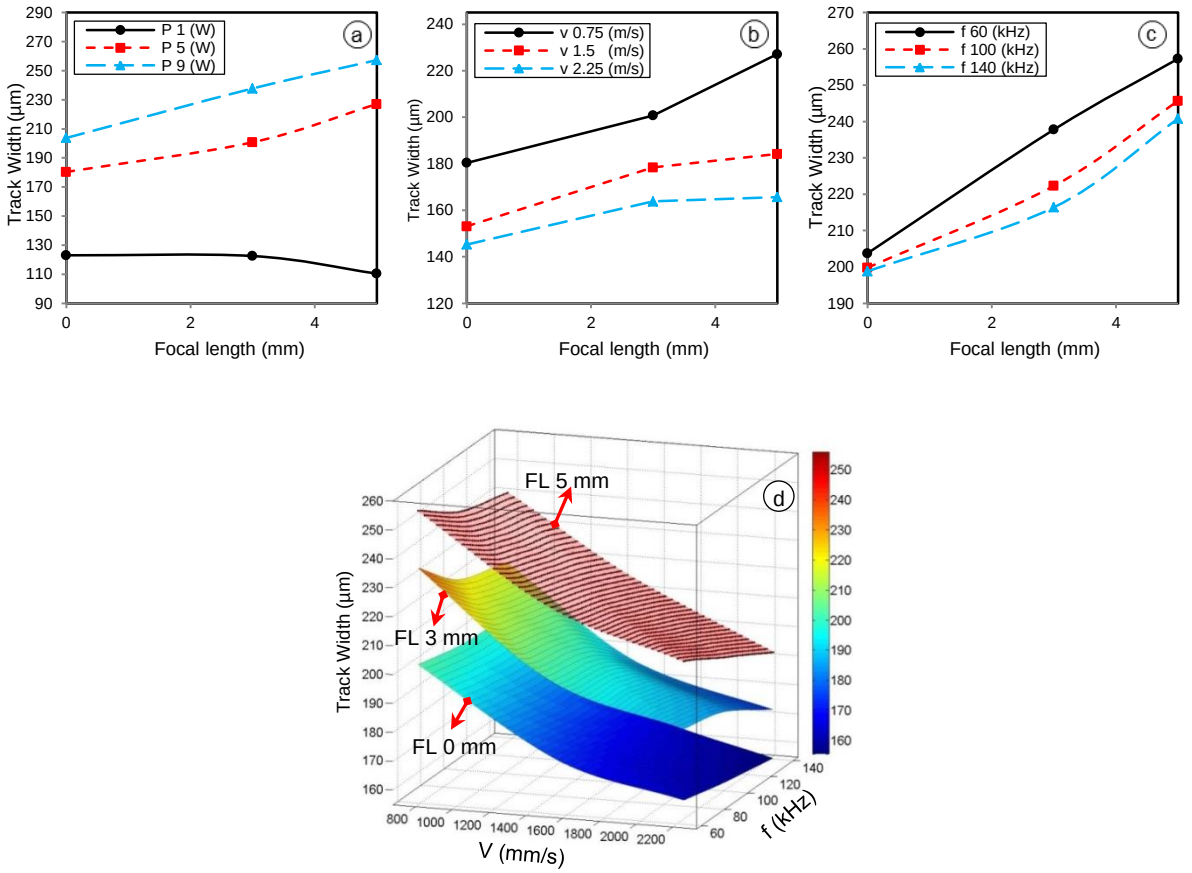

Figure 6.10: Track *width against focal length at (a) v 0.75 m/s and f 60 kHz. (b) P 5 W and f 60 kHz. (c) P 9 W and v 0.75 m/s. (d) P 9 W, 3D relation.*

Figure 6.11 shows the correlation between the track width and the incidence angle at various parameters. Figure 6.11(a) demonstrates the influence of the incidence angle on the track width at different levels of laser power. At a low power, the width decreases with the incidence angle. However, when the laser power is set to elevated values such as 5 W or 9 W, the behavior will be reversed. Thus the track width is increased with the incidence angle when it goes up to 20 °. After that the width is again decreased at an incidence angle of 40 °. Nevertheless, the width is still bigger than at an incidence angle of 0 °. In fact, this behavior is due to the effect of the incidence angle on the shape and size of the laser spot area and then on the density and distribution of the laser irradiation. This correlation is explained in this chapter and in the simulation chapter.

The effect of laser speed on the relationship between width and incidence angle is shown in figures 6.11(b) and (c). Both figures refer to the results of a laser power of 1 W and 5 W respectively. Here it is shown at a laser power of 1 W that the track width is declined with the incidence angle at different of laser speeds. Whilst at

parameter sets which include a power of 5 W and a laser speed of 0.75 m/s the width increases with a raise in the incidence angle. At elevated speeds in range of 1.5 m/s and 2.25 m/s and when the incidence angle is increased to 20 °, the track width will be raised. At an incidence angle of 40 °, it is decreased again, but it is generally higher than at an incidence angle of 0 °. This can be seen in figure 6.11 (a) and (c). The same behavior can be noted in figures 6.11 (d) and (e), which shows the influence of laser frequency on the mentioned relation.

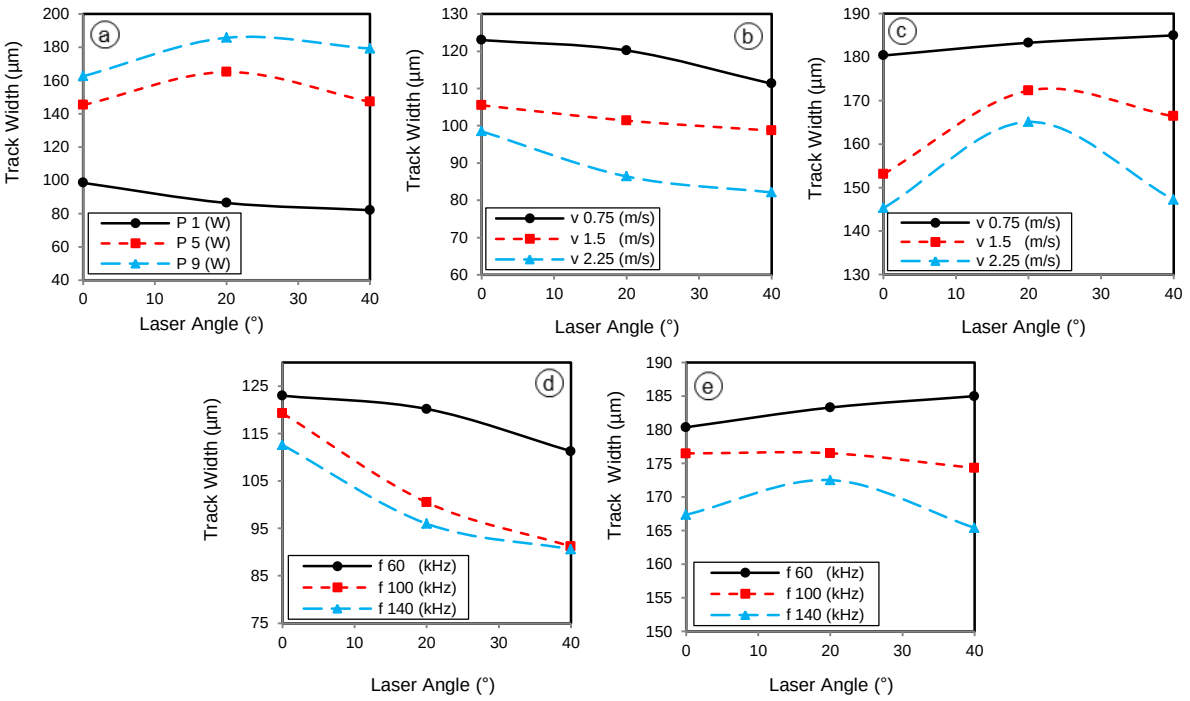

Figure 6.11: Track *width against incidence angle (a) v 2.25 m/s and f 60 kHz. (b) P 1 W and f 60 kHz. (c) P 5 W and f 60 kHz. (d) P 1W and v 0.75m/s. (e) P 5 W and v 0.75 m/s.*

The 3D-figures in figure 6.12 (a) and (b) demonstrate the impact of laser speed, frequency, and incidence angle on the track width at a laser power of 1 W and 5 W respectively. From figure 6.12 (a) it can be concluded that at a high laser speed the effect of frequency on the track width is bigger than at a low speed. The influence of laser speed on width is increased with the laser frequency. The track width is reduced with the incidence angle. Yet, this reduction also correlates with laser speed and frequency. At a laser power of 1 W the maximum track width can be produced with parameter sets of a low frequency of 60 kHz, a laser speed in the range of between 0.75 m/s to 1.5 m/s. Moreover, the effect of incidence angle at 20 ° at a high laser speed and frequency is approximately negligible in comparison with that at low values. At an elevated laser power of 5 W, the effect of incidence angle will be reversed. It can be clearly noted in figure 6.12 (b), which shows the raise in width with incidence angle. Moreover, the influence of angle 20 ° is more than that for angle

40 °. As it is explained, this is due to the effect of the incidence angle on the laser spot diameter, laser density and laser distribution. Furthermore, at a laser power of 5 W the suitable parameter settings, which include lower values for both velocity and frequency, are preferred to produce maximum track width.

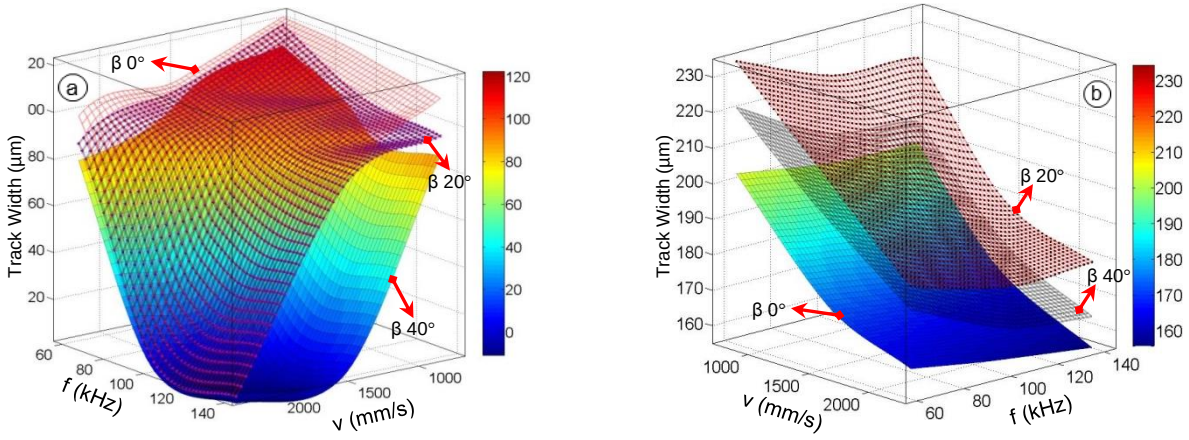

Figure 6.12: The 3D relations between the track *width and incidence angle at different velocities and frequencies and laser power of (a) 1 W. (b) 5 W.*

Once more, the interaction between the hatching, focal length, incidence angle, and track width should be investigated. Figure 6.13 (a) shows the effect of hatching on the relation between focal length and track width. The corresponding parameter sets of this figure include a laser power of 1 W, a speed of 0.75 m/s and a frequency of 60 kHz. It can be seen from this diagram that there are no variations in width when the focal length increases from 0 mm to 3 mm at different hatching values. However, this width decreases rapidly when the focal length is raised from 3 mm to 5 mm at various hatching values. The impact of the focal length can be reduced by increasing hatching, although, the influence of hatching on track width is limited with this parameter setup. Other important relationships are shown in figure 6.13 (b) and (c) which shows the effect of hatching on the correlation between track width and incidence angle at a laser speed of 0.75 m/s, a frequency of 60 kHz, and a laser power of 1 W and 5 W. From figure 6.13(b) it can be derived that the effect of hatching when it is changed from 0 % to 50 % is less than its effect when it is changed from 50 % to 75 %. Moreover, the impact of the incidence angle at 40 ° on the width is stronger than at 20 °. At elevated laser powers, the impact of the incidence angle on the width will be inverted. This can be seen in figure 6.13 (c), the track width increases with the incidence angle. With this parameter set it is preferred to minimize the hatching to reduce the effect of incidence angle.

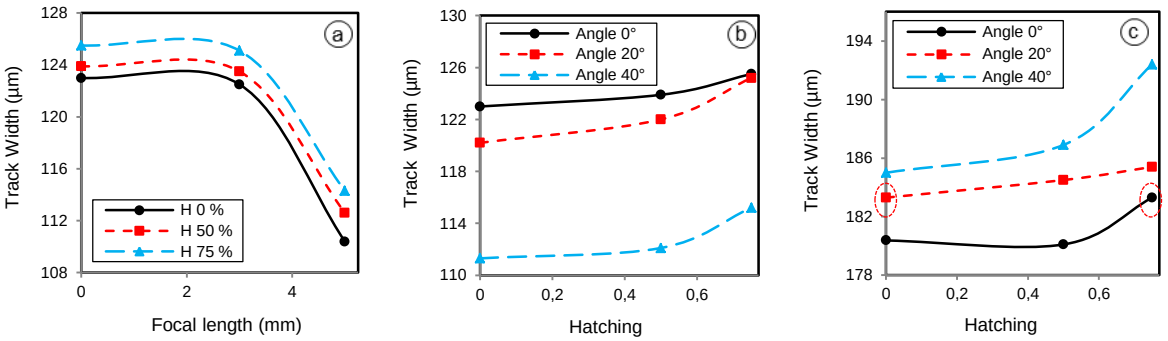

Figure 6.13: Track width and the interaction between the process parameters

B. Ceramic Based Material

Ceramic based materials have completely different physical and thermal properties than polymers. Consequently, the thermal behavior of these materials under the impact of laser irradiation should also be different. This produces a groove or structured area with different characteristics. One of the most vital and important differences is the edge lap, which does not exist for this material in comparison to polymers that show this formation. This means the groove width equals the track width because the edge width is equal to 0 µm. In the next section, the groove width or the track width of the ceramic material will be investigated in detail. Figure 6.14 shows the relationship between the investigated parameters and the track width. Figure 6.14 (a) describes the correlation between the width, the laser power, velocity, and the frequency. Here it can be seen that the width is increased with laser power or when velocity or frequency are reduced. By using new fabrication conditions, which include high sintering temperature of 1600 °C or a high additive percentage of 15 %, the width of the track will be increased. This is shown in figure 6.14 (b) and (c). The reasons behind the increase are the different thermal-physical properties of the ceramic materials, which are produced under new production conditions.

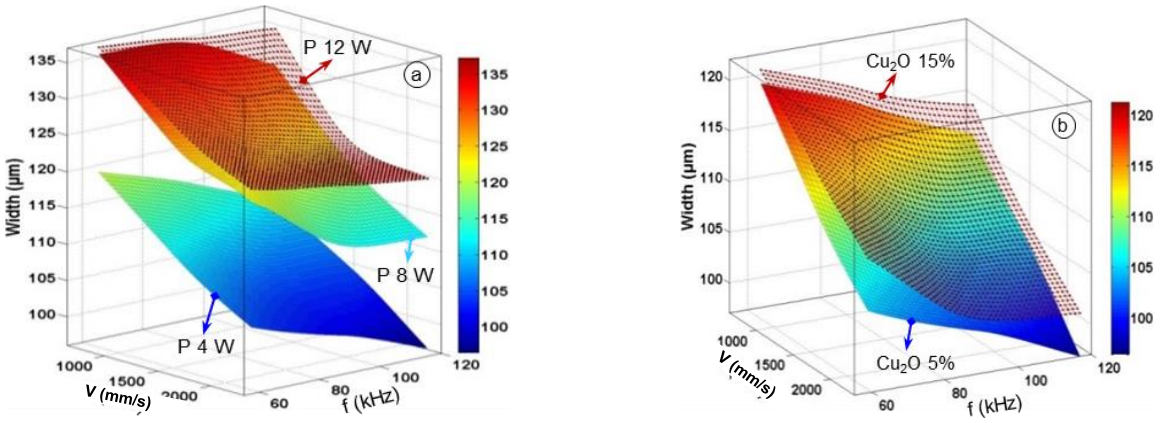

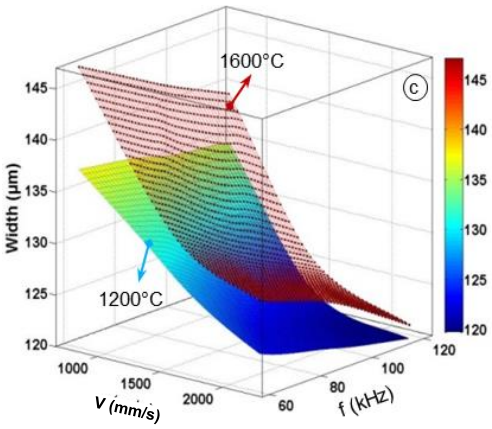

Figure 6.14: Track *width against laser power, velocity and frequency at (a) Cu_2O 5 %, TS 1200 °C and different power. (b) TS 1200 °C and P 4 W different copper oxide. (c) Cu_2O 5 %, P 12 W and different sintering temperatures T 1200 °C and 1600 °C.*

6.2.3. Groove Edge Dimensions-Edge Factor

It was concluded that the edge groove dimensions (lap width and height) impose a negative effect on the LDS quality and the final quality of MID products. This effect can be defined as *edge factor* [17]. Therefore, it is extremely important to explore the influence of adopted process parameters on these dimensions. This section will be employed for this purpose. Figure 6.15 shows the impact of the laser power, velocity, and frequency on both the width and height of the edge lap. They increase with the laser frequency or when the laser speed decreases. Furthermore, the effect of laser frequency on these dimensions reduces with laser speed. In other words, the effect of the frequency on the dimensions of the edge at lower speeds is greater than at high speed which can be clearly seen in figure 6.15 (a) and (d). Figure 6.15 (b) and (e) illustrate the effect of laser speed on these dimensions at different laser powers. At a laser power of 1 W, a laser frequency of 100 kHz, and a laser speed above 1.5 m/s, there is no edge formed for the groove. This case occurs when the amount of laser energy is not sufficient to form this formation. When the laser speed is reduced to 0.75 m/s at the same parameter set, the laser energy will be enough to produce a puffiness effect on the polymer surface with a certain height, as shown in figure 6.15 (e). Another important effect is shown in figure 6.15 (c) and (f). In general, any raise in laser power increases the edge dimensions, but this effect depends on the other parameters such as laser frequency. It can be seen from these two figures that, the impact of laser frequency on edge dimensions increases with laser power. Moreover, the effect on edge height is greater than on edge width. In fact, the influence of laser frequency on the edge height has different behavior can be noted in figure 6.15 (f). Where, at a laser power of 1 W, and a low laser velocity of 0.75 m/s, the edge height is reduced with laser frequency. At elevated laser power or velocity, this behavior will completely reverse, due to the extreme reduction in the laser energy under this parameter settings.

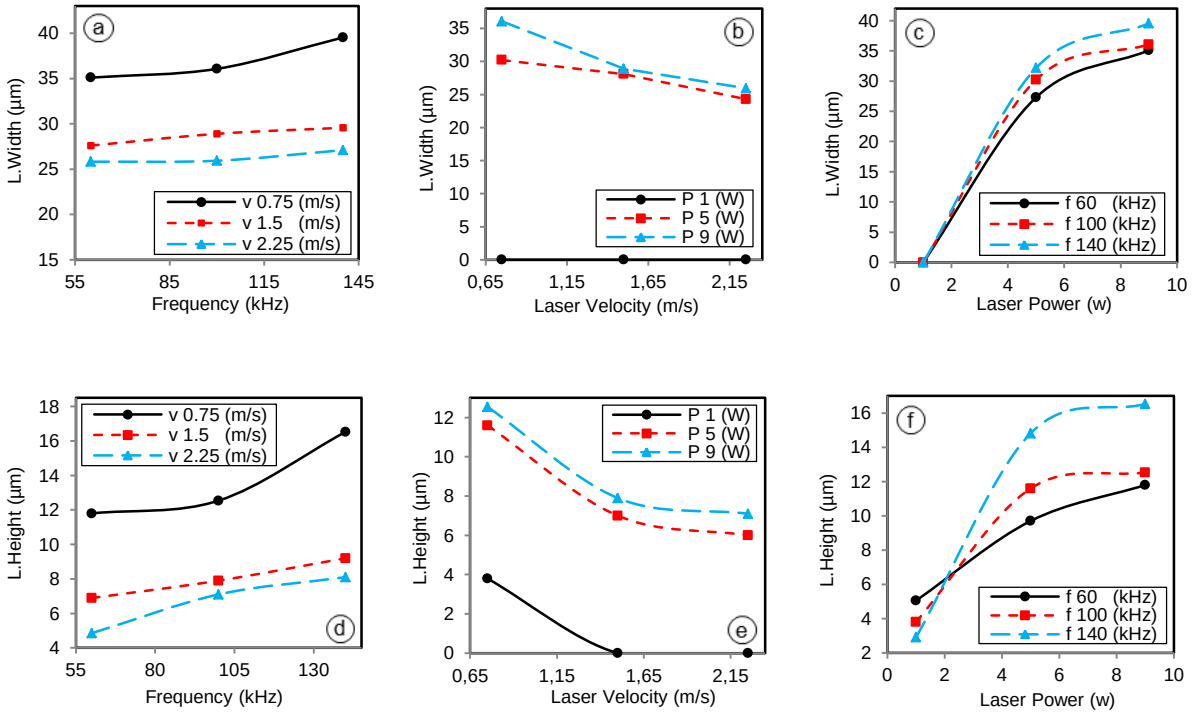

Figure 6.15: The groove edge dimensions against (a) Frequency at P 9 W. (b) Velocity at f 90 kHz. (c) Power at v 0.75 m/s. (d) Frequency at P 9 W. (e) Velocity at f 90 kHz. (f) Power at v 0.75 m/s.

The 3D relation between the working parameters and dimensions of the groove edge is shown in figure 6.16 (a) and (b). Again, it can be easy to note that the edge dimensions are increase; with the laser power and frequency or when the velocity is reduced. It is observed that the effect of the adopted parameters on edge dimensions is interdependent. At low laser power and frequency, the effect of velocity is less than at high frequency or laser power and the same follows for the effect of power on the edge which is dependent on laser velocity and frequency. It is very significant to mention that these three laser parameters which include the laser power, velocity, and the frequency are related to each other. According to the new classification of these parameters, the relationship between laser power and frequency can be defined as the laser fluence, while the irradiation dose is the relationship between laser power and velocity. Finally, pulses overlapping denote the correlation between laser velocity and frequency [42].

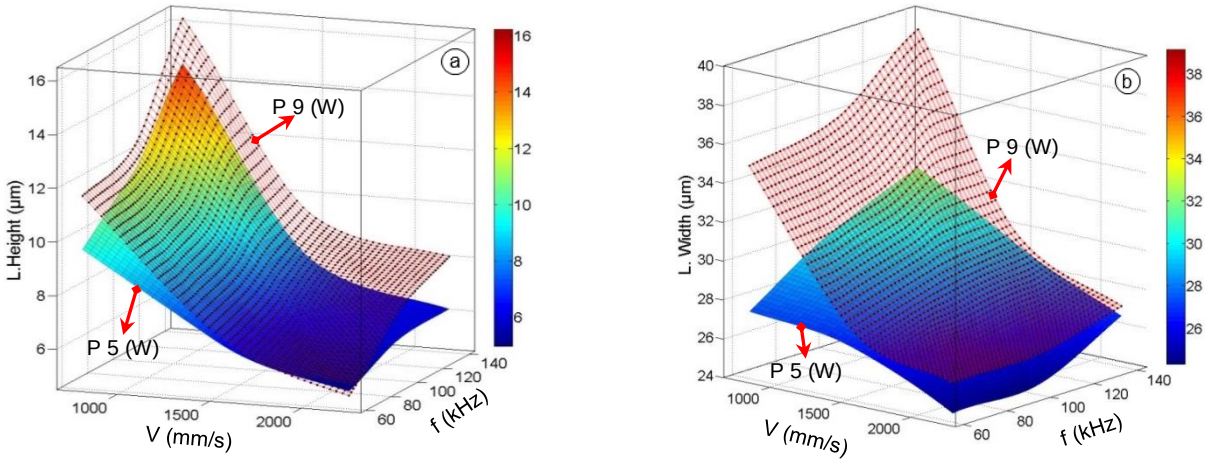

Figure 6.16: The 3D relation between the edge dimensions and laser power, velocity and frequency. (a) Height. (b) Width.

The correlation between focal length and edge dimensions, at various working parameters, is shown in figure 6.17 (a) to (f). Whereas, figure 6.17 (a) and (d), demonstrate the impact of focal length on width and height of the edge respectively at different laser power. The other parameters are fixed at certain values which include: a velocity of 0.75 m/s, frequency of 60 kHz, a hatching of 0 and an incidence angle of 0 °. Here it can be seen that under these parameters, the edge width increases and edge height reduces with focal length. In addition, the impact of focal length depends on laser power. The focal length shows the same influence on the edge width as shown in figures 6.17 (b) and (c). These figures show the effect of both the laser velocity and the frequency on this relationship. Figure 6.17 (e) shows another important impact for laser speed on the relationship between edge height and focal length, at a constant laser power of 9 W and a frequency of 60 kHz. It is clear to see that at a velocity of 0.75 m/s the edge height reduces with focal length, but as the laser velocity increases to more than 1.5 m/s, the above relation will change to an inverse proportionality. Finally, the effect of laser frequency on the above-mentioned relation is shown in figure 6.17 (f). In this figure, the parameter set were a laser velocity of 0.75 m/s and a laser power of 9 W.

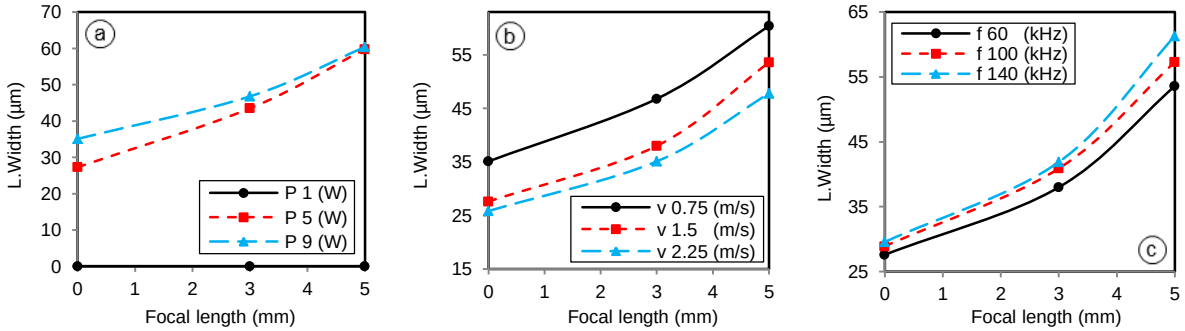

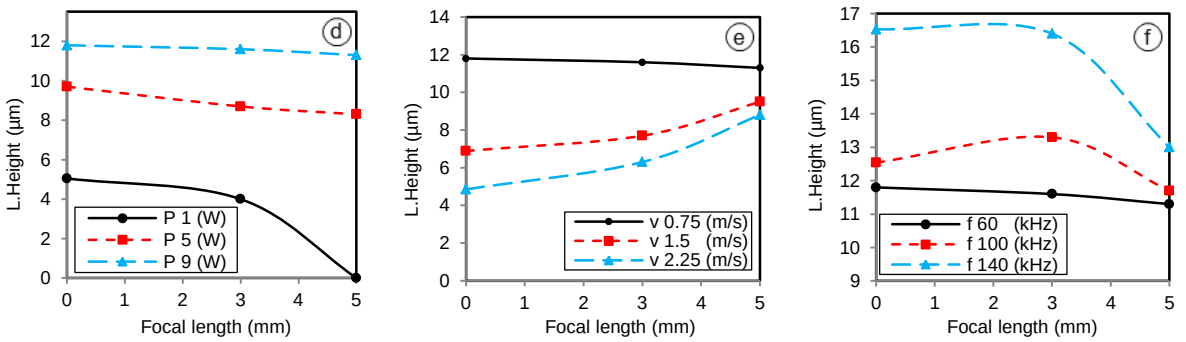

Figure 6.17: The edge dimensions against focal length at (a) v 0.75 m/s and f 60 kHz. (b) P 9 W and f 60 kHz. (c) P 9 W and v 1.5 m/s. (d) v 0.75 m/s and f 60 kHz. (e) P 9 W and f 60 kHz. (f) P 9 W and v 0.75 m/s.

A further 3D relationship between the edge dimensions and focal length at different working parameters is shown in figure 6.18. It is very important to mention that the edge width can be experimentally reduced by a reduction of the frequency or using high laser speed as seen in figure 6.18 (a). It shows the width as a function of the laser speed and frequency at a constant power of 9 W. The same setting of these two parameters tends to reduce the edge height as shown in figure 6.18 (b) and (c). Furthermore, it can be observed from these figures that at a laser power of 5 W, and a velocity less than 2 m/s, the edge height decreases with rise of the focal length, but as the laser speed increases above 2 m/s, at the same laser power of 5 W, the edge height will be increased. The same behavior can be seen for the edge height at elevated laser power, as it is clear in figure 6.18 (c). It illustrates the effect of focal length on edge height at an elevated laser power of 9 W. It can also be recognized from figure 6.18 (b) and (c) that the focal length does not show any impact on the edge height under this parameter sets. These parameters can be found from the intersection line between the 3D surfaces. In generally, it is preferred to use a laser power less than 5 W, low laser frequencies, and high laser velocities to reduce the edge dimensions and minimize the effect of focal length on the edge dimensions.

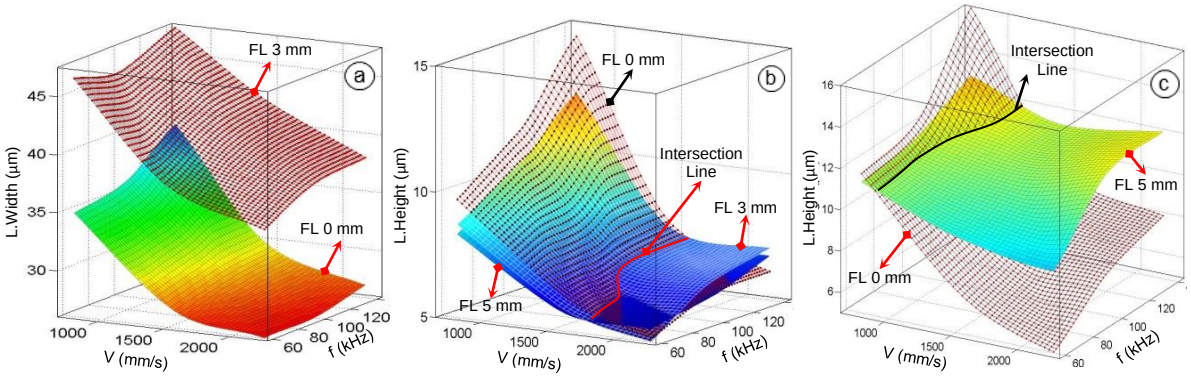

Figure 6.18: The 3D relation between the edge dimensions and the focal length, (a) Width at a laser power of 9W. (b) Height at a laser power of 5W. (c) Height at a laser power of 9W.

Figure 6.19 shows the influence of hatching on edge dimensions. It is clear to see that, as the hatching is set to elevated values, the edge dimensions including width and height are increased. For instance, the hatching value fixed between 0 % and 50 % does not affect the edge dimensions significantly. In addition, a parameter settings including, a low laser power of 1 W, a low frequency of 60 kHz, and a high velocity in range of 1.5 m/s to 2.25 m/s, the effect of the hatching is less than at a higher laser power more than 5 W, higher frequency in the range of 100 kHz to 140 kHz, and a low velocity of 0.75 m/s.

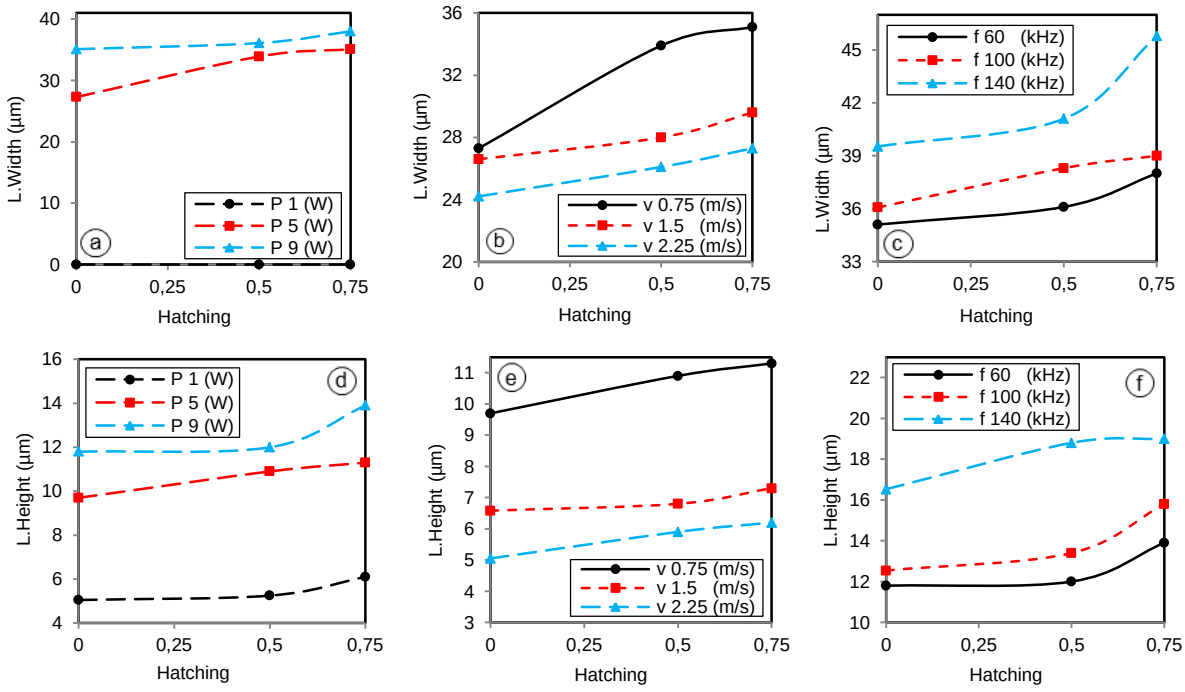

Figure 6.19: The edge dimensions against hatching at (a) v 0.75 m/s and f 60 kHz. (b) P 5 W and f 60 kHz. (c) P 9 W and v 0.75 m/s. (d) v 0.75 m/s and f 60 kHz. (e) P 5 W and f 60 kHz. (f) P 9 W and v 0.75 m/s.

The effect of the incidence angle on the edge dimensions, at different power, frequency and speed, is clarified in figure 6.20 (a) to (f). When the incidence angle increases, the edge width follows a positive relationship with incidence angle, whereas the edge height reduces. The influence of incidence angle on edge dimensions is related to the other parameters. This reaction between process parameters helps to propose the set of parameters that can be used to reduce the effect of incidence angle on edge dimensions. For example, installing the laser power and frequency at a low value or the laser velocity at a higher value helps to reduce edge height. This setting is also preferred to reduce the edge width. This can also be seen in the 3D relationship between the laser velocity, laser frequency, incidence angle, and edge dimensions, which is shown in figure 6.21.

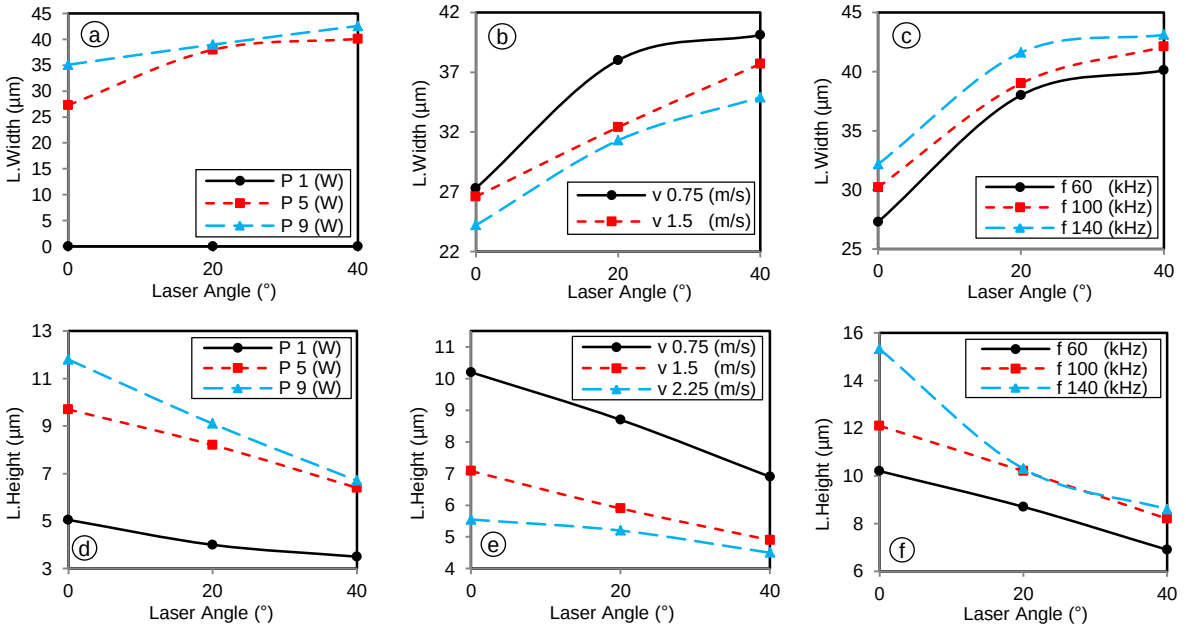

Figure 6.20: The edge dimensions against incidence angle at (a) v 0.7 5m/s and f 60 kHz. (b) P 5 W and f 60 kHz. (c) P 5 W and v 0.75 m/s. (d) v 0.75 m/s and f 60 kHz. (e) P 5 W and f 60 kHz. (f) P 5 W and v 0.75 m/s.

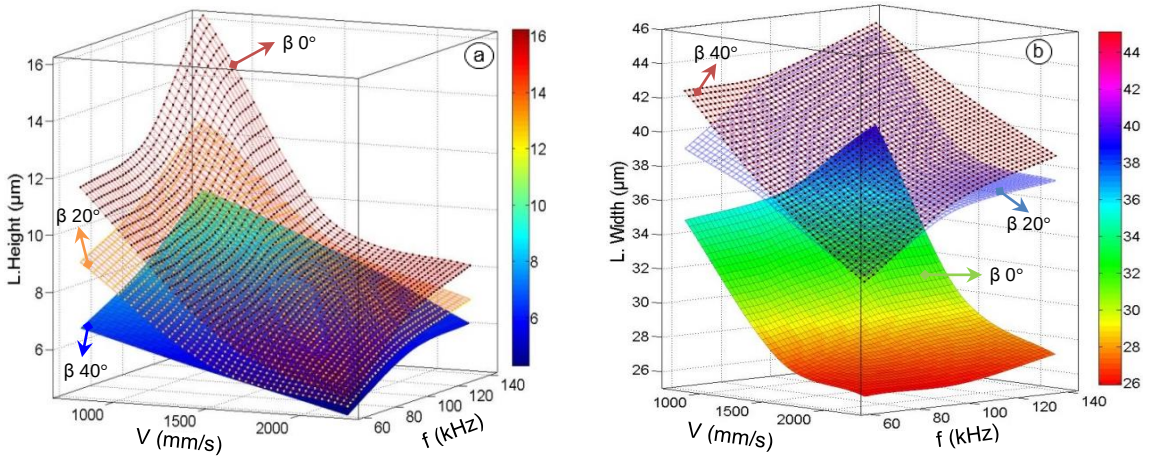

Figure 6.21: The 3D relation of the edge dimensions against incidence angle at P 9W (a) Height (b) Width.

The interaction between process parameters, which include the hatching, incidence angle and focal length as well as their influence on edge dimensions are shown in figure 6.22. It can be seen in this figure that the effect of hatching on edge dimensions when it is increased from 0 % to 50 % is not considerable in comparison with that at 75 % hatching. So that it is possible to raise the hatching to 50 %, but more than this range is not preferable due to its undesired effect on edge width. It can also be noted that the impact of the incident angle on the edge width and height is bigger than focal length and hatching effect under the corresponding parameters in the above mentioned figure.

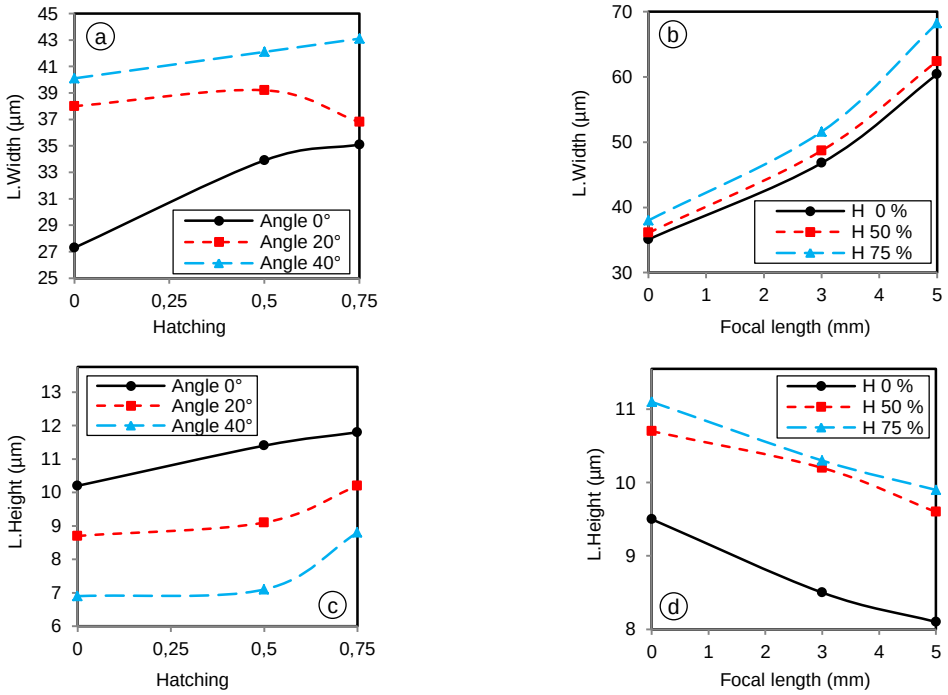

Figure 6.22: The interaction between process parameters at v 0.75 m/s and f 60 kHz; on edge width and: (a) P 5 W, (b) P 9 W. on edge height at; (b)P 5W , (c) P 5 W.

6.3. Groove Profiles

6.3.1. PEEK Polymer Material

The groove profile has a strong effect on the final LDS quality [17][18]. Therefore, the influence of the LDS parameters on this profile and its characteristics will be explored in this section. This helps to describe the profile's attribute in terms of its dimensions and ablation zones or types. Finally, this analysis could be used as one of the most significant icons to define the final LDS quality, as a function of LDS parameters, and their effect on the metallization step. This will be demonstrated in the following sections.

Figure 6.23 shows different types of the created grooves under different parameters. Figure 6.23 (a) shows the impact of laser power on the groove profiles. These grooves are formed under the parameter setup, which includes a laser velocity of 0.75 m/s, a frequency of 60 kHz, and laser power of 5 W and 9 W, the other parameters are fixed to zero. It is clear to see that the raising in laser power gives different groove profiles. Moreover, this structured area can be classified into two types of the ablation zone. The first can be defined as the puffing and resolidification zone (PZ). It occurs when the laser density is not sufficient to produce a melting and subsequent vaporization. Consequently, there is puffing or swelling occurring only on the surface under this laser irradiation [17][20]. Such phenomenon is always taking place at the groove edge; it is also accompanied by the resolidification effect. In general, this zone can be defined as a puffing and resolidification zone. The second zone can be defined as the removing zone (RZ). It takes place with laser energy

higher than for the previous type. This means the laser energy in this zone is enough for melting and vaporization of the molten materials. Figure 6.23 (a) also shows the distribution and the amount of these two different zones based on the laser power. Figure 6.23 (b) and (c) refers to the effect of laser speed and frequency on the groove profile. At a parameter setup including a low laser power of 1 W and a hatching of 50 % and 75 %, the laser energy is not sufficient for producing a groove inside the polymer surface. This will produce a structured area or groove with a type of PZ. Moreover, the height of this zone PZ is increasing with hatching, see figure 6.23 (d). A more complex impact is shown in figure 6.23 (e) and (f), which presents the influence of both the focal length and the incidence angle at parameter settings of a laser power with 5 W, a laser frequency of 60 kHz, and laser velocity of 2.25 m/s and 0.75m/s respectively. One can see from these figures that the focal length and the incidence angle increase the matching with adjacent grooves and reduce the groove depth and the edge height. Therefore, the percentage of the PZ and RZ will be changed and the final ablation type will be a mixture of both the PZ and RZ as shown in figure 6.23 (e) and (f). In fact, this is due to the distortion in the spot of the laser beam, which changes the distribution and the density of laser energy.

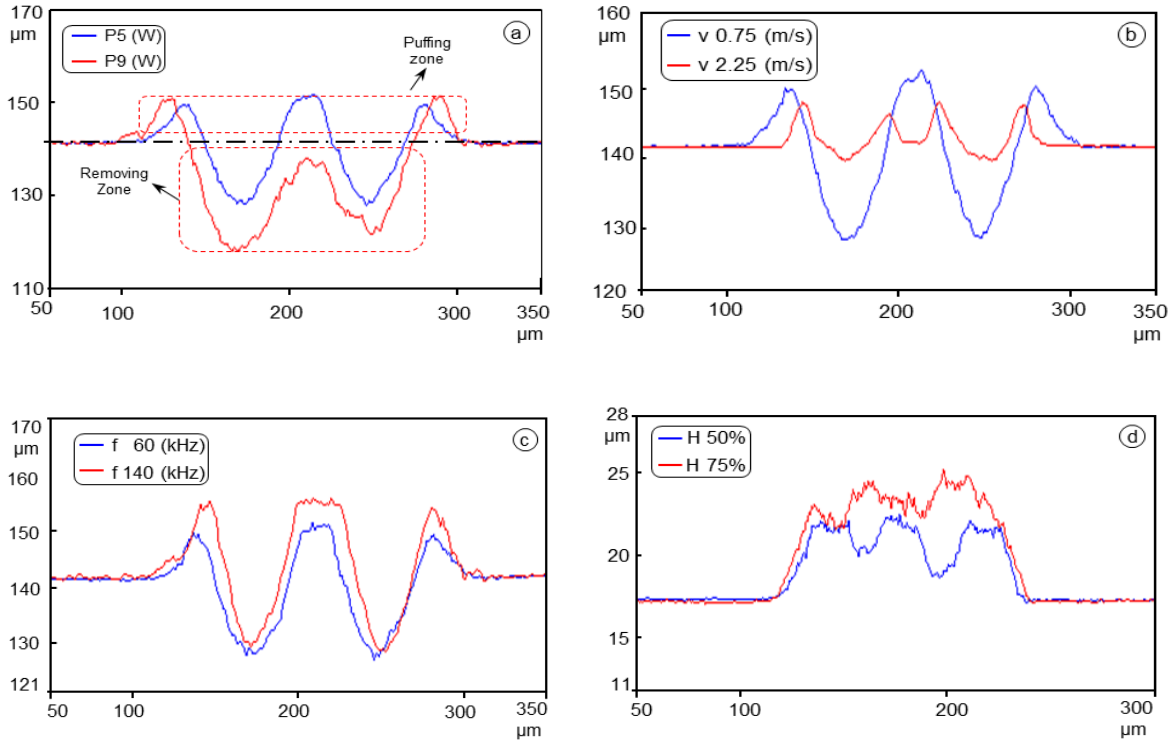

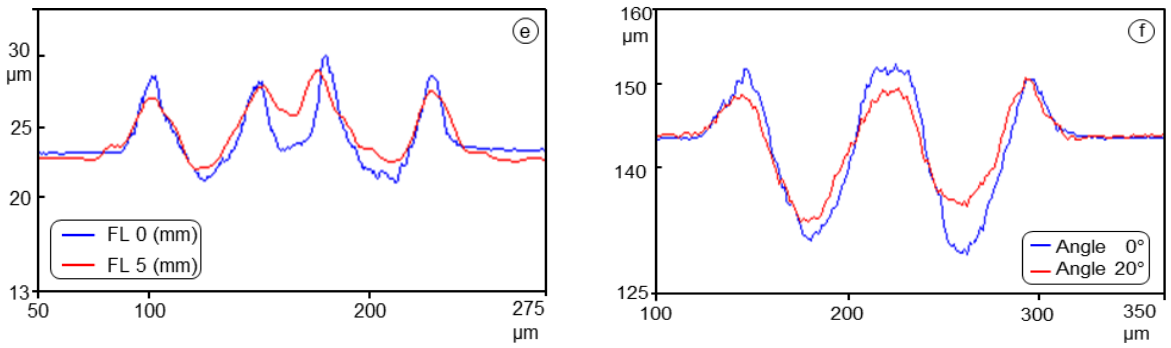

Figure 6.23: The grove profiles comparison at different (a) Power. (b) Velocity. (c) Frequency. (d) Hatching. (e) Focal length. (f) Incidence angle.

6.3.2. Ceramic Based Material

Due to the characteristics of the groove or structured area, the ceramic based materials provide a high LDS quality. It produces edges free of laps. In addition, it has high flexibility to draw very fine shapes by utilizing the LDS process. Two samples of the groove profile of these materials are shown in figure 6.24(a) and (b). It shows the comparisons between different cases under specific parameter settings which has a laser power of 12 W and velocity of 0.75 m/s, whereas the frequency is 60 kHz and 140 kHz for figure 6.24 (a) and (b) respectively. In figure 6.24 (a) the impact of the additive percentage on the groove profile can be seen, while figure 6.24 (b) shows the influence of the sintering temperature on the groove profile. In general, it can be seen that there are no laps at groove edges as mentioned.

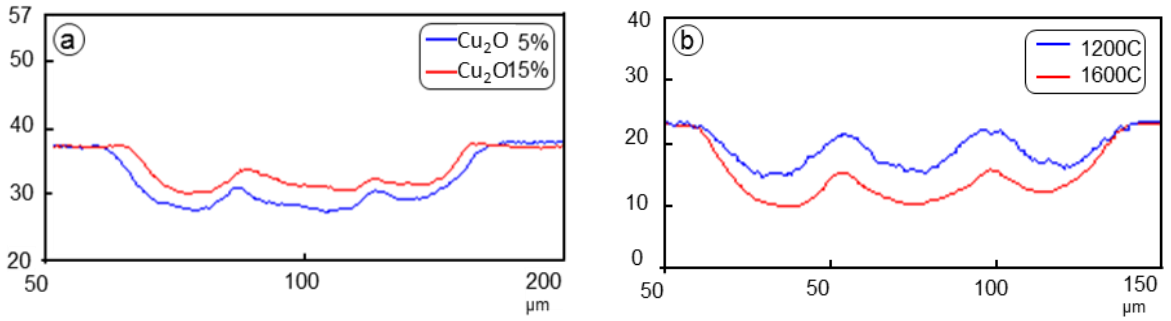

Figure 6.24: The comparison of grove profiles for ceramics at different (a) Additives percentage. (b) Sintering temperature.

6.4. Surface Roughness

After LDS and metallization steps, the surface roughness plays an important role in the surface texture or the surface topology. It is based on the setting of the LDS parameters. A structured area with varies surface roughness can be produced by regulating the LDS parameters. Moreover, the final MID responses such as surface roughness and adhesion strength of the metallized surface, are related to the surface

roughness of the structured area [30]. So, it is very significant to perform a series of experimental measurements for surface roughness considering the influence of parameter settings. Surface roughness is represented by many terms. Ra and Rz are most commonly used. They are calculated differently, Ra roughness is calculated as the average of the peaks and valleys of the measured surfaces. While Rz is obtained from the mean value of the five highest peaks (Yp) and lowest valleys (Yv), this is according to the Japanese Industrial Standard [96][97]. In this work, a laser scan microscope (Keyence VK-9700K) is used to measure the surface roughness, after which the software (VK analyzer) is employed to calculate and analyze the results [88]. The effect of all the investigated process parameters on the surface roughness including Ra and Rz will be deeply explored in this section.

6.4.1. PEEK Polymer Material

Figure 6.25 (a) to (d) shows the Rz and Ra roughness versus the laser power, velocity, and frequency. The continuous lines refer to Rz, whereas the dotted lines are Ra. It can be noted that the laser velocity at a constant frequency of 60 kHz and laser frequency at a constant power of 1 W, have a nearly equal influence on Rz and Ra, see figure 6.25 (a) and (b). The trend of Rz and Ra is inversely proportional to the laser velocity and the frequency according to these graphs. Figure 6.25 (c) demonstrates the influence of the laser power on Rz and Ra at different frequencies and constant velocity of 0.75 m/s. One can observe a direct relationship between laser power and Rz and Ra. The 3D relationship between the working parameters and Rz and Ra are illustrated in figure 6.25 (d). From this figure, it can be concluded that the effect of laser velocity and frequency at a low power is not the same as at a high power. The influence of both laser velocity and frequency on Rz and Ra are increased with laser power. In addition, the impact of frequency at a low power of 1 W will be reversed when the laser power increases to more than 5 W. It can also be concluded that the minimum surface roughness can be established under parameter sets which include minimum laser power and a maximum of both of the velocity and frequency, while the maximum Rz and Ra under a minimum velocity and a maximum of both the laser power and frequency, see figure 6.25(d).

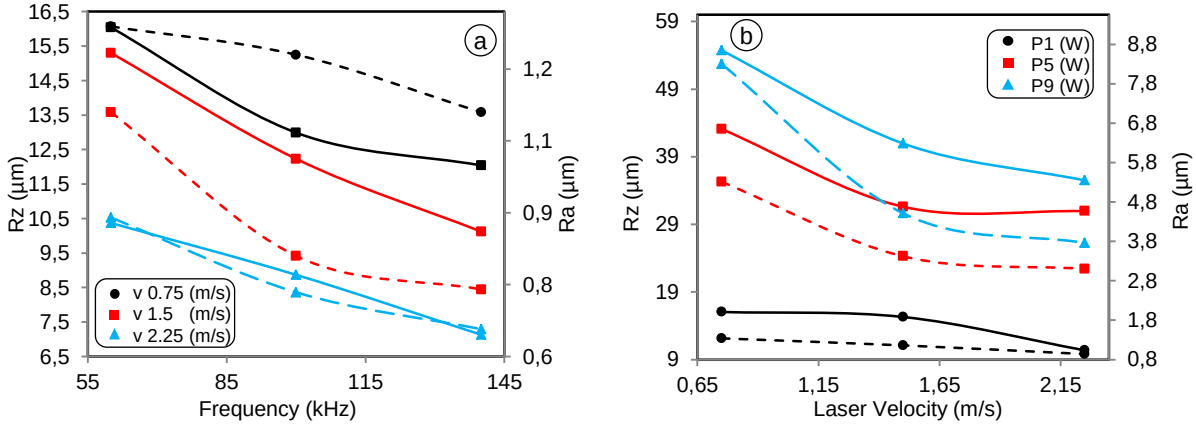

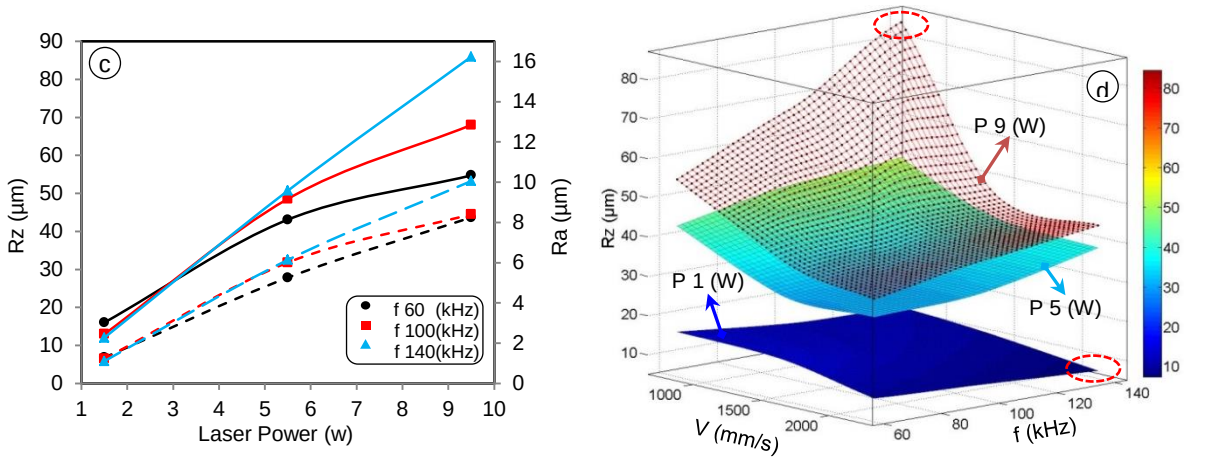

Figure 6.25: Rz and Ra against (a) Frequency at P 1 W. (b) Velocity at f 60 kHz. (c) Power at v 0.75 m/s. (d) 3D relation.

The impact of focal length on Ra and Rz roughness is presented in figure 6.26 (a) to (d). In general, the focal length reduces Rz and Ra, but this relationship refers to the other LDS parameters, namely the laser power, speed, and frequency. Figure 6.26 (a) shows the influence of the laser power on the relationship between surface roughness and focal length. The influence of focal length on Rz and Ra is reduced with raising the laser power, while it is increased with the laser velocity and frequency. This can be observed from figure 6.26 (b) and (c), which show the effect of the laser velocity and frequency on the mentioned relation. Another important behavior can be noted in figure 6.26 (c), which shows the impact of the laser frequency on this relationship at a laser power of 5 W and a velocity of 0.75 m/s. At a focal length of 5 mm, Rz and Ra decreases with frequency. This means, the impact of laser frequency is again reversed to be exactly same as with a low laser power. Under a laser power of 5 W and a focal length of 5 mm to maximize Rz and Ra, it is preferred to adjust the laser velocity and the frequency to minimum values whereas the maximum speed and frequency are preferred to minimize Rz and Ra. On the other hand, if it is desired to produce the same Rz and Ra even with changing the focal length, then it is preferred to use a low-to-moderate laser speed and a low frequency. This can be seen in figure 6.26 (d), which shows Rz versus the laser frequency, speed and focal length at a laser power of 5 W.

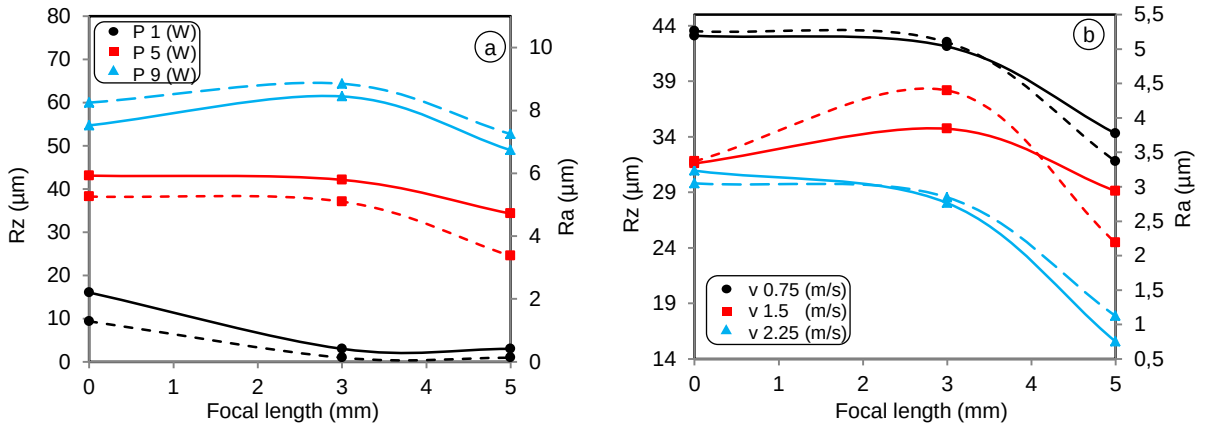

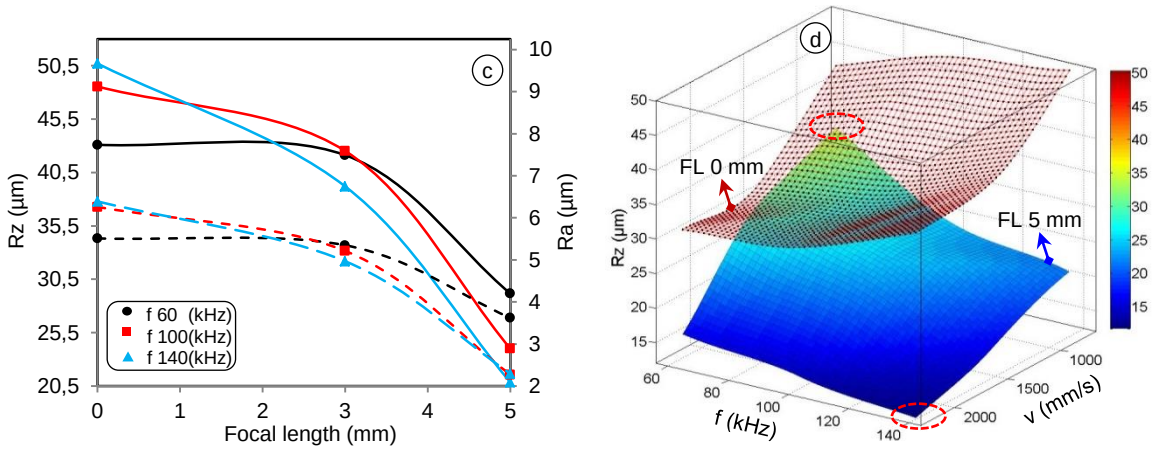

Figure 6.26: Rz and Ra against focal length at (a) v0.75 m/s and f 60 kHz. (b) P 5 W and f 60 kHz. (c) P 5 W and v 0.75 m/s. (d) 3D relation.

The influence of hatching on surface roughness is demonstrated in figure 6.27 (a) to (d), which also describes the effect of other LDS parameters, which include the laser power, speed, and the frequency, on this relationship. Roughly, Ra and Rz are reduced when the hatching changes from 0 % to 50 %. After that, when it is increased from 50 % to 75 %, Rz and mostly of Ra, increase again. The effect of hatching on surface roughness is more complex and interrelated in comparison to the previously investigated parameters, especially when the effect of working parameters on this relationship is considered. For example, at a laser power of 1 W, the effect of hatching on surface roughness is almost negligible in comparison with elevated laser power, as shown in figure 6.27 (a). The same influence can be noted in figure 6.27 (c), which demonstrates the impact of the laser frequency on the mentioned relation. It can also be seen from figure 6.27 (c) that the effect of hatching on the surface roughness is increased with raising the laser frequency, unlike the impact of laser velocity, where the reduction in the laser speed raises the impact of hatching on the surface roughness, see figure 6.27 (d). The 3D relationship between the laser speed, frequency, hatching and Rz at a laser power of 5 W is shown in figure 6.27 (d). It can be clearly seen that the effect of the laser frequency and velocity is increased at elevated hatching. Moreover, the influence of laser frequency on Rz is revised, particularly at a low velocity. As a conclusion, if it is desired to use a hatching percentage without any high change in the surface roughness, it is preferred to use a high laser frequency in conjunction with a low velocity, or a low frequency in conjunction with a high velocity at a laser power of 5 W, see figure 6.27 (d). In addition, there is an intersection line between the 0 % and 75 % hatching at which there is no change in Rz even when the hatching is changed.

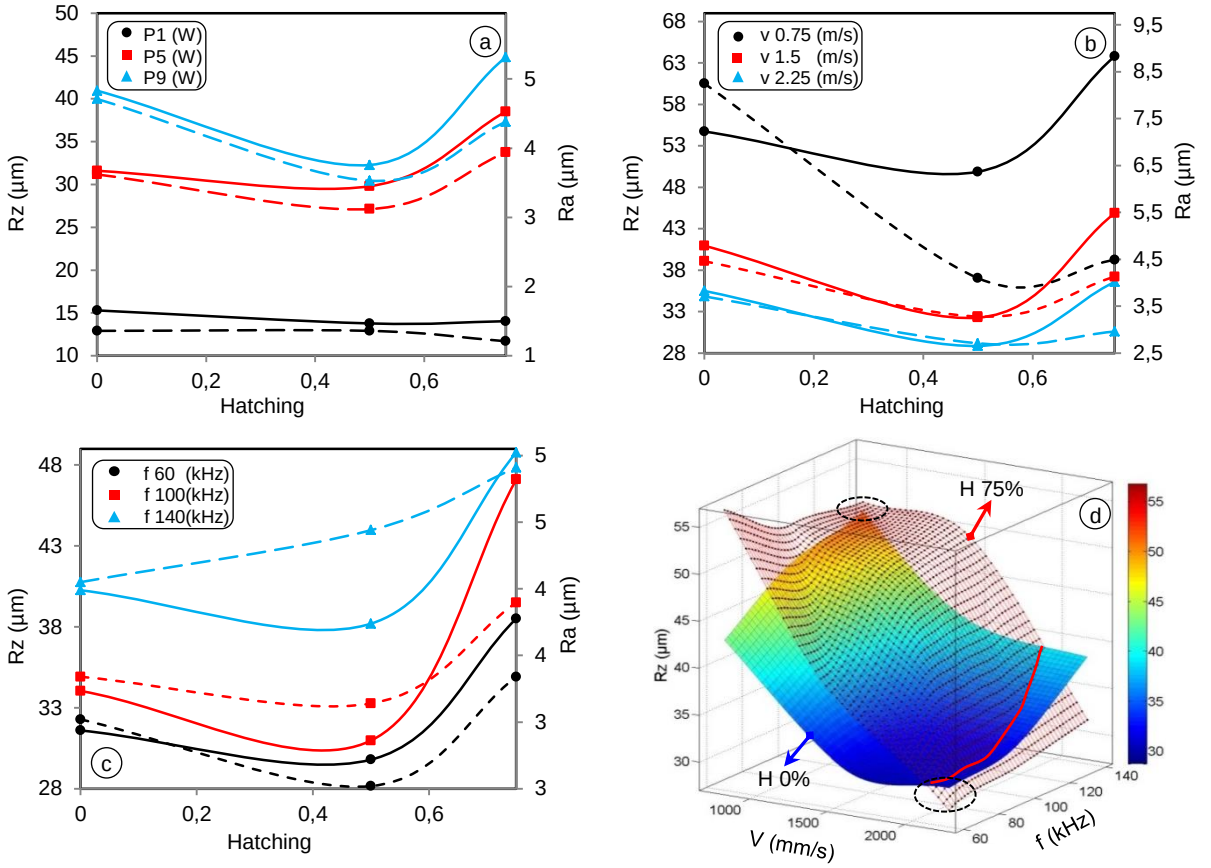

Figure 6.27: Rz and Ra against hatching at (a) v1.5 m/s and f 60 kHz. (b) P 9 W and f 60 kHz. (c) P 5 W and v 1.5 m/s. (d) 3D relation.

The incidence angle also has a complex impact on the surface roughness, as it were observed for hatching. Figure 6.28 (a) shows the effect of incidence angle on the surface roughness at a constant velocity of 2.25 m/s. Here it can be seen that at a low laser power of 1 W, Rz and Ra decrease with raising the incidence angle. At elevated laser power, Rz rises and falls again, but it is still higher than of the first point. The effects of the laser speed and frequency are shown in figures 6.28 (b) and (c). It is clear that both Rz and Ra are reduced with incidence angle at each value of the laser velocity and frequency. It is very important to mention that there is no high impact of the incidence angle on Rz and Ra when it is changed from 20 ° to 40 °. The 3D figure in 6.28 (d) shows a comparison between the incidence angle of 0 ° and 40 °, at different laser speeds, frequencies and a laser power of 9 W. It can be observed that the effect of laser frequency is changed from direct relationship at an incidence angle of 0 ° to an inverse relationship at incidence angle of 40 °, whereas the impact of the laser speed is reduced with incidence angle. Now, how to make a decision on the best or the optimum laser speed and frequency at a laser power of 9 W that should be used. It depends on the final requirement. If it is desired to keep the surface roughness at the same level then the optimum can be defined by the parameters at the intersection between the surface of 0 ° and 40 ° angles. Or, it is

preferred to use a low laser frequency. However, if the target lowers the surface roughness, in this case, it is preferred to raise the laser frequency, (see figure 6.28 (d)).

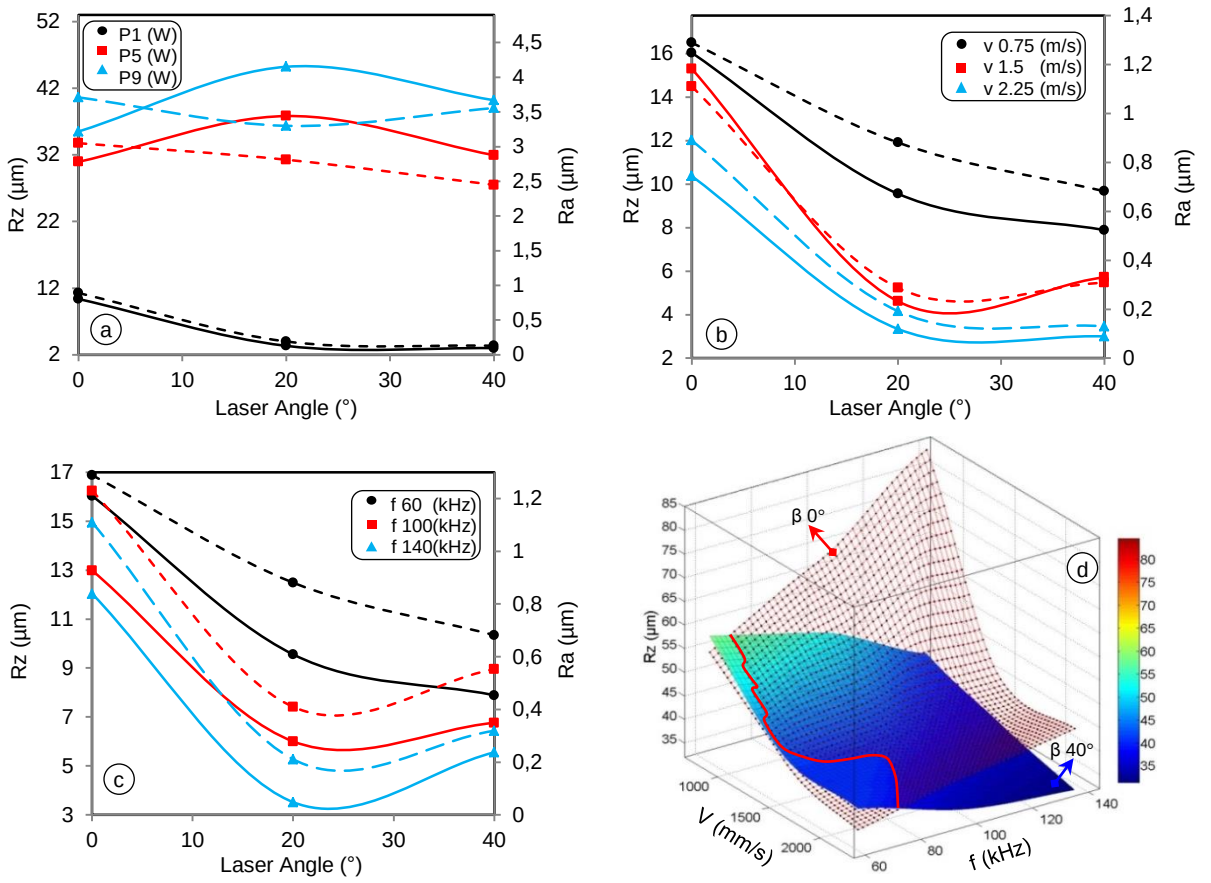

Figure 6.28: Rz and Ra against incidence angle at (a) v 2.25 m/s and f 60 kHz. (b) P 1 W and f 60 kHz. (c) P 1 W and v 0.75 m/s. (d) 3D relation.

Exploration and analysis of the interaction between the process parameters are helpful for obtaining further information about these parameters and their impact on the surface roughness. Consequently, a regulation can be proposed for the parameters setup. This helps to achieve the best combination between parameter setup and the desired process responses. Figure 6.29 (a) illustrates the effect of the hatching on the relationship between Rz, Ra and the focal length, at a laser power of 1 W, a laser speed of 0.75 m/s and a frequency of 60 kHz. From this figure, it can be seen that as the focal length increases from 0 mm to 3 mm Ra and Rz reduce from 1.289 µm and 16.04 µm to the minimum value or the original surface roughness of the substrate surface. They are still at these values even when the focal length increases again to 5 mm. This means under these conditions the laser energy is not sufficient to structure the surface or to change it. In this case, a rougher surface can be generated or structured by increasing the laser power or hatching. As discussed in figure 6.27 (a), Ra and Rz increases extremely when the laser power is changed to

5 W or 9 W. At 5 W Ra reaches an average of 4.577 µm and Rz an average of 39.84 µm. It can be concluded that the laser power has a strong impact on Ra and Rz in comparison with hatching. A further considerable interaction is shown in figure 6.29 (b). Here, one can see the effect of the incidence angle on the relationship between the surface roughness and hatching at different incidence angles, a laser power of 1 W, a frequency of 60 kHz, and a velocity of 0.75 m/s. The incidence angle reduces the effect of the hatching on both Ra and Rz, especially when the hatching is increased from 0 % to 50 %. For higher hatching values in the range between 50 % and 75 %, the hatching is more sensible to reduce the effect of the incidence angle. This means for the 3D-LDS applications where the product is under the effect of focal length and incidence angle, the rising in the hatching helps to reduce the effect of focal length and incidence angle in the case that the other parameters are constant.

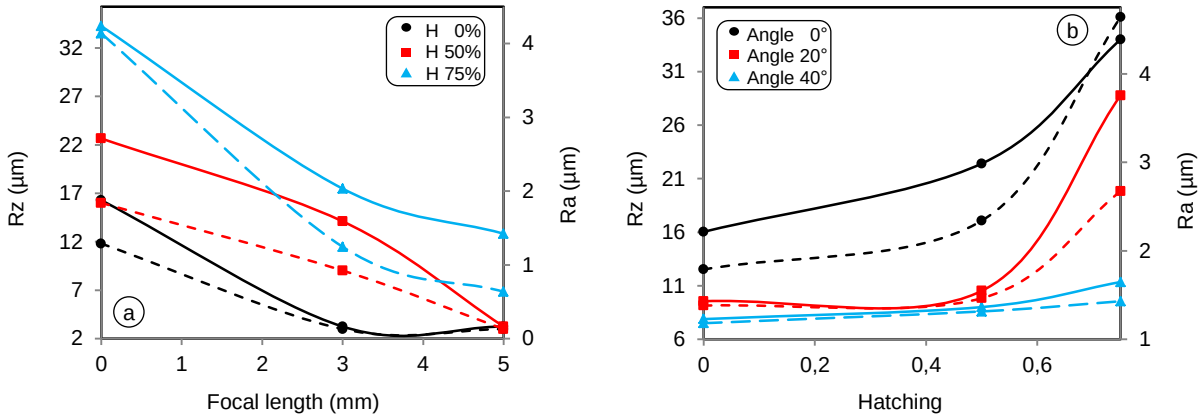

Figure 6.29: The surface roughness against (a) FL at different hatching, P 1 W, V 0.75 m/s and f 60kHz (b) Hatching at different incidence angle, P 1 W, V 0.75 m/s and f 60kHz

6.4.2. Ceramic Based Material

The surface roughness of the ceramic based materials has also been explored in this work. Figure 6.30(a) to (c) indicates the correlation between the surface roughness of the structured area and the investigated parameters including laser power, velocity, frequency, sintering temperature, and additive percentage. As a comparison between the ceramic based and polymeric materials, the impact of both the laser power and velocity on the roughness is the same. A rough surface is produced by elevating the laser power or minimizing the laser velocity. However, with a low laser power of 4 W, the roughness decreases with the laser frequency. By setting the laser power to value higher than 4 W, the impact of laser frequency on the roughness will depend on the laser velocity. The roughness is decreased with laser frequency when the laser velocity is set at 0.75 m/s. And it is increased with laser frequency at elevated velocities of more than 1.5 m/s, as shown in figure 6.30 (a). The influence of the manufacturing parameters, namely the sintering temperature and the additive percentage on the relationship between the parameter settings and surface

roughness are shown in figures 6.30 (b) and (c). It can be seen from these two figures that a rough surface can be produced by increasing the additive percentage from 5 % to 15 % or by elevating the sintering temperature from 1200 °C to 1600 °C. Moreover, the minimum influence of the sintering temperature on the roughness is at parameter settings including a laser velocity of 0.75 m/s and a frequency of 50 kHz, whereas the maximum influence is located at a high laser velocity of 2.25 m/s and a high frequency of 100 kHz.

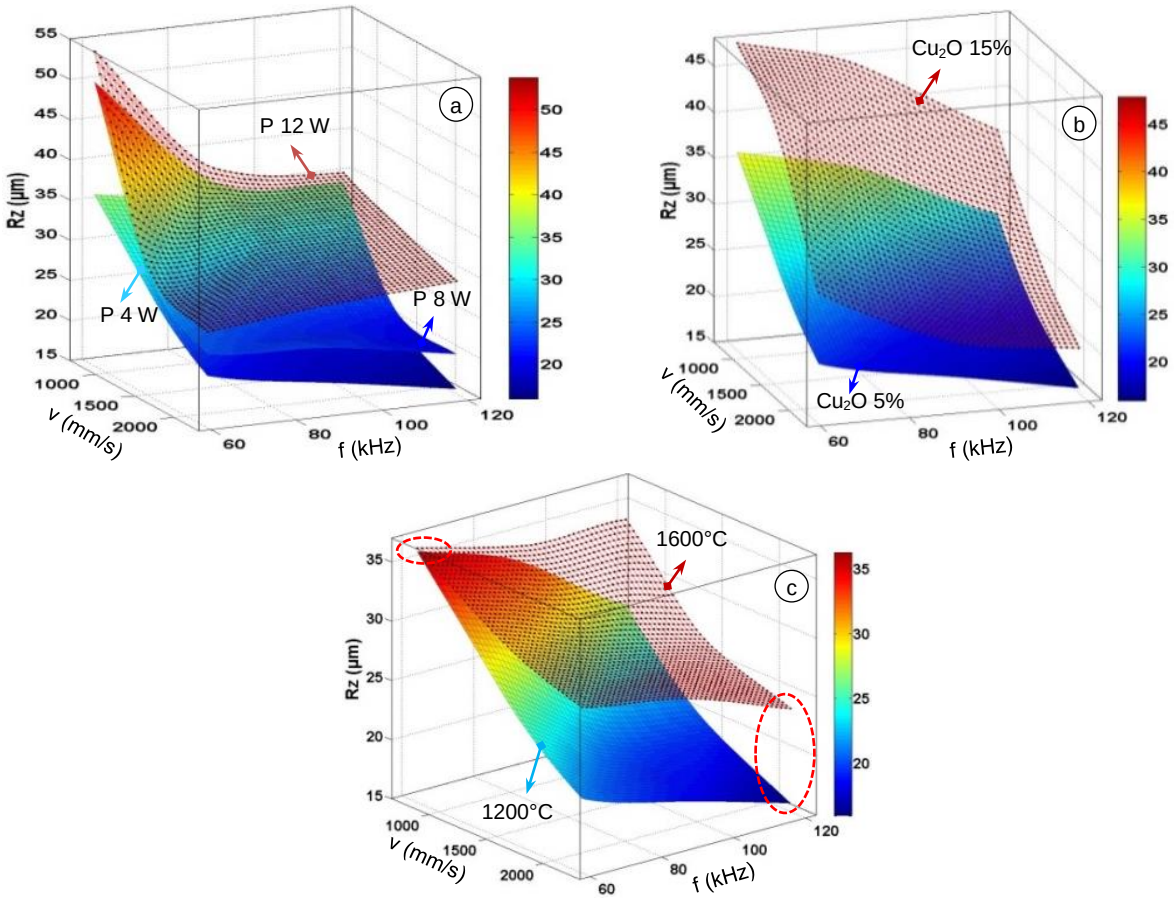

Figure 6.30: Rz against (a) power, velocity, and frequency. (b) Additive %. (c) Sintering temperature.

6.5. LDS Quality and Accuracy

The LDS quality and the accuracy are considerably important requirements, but *How can they be defined*? *What is their behavior under different parameter setting*? Moreover *How to keep them under control*? These questions and further topics on this subject are answered in this section of the thesis. In principle, the LDS quality for both 2D and 3D products should be high because the final MID quality depends on the LDS quality. Whereas, for micro-MID products, for which there is no high flexibility in the available dimensions, the accuracy is extremely desired in conjunction with high LDS quality. In the next section, the quality and the accuracy will be defined,

investigated by experimental work, and then analyzed. This helps to explain and describe their relationship with the adopted process parameters.

6.5.1. LDS Quality

The LDS quality can be defined as a combination of many characters. It comprises the percentage of the structured area, type of structuring, ablation type and last but not least the dimensions and shape of groove edge [17][42]. The percentage of the structured area can be calculated by measuring the actual structured area and then divided by the total designed area. This step should be applied to all parameter settings. More than 729 measurements are performed to investigate the impact of the process parameters on the percentage of structuring as well as the other factors that can be used to describe the LDS quality.

Structuring and Ablation Types

A. PEEK Polymer Material

In fact, the topography of the structured surface is not influenced by the impact of the surface roughness only. It is affected by other important factors such as ablation type, which is related to the ablation zone discussed in the previous section and the type or shape of the structuring. This classification could be used as one of the most significant icons to define the final LDS quality as a function of LDS parameters.
The ablation type can be classified into Puffing Ablation (PA) in which there is only (PZ) as defined in previous chapters, (see figure 6. 23 (d)). The second ablation kind is the Removing Ablation (RA). In this type there is only one (RZ) zone within the structured area, as shown in figure 6.24. The third is a Mixed Ablation (MA) between the two above-mentioned (PA and RA), as shown in figure 6.23 (e). Figure 6.31 shows the 3D laser microscope scan of the structured surface (circle area layout) with different process setups. Where figure 6.31 (a) to (c) demonstrates the effect of the laser power at a constant velocity and frequency on the topography of the structured area. Elevating the laser power produces a rough surface. This can be easily observed in these figures. It can be seen that the ablation type is changing from puffing PA, which occurs at a low laser power of 1 W to RA when the laser power is increased to 9 W while the ablation MA is produced at a laser power of 5 W. On the other hand, the structuring types can also be classified into three kinds, the first is the Lines Structuring (LS), as can be seen clearly in figure 6.31 (a), (b) and (d) which shows the formulated grooves or the structured area as parallel lines with uniform peaks and/or valleys. The second type creates random peaks and valleys so that it can be defined as Random Structuring (RS) as shown in figures 6.31 (c). The third is mixed between LS and RS, as shown in figure 6.31 (e) to (g). Such variations have a significant effect on the final LDS quality. The impact of the laser speed on surface roughness, structuring and ablation types at a constant laser power of 5 W and a frequency of 140 kHz are illustrated in figure 6.31 (d) and (e). The increase in the laser velocity gives a smoother surface, a mixed ablation type (MA) and

structuring type of (MS). There is no effect for the laser frequency on the ablation and structuring types when it is changed from 60 kHz to 140 kHz at a fixed laser power of 5 W and a velocity of 1.5 m/s, as shown in figure 6.31 (f) and (g). Under this parameters setup, the influence of laser frequency is limited on the surface roughness, which increases with the laser frequency.

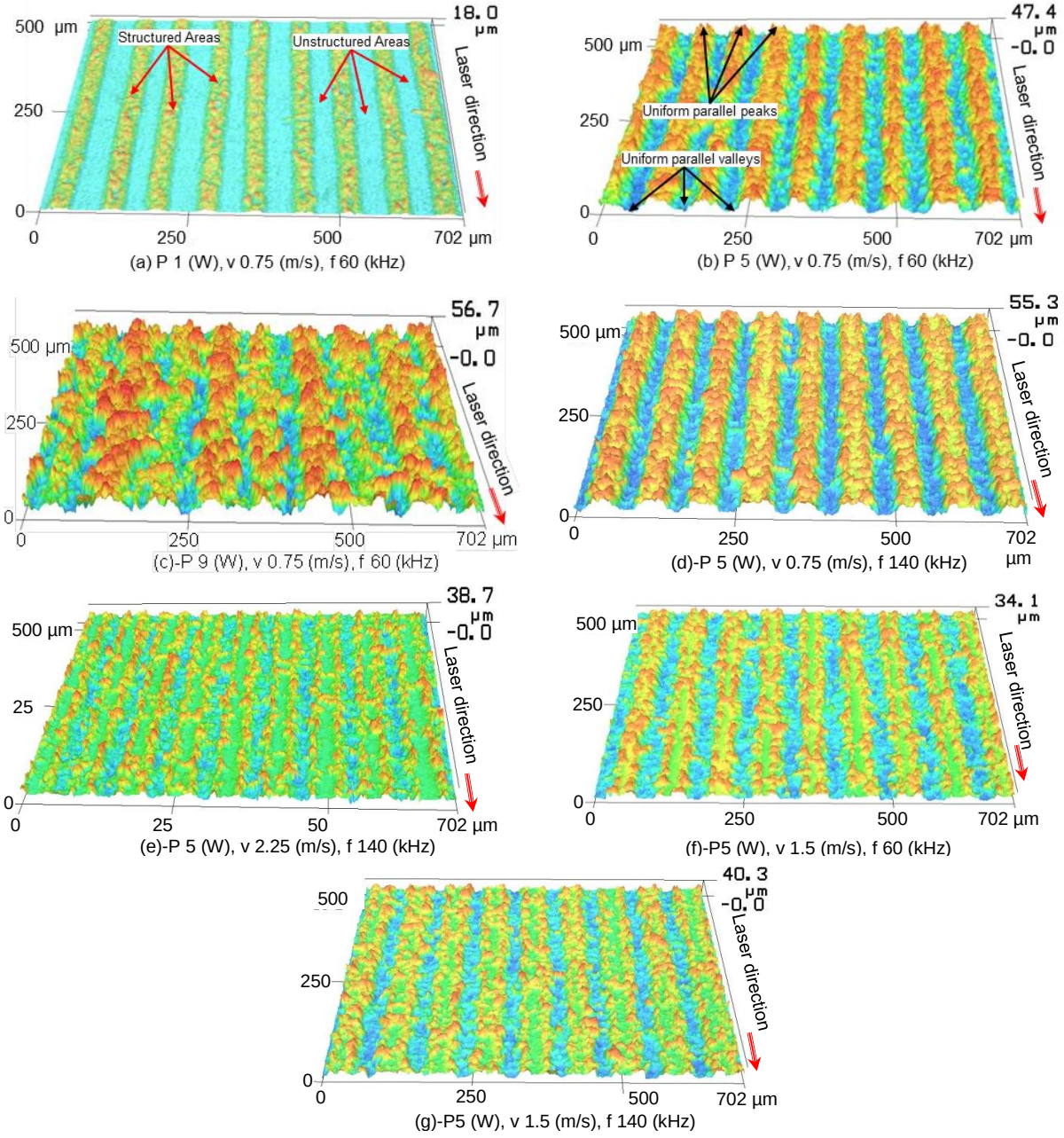

Figure 6.31: The surface topography at different process parameters.

Figure 6.32 (a) and (b) shows the 3D surface texture and the influence of the focal length on the topography and surface roughness at a constant laser power of 5 W, a velocity of 0.75 m/s and a frequency of 60 kHz. In general, as the focal length changes from 3 mm to 5 mm, the surface becomes smoother, whereas the structuring-ablation types will have almost the same form which is LS-MA.

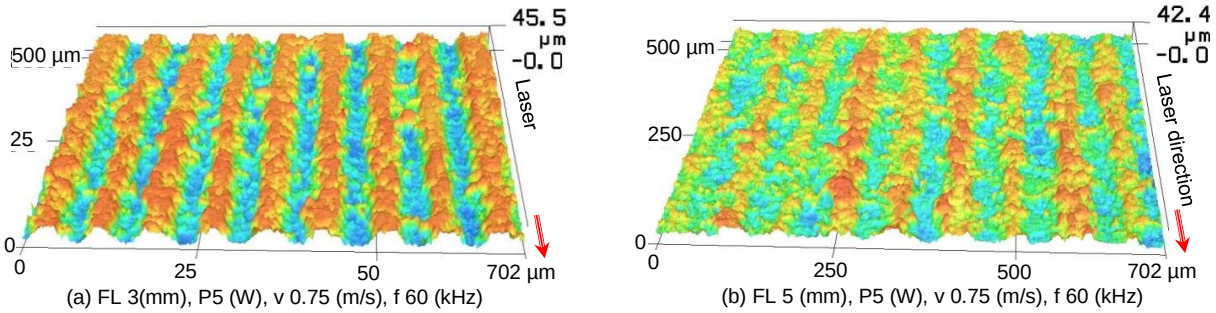

Figure 6.32: The impact of focal length on surface topography.

It is mentioned above that the hatching has a complex effect on the surface roughness, the same complex effect can be determined on the surface topography or structuring-ablation type that can be seen clearly in figure 6.33 (a) to (c). It shows the 3D surface at parameter settings including a laser power of 9 W, a velocity of 1.5 m/s and a frequency of 100 kHz, whereas the hatchings are 0 %, 50 %, and 75 % respectively. Here, as the hatching increases from 0 % to 50 % and then to 75 % the ablation is changed from MA to completely RA and the structuring type is varied from LS at hatching of 0 % to completely RS at 50 % and 75 %, whereas the surface roughness is reduced and then increased again.

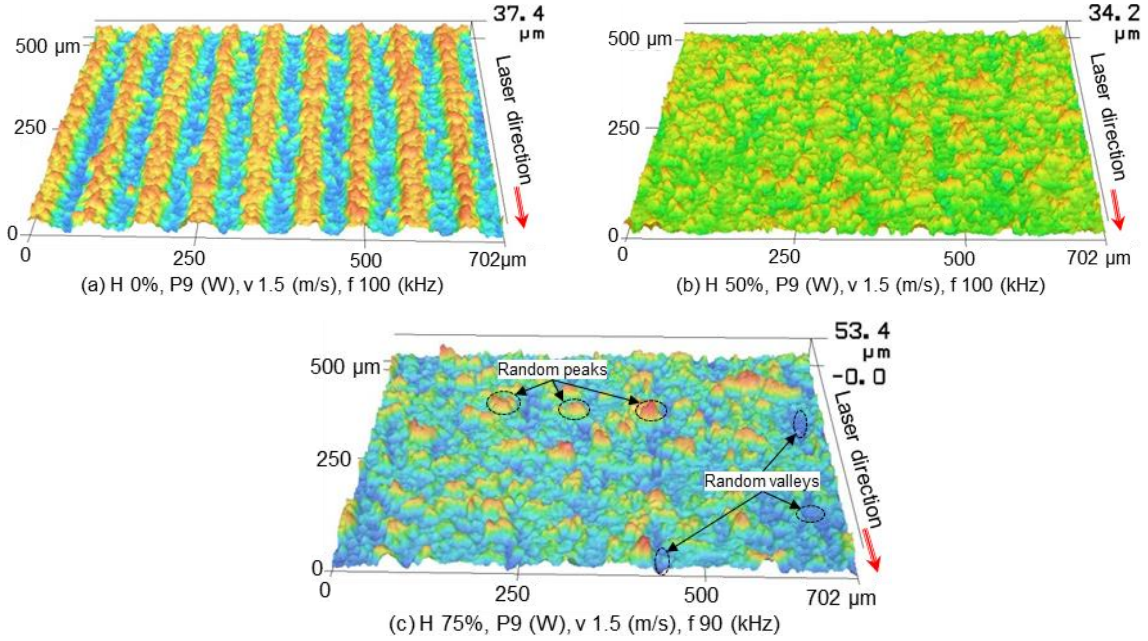

Figure 6.33: Surface topography at different hatching.

Figure 6.34 shows the real surface topography and the impact of the incidence angle on this surface with the corresponding parameter setts that are shown in this figure. As the incidence angle increases from 20 ° to 40 °, the structured surface becomes smoother and the structuring-ablation types remain the same, which is a mixed type for both MS-MA.

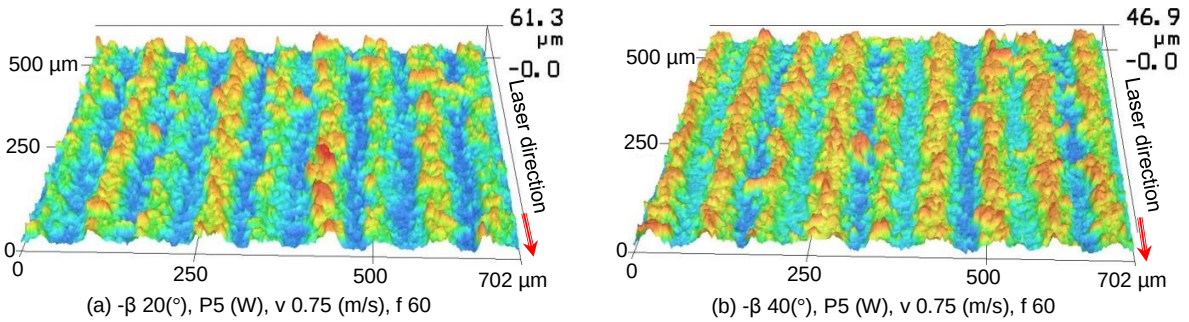

Figure 6.34: The surface topography at different incidence angle.

B. Ceramic Based Material

The thermal-physical properties of the new ceramic based material are completely different from the polymers. This also produces a variation in the structuring-ablation type, as shown in figure 6.35. It shows the possible produced structuring-ablation type. There are only two possible types namely, MS-RA or RS-RA as shown in figures 6.35 (a) and (b) respectively. This means there is only one possible ablation type which is removing (RA). Whereas for the structuring we have only two kinds namely, the random structuring (RS) and mixed structuring (MS). As mentioned earlier, this is due to the material properties and the elevated value of the used hatching of 60 %. However, this does not mean there is no possibility to produce the third structuring types of LS. It can be created by reducing the hatching percentage or adjusting the other parameters.

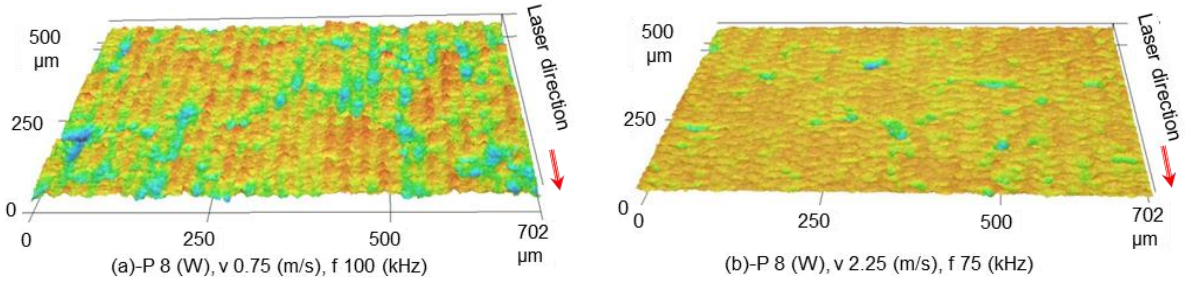

Figure 6.35: The surface topography of the ceramic material at different process parameters.

Structuring Percentage

During LDS process, a lot of defects may occur. The used parameter settings are responsible for the most frequent defects, which are the non-completed or non-full structuring. In this work, this type of defect is under investigation and analysis. This can be achieved by calculating the percentage of the non-structured area or in other words the structuring percentage.

The impact of the LDS parameters on the structuring percentage is analyzed in figure 6.36 (a) and (b), where figure 6.36 (a) describes the influence of the three parameters namely laser power, frequency, and velocity on the structuring

percentage. Here it can be seen that the structuring decreases with laser velocity and frequency or when the laser power is reduced. It can also be noted that, even at extremely high laser power, a 100 % structuring can be only achieved at low velocity. Under these parameter settings, the laser frequencies do not have a high effect on the structuring percentage. At low laser power of 1 W, a velocity of 0.75 m/s, and 0 % hatching, the maximum structuring percentage which can be produced is about 50 %. This value can be raised by elevating laser power or hatching. The structuring percentage reaches to 100 % when the hatching is set at 75 %, this can be seen in figure 6.36 (b). It can also be seen from this figure that the effect of laser speed on the structuring is stronger than that of the frequency. Moreover, at a high laser speed of 2.25 m/s, the effect of hatching is lower than the effect of the velocity in the range between 0.75 m/s to 1.5 m/s. In the experimental measurements, it is found that at a laser power of more than 5 W and hatching more than 50 % the produced structured area is completely structured (100 %) and activated regardless of other LDS parameters.

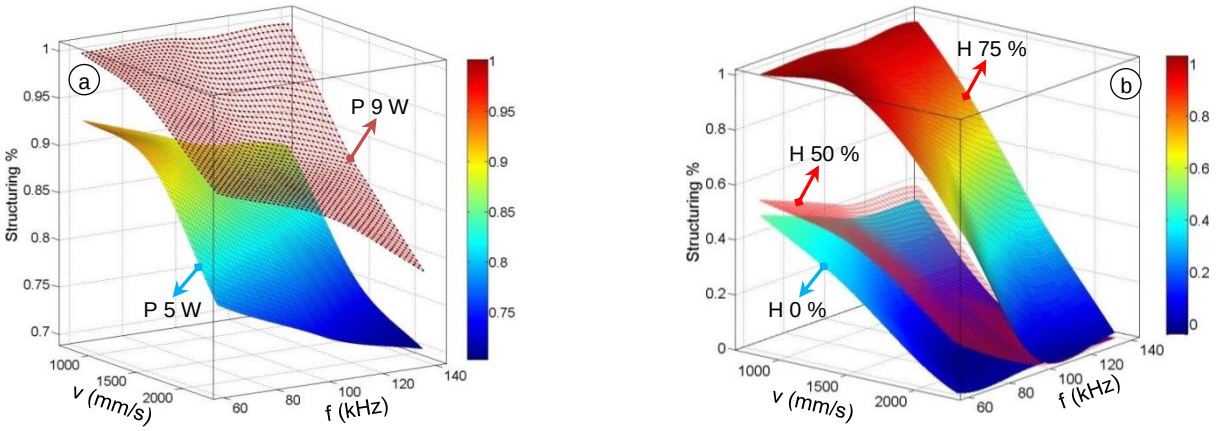

Figure 6.36: The structure percentage against laser velocity frequency at (a) Different power. (b) Different hatching and P 1 W.

The effect of focal length on the structuring is illustrated in figure 6.37 (a). It presents the relationship between the velocity, frequency, focal length, and the structuring with a constant laser power of 5 W. It can be seen that under these parameter setts the structuring percentage increases with rising focal length. When the focal length is installed at 5 mm, the structuring reaches 100 % at different velocities and frequencies. Figure 6.37 (b) demonstrates the influence of incidence angle. It shows that the incidence angle has an interconnected influence on the structuring. In general, this effect is related to other parameter settings. At a laser power of 5 W, a laser speed less than 1.5 m/s and different frequencies the structuring is raised when the incidence angle is changing to 20 °. At elevated laser speed of 2.25 m/s, the structuring reduces as the incidence angle increases to 20 °. This means there are two different behaviors for the relationship between the structuring and incidence angle based on laser velocity.

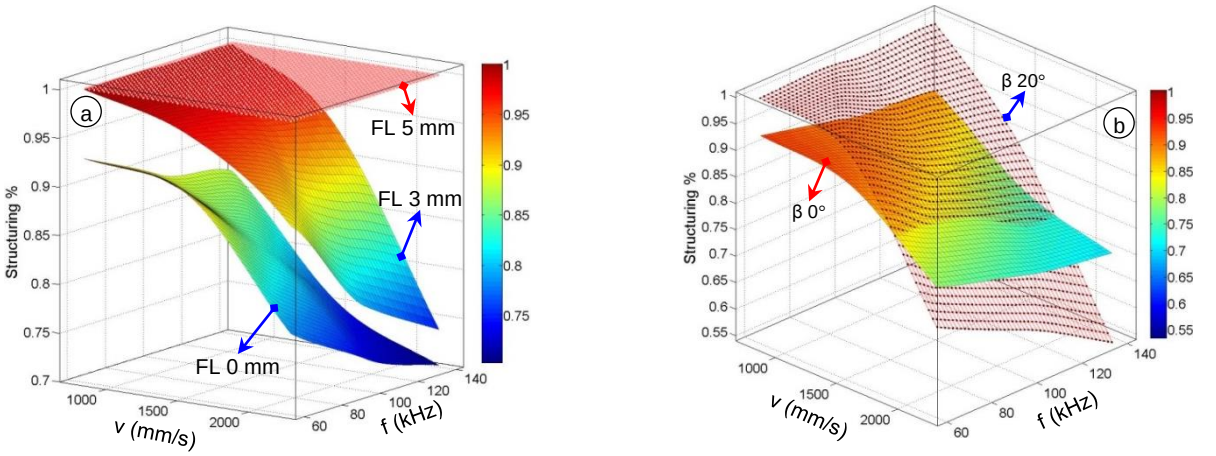

Figure 6.37: The structure against laser velocity and frequency at (a) Different focal length and P 5 W. (b) Different incidence angle and P 5 W.

A further investigation of the influence of the interaction between hatching, focal length, and incidence angle is shown in figure 6.38 (a) and (b). The impact of hatching on the relationship between the structuring and focal length is clarified in figure 6.38 (a), under the corresponding LDS parameters that are listed in this figure it can be seen that when the hatching value is changed from 0 % to 50 % or the focal length increases from 0 mm to 3 mm, the structuring is not highly affected. At a focal length of 5 mm and hatching of 0 %, the structuring is reduced to 0 %. However, it is raised to about 85 % when the hatching is set to 50 %. It can also be observed from this figure that the hatching of 75 % produces a complete structuring of 100 % at different focal lengths. The impact of incidence angle on the relationship between hatching and structuring is exemplified in figure 6.38 (b). From this figure, it can be concluded that when the hatching is increased from 0 % to 50 % the impact of the incidence angle on the structuring will be inverted. While at hatching of 75 % there is no effect for the incidence angle on the structuring. It is always reached to 100 % at this hatching value. This means, under this parameter setting, the effect of both focal length and incidence angle on the structuring can be reduced or removed by increasing the hatching.

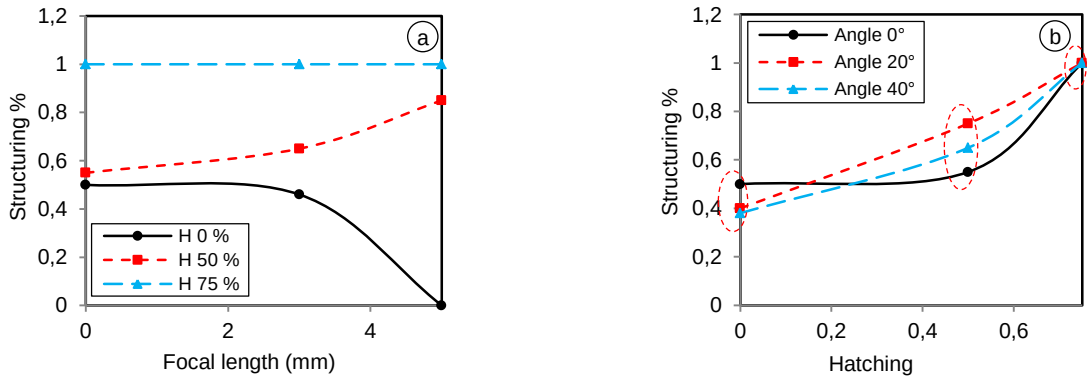

Figure 6.38: The structuring at P 1 W, v 0.75 m/s and f 60 kHz, against (a) Focal length at different hatching. (b) Hatching at different incidence angle.

6.5.2. LDS Accuracy

The LDS accuracy is quite required for the micro MIDs. It depends completely on the process setting. Therefore, it is important to experimentally investigate, evaluate and understand the LDS accuracy as well as the impact of the parameter settings on it. This helps to control or to propose a model for this accuracy. Basically, the accuracy can be calculated using equations 6.1 below

$$\text{Accuracy} = 1 - \left|\frac{W_d - W_e}{W_d}\right| (\%) \qquad 6.1$$

Where W_d is the designed conductor width (Track width) in µm, see figure 5.4, W_e is the experimentally measured conductor width in µm.

Each certain parameter settings gives specific groove dimensions, and the conductor width or the interaction zone can be regarded as one of the most important dimensions for LDS accuracy. According to the above equation, the accuracy is based on the conductor width. In the next section, the accuracy and its relation with LDS parameter settings will be explored deeply. Figure 6.39 (a) to (e) displays the correlation between the process parameters and the corresponding accuracy, where figure 6.39 (a) shows the variation of this accuracy with the laser power, velocity and frequency. From this figure, it can be seen that at a laser power of 1 W the accuracy is reduced with laser frequency and speed. In addition, the impact of laser velocity and frequency on this accuracy depends on each other. At high frequency the effect of velocity is much stronger than at low frequency. The opposite is also true; at an elevated velocity, the effect of frequency is much more than at low velocity. By raising the laser power to 5 W, the accuracy is increased. The effect of frequency at low velocities will be changed from decreasing at a laser power of 1 W to increasing at 5 W. At extremely high laser power of 9 W, almost the produced width is more than the designed width. Therefore, the accuracy at this laser power can be divided into two types as compared with the pervious laser power of 5 W. *The first type* is almost produced at laser velocities in the range of between 0.75 m/s to 1.5 m/s. It shows less accuracy than the 5 W results. In fact, the conductor width under these laser parameters is bigger than the designed width. This leads to an increase of the errors and reduction of accuracy. *The second type* is formed at a laser velocity of more than 1.5 m/s. The recorded errors for this type are lower than in all previous cases. It can also be seen that the accuracy is increased with rising of the laser velocity at a laser power of 9 W. This is quite opposite to the previous cases.

The influence of hatching on the accuracy is illustrated in figure 6.39 (b), which shows the accuracy at hatching of 0 % and 75 %. In general, the hatching enhances the accuracy little, except for the parameter settings, which includes a laser velocity of 2.25 m/s and a frequency of 100 kHz. Under these parameters, hatching has a maximum effect on the LDS accuracy. It is concluded that at a low laser power the focal length and the incidence angle have reduced conductor width, whereas, at a high laser power this width is increased with focal length and incidence angle. This helps to explain the attitude in figures 6.39 (c) and (d). It shows the influence of focal

length on the accuracy at different velocities, frequencies, and laser power of 5 W and 9 W respectively. It is obvious that at a laser power of 5 W and a laser velocity of 2.25 m/s, the setup of the focal length from 0 mm to 3 mm leads to an increase in the accuracy. This is the exact opposite of the situation when the laser velocity of 0.75 m/s is used. At a laser velocity of 1.5 m/s, the accuracy is almost the same for a focal length of 0 mm and 3 mm, see figure 6.39 (c). This behavior cannot be recorded with an elevated laser power of 9 W, as shown in figure 6.39 (d). Here, it can be seen that the accuracy is reduced with focal length. Quite similar behavior can be noted for the impact of incidence angle on the accuracy, which is demonstrated in figure 6.39 (e). According to this figure, the accuracy is reduced with incidence angle, but the influence of 20 ° incidence angle is much more than for 40 ° angle. This is due to the fact that the impact of the 40 ° on the conductor width is less than for the 20 °.

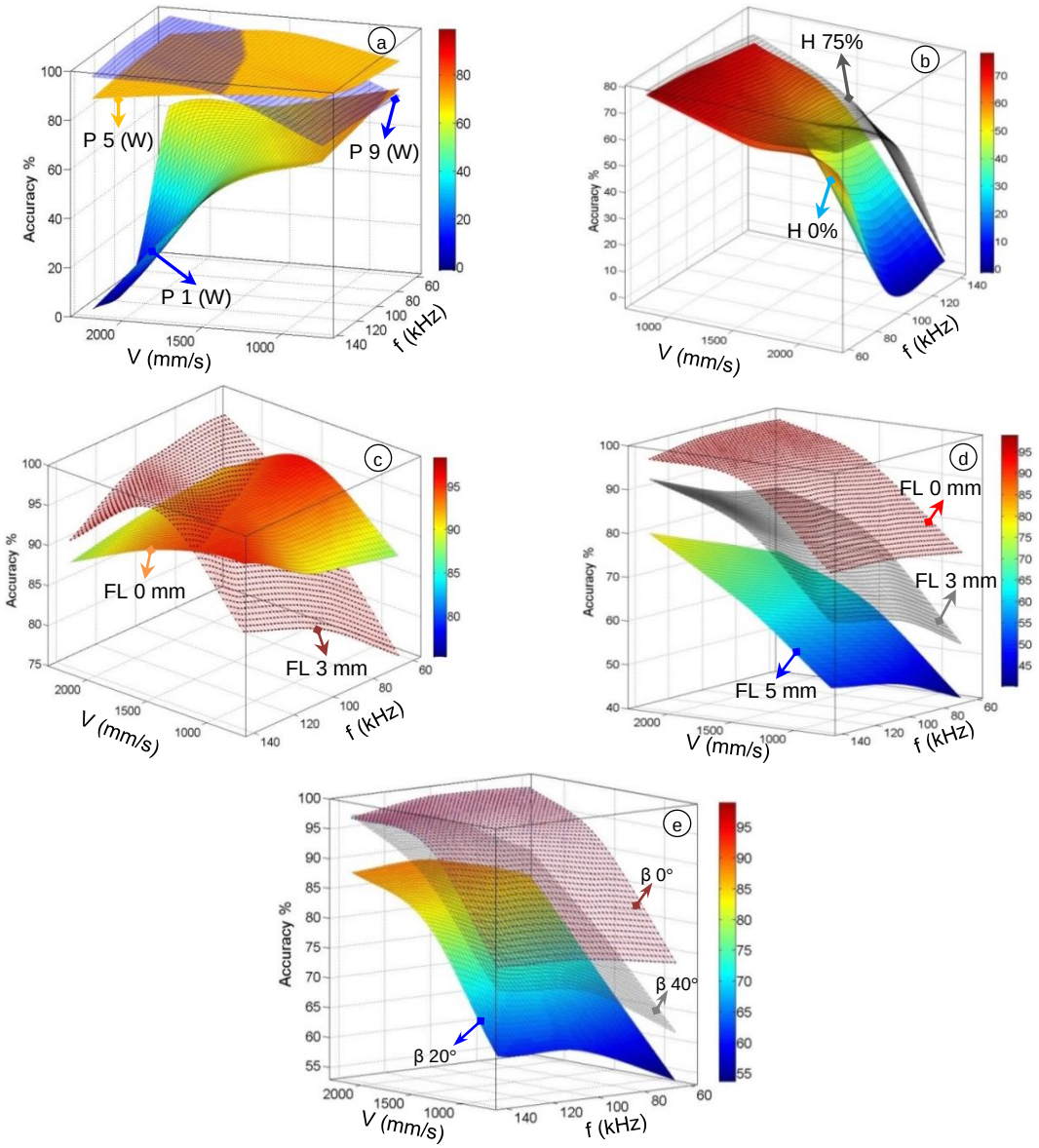

Figure 6.39: Accuracy against the laser velocity and frequency at different (a) Power. (b) Hatching and P 1W. (c) Focal length and P 5 W. (d) Focal length and P 9 W. (e) Incidence angle and P 9 W.

7. Experimental Results and Discussion of Metallization

The metallization step is represented as the final MID-LDS step. It is based on the responses of the LDS process or in other words, on the characteristics of the structured area, which relates to the parameter setting. The metallization quality can be defined as a set of requirements including optical quality of the metallization, the thickness of the metallization layers (Cu-Ni-Au), the surface roughness of the metallized surface and adhesion between the substrate surface and the metallization structure. In the following sections, these requirements will be explored, discussed and clarified with more details, as follows:-

7.1 Optical Inspection of the Metallization Quality

7.1.1. PEEK Polymer Material

A series of experimental measurements are carried out to investigate the quality of the metallization structure using the 3D laser scan microscope. Figure 7.1 illustrates the optical microscope image of the metallized surface for different LDS quality or responses and their corresponding parameter setup. The effect of laser powers on the metallization structure is shown in the pictures 1 to 3. It is clear to see that for the corresponding LDS parameters of picture 1, the produced responses include a structuring of 50 %, and structuring-ablation type of LS-PA. The metallization will only cover the structured or the activated area. This produces a metallization structure with parallel lines, see picture 1. With increase of the laser power to 5 W and then to 9 W, the structuring-ablation type changes to LS-MA and RS-RA, while the structuring rises to 93 % and 100 % respectively. This results in a continuous metallization structure, as shown in picture 2 and 3. On the other hand, the attributes of these two metallization structures seem different, as will be seen in the next sections, which explore the surface roughness, the thickness, and the adhesion of the metallization structure. It was found that the characteristics of the metallization structure are based on the characteristics of the structured area after the LDS step. The effect of the laser velocity is demonstrated in pictures from 4 to 6. It is also clear to see the differences between these metallization results. Under the corresponding parameters of picture 4, the structuring is 89 % and the structuring-ablation type is LS-MA. With increasing laser velocity, the structuring is reduced to 83 % and 73 %, whereas the structuring-ablation type changes to MS-MA for both velocities of 1.5 and 2.25 m/s respectively. These variations in the structure area produced are responsible for creating different metallization results, see picture 4, 5, and 6. In addition, the structuring of 73 % is sufficient to produce a complete metallization structure, see picture 6. Almost the same impact can be observed for the laser frequency on metallization structure, which is demonstrated in pictures 5, 7 and 8. At a low frequency of 60 kHz (picture 7), the structuring is about 91 %. As the frequency rises to 100 kHz (picture 5) and then to 140 kHz (picture 8) the structuring is reduced to 83 % and 75 % respectively, but the structuring-ablation type remains the same,

which is MS-MA. This means that the variations in the metallization structure are only due to the change in the structuring percentage. An increase of hatching percentage value leads to an increase in the structuring percentage as well as large variations in structuring-ablation type. This will also help to change the characteristics of the metallization structure. Pictures 2, 9 and 10 show the effect of hatching. Under the parameter set up for picture 2, the structuring is about 93 %, and structuring-ablation type has an LS-MA form. As the hatching elevates to 50 % or 75 % (pictures 9 and 10), the structuring increases to 100 % and the structuring-ablation convert to RS-RA. In previous sections, the impact of the important parameters including focal length and incidence angle on the structured area is explored. The distortion in the laser spot gives a further change in the structure area which leads to different metallization structure. Pictures 2, 11, and 12 show the impact of focal length, while the pictures 13 and 14 show the influence of incidence angle. The focal length of 3 mm and 5 mm of picture 11 and 12, results in 100 % structuring and the same LS-MA structuring-ablation form in comparison with the results in picture 2. But the incidence angle of 20 ° and 40 ° of pictures 13 and 14 gives 100 % structuring and changes the structuring-ablation type to MS-MA in comparison with the case of picture 2.

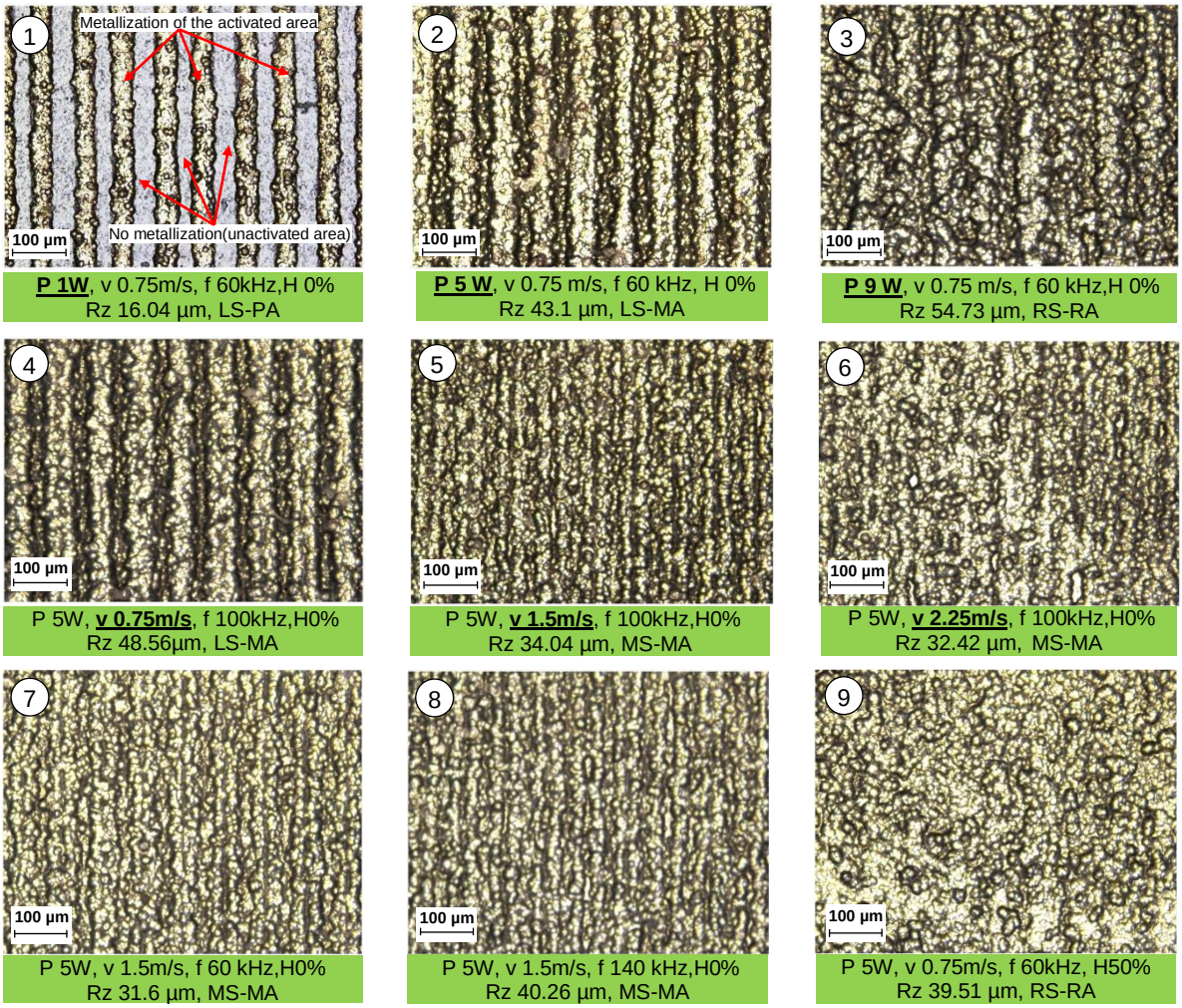

P 1W, v 0.75m/s, f 60kHz,H 0%
Rz 16.04 µm, LS-PA

P 5 W, v 0.75 m/s, f 60 kHz, H 0%
Rz 43.1 µm, LS-MA

P 9 W, v 0.75 m/s, f 60 kHz,H 0%
Rz 54.73 µm, RS-RA

P 5W, **v 0.75m/s**, f 100kHz,H0%
Rz 48.56µm, LS-MA

P 5W, **v 1.5m/s**, f 100kHz,H0%
Rz 34.04 µm, MS-MA

P 5W, **v 2.25m/s**, f 100kHz,H0%
Rz 32.42 µm, MS-MA

P 5W, v 1.5m/s, f 60 kHz,H0%
Rz 31.6 µm, MS-MA

P 5W, v 1.5m/s, f 140 kHz,H0%
Rz 40.26 µm, MS-MA

P 5W, v 0.75m/s, f 60kHz, H50%
Rz 39.51 µm, RS-RA

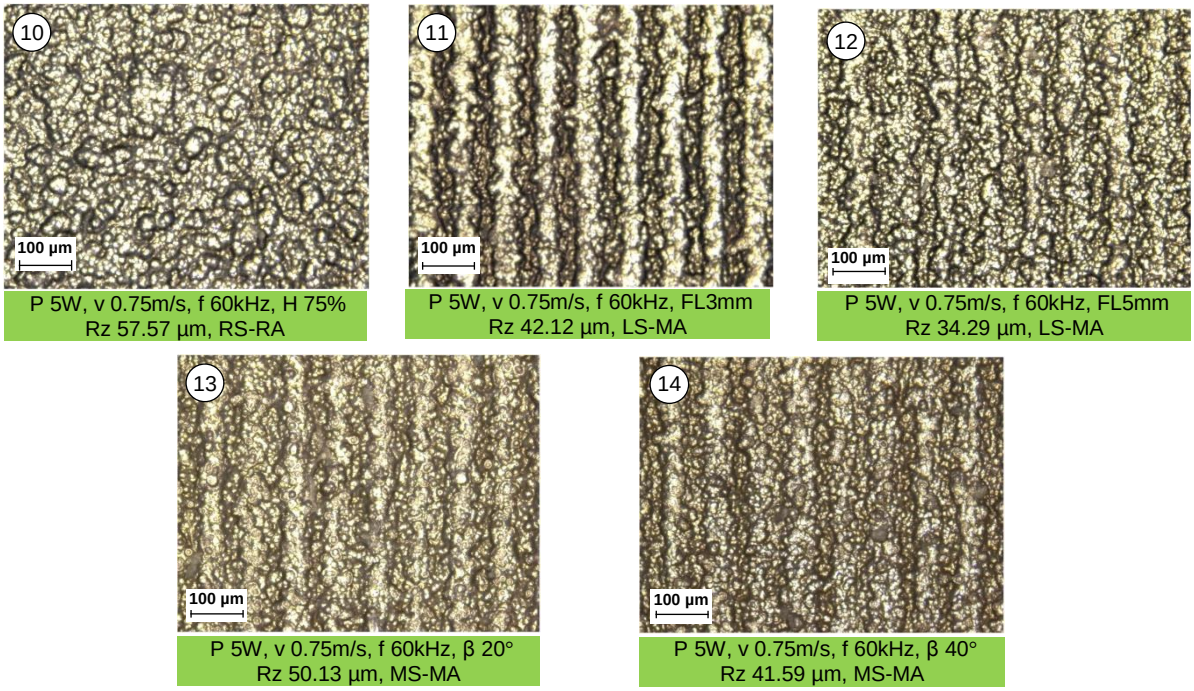

Figure 7.1: The quality of the metallization structure at different process parameters.

During the inspections of metallization structure quality, it was found that the metallization defects were always recorded under the following parameter setting:-

- Laser power of 1 W, 0% hatching and velocity up to 1.5 m/s, which produces a structuring-ablation type of LS-PA and a rough metallization surface.
- Laser power of 9 W, hatching of 75%, a velocity of 0.75 m/s and laser frequency of 140 kHz, which produces a structuring-ablation type of RS-RA and a rough metallization surface.

Whereas, almost the process parameter sets in between give good results for the metallized structure. It was found that the high laser power does not always have a bad effect on the metallization quality, due to the surface melting at elevated laser power. In fact, the impact of laser power is related to the other parameters such as velocity, frequency, and hatching. Figure 7.2 shows different metallization defects with different parameter settings. The discontinuous metallization structure can be seen in picture 1. The extremely high laser power, hatching percentage, and low laser velocity lead to an increase in the amount of input energy on the substrate surface and to increase the melting on this surface. A reduction in hatching to 0 % helps to remove this defect as shown in picture 2. Other types of defects are shown in picture 3 and 4. In picture 3, the defect is due to the effect of focal length at high laser power, frequency, and hatching. It can also be removed by reducing laser power or hatching. The defect in picture 4 is due to the decreasing of the laser power and the increasing of the incidence angle to 40 °, which results in a reduction of structuring percentage from 70 % to 44 %. This defect can be removed by increasing the laser power to 9 W, this will give a structuring of 83 % or by increasing the

hatching to 50 %, this will produce 100 % structuring or by reducing the laser velocity to 1.5 m/s to produce a 74 % structuring. All these proposed parameters help to increase the structuring percentage and then remove these defects.

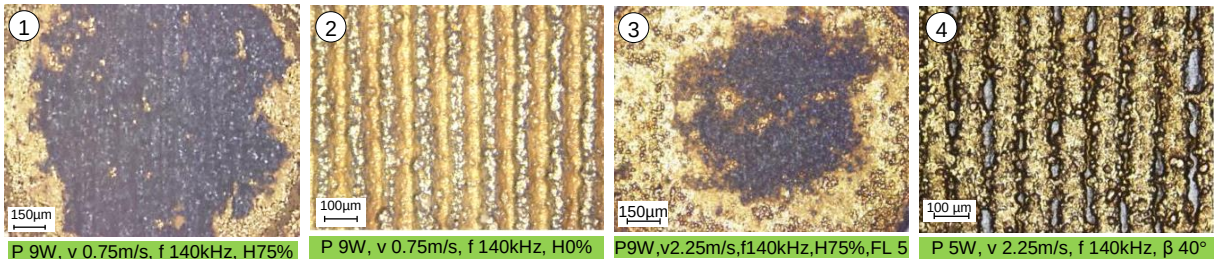

Figure 7.2: Samples of metallization results at different parameter setting.

The optical inspections of the metallization quality are presented in figure 7.3. These are belonging to conductors which have a line shape. In general, it was found that the parameter setting which gives metallization defects of circular conductors do not produce the same metallization defects for the conductors with line shape. This is perhaps due to the variations in the distribution of the laser track between two types of conductors which produce differences in thermal behavior and the subsequent temperature distributions which are responsible for the structuring of the area.

Figure 7.3, pictures 1 to 3 illustrate the metallization results of three different tests that are used to explore the effect of laser power on the final metallization quality. The laser power is installed at 1 W, 5 W, and 9 W whereas the other parameters are constant. Under these parameters, it can be seen that elevating laser power increases the conductor width and edge effect (L. height and L. width). Therefore the metallization quality will be reduced. These metallization qualities of the tests in pictures 2 and 3 could be improved by reducing the edge effect through regulating the other process parameters such as laser velocity or frequency. It is found that the edge effect can be reduced by reducing the laser velocity, due to the effect of velocity on the amount of accumulated energy per unit area that has been discussed. The pictures 4 and 5 show the effect of laser velocity in comparison with picture 2. Here, one can see the difference in quality when the laser velocity changes from 0.75 m/s to 1.5 m/s and then to 2.25 m/s, as shown in picture 2, 4 and 5 respectively. However, this improvement in the quality is based on the reduction in the edge factor but it also accompanied by a reduction in conductor width or track width. The pictures from 6 to 8 display the correlation between laser frequency and metallization quality. Based on the important effects of laser frequency in different LDS responses such as groove dimensions, structuring–ablation type and thickness of metallization, it can be concluded that the setting of the laser frequency at elevated value should be avoided as much as possible. This helps to improve the quality in general. Another important influence is shown in pictures 4, 6 and 9, which shows the impact of the hatching percentage. Various qualities are produced by modulating the hatching, but it should be related to the other parameters. Moreover, high hatching in conjunction with high

laser power is not preferable to support the metallization quality. The influence of both the focal length and the incidence angle on the metallization quality is almost the same. According to these optical inspections, this influence is also focusing on the changing in the conductor width and edge factor due to the distortion in the diameter of the laser spot, as shown in pictures 10, 11 and 12. It refers to the influence of focal length and pictures 13, 14 and 15, which represent the effect of the incidence angle.

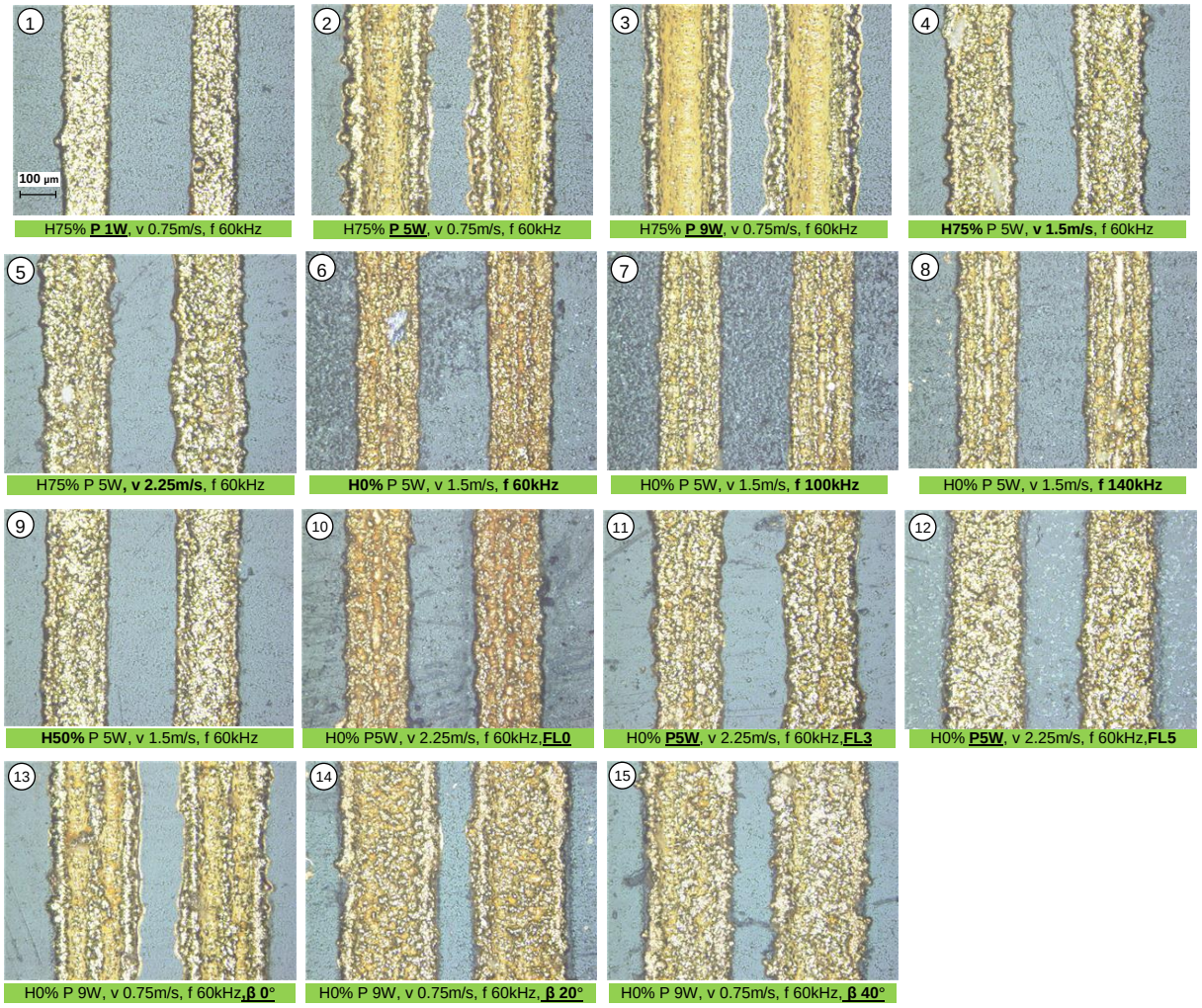

Figure 7.3: Samples of metallization results at different parameter setts for line layout.

In the experimental investigation of the PEEK material, it was found that a minimum of line/pitch of 45/28 µm with metallization thickness of 9 µm is produced under laser parameters which include laser power of 1 W, velocity of 0.75 m/s, and frequency of 60 kHz, as shown in figure 7.4(a). This line or conductor width could be reduced to about 30 µm by adjusting the focal length to 3 mm, see figure 7.4 (b).

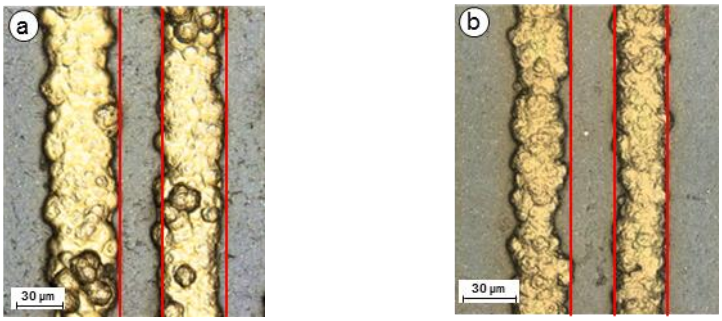

Figure 7.4: The minimum line/pitch at P 1W, v 0.75m/s and f 60kHz.(a) FL 0 mm (b) FL 3 mm.

7.1.2. Ceramic Based Material

The correlation between the parameter setts and the metallization quality for the ceramic based material has also been explored by optical inspection. This investigation includes two layouts, which are line and circular area conductors. Figure 7.5 displays a selected sample of optical inspections under different process parameters. Picture 1 shows the metallization results and the corresponding parameters including an additive percentage of 5 %, a sintering temperature of 1200 °C, a laser power of 4 W, a velocity of 0.75 m /s, and frequency of 60 kHz. Complete metallization can be seen under these parameter setts except black spots which are possibly due to the defects in substrate surface or due to the non-homogeneous which is expected during the manufacturing process [98]. By setting the laser frequency at an elevated value of 120 kHz, the metallization quality is reduced, as shown in picture 2. This is due to the bad effect of the high frequency on the metallization thickness as will be explained in the next section. Moreover, the extreme increase in laser frequency in conjunction with low laser power leads to a reduction in the structuring percentage as discussed above. In this work, it was found that the new innovative material is very sensitive to the structuring and metallization process. It can be used to create a metallization structure that cannot be produceed in other materials such as polymers. Picture 3 presents the optical image for the metallization structure under the corresponding parameters. From this picture, it is clear to see that the second type of structuring defect which occurs due to the slight overlapping or hatching between laser pulses. By regulating the parameter setting, it is possible to produce only one circle which is activated under the impact of only one laser pulse. Further results are shown in pictures 4, 5 and 6 for tests performed under the corresponding parameters including laser power of 8 W, a velocity of 1.5 m/s and frequencies of 60 kHz, 90 kHz and 120 kHz respectively for these three pictures. Optically, it can be noted that under these parameter settings the metallization quality is increased with laser frequency. This is in contrast to the previous effect for laser frequency on quality at a low laser power and velocity. By increasing the velocity it is also possible to produce a complete metallization structure, as shown in pictures 7 and 8.

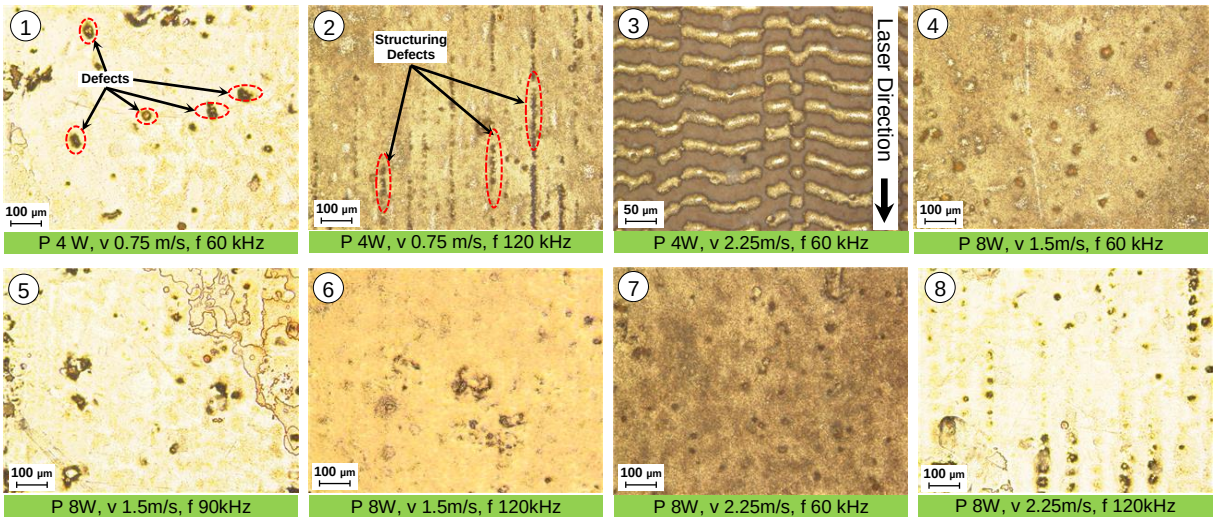

Figure 7.5: The metallization quality circle conductor layout at additive percentage of 5 %, T_s of 1200 °C *and different parameters for ceramics.*

Figure 7.6 shows the optical inspection results of the lines structured under the same process parameters that have been discussed in the figure 7.5. From this figure, one can see that the best metallization quality results according to the optical inspections shown in pictures 1, 3-5 and 7 whereas the pictures 2 and 8 shows some of the metallization defects. In addition, the zigzag formation at the edge groove occurred in the experimental test of picture 7 due to the small overlapping between the pulses resulting from a high laser velocity and a low laser frequency [42].

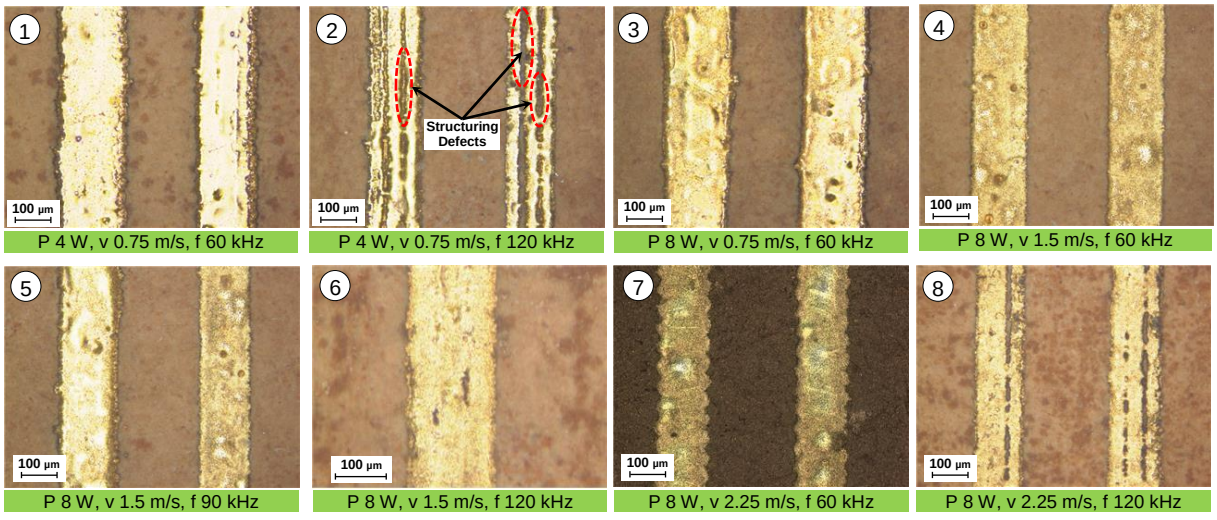

Figure 7.6: The metallization quality of the line conductor layout at additive percentage of 5 %, T_s of 1200 °C, *and different parameters for ceramics.*

The influence of the additive percentage on the metallization quality is presented in figures 5.45 and 5.46. They show samples of the metallization quality of both layouts including lines and areas at the same parameter setting. Figure 7.7 illustrates the

results of metallization quality and the corresponding process parameters. Picture 1 shows the quality of process parameters which include 15 % copper oxide, 1200 °C sintering temperature, a laser power of 4 W, a velocity of 0.75 m/s, and a frequency of 60 kHz. With the exception of the defects on the substrate's surface, good metallization quality is produced under these conditions. If there is a change in the parameters such as power of 12 W, a laser velocity of 1.5 m/s, and frequency of 120 kHz, it is also possible to produce a full metallization structure with different quality levels, as shown in pictures 2, 3 and 4.

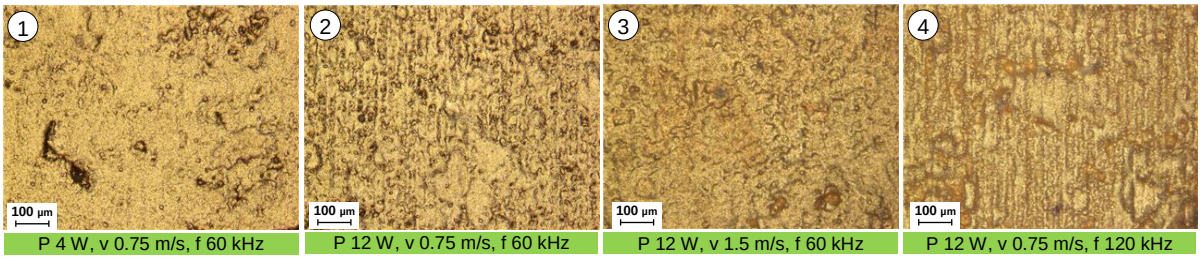

Figure 7.7: The metallization quality circle conductor layout at additive percentage of 15 %, T_s of 1200 °C, *and different parameters for ceramics.*

The increase in the additive-copper oxide to 15 % was able to produce a full metallization structure of different qualities as shown in figure 7.7. In fact, many metallization defects are produced when increasing the additive percentage to 15 %. This can be clearly seen in figure 7.8, which shows the metallization structure and quality of the line layout or conductor under the same parameters of figure 7.7. By increasing the additives percentage, the substrate surface will be very sensitive to produce such metallization defects. Therefore, a high copper oxide of 15 % is not preferred for this material.

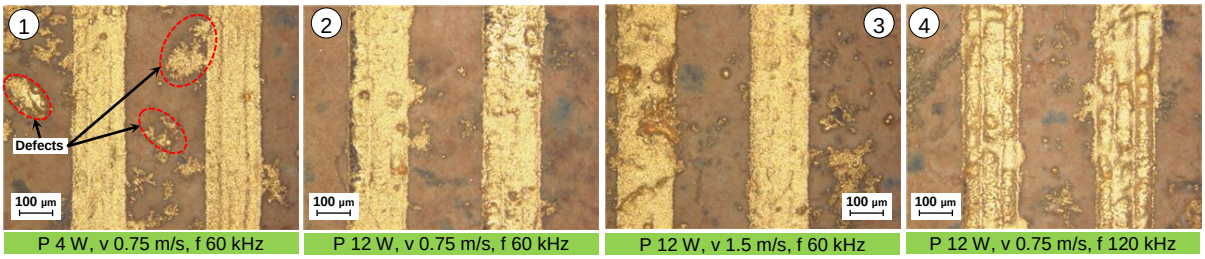

Figure 7.8: The metallization quality of line conductor layout at additive percentage of 15 %, T_s of 1200 °C, *and different parameters for ceramics.*

As mentioned in experiments set up, this study also considered the connection between sintering temperature and metallization structure or quality. The optical inspections for the samples, which are manufactured at sintering temperature of 1600°C, confirm that it is also possible to produce a full metallization structure under process parameters including a laser power of 4 W, a velocity of 0.75 m/s and

frequencies in the range of 60 kHz to 120 kHz, or a laser power of 8 W, a velocity in the range of 1.5 m/s to 2.25 m/s, and the same range of above-mentioned laser frequencies. However, these parameters are only suitable to produce large conductors, such as circle layouts. They are not suitable to produce a metallization structure with conductor width of less than 160 µm. This can be seen in figure 7.9. It shows three test samples of the conductor with area layout, (see figure 7.9, pictures 1, 2 and 3). These tests are performed under different process parameters. In addition, picture 4 shows the weak metallization structure of the line conductor.

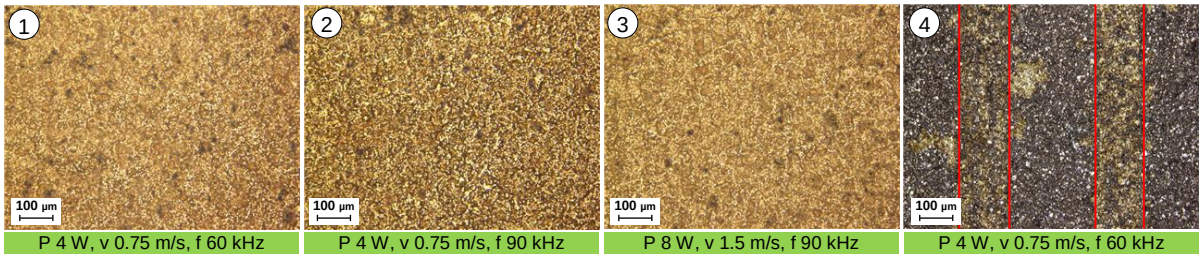

Figure 7.9: The metallization quality at additive percentage of 5 %, T_s of 1600 °C, *and different parameters for ceramics.*

According to the optical inspections of the ceramic material, it can be concluded that the sintering temperature of 1200 °C and additive copper oxide of 5 % can be regarded as the optimum manufacturing conditions for this innovative material. In addition, these materials are suitable to produce a fine line/pitch of 16/20 µm under the manufacturing and process parameters, including an 5 % additive, a sintering temperature of 1200 °C, a laser power of 4 W, a velocity of 1.5 m /s, and a frequency of 120 kHz, as shown in figure 7.10.

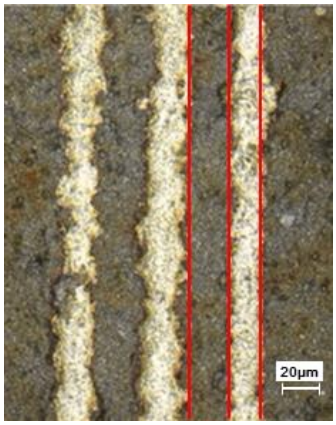

Figure 7.10: The minimum line/pitch at an additive percentage of 5 %, T_s *1200 °C, P 4 W, v 1.5 m/s, and f 120 kHz.*

It is significant to mention that based on the optical inspection a wide range of parameters is possible to produce a good metallization structure. However, the optical inspections are not the only necessary tests for the description of the final MIDs quality. The next sections will discuss in detail the other required inspections.

7.2 Metallization Thickness

7.2.1. PEEK Polymer Material

Further experimental measurements are performed in the work of this thesis to measure the thickness of the coating or metallization layers using the Fischer Scope machine. They are carried out to investigate the correlation between the adopted process parameters and the metallization thickness. Almost all results are within the standard range of the coating system (Cu-Ni-Au). Moreover, some of these results contain metallization defects and the other is sound or free, depending on the process parameters used. The discussions in this analysis relate to the total metallization thickness of the results corresponding to the standard criteria of the coating layers thickness of (Cu-Ni-Au). It is very important to explore the impact of parameter sets up that are based on the produced metallization thickness. This will help to analyze and understand this sophisticated relationship, and propose the optimum process parameters that could be used to achieve and support the metallization quality. Figure 7.11 illustrates the relationship between process parameters including laser power, velocity, frequency and the overall metallization thickness. Where figure 7.11 (a) shows the impact of frequency and velocity on metallization thickness at a laser power of 5 W. In general, the thickness decreases with an increasing of the laser frequency, whereas it is increased when the laser power is increased from 1 W to 5 W, but the rise in laser power to 9 W reduces the thickness again. This is clearly seen in figure 7.11 (b). In figure 7.11 (c) a complex impact of laser velocity and laser power on the metallization thickness can be seen. At low laser power of 1 W, the increment in velocity minimizes the thickness, but at an elevated laser power of 5 W or 9 W, the thickness will be increased with rising laser velocity. Again, from this figure, one can see that the thickness reduces as the laser power is raised from 5 W to 9 W. Moreover, the effect of frequency depends on the velocity and laser power.

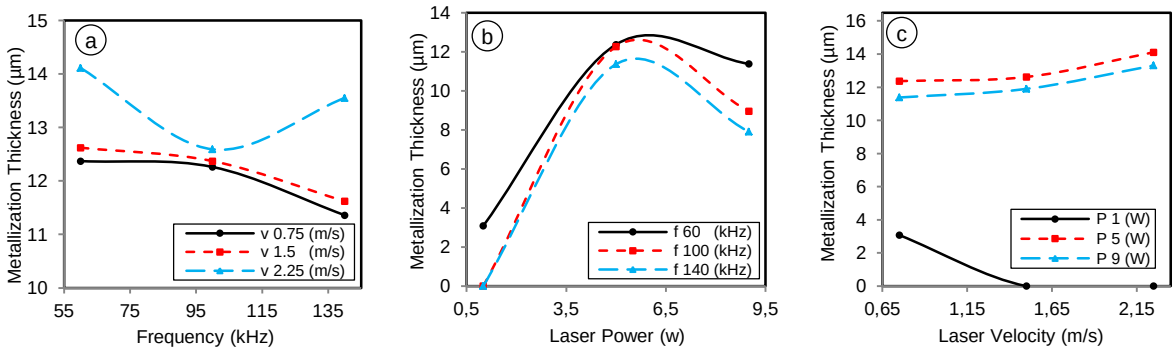

Figure 7.11: The metallization thicknesses against process parameters and (a) P 5 W. (b) v 0.75 m/s. (c)f 60 kHz.

Figure 7.12 shows the impact of hatching and laser power on thickness. In fact, the influence of hatching is related to other parameters. For example, at a low laser

power of 1 W, the increase in hatching from 0 % to 50 % has no effect on the thickness. While at hatching of 75 %, the thickness is about 9.92 µm. When the laser power increases by more than 5 W, the impact of hatching on the metallization thickness will be changed to negative effect, as in figure 7.12 (a). This action is due to the increasing amount of input heat with increases the hatching with elevated laser power. Consequently, the melting of the substrate surface will also be increased. At a low laser velocity, frequency, and high laser power, the increment in hatching from 0 % to 50 % produces a corresponding raise in thickness. However, the adjustment of hatching at 75 % reduces the thickness from 10.8 µm to 5.15 µm. The regulation of velocity to a range of from 1.5 m/s to 2.25 m/s helps to increase the thickness in the range of 1.05 µm to 13.49 µm with different hatching, see figure 7.12(b). The influence of laser frequency on the relationship between hatching and thickness is shown in figure 7.12 (c). It can be seen from this figure that with a laser power of 1 W and a frequency of 140 kHz, there is no impact for hatching when it changes from 0 % to 50 %. In these cases and under such parameters, there is no metallization layer above the substrate surface. If the hatching is installed at 75 %, a coating thickness of 8.33 µm will be created on the substrate surface. Furthermore, if the laser frequency reduces to 100 kHz, the metallization thickness increases from 0 µm to 8.52 µm and then to 9.45 µm when the hatching increases from 0 % to 50 % and then to 75 % respectively. The additional reduction of laser frequency to 60 kHz produces thicker metallization layers.

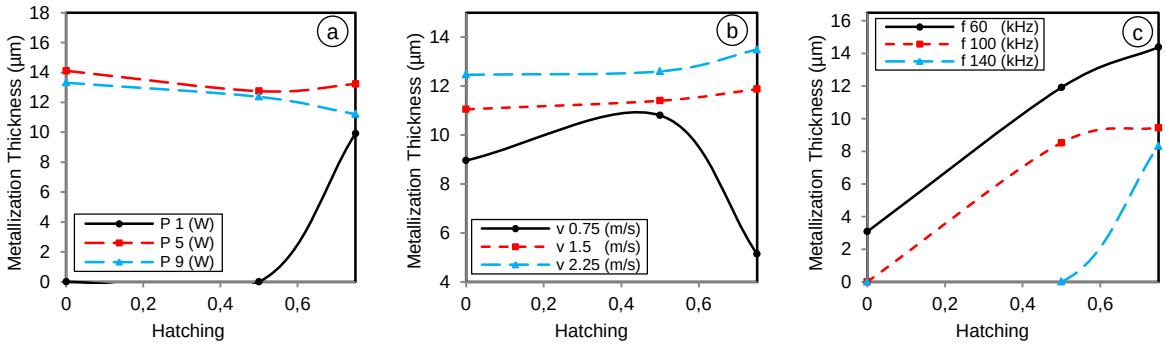

Figure 7.12: The metallization thicknesses against hatching at different (a) Power, f 60 kHz and v 2.25 m/s. (b) Velocity, P 9 W and f 90 kHz. (c) Frequency, P 1 W and v 0.75 m/s.

The effect of focal length is illustrated in figure 7.13. Here it can be seen that with a laser power of 9 W and a velocity of 0.75 m/s, the thickness slightly increases with focal length at different frequencies, as shown in figure 7.13 (a). At a laser velocity of 0.75 m/s, a frequency of 60 kHz, and a focal length of 0 mm, it was found that the thickness is increased when the laser power changes from 1 W to 5 W. This thickness decreases again as the laser power rises to 9 W, as shown in figure 7.13 (b). From the same figure, also it can be noted that the thickness always increases with laser power when the focal length is set at 3 mm or 5 mm. Furthermore, it can be

observed that the thickness increases with focal length at an elevated laser power, while it is decreased with focal length at a laser power of 1 W and 5 W. In fact, this is concerned with the effect of focal length on laser spot diameter, laser density, and its distribution. The increase in the focal length reduces the bad effect of excessive high laser power on the characteristics of structured area and then on metallization thickness. With a laser power of 5 W and a frequency of 60 kHz, there is no high effect for focal length on thickness at different laser velocities except the reduction in thickness to 9.2 µm when the focal length rises from 3 mm to 5 mm at a velocity of 2.25 m/s, see figure 4.46 (c).

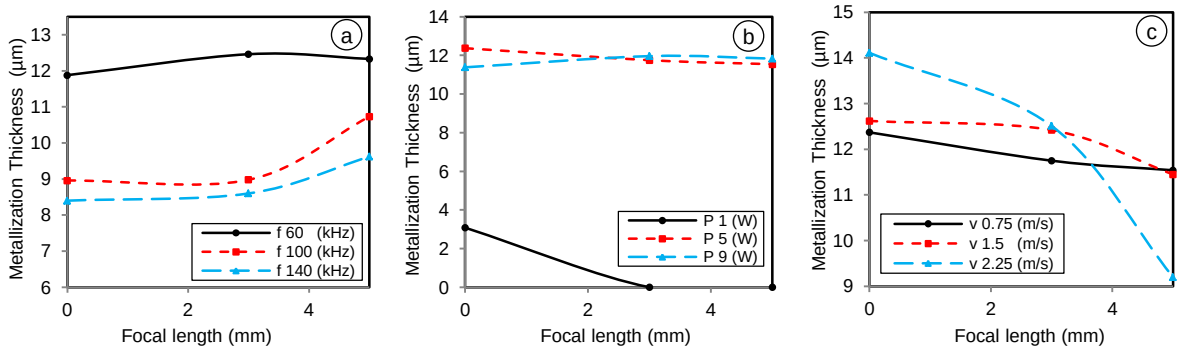

Figure 7.13: The metallization thickness against focal length at different (a) Frequency, P 9 W and v 0.75 m/s. (b) Power, f 60 kHz and v 0.75 m/s. (c) Velocity, P 5 W and f 60 kHz..

The complex influence of incidence angle on the metallization thickness should be also explored in this topic. Figure 7.14 shows a sample for this effect with different process parameters. The influence of laser frequency on the relationship between thickness and incidence angle is presented in figure 7.14 (a). In general, at a laser power of 5 W and different laser frequencies, the same inverse relationship between incidence angle and thickness can be noted. In comparison with the effect of focal length, the incidence angle has the same effect, which was discussed in the influence of focal length and laser power, see figure 7.13 (b). At laser power in the range of 1 W to 5 W, the thickness decreases with raising the incidence angle. This effect for the incidence angle can be removed or reduced by increasing the laser power. This enhances the increase in metallization thickness at an elevated incidence angle, as shown in figure 7.14(b). A clear interaction between the incidence angle and laser velocity can be noted in figure 7.14 (c). It shows the impact of laser velocity on the thickness at a laser power of 5 W and a frequency of 60 kHz. It can be seen from this figure that at an incidence angle of 0 ° the same relationship is present that has been discussed in previous sections (figure 7.13(c)). In addition, at a laser speed of 2.25 m/s, the effect of incidence angle is greater than at low laser velocities. Therefore, it is preferable to avoid the high laser velocities in order to minimize the effect of the incidence angle on the metallization thickness.

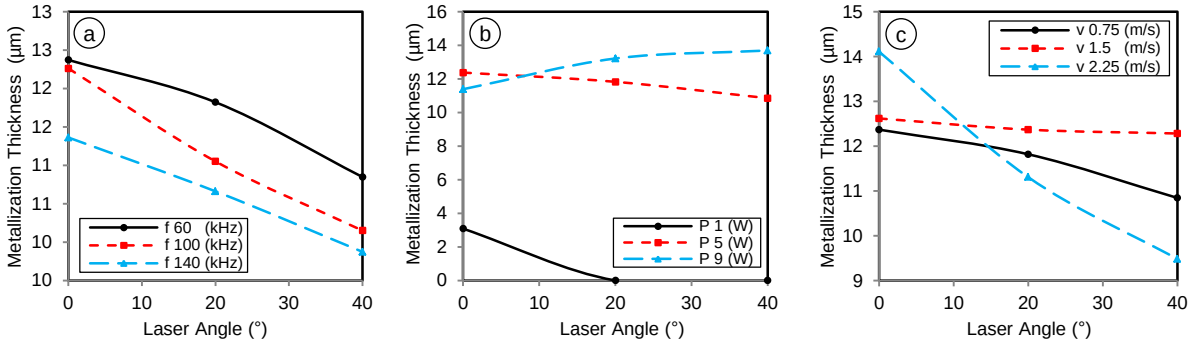

Figure 7.14: The metallization thickness against incidence angle at different (a) Frequencies, P 5 W, and v 0.75 m/s. (b) Powers, f 60 kHz and v 0.75 m/s. (c) Velocities, P 5 W and f 60 kHz.

The minimum measurement of the Fischerscope machine, which is about 0.2 mm, does not make it suitable to measure the metallization thickness of conductor width less than 0.2 mm. This was motivated to use a new method based on the comparison between the measured profiles after and before metallization step. This is implemented using 3D laser scanning microscope (Keyence VK-9700 K) and then utilizes the VK Analyzer software to calculate the metallization thickness. This method provides a measuring step of less than 10 µm. Due to the flexibility in this measuring step, this method can be used as an alternative method to perform the thickness measurements of micro conductors. Different samples of measurements are illustrated in figure 7.15, which shows three comparisons between the measured profile before and after metallization and its corresponding process parameters. In the first case, which is shown in figure 7.15(a), the profiles are created under a laser power of 5 W, a velocity of 1.5 m/s, a frequency of 140 kHz, and the other parameters are set 0. With these parameters, the characteristics of the structured conductor include a structuring of 75 %, the structuring-ablation type is MS-MA and the profile is presented in this figure in the red line. The blue line refers to the profile after metallization. Although the structuring is not 100 %, the metallization is covered all conductor width. In addition, the minimum thickness of the metallization layer is about 6.7 µm and the maximum is 16.45 µm. The case in figure 7.15(b) shows the comparison at a laser power of 1 W, a frequency of 60 kHz, a velocity of 0.75 m/s, hatching of 75 %, and the other parameters are chosen to be 0. The structuring percentage is about 100 % and the structuring-ablation type is RS-PA. The metallization thickness produces an average of 13.83 µm. With an elevated laser power of 9 W, a laser velocity of 0.75 m/s, a frequency of 140 kHz, and hatching 50 %, a metallization thickness of 13.75 µm can be also produced, see figure 7.15 (c).

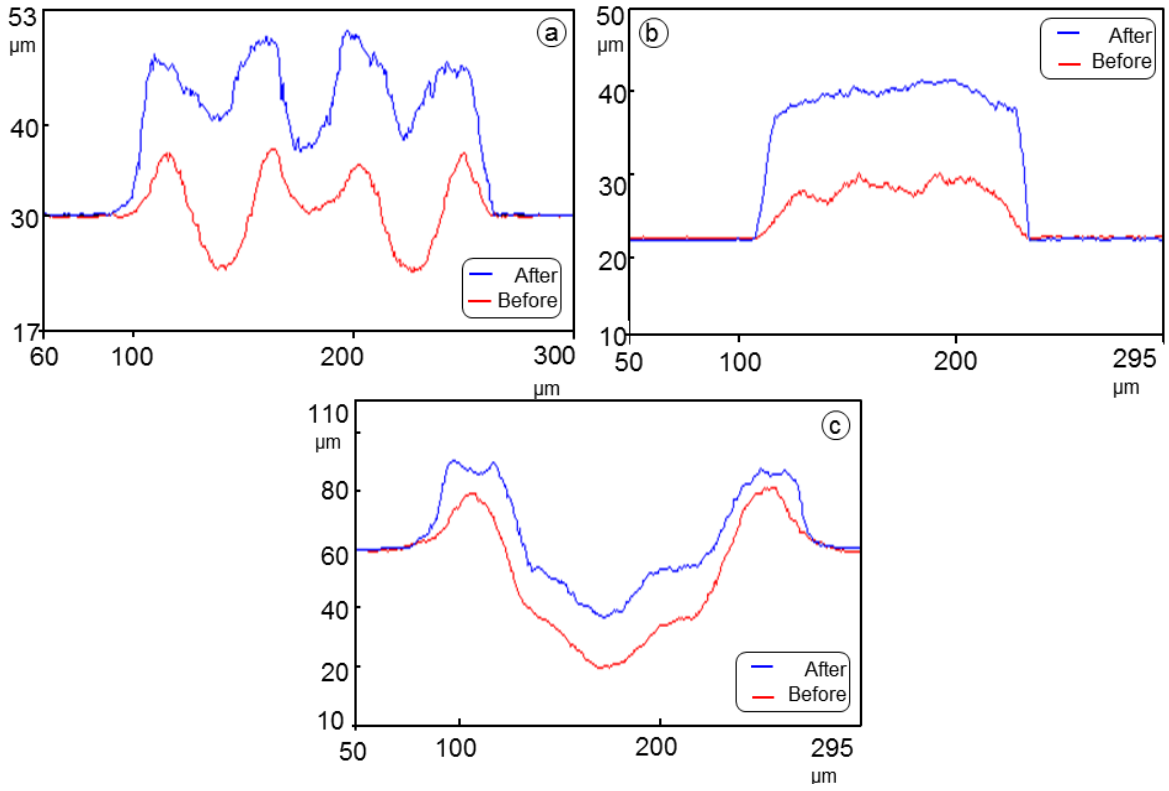

Figure 7.15: Comparison between the surface before and after metallization. (a) P 5 W, v 1.5 m/s, f 140 kHz, (b) P 1 W, v 0.75 m/s, f 60 kHz, H 75 %, (c) P 9 W, v 0.75 m/s, f 140 kHz, H 50 %.

The second type of polymers (VESTAMID® HT plus LDS 3031 black) has shown the same profile behavior before and after the metallization [17]. Therefore, further comparisons will not be shown for this material.

7.2.2. Ceramic Based Material

For the ceramic base materials, the metallization thickness measurements are recorded with different results on the basis of additive percentage and sintering temperature. Table 7.1 contains the range of thickness measured for the three samples group.

Table 7.1: The range of the metallization thickness measures for ceramics.

Samples Group	Coating Thickness (µm)
AL_2O_3 95 Vol %- T_S 1200 °C	8,2 - 11,21
AL_2O_3 85 Vol % - T_S 1200 °C	7 - 10,76
AL_2O_3 95 Vol % - T_S 1600 °C	7,32 - 9,07

As mentioned previously, the ceramic based materials have shown only one ablation type, which is removing (RA), so the produced groove profiles differ from those for polymers. Figure 7.16 demonstrates the profile comparison of a case implemented

under parameter setting include additive of 5 %, a sintering temperature of 1200 °C, a laser power of 8 W, a velocity of 2.25 m/s, and a frequency of 60 kHz. The comparison shows that under such parameter setting a coating thickness of 11.23 µm can be produced.

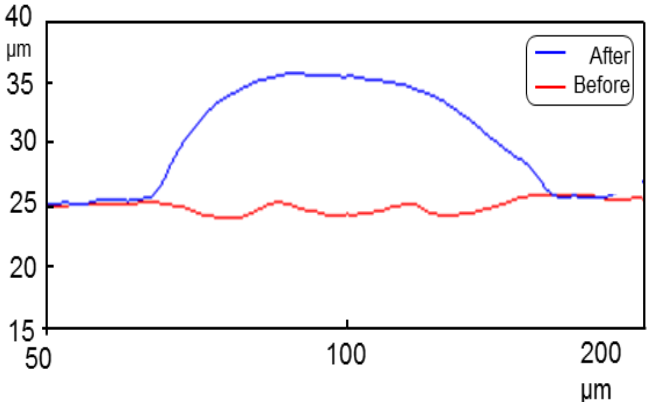

Figure 7.16: Comparison between the ceramic surface before and after the metallization.

7.3 Surface Roughness after Metallization

7.3.1. PEEK Polymer Material

The surface roughness of the metallized surface is in demand for the final assembly of components of final MID products. This surface roughness should be as far as possible under control. A smooth, metallized surface is preferable for such cases [16]. In this work, it was found that the variations in roughness after the metallization step are related to the characteristics of the structured area, which in turn is related to parameter setting. A set of experimental measurements for the surface roughness was carried out with different parameter settings. As for the measurements of Ra and Rz after the structuring, these measurements are repeated three times and the final data are based on the average. It is concluded that the structure-ablation types of the structured areas depend on the parameter set up. The Tables B.1 to B.4 in the appendix-B contain the experimental measurements of the surface after and before metallization with their corresponding parameters and the characteristics of the structured area. According to these measurements, one can conclude that the roughness after metallization can increase or decrease. This behavior relates to the structure-ablation type as well as laser power. Figure 7.17 shows a comparison between the roughness before and after the metallization. Where, figure 7.17 (a) shows these measurements, which have a structuring type of MS (see Table B.1 in Appendix B), while figure 7.17 (b) shows these have a structuring type of RS at a laser power of 5 W (see Table B.2 in Appendix B). Under these conditions of the Tables 1 and 2, the surface roughness is always reduced after the metallization, except test number 13, in which the roughness is increased after metallization due to the metallization defect (see picture 4 in figure 7.2).

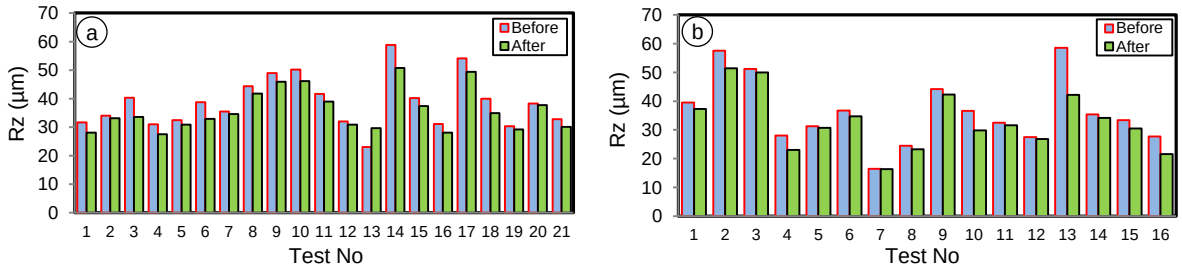

Figure 7.17: The roughness before and after metallization of structuring type (a) MS. (b) RS at P 5 W.

In the second behavior type the roughness increases after metallization. This can be seen in figure 7.18 (a) and (b), where figure 7.18 (a) belongs to the measurements that have a structuring type of RS under laser power of 9 W (see Table B.3 in appendix B). In addition, the structuring type of LS also leads to an increase of the surface roughness as shown in figure 7.18(b), which shows the LS structuring type measurements in Table B.4 in appendix B.

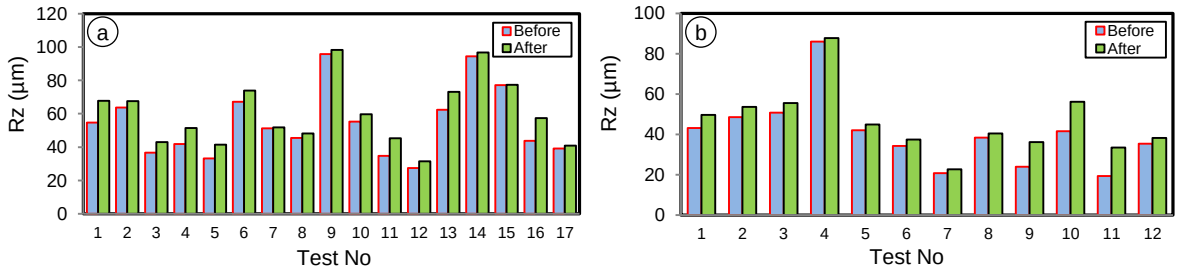

Figure 7.18: The surface roughness before and after the metallization of structuring type (a) RS at a laser power of 9 W. (b) LS.

As a conclusion, the relationship between the roughness before and after the metallization as well as the effective variables on this roughness can be summarized in Table 7.2. According to Table 7.2, the surface roughness of the metallization is increased if the produced structuring type is LS independent of ablation type and laser power, or the structuring type is RS at a laser power of 9 W, regardless of ablation type. Finally, the structuring-ablation type is RS-PA, without any effect for the laser power. On the other hand, the roughness after metallization can be reduced only in the following cases. First, the structuring type is MS without any effect for ablation type and laser power. Second, the structuring-ablation type is RS-(RA or MA) and the laser power is in the range of 1 W to 5 W.

Table 7.2: The relation between the surface roughness of the metallization and LDS output.

Structuring Type	Ablation Type	Type of effect on Roughness	
		P 1 to 5 (W)	P 9 (W)
RS	PA	+↑	+↑
RS	RA	-↓	+↑
RS	MA	-↓	+↑
MS	PA	-↓	-↓
MS	RA	-↓	-↓
MS	MA	-↓	-↓
LS	PA	+↑	+↑
LS	RA	+↑	+↑
LS	MA	+↑	+↑

7.3.2. Ceramic Based Material

For the ceramic based materials, the surface roughness of the metallization structure also relates to the topography of the structured area and its characteristics, as for the polymers. In general, the metallization roughness depends on the structuring-ablation type. However, in the ceramic material, only two structuring-ablation types including RS-RA or MS-RA were recognized. These are depending on the adopted parameter setting and thermal-physical material properties. It is also possible to produce a third type, which is LS-RA by setting low hatching percentage. However, the third type is not preferred due to its bad effect on the roughness of the metallization structure. Figure 7.19 displays the comparison of surface roughness before and after metallization. Here the two different behaviors for roughness after metallization. In the first, the roughness is reduced after metallization can also be seen, as shown in figure 7.19(a). The second behavior can be seen in figure 7.19(b); it leads to produce a rough metallized surface. In fact, both of the above-mentioned cases are relevant to the LDS characteristics and quality, as discussed previously.

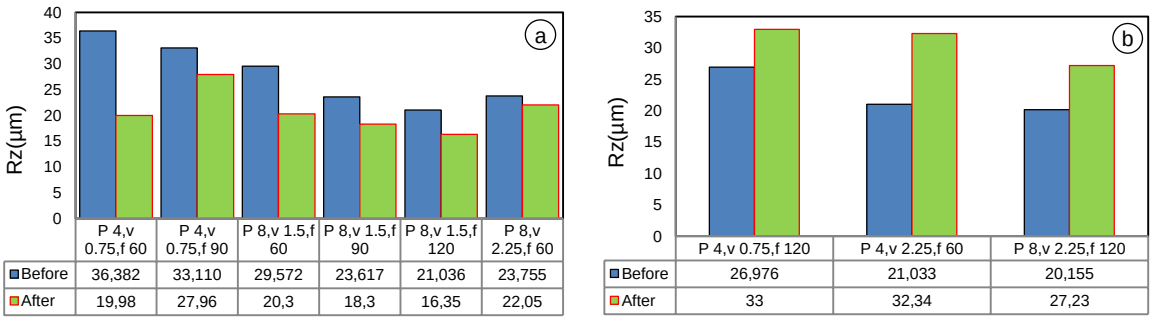

Figure 7.19: Rz of ceramic based material before and after metallization at different parameters.

7.4 Adhesion and its Relation with LDS Quality.

The adhesion strength between the metallization structure and substrate surface can be regarded as one of the most important prerequisites for the MIDs quality and reliability. It should be sufficient to withstand the mechanical and thermal stresses [1][27]. Therefore, a set of adhesion tests was performed at different process parameters to investigate the correlation between these parameters and the adhesion strength of the metallization structure. To perform these adhesion tests a DAGE 4000 Plus hot-pin pull testing system was used [29].

In previous publications in [16] [99], the results show that the adhesion is only related to the surface roughness of the structured area. In the present work, it was found that the adhesion depends on the structuring quality and on the other characteristics of the structured area, not only the surface roughness. These characteristics are summarized so far by the structuring percentage, metallization thickness as well as the surface roughness, as shown in figure 7.20. This figure shows the results of the adhesion tests, which are performed under different laser parameters including laser velocities of 0.75 m/s, 1.5 m/s and 2.25 m/s, frequencies of 60 kHz, 100 kHz and 140 kHz, laser power of 5 W, and the other parameters, were chosen to be 0. This figure also includes the surface roughness of the structured areas, the thickness of the metallization layers, and the structuring percentage. In this case, it must be noted that, given the same laser velocity, the surface roughness is increased with laser frequency whereas the structuring percentage, coating thickness, and adhesion are reduced. In addition, at a constant frequency, the structuring, surface roughness and adhesion increase with velocity, in contrast with the coating thickness, which is reduced with laser velocity. In fact, the results in this figure have been given a new explanation for the effective factors that play an important role in the adhesion strength of the metallization. According to the analysis of results in this figure, it is found that the adhesion is influenced by: first, the structuring percentage, second the surface roughness. For instance, the first three points refer to the effect of laser frequency on the adhesion at constant laser velocity of 0.75 m/s. The increases in the laser frequency result in a reduction of the structuring, a minimization of the coating thickness and rough surface. In general, this behavior leads to a reduction in adhesion strength despite the increase in surface roughness, see figure 7.20. The same behavior for the relationship between frequency and adhesion can be recorded at different laser velocities. The second case can be used to explain the influence of laser velocity at constant frequency and power. It can be seen from the same figure that the surface and the structuring decrease with laser velocity whereas the coating thickness is directly proportional to the laser velocity. In this case, the reduction in both the roughness and structuring percentage will assist to decrease the adhesion. The same behavior can also be noted at different laser frequencies, as shown in figure 7.20.

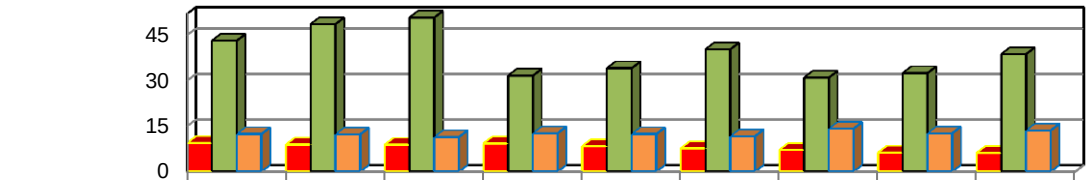

	v 0.75 f 60	v 0.75 f 100	v 0.75 f 140	v 1.5 f 60	v 1.5 f 100	v 1.5 f 140	v 2.25 f 60	v 2.25 f 100	v 2.25 f 140
Adhesion (N/mm2)	9,41	8,92	8,85	9,27	8,36	7,67	7,15	6,23	6,13
Rz (µm)	43,10	48,56	50,71	31,60	34,04	40,26	30,95	32,42	38,68
Meta.Thic. (µm)	12,37	12,26	11,36	12,62	12,37	11,62	14,11	12,59	13,55
Structuring %	0,93	0,89	0,87	0,91	0,83	0,75	0,78	0,73	0,70

Figure 7.20: The relation between Rz, metallization thickness, structuring and adhesion at different velocities and frequencies for PEEK polymer.

Further tests are performed to explore the influence of other parameters on adhesion, as shown in figure 7.21. In figure 7.21(a) one can see the impact of the laser power on the characteristics of structured area and then on the adhesion strength. The roughness and structuring increase with laser power, consequently the adhesion is also increased. This agrees with the previous publications in [100] [101]. The effect of hatching percentage is shown in figure 7.21 (b). As the hatching changes from 0 % to 50 %, the structuring rises from 93 % to 100 % while the surface becomes smoother. It changes from 43.1 µm to 39.51 µm. This will help to increase the adhesion strength, based on the increase in the structuring. In fact, it is concluded, a structuring percentage of 75 % is sufficient to produce a full metallization structure, but increasing the structuring percentage to 100 % produces a structuring area without effects of edge factor in the inner area where the groove edges are not preferred inside the structured area. The setting of hatching at 75 % does not provide any changing the structuring. It is still at 100 %, while it helps to raise the roughness. As a result, the adhesion is slightly increased from 9.63 N/mm^2 to 9.66 N/mm^2 based on the increase in roughness. The effect of the focal length is presented in figure 7.21 (c). The increase of focal length to 3 mm results in slightly increased adhesion due to the increase in the structuring percentage, while a reduction in the surface roughness decreases the adhesion when the focal is changed from 3 mm to 5 mm. Under the corresponding parameter setting of figure 7.21 (c), the increase in incidence angle leads to produce a full structured area. On the other hand, the roughness is changed based on incidence angle. A rough surface is produced when the angle is changed from 0 ° to 20 °, but at an incidence angle of 40 °, the surface will be smoother. In any case, this relationship between the incidence angle, surface roughness, and structuring can be used to explain the effect of the incidence angle on the adhesion strength, see figure 7.21(c).

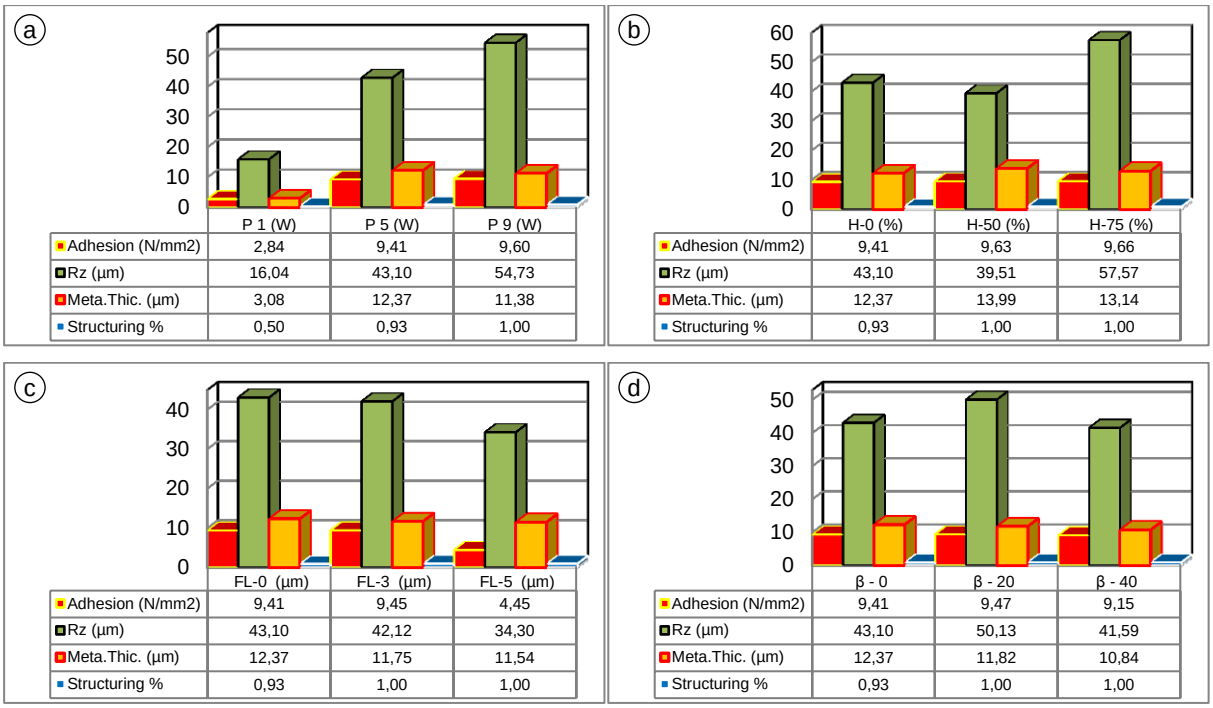

Figure 7.21: The relation between Rz, metallization thickness, structuring, and adhesion at v 0.75 m/s and f 60 kHz with different, (a) Power. (b) Hatching. (c) Focal length. (d) Incidence angle.

In order to explore the influence of both incidence angle and focal length on the relationship between adhesion strength and the laser power, velocity, and frequency additional adhesion tests are carried out at an incidence angle of 40 °, a focal length of 5 mm, laser power of 5 W and 9 W, velocity of 0.75 m/s and 2.25 m/s and frequency of 60 kHz and 140 kHz. The results of these tests are shown in figure 7.22. Here, the same behaviors, which are already discussed for the effect of laser power, velocity and frequency on the adhesion strength, can also be seen in this figure.

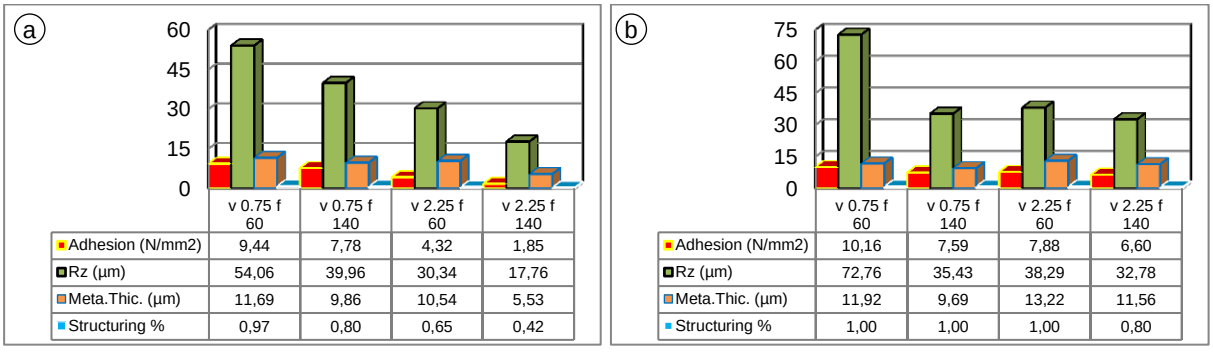

Figure 7.22: The relation between Rz, metallization thickness, structuring and adhesion at an incidence angle of 40 ° and FL 5mm and (a) Power 5 W. (a) Power 9 W.

8. Process Modeling and Optimization

8.1 Introduction

As described in the previous chapter, the MID-LDS process is affected by complex parameters. These parameters, as well as their interactions, are responsible for the final characteristics of the MID such as quality, accuracy, and reliability. Mathematical and statistical modeling is used to propose a series of process parameters, which can be used to provide the requirement of MID structures under particular processing constraints. In the last decades, the numerical methods and their applications such as the artificial neural networks (ANN), response surface methodology (RSM), genetic algorithms, fuzzy logic, etc. have been sophisticated. These methods can be used as important and powerful tools to develop a mathematical model for a large number of problems in several application fields [102]. These tools can be considered as a black box, which are capable to predict an output or response when implementing specific input factors [103]. It is able to recognize similarities of new input factors that produce a predicted output response. In general, the modeling tool can be employed to achieve the following objectives [104] [105]:

1- To establish a relationship between the process responses and the input factors or the process parameters that can be used to predict response values for the specific setting of the input process parameters.
2- To find the importance of each process parameter as well as the interaction between them.
3- To suggest the optimum setting of the input parameter that lead to optimize responses.

In this chapter, mathematical models with two different approaches or modeling tools will be developed based on the experimental results that were used in chapter 6 and 7.

8.2 Artificial Neural Network (ANN) Model

8.2.1 Introduction to ANN Method

The artificial neural networks (ANN) can be defined as a type of Artificial Intelligence (AI). They are computational models, which, unlike traditional computing, are inspired by the biological nervous system and use neurons to carry and transmit signals through synapses. By using the samples of experimental results, ANN can be used to produce new knowledge for the different domains through learning. Therefore, the ANN approach was used to propose a mathematical model in many different fields. It is selected for this work due to its ability to model non-linear very noisy and

multidimensional systems or problems, as well as its versatility for data analysis [106][107].

8.2.2 Structure and Procedures of the ANN Model

The figure 8.1 shows the set of procedures and mean steps for the ANN method [108][109]. In the first step, the input and the target or the output data must be defined. In this work, the inputs to the neural networks are the number of significant parameters including the incidence angle, the hatching percentage, the focal length, the laser power, the laser speed and finally the laser frequency. These inputs influence the process outputs or responses such as the groove depth, the conductor width, the lap width, the lab height, the surface roughness, the structuring percentage, the LDS accuracy, structuring type, ablation type and the metallization thickness, see appendix A.

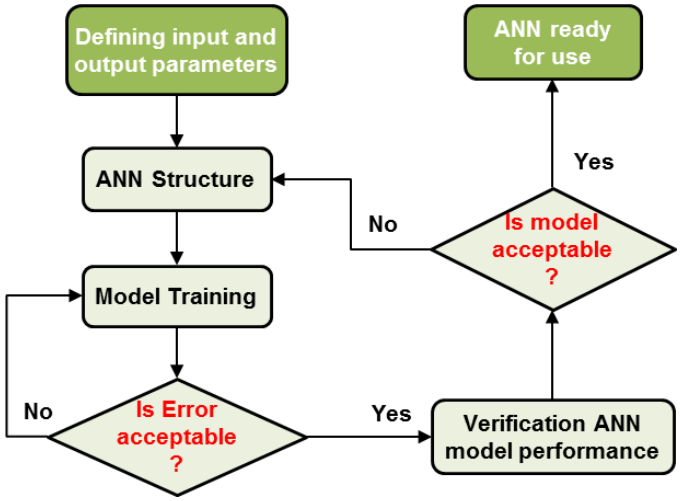

Figure 8.1: The ANN procedures.

One of the most important and difficult steps in ANN modeling is the structure or the architecture. Figure 8.2 shows the neural network architecture employed in this work, this architecture consists of three layers: the first layer is the input layer representing the input vector or parameters, where the output of each neuron in the input layer is represented by $w_{xy}x_i$, w_{xy} represents the weight associated with the connection between input factor i (x_i) and the processing element I_{ji}. The second layer is the hidden layer, which receives the signals from the processing element layer as well as the bias function. Equation 8.1 shows the net input of each neuron in the hidden layer.

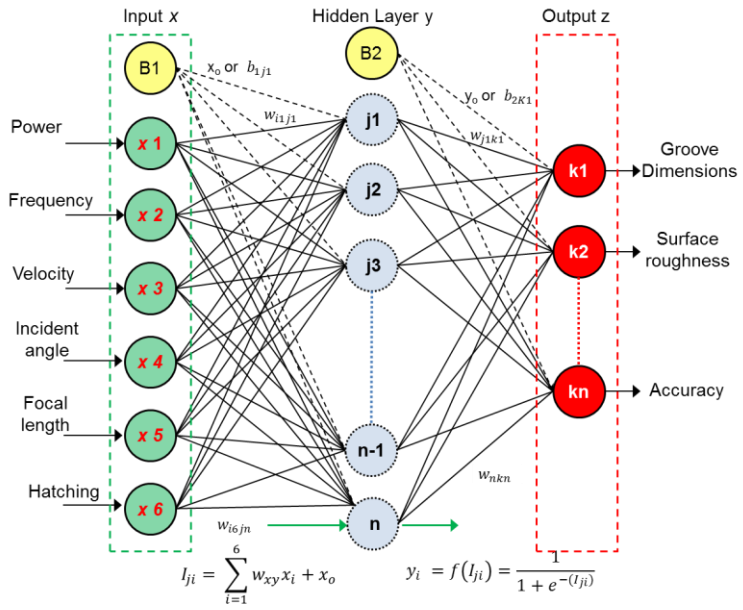

Figure 8.2: The ANN architecture.

$$I_{ji} = \sum_{i=1}^{6} w_{xy} x_i + x_o \qquad 8.1$$

Where, w_{xy} is the weight from the input layer to hidden layer and x_o is the bias of the input layer. The actual output of the hidden layer is calculated by applying the sigmoid activation function to activate each neuron [109] equation (8.2) shows the above mentioned sigmoid function.

$$y_i = f(I_{ji}) = \frac{1}{1+e^{-(I_{ji})}} \qquad 8.2$$

The output layer is the final layer. It is received in neuron k, the outputs of the hidden layers as well as the bias of the input, hidden layer (b1) and (b2) respectively, shown in the below equation (7.3).

$$I_{zi} = \sum_{i=1}^{6} w_{xy} x_i + x_o + \sum_{j=1}^{n} w_{yz} y_j + y_o \qquad 8.3$$

Where n is the number of neurons in the hidden layer and w_{yz} is the weight from the hidden layer to output layer and y_o is the bias for the hidden layer. By applying the same sigmoid function as applied to the hidden layer, the actual output of the output layer is calculated using equation 8.4.

$$z = f(I_{zi}) \qquad 8.4$$

The training process for the ANN model is the next step to find the sets of weight values that can match the actual net output with the current target values. And then, the error between the desired and the output values of the network is computed for each output neuron. The other steps for the ANN model can be seen in figure 8.1.

8.3 Response Surface Methodology (RSM)

8.3.1 Introduction to RSM Method

RSM is a mixture of a mathematical and a statistical tool. It is often used for modeling the different domain problems, especially in engineering applications. It is a powerful tool that can be used to propose a model of complex process, their unknown underlying structure to optimize the responses of the processes. The RSM method is mainly used to describe the relationship between the responses and the input variables and moreover to determine the effect of each parameter on the output responses as well as the interaction between them [110][111]. In order to build the RSM model and achieve its objectives, a series of experimental tests should first be implemented, in which the responses are measured (or observed) regarding specific settings of the input variables. These steps are defined as response surface design.

8.3.2 RSM steps and Procedures

The first step of the RSM method is to select a suitable model that describes the relevance between process parameters and responses variables, which are unknown. In general, the response surface can be expressed as follows [112][113]:

$$y = f'(x) + \dot{\varepsilon} \qquad 8.5$$

Where, the term y represents the responses (output) of the process, x is the input parameter and ε is the residual error. There are two important models that are used to construct the RSM models. These are the first-degree model and the second-degree model. The first model is used, when the relationship between the input variables and the responses of the investigated system corresponding to a linear function.

$$y = b_0 + \sum_{i=1}^{n} b_i x_i \; + \; \dot{\varepsilon} \qquad 8.6$$

Where, x_i is the encoded variable or parameter, b_0 is constant to the regression equation, n is the number of investigated parameters, the coefficient b_i is linear term. Therefore, a second-degree model of the RSM is used for the complex responses of the LDS process to propose a mathematical model for the examined process. A quadratic polynomial model or second order equation is used to represent the response surface for the input factors as follows [114]:

$$y = b_0 + \sum_{i=1}^{n} b_i x_i \; + \sum_{i=1}^{n} b_{ii} x_i^2 + \sum_{i=1}^{n-1} \; \sum_{j=i+1}^{n} b_{ij} x_i x_j + \dot{\varepsilon} \qquad 8.7$$

Where, x_i x_j are the coded variables or parameters, the coefficient b_{ii} is quadratic term, the coefficient b_{ij} is interaction term and ε is the residual error.

The above second order response model can be expressed as follows:

$$\sum_{i=1}^{n} b_i x_i = b_1 P + b_2 v + b_3 f + b_4 FL + b_5 H + b_6 \beta$$

$$\sum_{i=1}^{n} b_{ii} x_i^2 = b_{11} P^2 + b_{22} v^2 + b_{33} f^2 + b_{44} FL^2 + b_{55} H^2 + b_{66} \beta^2$$

$$\begin{aligned} \sum_{i=1}^{n-1} \; \sum_{j=i+1}^{n} b_{ij} X_i X_j = \; & b_{12} P * v + b_{13} P * f + b_{14} P * FL + b_{15} P * H + b_{16} P * \beta \\ & + b_{23} v * f + b_{24} v * FL + b_{25} v * H + b_{26} v * \beta + b_{34} f * FL + b_{35} f * H \\ & + b_{36} f * \beta + b_{45} FL * H + b_{46} FL * \beta + b_{56} H * \beta \; + \dot{\varepsilon} \end{aligned} \qquad 8.8$$

The above equations 7.7 and 7.8 are used to determine the response equation for the MID-LDS outputs including the groove depth (GD), the conductor width (CW), the lap width (LW), the lap height (LH), the structuring accuracy, the metallization thickness, and the surface roughness (Ra, Rz).

8.4 Results and Discussion

The experimental works on the PEEK polymer described in chapter 5 are used in this chapter as a data base for proposing the model, for both methods including ANN and RSM approaches. As it has been discussed, these full factorial operations includes 1.458 experiments, consisting of 729 tests for lines and 729 tests for area, which were performed to investigate the relevance between the mentioned process parameters and its responses. Different software such as MATLAB R2014a [115], IBM SPSS 22 and Minitab® 17.2.1 [116], has been used to find the final solutions of these two approaches (RSM and ANN). This section presents and discusses the modeling results regarding the model description, the influence and importance of parameters and the interaction between them. This will be separately discussed for each process output and for all modeling methods as follows.

8.4.1 Results of RSM model

Groove Depth

According to the RSM modeling results, the order of the assumed parameters with regard to their effect on the groove depth is: laser power, velocity, hatching, laser frequency and finally focal length which are shown in figure 8.3. The impact of the incidence angle is not completely clear in this figure. However, according to Table 8.1, it is clear to see that the effect of the linear term β is about 0.138, this means it has a positive effect, whereas the constant β * β is -1.58, has a negative effect. Therefore, the overall effect of incidence angle on the depth is considered as negative, which is in agreement with the previous experimental analysis in chapter 5. Furthermore, this figure also shows that the effect of laser velocity, frequency, focal length and incidence angle is negative on depth, contrary to others parameters such as laser power and hatching that have positive impact on depth. In fact, these terms refer to the constants from b_1 to b_6 mentioned in equation 8.8

Table 8.1: The process responses and the coefficients of the parameters.

Responses / Eq.Terms	**Conductor Width**	**Groove Depth**	**Edge Height**	**Edge Width**	Rz	**Metal. Thickn**	**Structu. %**
constant	152,82	4,98	5,472	29,688	32,684	11,709	0,8907
β	-9.957	0,138	-1,3167	-4,036	1,031	0,4263	-0,03881
FL	-2,123	-0,996	-0,3332	2,123	-1,701	-0,6493	-0,01517
H	3,853	5,574	0,8393	1,808	2,133	0,7275	0,10463
P	60,314	9,632	3,7534	19,38	20,396	5,0844	0,36699
v	-26,081	-6,093	-1,7116	-1,665	-7,874	-0,2048	-0,09958
f	-11,381	-1,53	0,5752	1,803	-2,902	-1,002	-0,03689
β*β	1,09	-1,58	0,6625	5,069	-2,178	-0,777	0
FL*FL	6,79	-2,469	0,2684	5,976	-1,676	-0,612	0
H*H	2,08	4,74	0,47	0,829	3,48	0	0,043
P*P	-32,73	1,941	-1,9225	-19,3	-6,928	-4,502	-0,3204
v*v	-0,92	3,331	0,8011	1,29	2,717	0	0,0225
f*f	3,36	0	0	0	0	0,262	0
P*v	11,283	-6,451	-0,4839	-1,822	-4,983	0,914	0,1166
P*f	6,754	-1,39	0,9979	1,145	-1,063	0	0,03756
P*FL	4,924	-0,536	0,1971	1,195	1,013	0,208	0,02697
P*H	-1,747	5,505	0,4342	1,356	0,63	-0,615	-0,08466
P*β	0,61	0,627	-1,2162	-2,891	0,986	0,24	0,04315
v*f	-3,271	0,969	0	0,504	0,787	0,472	0
v*FL	-3,493	0,528	0,4743	0	0	0	0
v*H	0,671	-3,467	-0,1526	0	-1,21	0	-0,01918
v*β	2,854	0	0,2584	-0,609	-0,964	0	0
f*FL	2,333	0	0	0	-1,084	0	0
f*H	0,191	-0,898	0	0	-0,724	-0,38	0
f*β	-1,42	0	-0,1673	0	0	0,206	0
FL*H	-1,328	0	0	0	0	0	0
FL*β	-7,809	1,906	-0,1876	-7,18	3,883	0,661	-0,01388
H*β	1,134	0,559	0	0	1,154	0,44	0

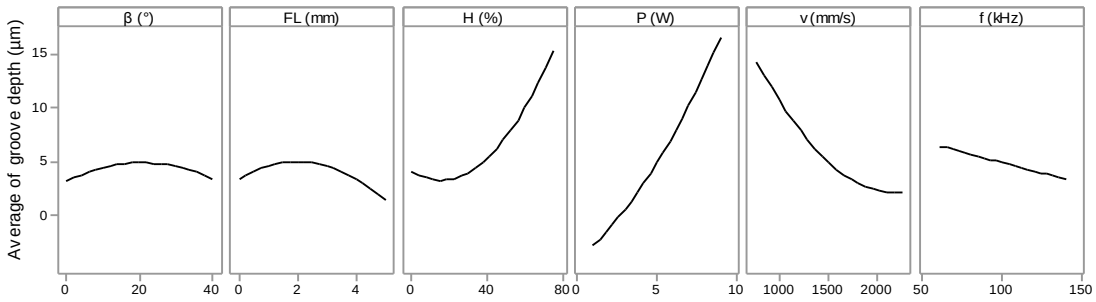

Figure 8.3: The influence of the adopted parameters on groove depth according to the RSM results.

The second objective of the RSM modeling, which is the interaction between the process parameters, is shown in figure 8.4. These interactions also represent the constants in equation 8.8 (b_{12} to b_{56}). It can be seen from figure 8.4 that there is no interaction between FL and H %, FL and f, β and v, and β and f, while there is an interaction between laser power with all parameters, v with f, P, H, and FL, and the angle of incidence also interacts with P, H % and FL. All these terms will contribute to construct the final form of the proposed model or empirical equation. The parameters that interact with each other are added to the final model. Those, which are not interacted, are eliminated from the final model, as presented in Table 8.1, which shows the final equation for the responses. As a conclusion, the final model of groove depth can be represented by empirical equation 8.9 with average errors of 2.66%.

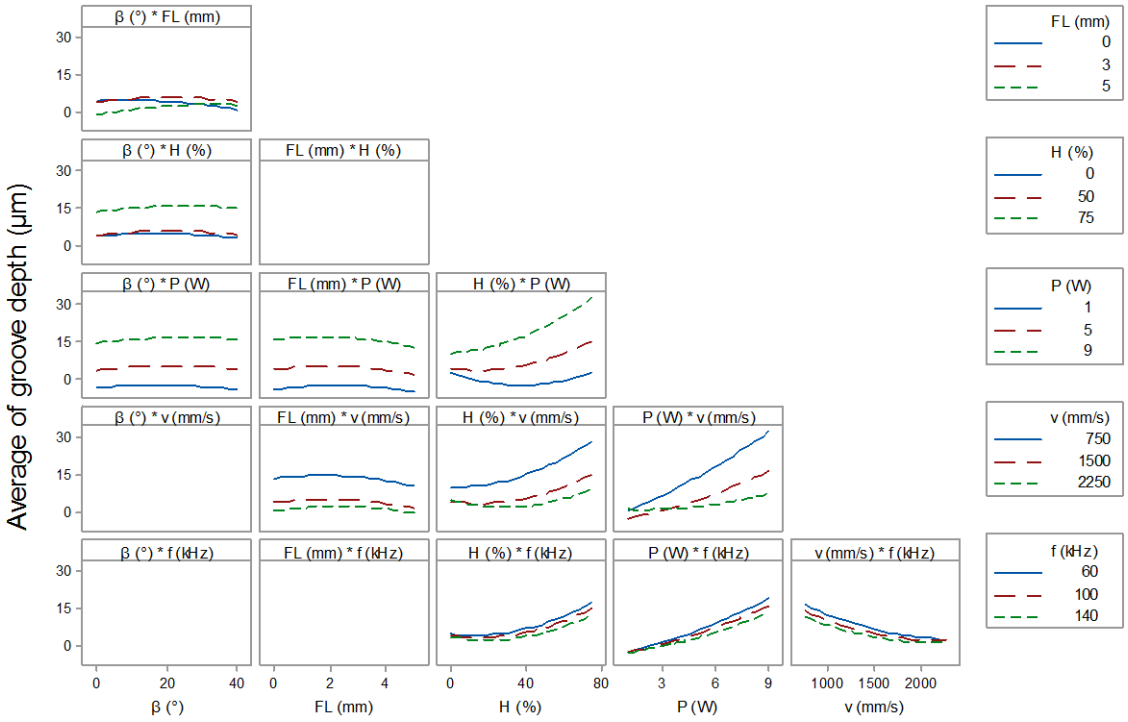

Figure 8.4: The interaction between the process parameters and its effect on groove depth.

$$\begin{aligned}\text{Groove Depth} = {} & 4{,}98 + 9{,}632\text{P} - 6{,}093\text{v} - 1{,}53\text{f} - 0{,}996\text{FL} + 5{,}574\text{H} + 0{,}138\beta + \\ & 1{,}941\text{P}^2 + 3{,}331\text{v}^2 - 2{,}469\text{FL}^2 + 4{,}74\text{H}^2 - 1{,}58\beta^2 - 6{,}451\text{P} * \text{v} + \\ & -1{,}39\text{P} * \text{f} - 0{,}536\text{P} * \text{FL} + 5{,}505\text{P} * \text{H} + 0{,}627\text{P} * \beta + 0{,}969\text{v} * \text{f} + \\ & 0{,}528\text{v} * \text{FL} - 3{,}467\text{v} * \text{H} - 0{,}898\text{f} * \text{H} + 1{,}906FL * \beta + 0{,}559H * \beta\end{aligned} \quad 7.9$$

Track or Conductor Width

The effect of the input parameters on the average of the conductor width according to the results of the model analysis is demonstrated in figure 8.5 and figure 8.6. Figure 8.5 shows that the importance sequence is: P, v, f, β, FL and H %. Furthermore, from this figure it is clear that the laser power and the hatching have a positive influence, whereas the laser velocity, the frequency, and the incidence angle have a negative effect. The focal length does not have a high effect on the average of this width, but according to the Table 8.1 the effect of linear term FL is about -2.123, it means the effect is negative, whereas the constant FL*FL is 6.79, has a positive effect. Therefore, the overall effect of focal length can be regarded as positive, which is in agreement with the previous experimental analysis in chapter 6.

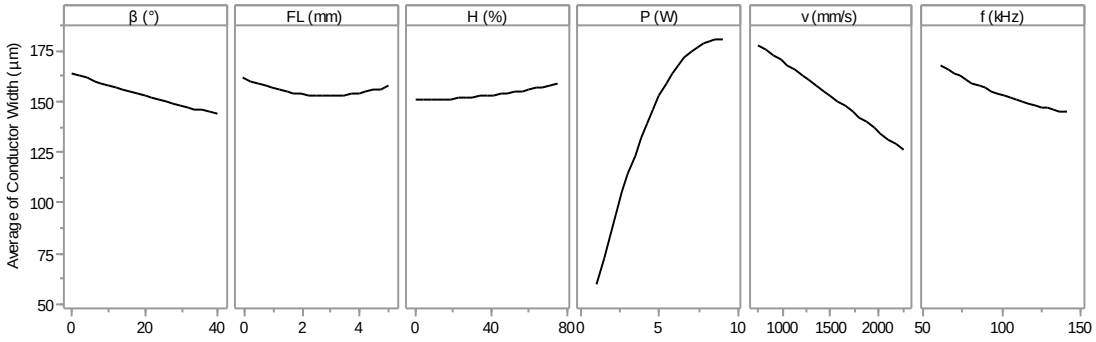

Figure 8.5: the influence of parameters on the conductor width.

Figure 8.6 shows the interaction between input factors, where it can be seen that all parameters have an interaction with each other. The final equation for this response and the other responses are presented in Table 8.1, so, there is no need to re-write the final form for this equation.

Groove Edge Dimensions

The dimensions of groove edge, which include height and width, are very important especially for the quality of micro MID products. The influence of adopted parameters has been explored in chapter 6, by an experimental investigation. This part, modeling results, provides more details about the effect, interaction and the importance of these parameters on the groove edge dimensions. This is presented in Figure 8.7. Figure 8.7(a) illustrates this influence on the lap height.

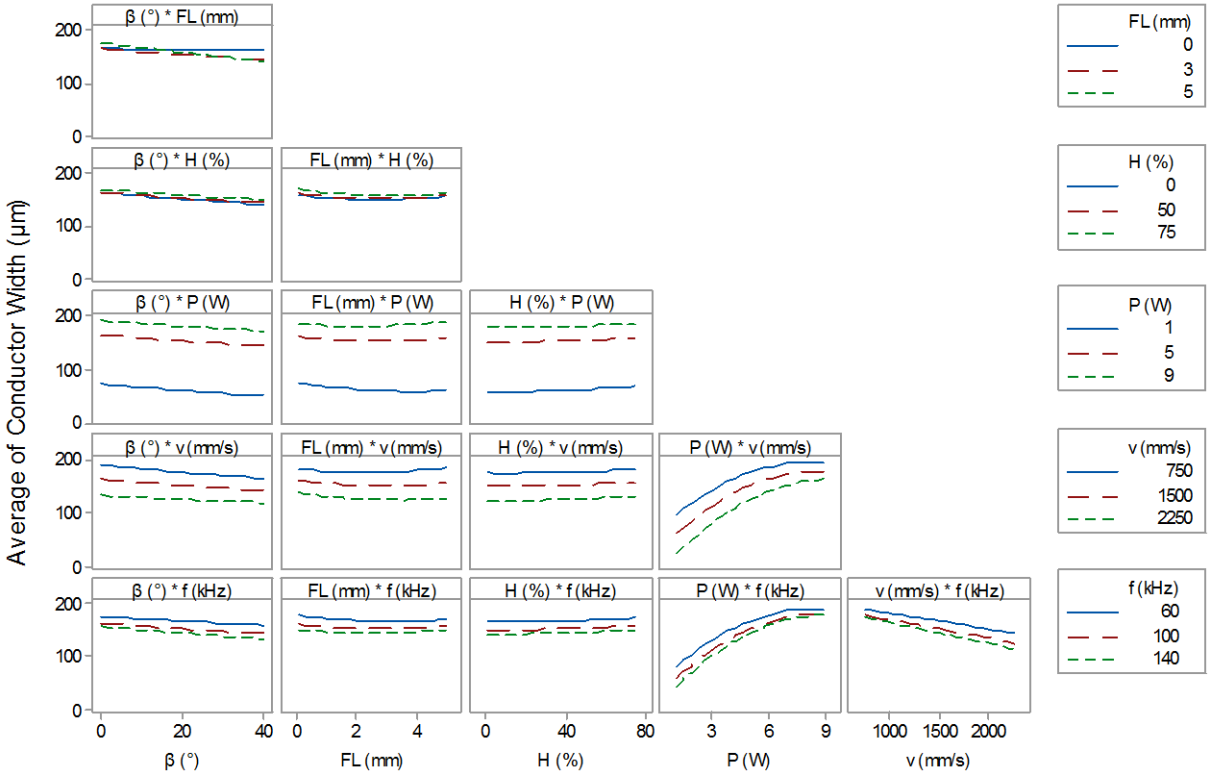

Figure 8.6: The interaction between the process parameters and its effect on conductor width.

It is clear to view that the order of importance for the input factors is: P, v, β, f, H %, and FL. In addition, the laser power, the frequency, and the hatching have a positive impact on the lap height, whereas the laser velocity, the angle of incidence, and the focal length have a negative effect. Figure 8.7(b) shows the impact of inputs factors on the lap width. It can be concluded that the laser power is the most important influence on this width, then followed by the incident angle and focal length, whereas the velocity, frequency, and hatching have almost the same importance. In addition, the laser power, frequency, hatching and focal length have positive impact contrast to laser velocity and incidence angle, which have a negative effect on this width. The interaction between the input factors and their effect on the groove edge dimensions, according to the RSM model, is shown in figure 8.8, where figures 8.8(a) and 8.8(b) show the lap height and lap width. From this figure, one can also see for the models of height and width, that there is no effect for the interaction between: β*H, FL*H, FL*f, and H*f. Furthermore, the interaction between v and f is not included in the final model of the lap height, whereas, the model of lap width excludes additional terms including FL*v, H*v, and β*f from the empirical equation of this model, which is presented in Table 8.1.

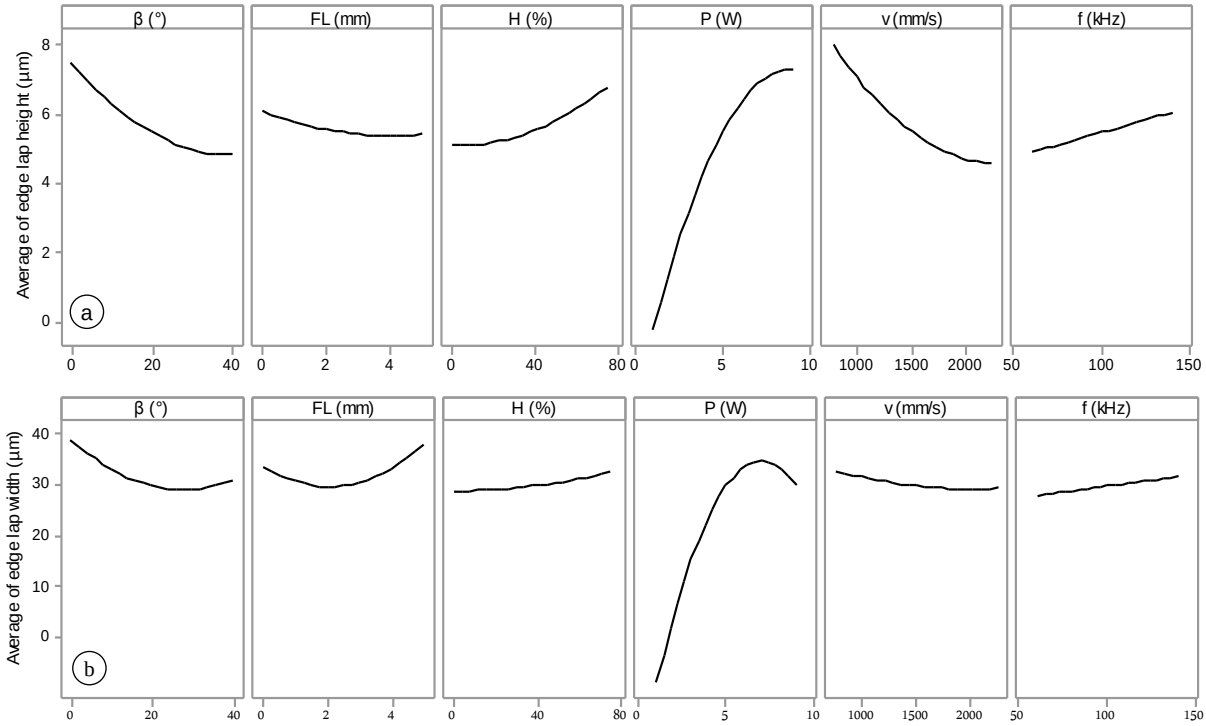

Figure 8.7: The influence of parameters on lap edge (a) height. (b) Width.

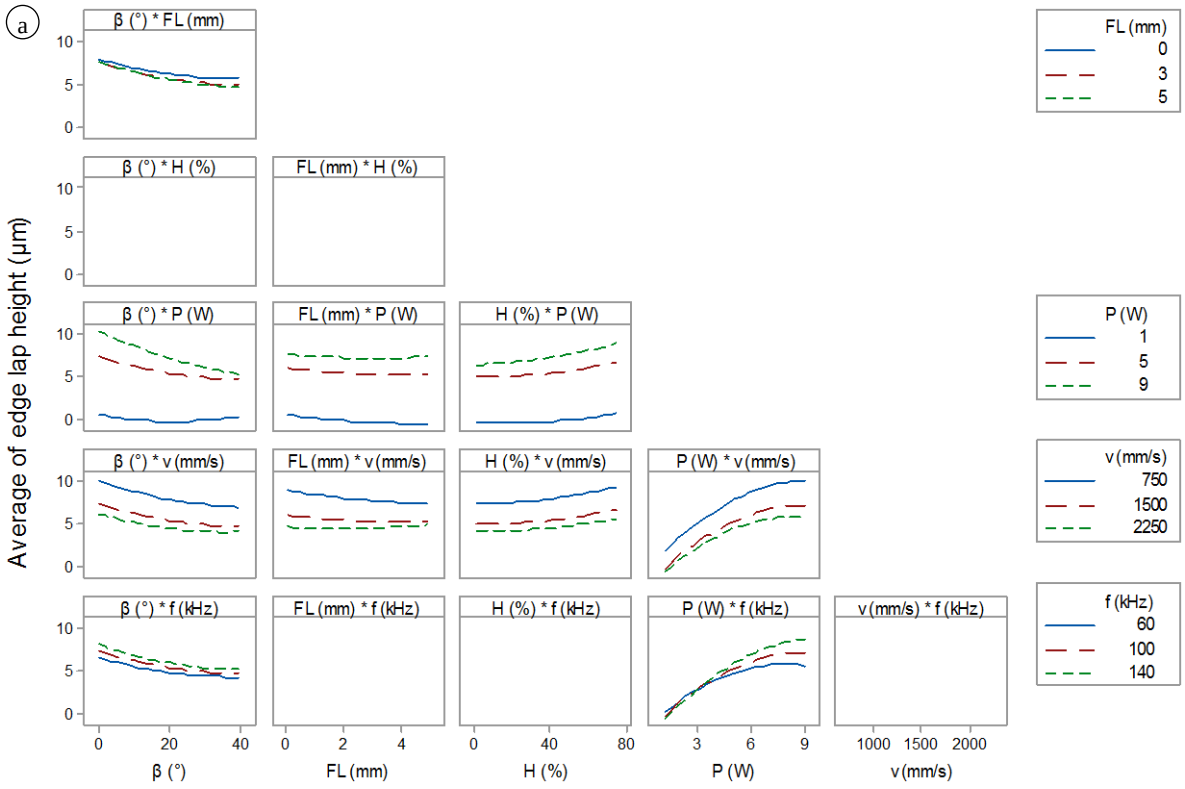

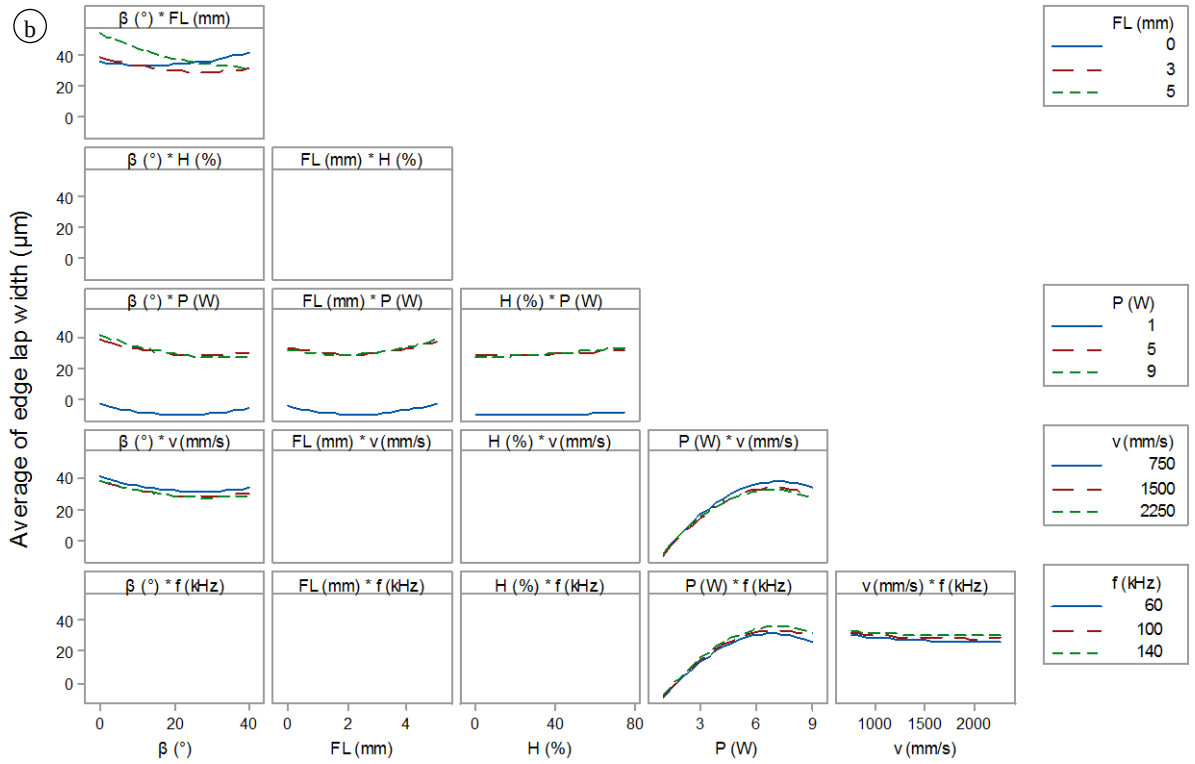

Figure 8.8: The interaction between process parameters and its effect on edge (a) Height. (b) Width.

Further details on the other responses involving surface roughness, structuring percentage, and thickness of the metallization are not included in this section in order to avoid repetition. But the model descriptions and analysis of these responses are summarized in Table 8.1.

According to Table 8.1, the surface roughness, which is denoted by Rz, is influenced by all the adopted input factors, and the importance sequence of these factors is: P, v, H%, f, β, and FL. The average Rz is reduced with the laser velocity, the frequency, the focal length, and the incidence angle whereas it is increased by the laser power and the hatching. Furthermore, all input factors interact with each other except the interaction between v*FL, FL*H% and f*β which does not exist, the corresponding constants are listed in Table 8.1. The correlation between input factors and coating thickness was analyzed by the use of RSM modeling. The results show that this thickness is affected by almost all input factors. The importance sequence starts from: the laser power, the frequency, the hatching, the incidence angle, the focal length and the laser velocity. According to Table 8.1, the coating thickness increases with the laser power and the hatching, and is reduced with the velocity, the frequency, the focal length, and the incidence angle. An interaction between the input factor does not exist between P*f, v*FL, v*H%, v*β, f*FL and FL*H %. It was also found that the structuring percentage, which is very important for the LDS quality, is affected by all the input parameters, and the importance sequence for these

parameters is: the laser power, the hatching, the velocity, the frequency and the focal length. These parameters have the same effect as observed on the metallization thickness. Additionally, the laser power interacts with all other parameters, and the interaction between v*H% and FL*β is also existent.

8.4.2 Results of ANN model

The same experimental results, which are used as a database for the RSM, are also used for training the ANN models. It was found that the best ANN structures were obtained with one hidden layer. Moreover, the number of neurons in the hidden layer that has reached best predictions of responses is varied depending on these responses. The developed ANN models were used to find the final equations for each process response using equations 7.1 to 7.4, as well as to find the importance of each process parameter. Table 8.2 shows the importance of LDS parameters for each process response as well as the best ANN architecture of the developed models. The above table also shows the importance of all factors that have been analyzed by the RSM models. They show good agreements compared to RSM results. In addition, the ANN approach provides good prediction results for the structuring and ablation types compared to other approaches, especially when a broad database is available for training the ANN model. The ANN results indicate that the structuring type is affected by: First the laser power, second the hatching and then the frequency. While the laser velocity and the incidence angle, have the same effect. The focal length has minimum effect on the structuring type. The same importance sequence for the laser power, the hatching and the frequency can be determined in predictive results of the ablation type. The effect of the other parameters is shown in Table 8.2.

Table 8. 2: The importance of the LDS parameters and the ANN architecture.

Responses / Factors	Cond. Width	Groove Depth	Edge Height	Edge Width	Rz	Metal. Thickn	Structu. %	Str. Type	Ablat. Type
Incidence Angle	0.086	0.023	0.157	0.186	0.043	0.098	0.065	0.092	0.085
Focal Length	0.042	0.029	0.076	0.194	0.032	0.085	0.037	0.082	0.098
Hatching	0.028	0.222	0.085	0.041	0.083	0.109	0.167	0.246	0.179
Power	0.524	0.395	0.406	0.491	0.554	0.523	0.531	0.372	0.413
Velocity	0.226	0.266	0.176	0.046	0.214	0.076	0.145	0.116	0.170
Frequency	0.093	0.064	0.101	0.042	0.073	0.110	0.054	0.092	0.056
ANN Architecture	6–3–1	6–8–1	6–5–1	6–8–1	6–3–1	6–6–1	6–5–1	6–6–1	6–7–1

8.5 Verifications and Comparison of ANN and RSM Models

In order to verify the results of RSM and ANN model, the predicted results should be compared to the experimental data to calculate the errors generated or the accuracy of model predictions. On one hand, the comparisons were made between RSM, ANN and the experimental results for all the responses, has been implemented for this purpose. On the other hand, the Mean Absolute Percentage Error (MAPE) has been used as comparison criterion in order to quantify the difference between values produced by models and the experimental data [117][118].

Figure 8.9(a) illustrates the comparison between RSM and ANN compared to the groove depth test. In order to show a clear comparison between models results and experimental results, the results of 61 tests will only be shown in this figures. This helps to distinguish between the theoretical model results and experimental results. The predicted errors of ANN and RSM are presented in figure 8.9(b). And it is clear that the errors of ANN are less than RSM.

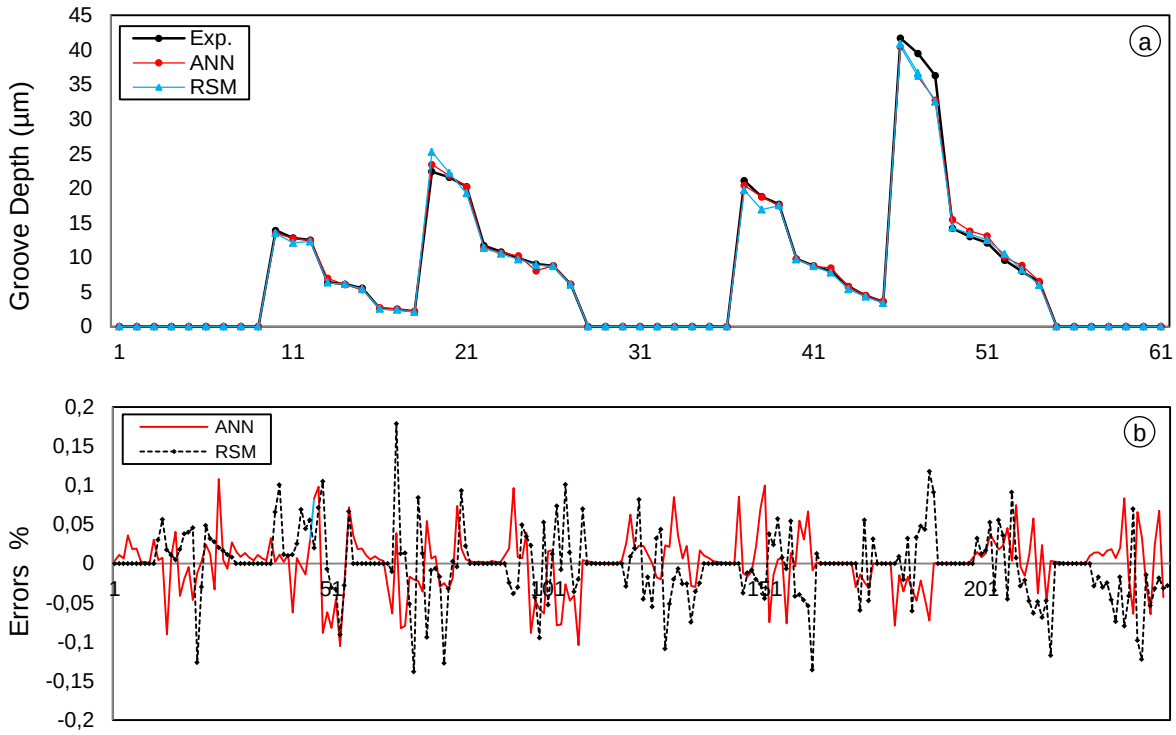

Figure 8.9: Comparison between. (a). Results of 61 tests including experimental data of groove depth, ANN and RSM. (b). % errors of 243 tests.

Figure 8.10 to 8.15 shows the comparison of results obtained by ANN and RSM models with the experimental tests. It is observed that the predicted values by RSM and ANN models are consistent with the measured values of all responses comprising conductor width, edge lap height, edge lap width, the surface roughness Rz, structuring percentage and metallization thickness.

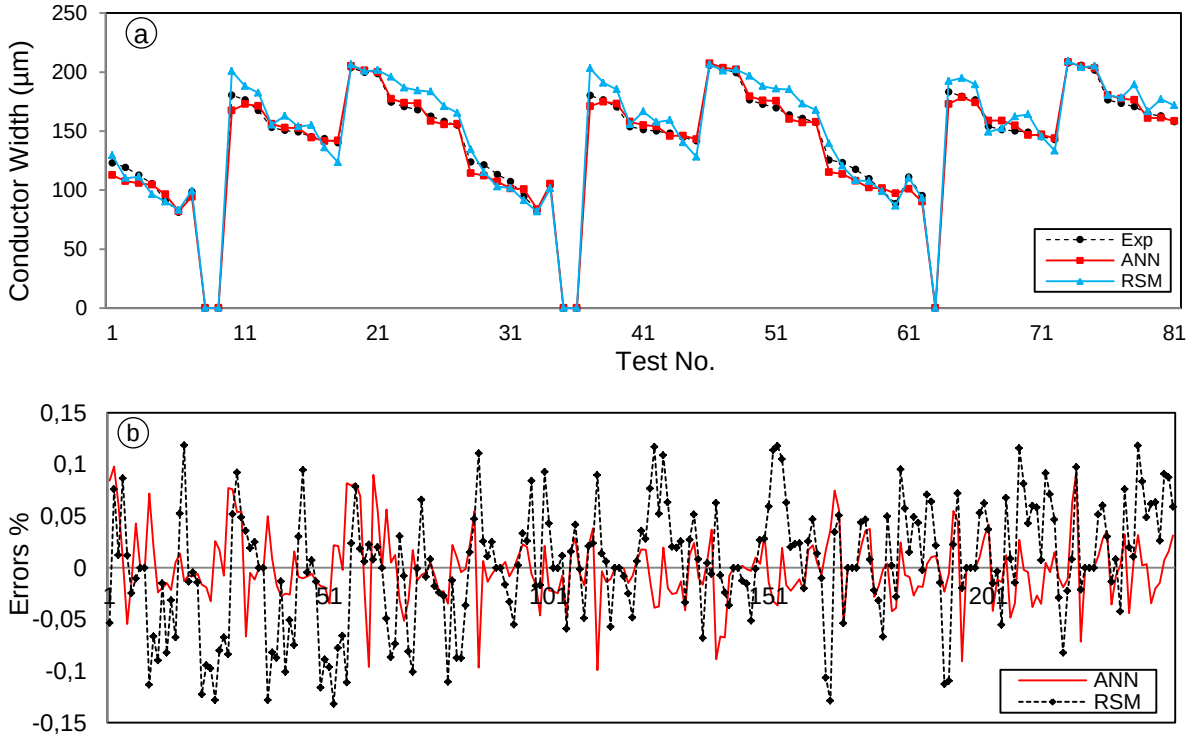

Figure 8.10: Comparison between. (a). Results of 81 tests including experimental data of conductor width, ANN and RSM. (b). % errors for 243 tests.

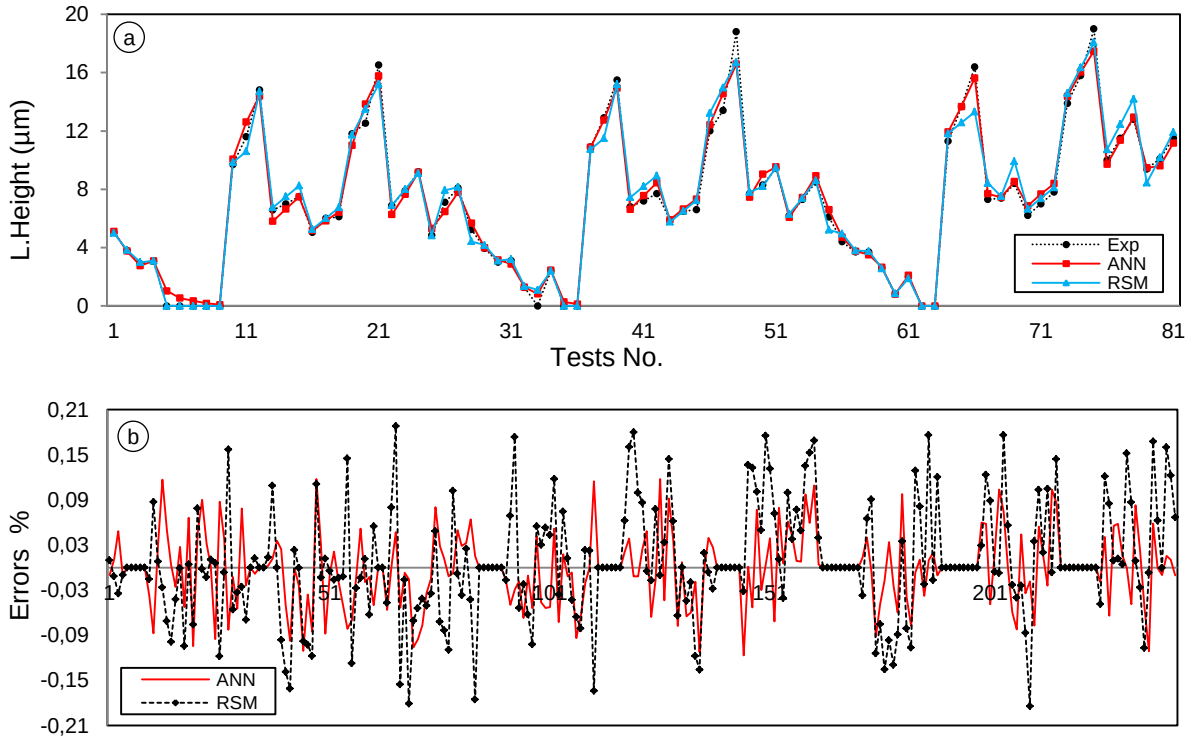

Figure 8.11: Comparison between. (a). Results of 81 tests including experimental data of lap height, ANN and RSM. (b). % errors for 243 tests.

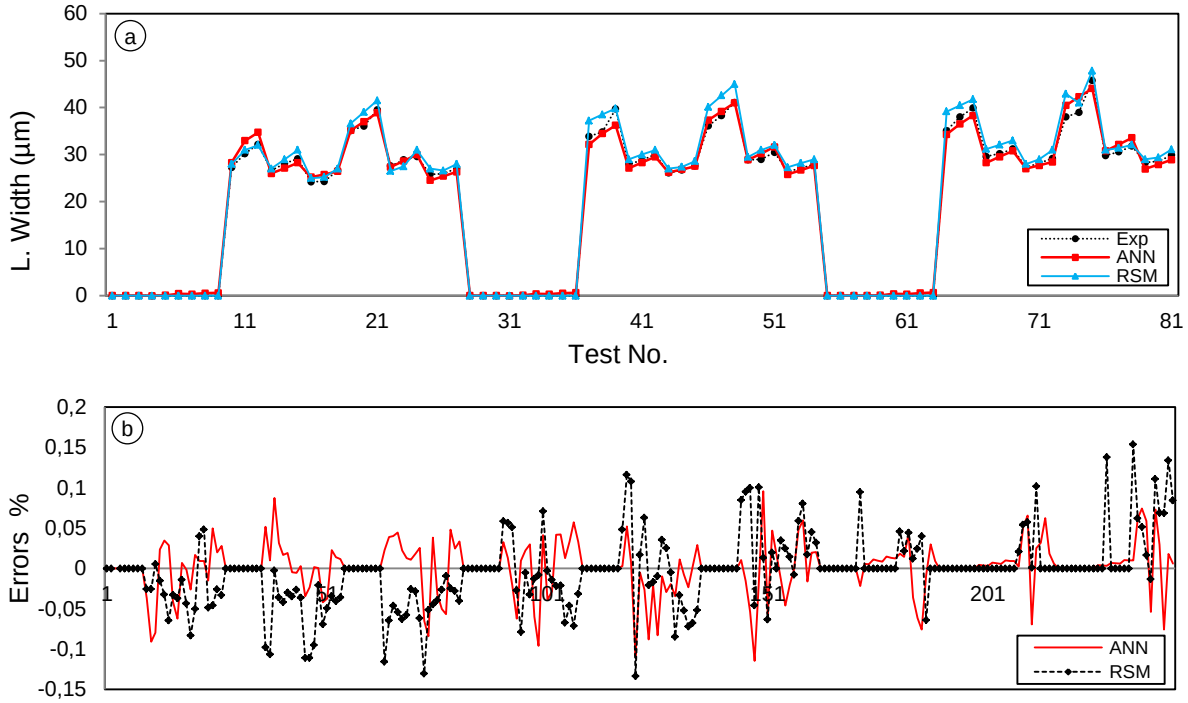

Figure 8.12: Comparison between. (a). Results of 81 tests including experimental data of lap width, ANN and RSM. (b). % errors for 243 tests.

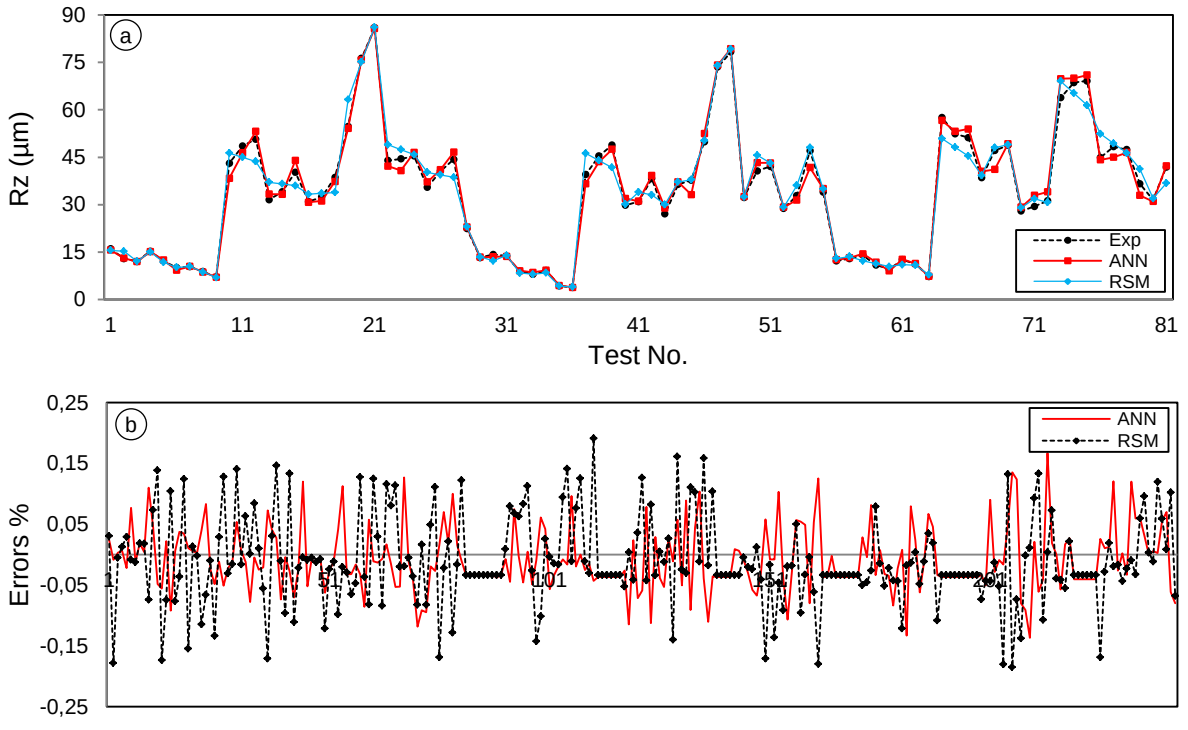

Figure 8.13: Comparison between. (a). Results of 81 tests including experimental data of Rz, ANN and RSM. (b). % errors for 243 tests.

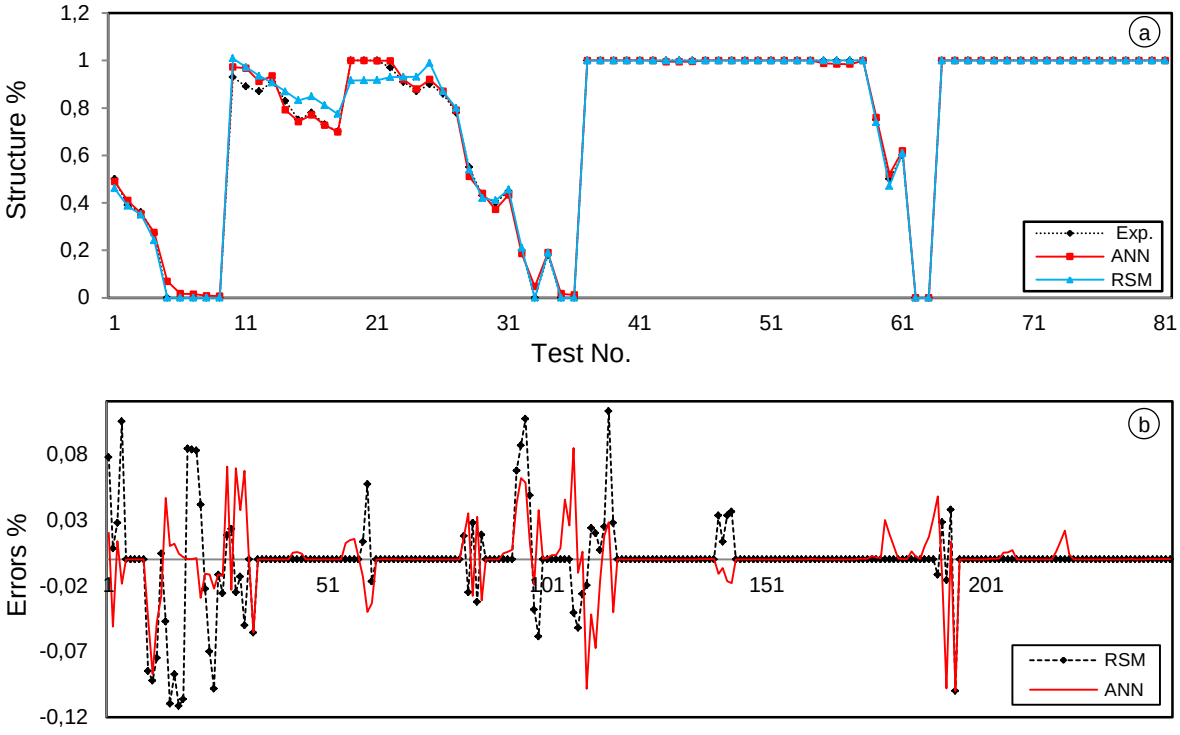

Figure 8.14: Comparison between. (a). Results of 81 tests including experimental data of Structuring percentage, ANN and RSM. (b). % errors for 243 tests.

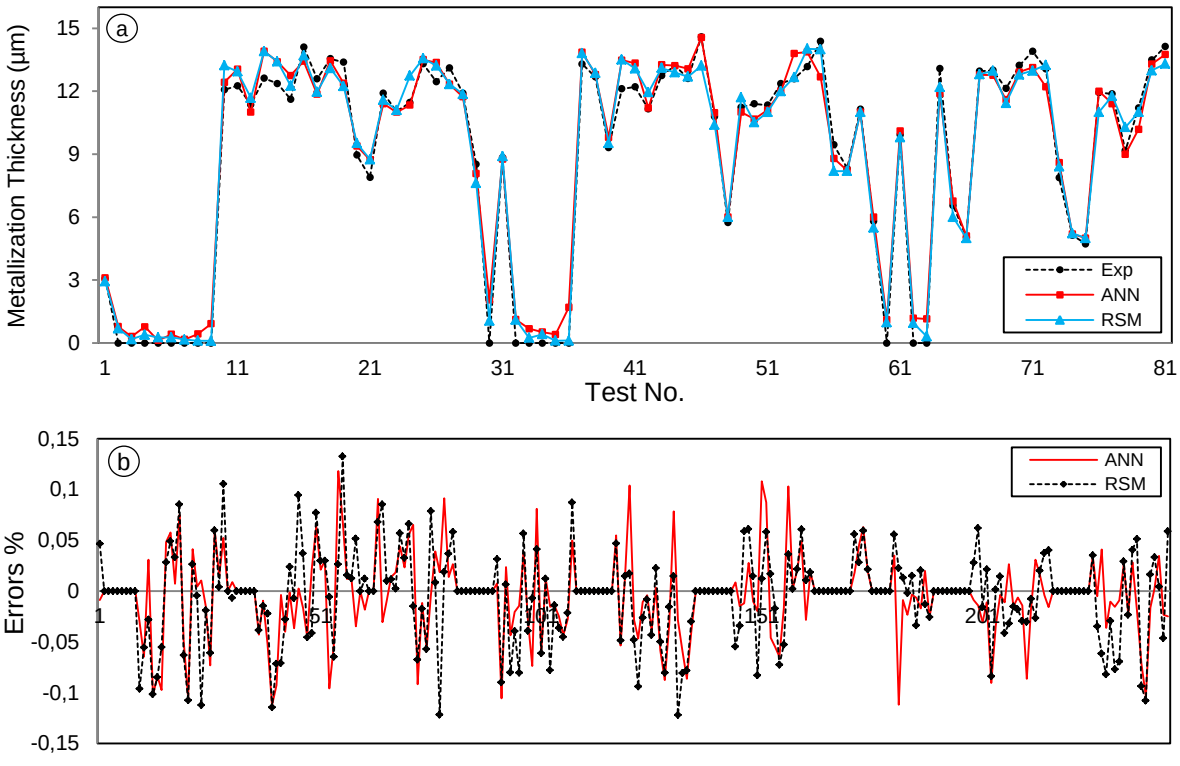

Figure 8.15: Comparison between. (a). results of 81 tests include experimental data of Metallization thickness, ANN and RSM. (b). % errors for 243 tests.

Also the mean absolute percentage error (MAPE) was recorded for the above responses. The errors of the ANN models were less than that of the RSM models. Moreover, the prediction of the RSM model shows a maximum (MAPE) value of 5.942% for the Rz model, while the minimum was 1.027% for the structuring percentage model. On the other hand, the maximum recorded (MAPE) of ANN was 4.376% for the Rz model and the minimum was also for the structuring percentage model which is 0.927%. Table 8.3 shows the mean absolute percentage errors (MAPE) of the predicted response of both RSM and ANN models. From this table, it can be concluded that both models are accurate, but the ANN model predicts the process more accurately than the RSM model, based on the minimum and maximum values in Table 8.3.

Table 8.3: Comparison between the mean absolute percentage error of RSM and ANN models.

Approaches \ Responses	Cond. width	Groove Depth	Edge Heigth	Edge Width	Rz	Metal. Thickn	Struct. %
% MAPE of ANN	2.112	2.631	3.686	2.187	4.376	2.903	0.927
% MAPE of RSM	4.061	2.666	5.197	3.186	5.942	3.229	1.027

8.6 Modeling and Analysis of Metallization Quality Based on LDS Responses

In previous chapters, the metallization quality was defined as a combination of characteristics including thickness, surface roughness, and adhesion of the metallization structure. This quality deeply describes on the basis of adopted LDS input parameters, whereas the LDS responses considers as an explanation for the different behavior of the examined quality. However, the LDS responses are extremely important to consider their impact on the above-mentioned metallization responses. Thus, this part will be dedicated to analyze and determination of the direct relationship between the metallization responses and the LDS responses including dimensions of the laser groove, edge factor, surface roughness, and structuring-ablation type as follows.

8.6.1. Thickness of Metallization

The total thickness of the metallization layers including (Cu-Ni-Au) realizes as a basis for the metallization quality. A metallization structure with typical thickness should be provided [1][16]. It is related to the LDS responses, but what is the importance sequence of the LDS responses in this respect? Or, which responses are the most significant. Models based on the RSM and ANN approaches are used as an important tool for this purpose. Figure 8.16 shows the impact of the structuring-

ablation type on the metallization thickness. They refer to the most important LDS responses to the thickness of metallization. According to the analysis results, the structuring-ablation type has direct influence on the thickness of the metallization layers. It is clear to see from figure 8.16 that the ablation type PA is not preferable when compared with other ablation types, including MA and RA. They produce a higher metallization thickness. But the difference between them is not too much. The structuring type also has an important effect on the metallization thickness but it is smaller than the ablation type. Anyway, the structuring type MS is eligible to support the metallization thickness, RS is the second and then LS. In general, the influence of structuring-ablation type on metallization thickness assists its effect on the surface roughness of the metallization.

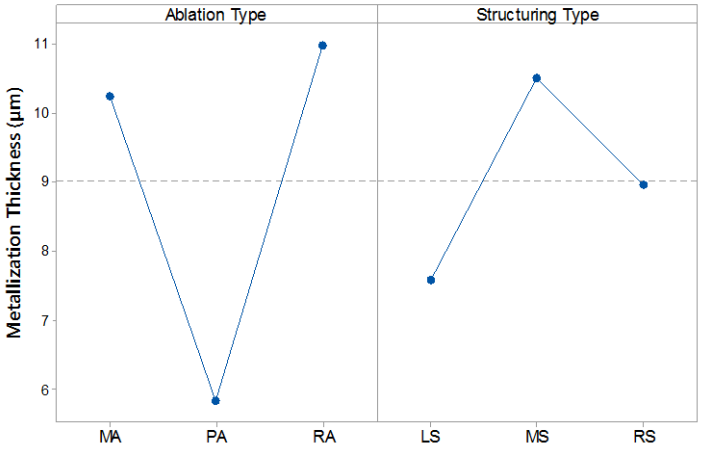

Fgire 8 16: The influence of structuring-ablation type on the metallization thickness.

Table 8.4 shows the importance for the LDS responses, namely groove depth, edge dimensions (width and height), structuring-ablation type, and surface roughness on the metallization thickness. These results are based on the ANN tool, which shows a good agreement with the experimental measurements of the metallization thickness, with an average error of 3.24%, (see figure 8.17).

Table 8.4: The importance of LDS responses for the metallization thickness

LDS Responses	Importance
Surface roughness (Rz)	0.271+
Lap height	0.225-
Ablation type	0.189
Lap width	0.114-
Structuring type	0.103
Groove depth	0.099+

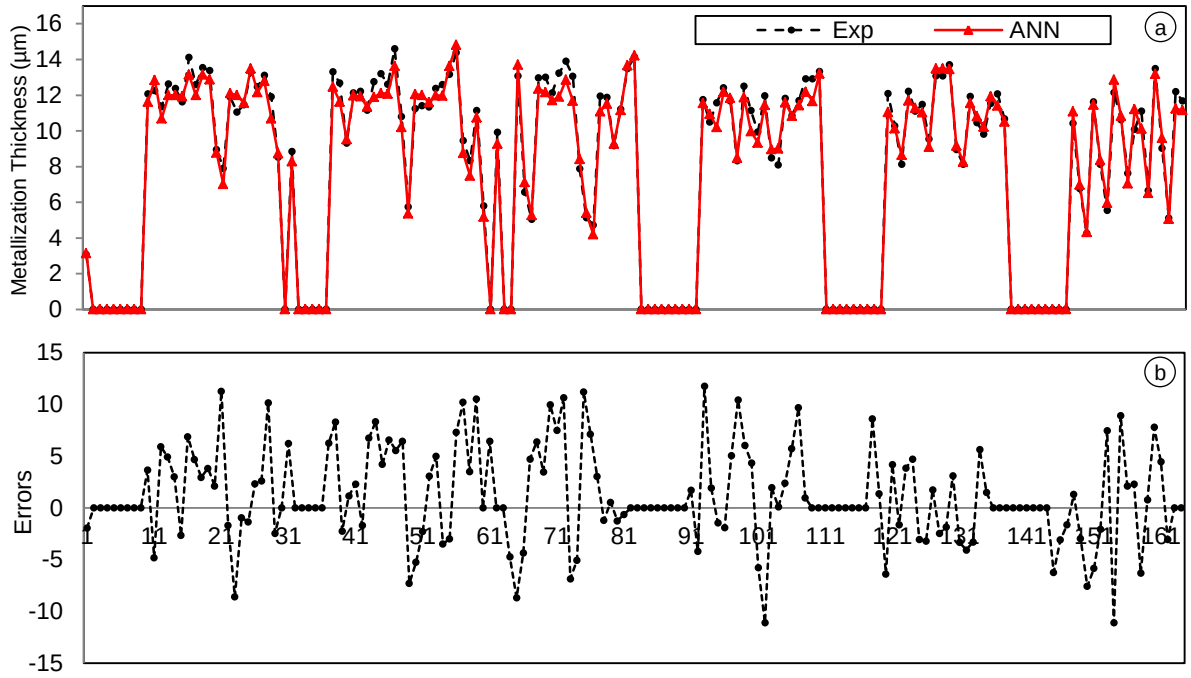

Figure 8. 17: (a) Comparison between the results of experimental data of the metallization thickness with ANN. (b). The predicted errors of ANN.

8.6.2. Surface Roughness of Metallization

The roughness of the metallization structure was defined as one of the most important characteristics of the metallized surface. A smooth metallized surface is preferable for the next assembly step [1] [16]. It is found that the variations in roughness after metallization step are related to the characteristics of the structured area, which is related to parameter setting. In this part, the surface roughness of the metallization structure is analyzed and modeled using the LDS responses.

Figure 8.18 shows the influence of structuring-ablation type on this roughness. One can be seen that the structuring type of MS is preferable to produce a smooth metallization surface, while LS has a bad effect on this surface, and RS is in between. The ablation type also has a direct influence on metallization roughness. A smooth surface can be produced when the ablation type changes from RA to PA and then to MA. Again, it can be concluded that the structuring-ablation type of MS-MA better supports the metallization quality due to its desirable effect on the metallization roughness.

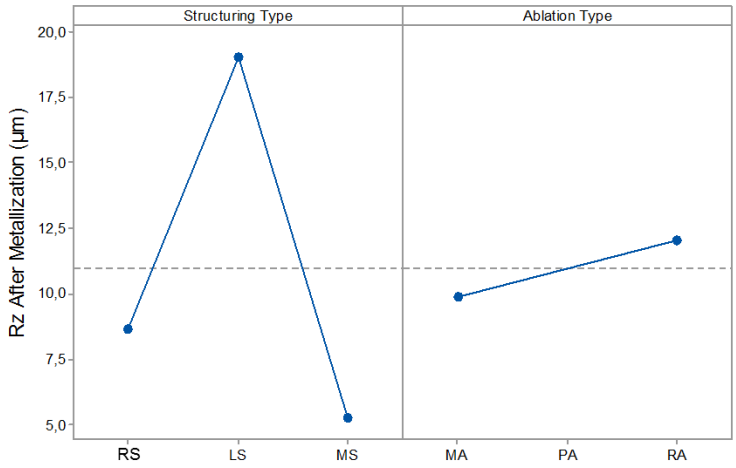

Figure 8.18: The influence of structuring-ablation type on Rz after metallization.

The buildup of the metallization layers during the metallization step relates to the activation process, which depends on the structuring-ablation type. MS means more uniform activation in comparison with LS. However, a uniformly activated region generates during RS under laser energy higher than MS, in particular if an average laser power use to produce such structuring type (RS). For the above reasons, MS and RS prefer to produce a thicker metallization surface. A smoother metallization surface can be produced using MS or RS in conjunction with a middle laser power. The ablation types related to the laser energy, which depends on the parameter setting. The increase in the laser energy leads to change the ablation type from PA to MA. Similar to the structuring type, the MA ablation gives a more uniform activated area in comparison with PA. Thus, MA is preferable to produce a uniformly activated area. By increasing the laser energy more than that, ablation type of RA could be produced. This type of ablation is also desirable but in a condition when it produces by a middle laser power. High laser power or laser energy may lead to excessive burning or combustion for the activated surface. Therefore, ablation type MA is suitable for producing a thick and a smooth metallization surface.

The influence of other LDS responses is listed in Table 8.5. It can be seen that the structuring type is the first important while the importance sequence of the other responses is Rz, LH, groove depth, ablation type, and lap width. These results are based on the ANN model, which shows a good agreement with the experimental data and the recorded errors show an average error of 6.48 %, see figure 8.19.

Table 8.5: The importance of LDS responses for the Rz after metallization

LDS Responses	Importance
Structuring type	0.239
Surface roughness (Rz)	0.212 +
Lap height	0.206 +
Groove depth	0.169 +
Ablation type	0.104
Lap width	0.071 +

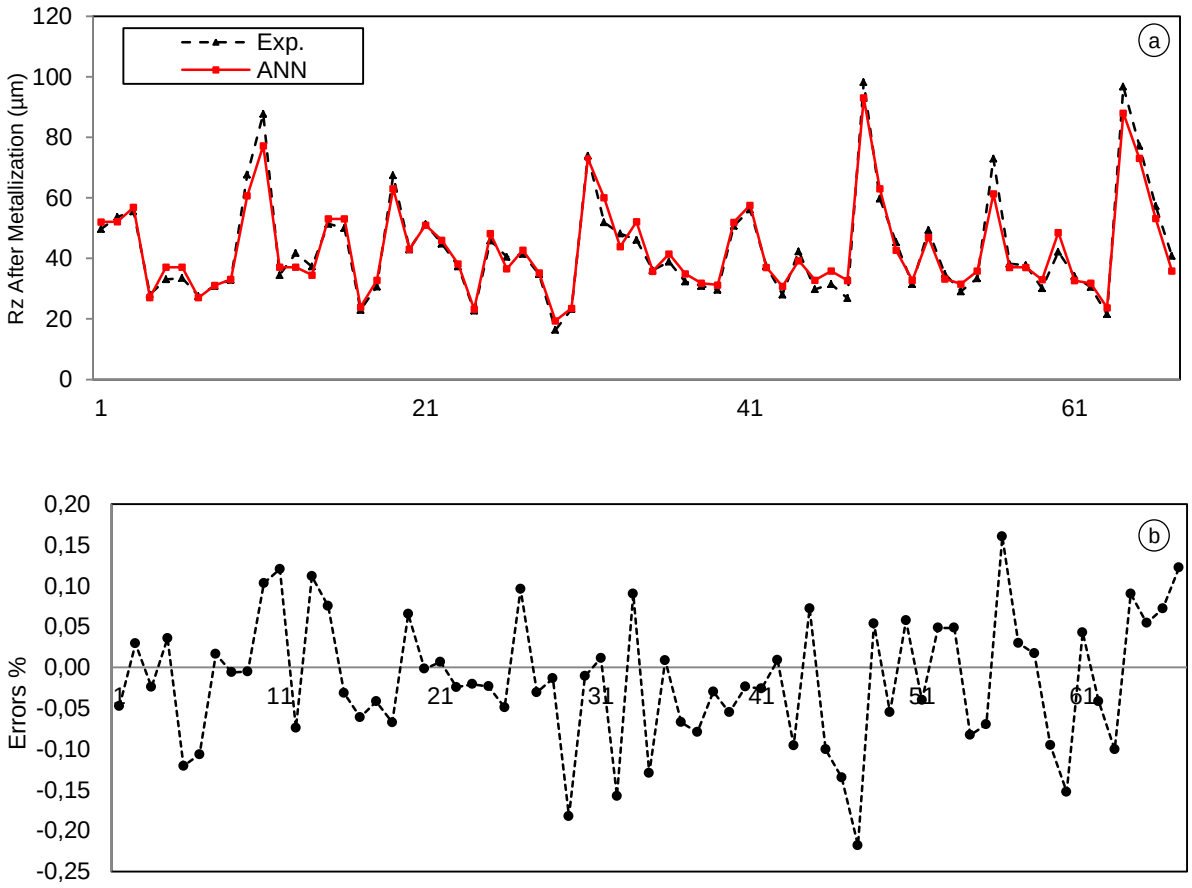

Figure 8.19: (a) Comparison between results of experimental data of Rz of metallization with ANN model. (b). The predicted % errors of ANN model.

8.6.3. Adhesions Strength of Metallization

The adhesion of the metallization structure can be explained based on two hypotheses. The first is related to the mechanical contact between the activated surface and the metallization layers, particularly the Cu layer. The second is based on the physical-chemical bond between the surface of activated area and the Cu layer. Both of these hypotheses refer to the characteristics of the structured area, in particular the activation quality or the structuring quality as well as the structuring-

ablation type. This part dedicates to explain the behavior of adhesion as a function of the LDS responses.

Figure 8.20 demonstrates the relationship between the structuring-ablation type and the corresponding effect on adhesion. From this figure, it can be seen that ablation type PA is undesirable to support the adhesion quality. As already mentioned, this type of ablation can be produced using low laser energy. Such activation energy is not appropriate for a uniformly activated area or it is not sufficient to give a steady interaction with all the additives. In other words, the laser energy is not sufficient to activate an adequate numbers of additives. In this case, the adhesion will be weak even when a rough surface produces. When the laser energy increases the created ablation type will be changed to MA or RA. Both MA and RA are desirable to support the adhesion quality as shown in figure 8.20. Again, it should be mentioned that MA and RA generate a regular activated structure. However, RA should not be accompanied with excessive laser energy, which leads to burning of the structured area. The relationship between the structuring type and adhesion is also shown in figure 8.20. It can be seen that the modification of structuring type from LS to MS and then to RS supports the adhesion quality. This is due to the reasons mentioned with present to the metallization thickness and surface roughness.

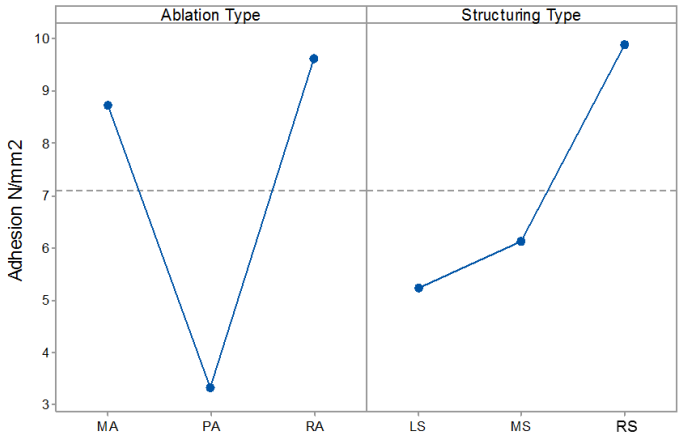

Figure 8.20: The influence of structuring-ablation type on the metallization adhesion.

The influence and importance of the other LDS responses describes in Table 8.6. It is clear to see that the LDS defects such as unstructured area (structuring percentage) with an importance of 26.9% are most significant. Any defect reduces the adhesion quality. The ablation type and then structuring type are the next important responses. The surface roughness has a positive importance of 12.2%. The other responses including groove depth, the height of edge lap, and width have an importance of 11.5%, 10.9%, and 8.1% respectively. The results of Table 8.6 are concluded using the ANN model. This model, when compared with experimental data

of adhesion shows a good agreement with an average error of 4.04 %, as shown in figure 8.21.

Table 8.6: The importance of the LDS Responses for the adhesion strength.

LDS Responses	Importance
LDS Defect %	0.269 -
Ablation type	0.177
Structuring type	0.127
Surface roughness (Rz)	0.122 +
Groove depth	0.115 +
Lap height	0.109 -
Lap width	0.081 -

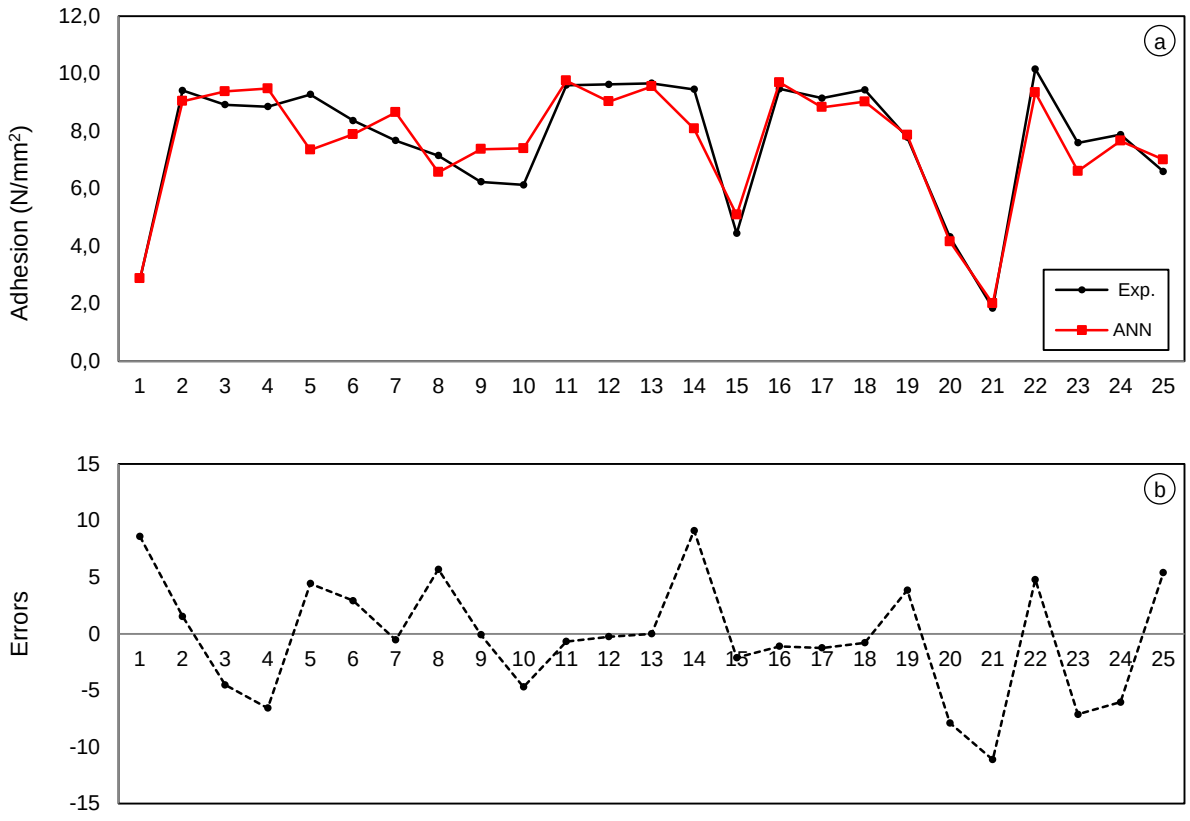

Figure 8.21: (a) Comparison between results of experimental data of metallization adhesion with ANN model. (b). The predicted errors of ANN model.

In order to describe the relationship between LDS responses and the behavior of adhesion strength, the mechanism of the adhesion failure should be explained. The adhesion strength depends on the characteristics of the area under the subjected load or stress. The failure in such tests begins at the weakest area or point. At this point, the stress will be concentrated till the strain reaches a maximum value. Thereafter, the crack starts at this point and the crack propagation moves very rapidly to enclose the entire area under the load. Thus, any defect on the surface of the activated area will act as the start point of failure. The stresses will attack and concentrate at this point and the failure starts under lower load or stress, as this structured area shows low adhesion strength. Therefore, the structuring defects such as unstructured area that is being investigated refer to a serious problem in the LDS quality. It results in low adhesion quality.

The edge factor also has an undesirable effect on the adhesion quality. The characteristics of the activated area at the edge lap are quite different than in the center. Therefore, the failure may be started at the edges which represent the weakest point, stress concentration point, and the crack point. As a conclusion, the edge dimensions (height and width) should be reduced as much as possible due to their bad impact on the adhesion quality.

8.7 Process Optimization

The optimization is an important tool to improve experiments. Its applications can be found in almost all areas of engineering and sciences, in the fields of process design, process control, model development and process identification. The desirable performance of any system or product can be achieved by a deep understanding of the influences of their factors. In such cases, systematic and efficient decision-making approaches that can be provided through optimization strategies [119][120]. This introduction provides the motivation for using the optimization tool in MID-LDS technology. In general, the optimization mission can be defined as the set of procedures with which one can suggest or find the best solution for any specific system or process over a finite set of discrete variables. In other words, the optimization task is an efficient key tool that can be employed as a decision maker to maximize, minimize or to find specific responses of a process, based on specific criteria. The optimization assignment requires three important elements, which are:

- An accurate and efficient model that describes the system and can be used to predict the system responses as a function of the system variables or input factors.
- System parameters or the model variables, which contribute to the creation of the model used. And it should be controllable.
- Criteria or objective functions for optimization, which can be considered as a guide for the optimization.

This part of the chapter provides an overall description for optimization in the MID-LDS technology based on multi-criteria [121] including accuracy, quality, and reliability of two different conductors.

8.7.1 Optimization of Conductor Width-Based on Accuracy

As described previously, the experimental work involves two conductor shapes comprising a circle area with a diameter of 1.5 mm and a line with a width of 0.16 mm. In addition, the accuracy of the produced conductor width is important especially for micro MID products. Therefore, in this part, the accuracy is the main objective that will be optimized in this part. The other characteristics such as the groove edges dimensions (height and width), structuring percentage, structuring type and the ablation type will be regarded as additional important criteria for this optimization task.

The optimization criteria that relate to the most important requirement in the process optimization have been defined. For the other requirements, the proposed model of the conductor width that constructed in the modeling part will be used as well as their adopted parameters including the incidence angle, focal length, hatching, laser power, laser velocity and laser frequency for this purpose. One may assume that a conductor width of 0.18 mm with an accuracy of 100 % is required. It can be manufactured using various process parameters of 2D and 3D applications. As an example, figure 8.22 shows a case study to propose the optimum process parameters including the hatching, the laser power, the velocity, and the frequency at fixed incidence angle and focal length (2D-applications). In this task, the optimization was presented on the basis of various criteria, the main determination being based on certain responses that are conductor width of 0.18 mm, the second is to minimize both the edge lap width and height, and the third based on the maximization of structuring percentage. According to these criteria, the proposed setting of process parameters that is predicted by the used model are a hatching of 70.7 %, a laser power of 9 W, a velocity of 1.769 m/s, and frequency of 140 kHz, as shown in figure 8.16. The predicted responses have a conductor width of 180 µm, a lap width of 43.15 µm, a lap height of 12.92 µm and structuring percentage of 94 %. This was one example of using the modeling for prediction of optimal parameters setting. However, Table 8.4 shows the various settings of the process parameters, which can be used to produce a conductor width with 100 % accuracy.

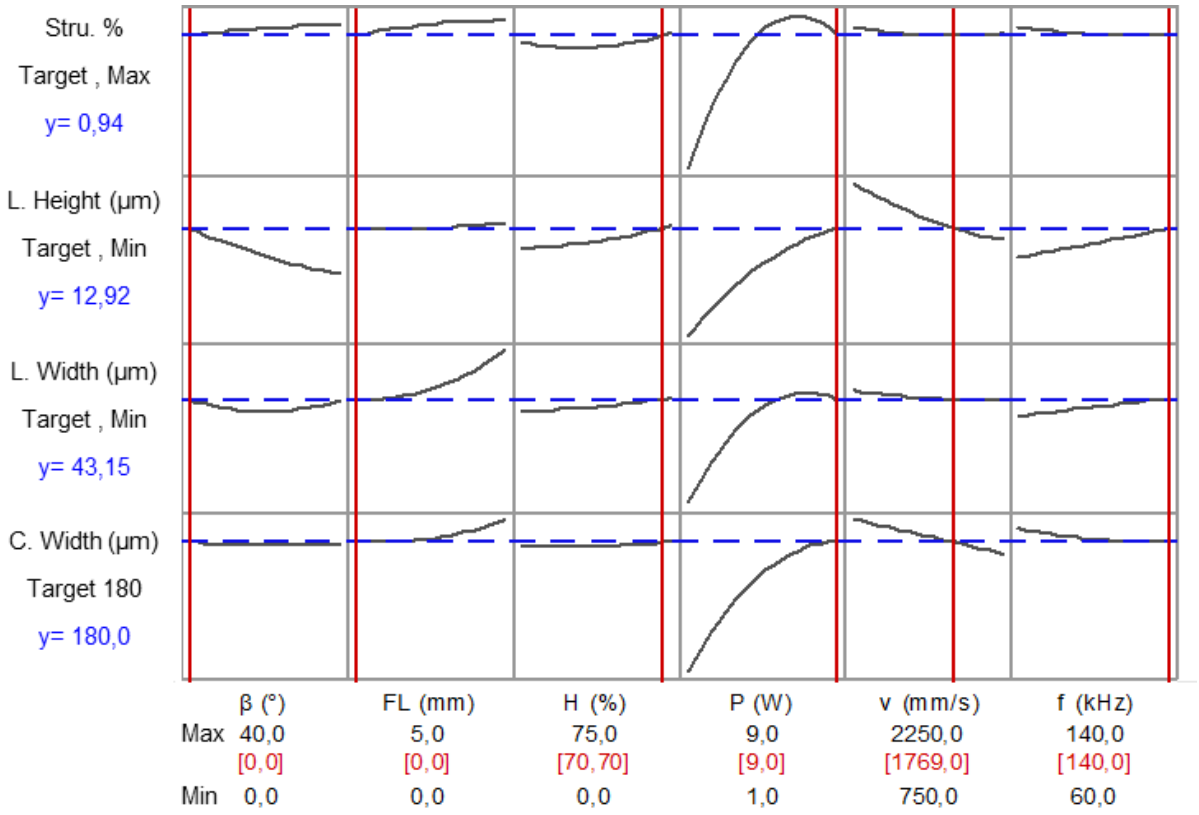

Figure 8.22: Conductor width optimization, a case study in accuracy optimization.

The setting numbers from 1 to 8 indicate the optimum parameters, which can be used for 2D by neglecting the impact of the incidence angle and focal length. It can be seen that all these parameter groups can be used to achieve 100 % accuracy. All these parameters are optimal if only the accuracy is considered as an optimization target. All of these settings provided a structuring of a 100 % except the numbers 1 and 8, which had a structuring percentage of 94 % and 93 % respectively. If the other criteria such as the dimensions of groove edge are considered, the optimum setting will be limited to the setting number 7 and then 5. Both these settings produce a structuring-ablation type of MS-RA, see Table 8.7.

The setting numbers from 9 to 15 summarize other suggestions for optimal parameters, but in these cases, the influence of focal length was taken into account by the installation at 4 mm. These selected examples show that all the suggested parameters are suitable to produce the desired accuracy of the conductor width. However, if other criteria such as the structuring percentage are considered, the setting number 9 should be eliminated from this list. On the other hand, if the edge dimensions are taken into account, then the setting number 15 and then 13 are the optimal parameter groups, based on their results regarding the edge dimensions, which indicate the minimum values. The effect of the incidence angle on the optimal parameterization is also investigated. It is listed in the setting from 16 to 20, in which

the incidence angle is installed at 30 °. By the same optimization procedures, one can conclude that the setting 20 and then 18 can be regarded as the optimal parameter groups. Moreover, both of these groups produce the ablation type RA, while the structuring type of group 18 is RS and for group 20 MS. It was found that the surface roughness after the metallization increases for the structuring-ablation type RS-RA at elevated laser power, whereas, the structuring-ablation type MS-RA, results in a reduction of roughness at each laser power. Therefore, group 20 is preferable to produce a metallization structure with a smooth surface. The setting numbers from 21 to 24 present the influence of both incidence angle and focal length on the expected optimum parameter setting. With the same optimization analysis, it can be concluded that the setting number 22 is the optimum parameter, which provides all the optimization criteria that have been discussed.

Table 8.7: The results of the conductor width optimization.

Setting No	Parameters						Responses					
	β (°)	FL (mm)	H (%)	P (W)	v (mm/s)	f (kHz)	C.W (µm)	L.H (µm)	L.W (µm)	Stru %	Stru. Type	Abla. Type
1	0	0	45,7	9,0	1769,0	140,0	180,0	12,9	43,1	0,94	RS	RA
2	0	0	75,0	7,4	1809,9	107,4	180,0	8,7	37,8	1,00	RS	RA
3	0	0	37,9	5,6	1446,4	85,3	180,0	12,7	42,7	1,00	MS	MA
4	0	0	67,5	9,0	1762,5	139,8	180,0	11,4	30,8	1,00	RS	RA
5	0	0	75,0	4,1	750,0	112,9	180,0	11,3	25,1	1,00	MS	RA
6	0	0	75,0	9,0	1983,0	104,3	180,0	10,3	28,7	1,00	RS	RA
7	0	0	75,0	2,9	750,0	60,0	180,0	9,9	20,4	1,00	MS	RA
8	0	0	0,0	9,0	2250,0	74,9	180,0	5,7	24,2	0,93	MS	MA
9	0	4	0,0	8,7	1874,8	140,0	180,0	10,3	45,1	0,94	MS	MA
10	0	4	70,3	8,9	2012,2	140,0	180,0	12,3	49,9	1,00	RS	RA
11	0	4	67,8	9,0	2018,8	140,0	180,0	12,0	51,3	1,00	RS	RA
12	0	4	75,0	5,6	1828,9	60,0	180,0	8,3	43,5	1,00	MS	RA
13	0	4	37,8	5,5	1450,6	82,9	180,0	7,8	42,7	1,00	MS	RA
14	0	4	75,0	7,0	1832,6	102,5	180,0	6,9	54,5	1,00	MS	RA
15	0	4	75,0	3,8	750,0	106,2	180,0	10,8	37,1	1,00	RS	RA
16	30	0	70,4	9,0	1680,9	140,0	180,0	8,9	47,1	1,00	RS	RA
17	30	0	0,0	9,0	1485,3	140,0	180,0	7,5	41,1	0,95	MS	MA
18	30	0	65,9	9,0	1668,6	140,0	180,0	8,7	38,7	1,00	RS	RA
19	30	0	75,0	4,6	750,0	110,0	180,0	9,5	40,2	1,00	MS	RA
20	30	0	75,0	3,3	750,0	60,0	180,0	19,0	28,8	1,00	MS	RA
21	30	4	75,0	9,0	1420,3	140,0	180,0	9,6	34,2	1,00	RS	RA
22	30	4	75,0	4,5	832,6	60,0	180,0	8,3	30,2	1,00	MS	RA
23	30	4	0,0	9,0	1148,0	115,5	181,4	7,7	29,3	0,99	LS	MA
24	30	4	70,5	9,0	1308,7	120,1	181,5	8,9	33,8	1,00	RS	RA

8.7.2 Optimization Based on Quality

The quality and reliability of MID products are influenced by various factors. In the previous chapter, it was found that the features of the structured area including the structure-ablation type, the surface roughness, and the structuring percentage, are extremely important for the characteristics of quality and reliability of the metallization structure or final MIDs structure. This quality and reliability include the adhesion strength, thickness of the metallization layers and the surface roughness of the metallized surface. These can be all considered as a basic criterion for the optimization of MID quality. Again, a predictive model that contains a set of adopted controllable parameters should be used. The proposed models used in the previous chapter to predict the properties of the structured area are used here for this purpose. One can assumed that a surface roughness of 30 µm, which provides suitable adhesion strength as observed in adhesion tests, should be produced. According to the model prediction results of Rz, it is possible to produce such responses (Rz of 30 µm) by employing various parameter settings as listed in Table 8.8.

Figure 8.23 shows the results of the proposed optimal setting parameters of group number 1 in Table 8.8. From this figure, it can be seen that the parameter setting, which includes an incidence angle, a focal length and a hatching of 0, a laser power of 4.2 W, a velocity of 2.25 m/s, and a frequency of 140 kHz could be used to produce this value of Rz. In addition, this parameterization produces a metallization thickness of 9.43 µm and a structuring of 61 %, whereas the structuring-ablation type RS-MA will be produced with these parameters. The analysis of these responses indicates that all the produced responses, such as Rz, the metallization thickness, and the structuring-ablation type, support the quality except the structuring percentage. It shows a low percentage value of 61 %. This may lead to metallization defects, as shown in figure 7.2 (picture 4), as well as it has a bad effect on the characteristics of metallization structure. Therefore, the final decision regarding this setting is a rejection of this parameter group.

It can be seen from Table 8.8 that the setting number from 1 to 11 shows the expected optimum parameters that can be used to produce Rz of 30 µm for 2D applications by installing the incidence angle and focal length at 0. Using the same analysis procedures as shown above, one can conclude that the set-up groups in 2, 4 and 9 should be eliminated from this optimal list, due to the same reasons as mentioned in setting number 1. The setting number of 6-8 and 11 provide a suitable combination of responses which include Rz, metallization thickness and 100 % structuring. However, they produce a structuring-ablation type of RS-RA, as shown in setting 7, 8 and 11 or type RS-MA as shown in setting 6. These setting groups may lead to increase the surface roughness of metallization structure, as discussed in the previous chapters. Therefore, they should also be removed from the optimum list. As

a conclusion, the optimal settings which support quality and reliability are 3 followed by 5 then 10.

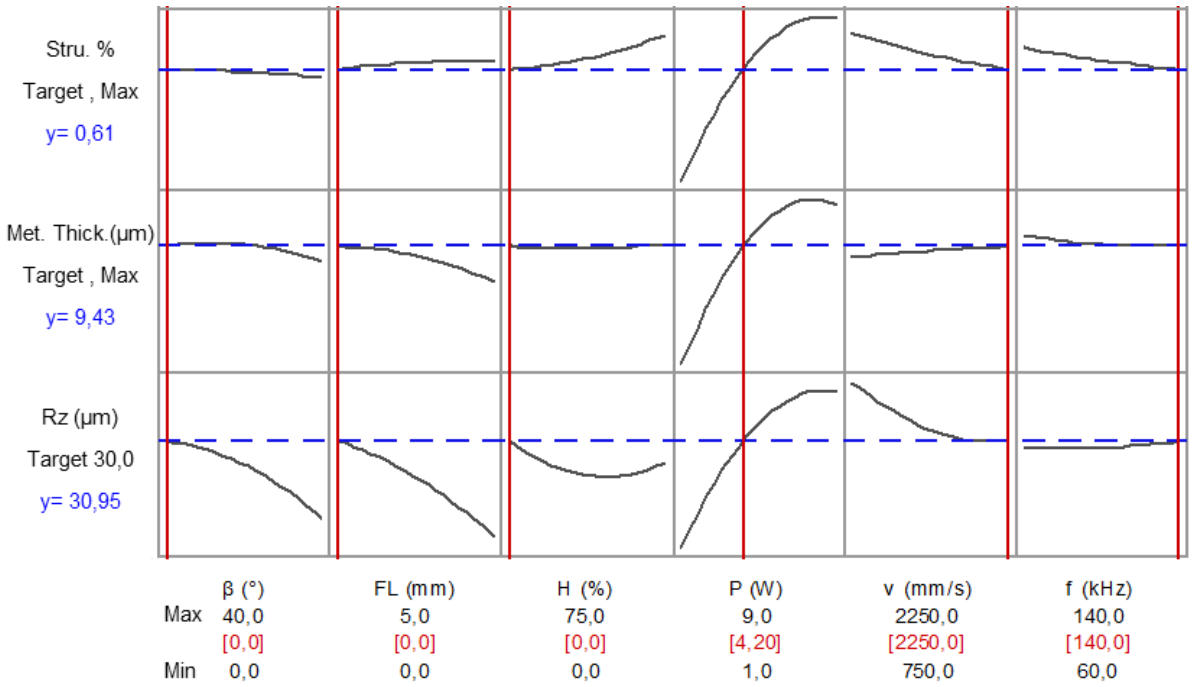

Figure 8.23: Surface roughness (Rz) optimization, a case study in quality and reliability optimization.

The settings from number 12 to 20 listed the influence of the focal length on the proposed optimal parameters. In this case, the focal length was installed at 4 mm. By using the same analysis, it can be summarized that the optimum parameter settings parameters are 20 followed by 14 then 12 and 17. They have almost the same results, except the metallization thickness, as shown in Table 8.8.

The settings from number 21 to 28 listed the proposed optimal parameters in consideration of the impact of the incidence angle, which is chosen to be 30 °. It can be concluded that the settings of 21, 22 and 26 should be eliminated from the optimal list because of their low structuring percentage. The settings 25, 27 and 28 are also eliminated due to the structuring-ablation type of RS-RA with elevated laser power. Consequently, the setting 24 and then 23 have a chance to be the optimal parameters. The setting from number 29 to 33 show the suggested optimal parameters in which the impacts of both incidence angle and focal length have been considered. The setting number 32 can be neglected due to the structuring-ablation type RS-MA in conjunction with high laser power as well as the setting 33 due to the low structuring percentage of 51 % and a metallization thickness of 7.15 µm. Therefore, the optimal settings are 31 then 30 and then 29.

Table 8.8: The results of the quality optimizations based on the Rz.

Setting No	Parameters						Responses				
	β (°)	FL (mm)	H (%)	P (W)	v (mm/s)	f (kHz)	Rz (µm)	Met.Thik (µm)	Stru %	Stru. Type	Abla. Type
1	0	0	0	4,2	2250,0	140,0	30,9	9,43	0,61	RS	M
2	0	0	0	2,7	750,0	60,0	30	5,97	0,62	RS	M
3	0	0	75	4,0	2250,0	60,0	30	13,49	1,00	MS	R
4	0	0	12	4,8	2250,0	140,0	30	12,41	0,89	RS	M
5	0	0	75	2,1	750,0	66,1	30	12,78	1,00	MS	R
6	0	0	33	5,6	2250,0	140,0	30	13,38	1,00	RS	M
7	0	0	41	5,7	2250,0	140,0	30	13,59	1,00	RS	R
8	0	0	53	5,6	2250,0	140,0	30	13,68	1,00	RS	R
9	0	0	16	5,1	2250,0	140,0	30	12,76	0,96	RS	M
10	0	0	38	5,0	1720,6	140,0	30	12,32	1,00	RS	R
11	0	0	49	5,2	1938,3	140,0	30	12,98	1,00	RS	R
12	0	4	38	5,0	1500,0	78,1	30	11,91	1,00	MS	R
13	0	4	0	3,3	750,0	71,0	30	8,94	0,97	LS	M
14	0	4	75	5,2	2236,7	74,1	30	12,51	1,00	MS	R
15	0	4	0	5,2	2250,0	60,0	30	13,71	0,91	MS	M
16	0	4	0	3,2	750,0	60,0	30	9,03	0,80	LS	M
17	0	4	59	6,6	1794,3	140,0	30	10,20	1,00	MS	R
18	0	4	10	6,7	1918,4	140,0	30	12,85	0,92	MS	M
19	0	4	75	2,6	750,0	60,0	30	6,56	1,00	RS	R
20	0	4	65	6,2	2211,7	99,5	30	13,21	1,00	MS	R
21	30	0	0	3,1	750,0	60,0	30	11,65	0,53	MS	M
22	30	0	42	6,9	2250,0	140,0	30	11,88	0,97	RS	M
23	30	0	75	2,1	750,0	60,0	30	11,26	1,00	MS	R
24	30	0	75	3,6	1608,4	70,0	30	13,93	1,00	RS	R
25	30	0	49	5,5	1726,9	140,0	30	12,14	1,00	RS	R
26	30	0	0	5,7	2250,0	60,0	30	11,44	0,93	MS	M
27	30	0	53	6,2	2016,1	140,0	30	12,39	1	RS	M
28	30	0	75	5,4	2250,0	135,0	30	13,02	1	RS	R
29	30	4	38	5,0	1500,0	133,8	30	13,24	1,00	RS	M
30	30	4	48	5,1	1667,1	129,1	30	13,43	1,00	MS	M
31	30	4	53	5,9	2044,6	140,0	30	14,08	1,00	MS	M
32	30	4	15	6,5	2250,0	140,0	30	15,04	1,00	RS	M
33	30	4	0	2,8	750,0	60,0	30	7,15	0,51	RS	M

9. Summary

MID-LDS technology involves multiple and overlapping steps. It includes complex and interconnected process parameters. The previous works deal with this process as a closed box including all the MID-LDS steps. They investigated the relationship between limited input parameters and the main output of MID processes, without any consideration for the interaction between the MID steps. In this work, the steps of MID-LDS processes are separated into main steps including LDS and metallization. This helps to examine these two important steps and their interaction, importance, and dependency. For the above reasons, a combination of theoretical and experimental works was utilized to investigate the MID-LDS process. They summarize as follow:

The first part of the theoretical work is the thermal simulation of 2D/3D LDS processes. It is based on a physical model that includes non-linear 3D transient heat conduction with a moving heat source. An important classification employed in this simulation includes laser fluence, laser dose, and the number of pulses or pulse overlapping. This is helpful to explain the interaction between the LDS parameters and their effect on the structured area. According to the simulation results and based on the above classification, the groove dimensions and the maximum temperature increase with laser fluence. Low laser fluence results in a discontinuous structured area with ablation type PA. So that the laser fluence used should be sufficient to prevent such formations. The regulation of the pulses number could help to support the quality of the structured area, by reducing or eliminating the bad effects of the non-uniformity and zigzag formations on the structuring quality.

One of the most important advantages of this simulation is the good ability to analyze the interaction between pulses during LDS processes. This interaction results in different temperature distributions. Thus, a significant change in the characteristics of the structured area, particularly between the boundary and the internal area, is generated. A further result of 3D MID applications is concluded on the basis of simulation work. For 3D applications, it is preferred to increase the laser fluence to compensate for the decrease in laser density. This can be achieved by increasing laser power or decreasing laser frequency. The effect of the focal length can be removed or minimized by dividing the structured area into smaller areas, and different focal lengths should be defined or used for each area. The simulation results show a good agreement with experimental data. The minimum percentage error is 2.38 %, whereas the maximum is 7.89 % and the overall percentage of the predicted error is 4.15 %. These fall within an acceptable range of simulation and modeling standards.

Experimental works were performed to find out the correlation between the process parameters and the measured responses for different materials containing standard

MID polymers and ceramic-based materials. These works cover both LDS and metallization steps. The first experiments are performed to investigate the correlation of LDS input parameters and their responses. The characteristics of the structured area or the responses of LDS processes are quite related to the laser energy distribution, which depends on the parameter setting. This is the main hypothesis that could be used to explain the relationship between the parameter setting and the LDS responses.

The increase in laser power or hatching and the reduction in laser velocity or incidence angle leads to increase all the LDS responses involving groove dimensions (width and depth), edge dimensions (height and width), the surface roughness (Rz and Ra), and the structuring percentage. The laser frequency has a direct relationship with edge dimensions and an inverse relationship with the conductor or track width, groove depth, surface roughness and structuring percentage, but the focal length has an inverse relevance with groove depth, edge height, and surface roughness, structuring percentage in opposite to the relation with conductor width and edge width. In addition, the influence of the LDS parameters on the LDS responses is related to each other. The ceramic based material shows the same behavior under the effect of laser power, velocity, and frequency. However, this effect relates to the sintering temperature and copper oxide percentage. It is very important to mention that ceramic-based materials have good results in terms of groove edge dimensions or edge factor as compared to the polymer. They produce edge-free laps that support the quality of the structured area.

It has been found that the characteristics and topography of the structure area are extremely important for the final quality of MID structure comprising the groove profile and structuring-ablation type. The groove profile refers to one of the most important icons in the characteristics of the structured area or LDS responses. The metallization quality refers to this profile. It has a significant correlation with the parameter setting. Regulation of parameter setting produces different profiles types. In addition, there are two different zones for the same profile groove on the basis of the parameters used. They are classified into removing zone and puffing zone according to the ablation type. This behavior is visible in the polymer, whereas it doesn’t exist in ceramics. Accordingly, the ceramic shows only one possible zone, which is the removing zone. There are three possible structuring types that can be produced namely, line structuring, random structuring and mixed structuring. And the ablation can also be classified into three types including the puffing ablation, removing ablation and mixed ablation. This structuring-ablation type has a strong effect on the final MID quality and reliability due to its effect on the metallization structure. In addition, the investigated process parameters have a great effect on the type of structuring and ablation, especially the laser power, hatching, and laser velocity, which have a high effect when compared to laser frequency, incidence angle, and focal length. For the ceramic material the possibly structuring-ablation

types are MS-RA or RS-RA. However, it is possible to produce another structuring type, which is LS by changing the parameter setting such as hatching, power, velocity and frequency.

The second group of experiments covers the metallization step. The metallization quality has been defined as a set of requirements involving optical quality of the metallization, the thickness of the metallization layers, and the surface roughness of the metallized surface, and adhesion strength of the metallization structure. They are quite related to the responses of the LDS process or in other words, the characteristics of the structured area.

The optical inspections of the metallization quality show that metallization defects could occur under the parameters setting of a laser power of 1 W, a 0 % hatching and velocities up to 1.5 m/s or a laser power of 9 W, a hatching of 75 %, a velocity of 0.75 m/s and laser frequency of 140 kHz. The other parameter setts give good optical results with respect to the metallization structure. In addition, the setting of laser power at elevated value does not always have undesirable effects on the metallization quality. The effect of laser power is related to the other parameters such as velocity, frequency, and hatching. A minimum line/pitch of 45/28 µm with a metallization thickness of 9 µm are produced with laser parameters including a laser power of 1 W, a speed of 0.75 m/s, and a frequency of 60 kHz. This conductor width could be reduced to 30 µm by adjusting the focal length to 3 mm. For the ceramic-based material, it was concluded that the sintering temperature of 1200 °C and additive percentage of 5% are regarded as the optimum manufacturing conditions for this material. In addition, these materials are suitable for producing a fine line/pitch of 16/20 µm under the manufacturing and process parameters including additive percentage of 5 %, a sintering temperature of 1200 °C, a laser power of 4 W, a velocity of 1.5 m /s, and a frequency of 120 kHz.

A smoother metallization surface could be produced with a structuring type MS or the structuring type RS in conjunction with a laser power of low to middle, regardless of the ablation type. The other structuring-ablation type produces a rough metallization surface. The ablation types MA and RA are preferred to increase the thickness of the metallization and to support the adhesion quality of the metallization, in opposite to PA, which has a bad effect on the metallization quality. On the other hand, the metallization thickness can be increased since the produced structuring type changes from LS to RS and then to MS, whereas the structuring of RS produces the highest adhesion and the LS provides lower adhesion while the MS is in between. In general, the correlation between the LDS responses and the metallization quality can be summarized as follow.

The metallization thickness is significantly influenced by the following factors: First, Rz with an importance of 0.271, lap height, ablation type, lap width, structuring type and finally the groove depth which has an importance of 0.099. *The roughness of metallization* is depending on: First, structuring type with an importance of 0.239,

surface roughness, lap height, groove depth, ablation type and finally lap width which has importance 0.071. The increase in the LDS responses including lap dimensions (height and width), surface roughness, and groove depth results in a rough metallization surface. Therefore, it is important to control the produced structuring-ablation type to ensure a smooth metallization surface which is in demand for the final MID step. The importance sequence of the LDS responses on the *adhesion of the metallization* is as follows: First, the percentage of LDS defects has an importance of 0.269, structuring type, surface roughness, groove depth, lap height, and finally the lap width, which has 0.081. The increase in the edge factor (dimensions) has a bad influence on the adhesion quality whereas the surface roughness and groove depth support the adhesion quality.

The second part of the theoretical work is the modeling, which is performed using ANN and RSM approaches. The proposed models are used to correlate the adopted parameters with responses, analyze their effect, to find out their interaction and to optimize the process. The results of ANN and RSM models and the experimental data show good agreement. The minimum error is 0.927 % for ANN and 1.027% for the RSM, whereas the maximum error is 4.376% for the ANN and 5.197% for the RSM. The proposed models by ANN and RSM have the ability to provide a wide range of optimal parameter settings based on desired criteria.

10. Zusammenfassung

Die MID-LDS-Technologie umfasst vielseitige und überlappende Schritte. Sie umfasst komplexe und miteinander verbundene Prozessparameter. Die bisherigen Arbeiten behandeln diesen Prozess *als geschlossene Box* (als Ganzes) mit allen MID-LDS-Schritten. Sie untersuchten die Beziehung zwischen den begrenzten Eingangsparametern und dem *Hauptausgang* des MID-Prozesses, ohne Rücksicht auf die Wechselwirkung zwischen den MID-Schritten. In dieser Arbeit werden die Schritte des MID-LDS-Prozesses in Hauptschritte einschließlich LDS und Metallisierung getrennt. Dies wird dazu beitragen, jene beiden wichtigen Schritte und ihre Wechselwirkung, Bedeutung und Abhängigkeit zu untersuchen. Für die oben genannten Gründe wird eine Kombination von theoretischen und experimentellen Arbeiten vorgeschlagen, um das MID-LDS-Verfahren zu untersuchen. Diese werden wie folgt zusammengefasst:

Der erste Teil der theoretischen Arbeit beinhaltet eine thermische Simulation des 2D/3D LDS Prozesses. Sie basiert auf einem physikalischen Modell, das nichtlineare transiente 3D Wärmeleitung mit einer bewegten Wärmequelle umfasst. Eine wichtige Klassifikation, die in dieser Simulation verwendet wird, umfasst Laserfluenz, Laserdosis und die Anzahl von Impulsen oder Pulsüberlappungen. Dies ist hilfreich, um die Wechselwirkung zwischen den LDS-Parametern und deren Auswirkung auf den strukturierten Bereich zu erklären. Entsprechend den Simulationsergebnissen und basierend auf der obigen Klassifikation steigen die Rillenmaße und die maximale Temperaturerhöhung mit der Laserfluenz. Eine niedrige Laserfluenz führt zu einem diskontinuierlichen strukturierten Bereich mit Ablationstyp PA. Um solche Formationen zu verhindern, sollte die verwendete Laserfluenz ausreichend hoch sein. *Die Regulierung der Impulszahl könnte ebenso dazu beitragen, sowohl die Qualität der strukturierten Fläche zu beeinflussen als auch durch die Verringerung oder Beseitigung der schlechten Auswirkungen der Ungleichförmigkeit und Zickzack-Formationen auf die Strukturierungsqualität.*

Einer der wichtigsten Vorteile dieser Simulation liegt in der guten Möglichkeit, die Wechselwirkung zwischen Impulsen während des LDS-Prozesses zu analysieren. Diese Wechselwirkung führt zu unterschiedlichen Temperaturverteilungen. Somit wird eine wesentliche Änderung der Eigenschaften des strukturierten Bereichs, insbesondere zwischen der Grenze und dem inneren Bereich, erzeugt. Ein weiteres Ergebnis für 3D-MID Anwendungen wird auf der Basis von Simulationsarbeiten abgeschlossen. Für die 3D-MID Anwendungen eignet es sich, die Laserfluenz zu erhöhen, um die Abnahme der Laserdichte zu kompensieren. Dies kann durch Erhöhung der Laserleistung oder Abnahme der Laserfrequenz erreicht werden. Die Wirkung der Brennweite kann durch Aufteilung des strukturierten Bereichs in kleinere Flächen entfernt oder minimiert werden und für jeden Bereich können unterschiedliche Brennweiten definiert oder verwendet werden. Die Simulationsergebnisse zeigen eine gute Übereinstimmung mit experimentell ermittelten Daten. Der minimale Prozentale Fehler beträgt 2.38%, während das Maximum 7,89% beträgt und der Gesamtprozentsatz des vorhergesagten Fehlers 4.15% beträgt. Diese Werte fallen in den akzeptablen Bereich von Simulations- und Modellierungsstandards.

Experimentelle Arbeiten werden zur Ermittlung der Korrelation zwischen den Prozessparametern und den gemessenen Reaktionen für verschiedene Materialien, die Standard-MID-Polymere und keramikbasierte Materialien enthalten, durchgeführt. Diese Arbeiten umfassen sowohl LDS- als auch Metallisierungsschritte. Die ersten Experimente werden durchgeführt, um die Korrelation der LDS-Eingangsparameter und ihrer Antworten zu untersuchen. Die Eigenschaften des strukturierten Bereichs oder die Reaktionen des LDS-Prozesses stehen in engem Zusammenhang mit der Laser-Energieverteilung, die wiederum von der Parametrierung abhängt. Dies ist die Haupthypothese, die verwendet werden könnte, um die Beziehung zwischen den Parametern und den LDS-Antworten zu erklären. Die Erhöhung der Laserleistung oder der Werkzeugbahndichte und die Verringerung der Lasergeschwindigkeit oder des Einfallswinkels führen zu einer Erhöhung aller LDS-Reaktionen mit Rillenmaßen (Breite und Tiefe), Kantenabmessungen (Höhe und Breite), der Oberflächenrauhigkeit (Rz und Ra) und des Strukturierungsprozentsatzes. Die Laserfrequenz ist direkt proportional zu den Kantenabmessungen und indirekt proportional zur Leiter- oder Spurbreite, Rillentiefe, Oberflächenrauhigkeit und Strukturierungsprozentsatz, aber die Brennweite besitzt eine indirekte Beziehung zur Rillentiefe, Kantenhöhe und Oberflächenrauhigkeit, Strukturierungsprozentsatz entgegengesetzt zur Beziehung zur Leiterbreite und Kantenbreite. Darüber hinaus ist der Einfluss der LDS-Parameter auf die LDS-Antworten aufeinander bezogen.

Das keramikbasierte Material zeigt das gleiche Verhalten in Bezug auf die Wirkung von Laserleistung, Geschwindigkeit und Frequenz. Dieser Effekt bezieht sich jedoch auf die Sintertemperatur und den Kupferoxidanteil. Es ist sehr wichtig zu erwähnen, dass keramikbasierte Materialien gute Ergebnisse hinsichtlich der Rillenrandabmessungen oder des Randfaktors im Vergleich zum Polymer aufweisen. Sie produzieren kantenfreie Runden, die den qualitätsstrukturierten Bereich unterstützen.

Es wurde festgestellt, dass die Eigenschaften und die Topographie des Strukturbereichs für die endgültige Qualität der MID-Struktur, die das Rillenprofil, mit dem Strukturierungsablationstypen umfasst, extrem wichtig sind. Das Rillenprofil bezieht sich auf eines der wichtigsten *Symbole* in den Merkmalen des strukturierten Bereichs oder der LDS-Antworten. Die Metallisierungsqualität bezieht sich auf dieses Profil. Es hat eine signifikante Korrelation mit den Parametern. Die Regulierung der Parametrierung führt zu unterschiedlichen Profiltypen. Darüber hinaus gibt es auf der Basis der verwendeten Parameter zwei verschiedene Zonen für die gleiche Profilrille. Sie werden nach dem Ablationstyp in die Entfernungszone und die *Pufferzone* eingestuft. Dieses Verhalten ist im Polymer sichtbar, während es in der Keramik nicht existiert. Dementsprechend zeigt die Keramik nur eine mögliche Zone, nämlich die Entfernungszone. Es können drei mögliche Strukturierungsarten hergestellt werden, nämlich Linienstrukturierung, zufällige Strukturierung und gemischte Strukturierung. Und die Ablation kann auch in drei Arten einschließlich der Pufferablation, Entfernen durch Ablation und gemischte Ablation definiert werden. Dieser Strukturierungs-Ablationstyp hat einen starken Einfluss auf die endgültige MID-Qualität und Zuverlässigkeit aufgrund seiner Wirkung auf die Metallisierungsstruktur. Darüber hinaus haben die untersuchten Prozessparameter einen

großen Einfluss auf die Art der Strukturierung und Ablation, insbesondere die Laserleistung, die Werkzeugbahndichte und die Lasergeschwindigkeit, die im Vergleich zu Laserfrequenz, Einfallswinkel und Brennweite einen hohen Effekt haben. Für das keramische Material sind die wahrscheinlichen Strukturierungsablationstypen MS-RA oder RS-RA. Es ist jedoch möglich, einen anderen Strukturtyp zu erzeugen, nämlich LS, indem die Parametereinstellung wie Werkzeugbahndichte, Leistung, Geschwindigkeit und Frequenz ändert.

Die zweite Gruppe von Experimenten umfasst den Metallisierungsschritt. Die Metallisierungsqualität wurde als ein Satz von Anforderungen definiert, der die optische Qualität der Metallisierung, die Dicke der Metallisierungsschichten und die Oberflächenrauhigkeit der metallisierten Oberfläche sowie die Haftfestigkeit der Metallisierungsstruktur einschließt. Wer stehen eng im Verhältnis zu den Reaktionen des LDS-Prozesses oder mit anderen Worten, zu den Merkmalen des strukturierten Bereichs. Die optische Prüfung der Metallisierungsqualität zeigt, dass bei der Einstellung der Laserleistung von 1 W, einer 0% Werkzeugbahndichte und Geschwindigkeiten bis zu 1.5 m/s Metallisierungsdefekte auftreten können, oder einer Laserleistung von 9 W, einer Werkzeugbahndichte von 75%, eine Geschwindigkeit von 0.75 m/s und einer Laserfrequenz von 140 kHz, während andere Parametereinstellung gute optische Ergebnisse in Bezug auf die Metallisierungsstruktur ergeben. Darüber hinaus hat die Einstellung der Laserleistung bei erhöhtem Wert nicht immer unerwünschte Auswirkungen auf die Metallisierungsqualität. Die Wirkung der Laserleistung bezieht sich auf die anderen Parameter wie Geschwindigkeit, Frequenz und Werkzeugbahndichte. Eine Mindestlinie / Tonhöhe von 45/28 µm mit einer Metallisierungsdicke von 9 µm wird mit Laserparametern einschließlich einer Laserleistung von 1 W, einer Geschwindigkeit von 0.75 m/s und einer Frequenz von 60 kHz erzeugt. Diese Leiterbreite konnte durch Einstellen der Brennweite auf 3 mm auf 30 µm reduziert werden. Für das keramikbasierte Material wurde festgestellt, dass die Sintertemperatur von 1200 ° C und der additive Prozentsatz von 5% als optimale Herstellungsbedingungen für dieses Material betrachtet werden. Darüber hinaus eignen sich diese Materialien zur Herstellung einer feinen Linie / Pitch von 16/20 µm unter den Herstellungs- und Prozessparametern, einschließlich des Prozentsatzes Additiver von 5%, einer Sintertemperatur von 1200 ° C und einer Laserleistung von 4 W, eine Geschwindigkeit von 1.5 m/s und einer Frequenz von 120 kHz.

Eine glattere Metallisierungsoberfläche könnte mit einem Strukturierung MS hergestellt werden oder dem Strukturierung RS in Verbindung mit einer niedrigen bis mitlleren Laserleistung, unabhängig von dem Ablationstyp. Der andere Strukturierungs-Ablationstyp erzeugt eine grobe Metallisierungsoberfläche. Die Ablationstypen MA und RA werden für eine Erhöhung der Dicke der Metallisierung und zur Verbesserung der Adhäsionsqualität der Metallisierung bevorzugt, entgegengesetzt zu der PA zu unterstützen, was eine schlechte Wirkung auf die Metallisierungsqualität hat. *Andererseits kann die Metallisierungsdicke erhöht werden, da sich der erzeugte Strukturtyp von LS zu RS und dann zu MS ändert, während die Strukturierung RS die höchste Adhäsion erzeugt und die LS eine geringere Adhäsion, während MS*

dazwischen liegt. Im Allgemeinen kann die Korrelation zwischen den LDS-Reaktionen und der Metallisierungsqualität wie folgt zusammengefasst werden:

Die Metallisierungsdicke wird maßgeblich durch folgende Faktoren beeinflusst: Erstens, Rz mit einer Wichtigkeit von 0.271, Schoßhöhe, Ablationstyp, Schoßbreite, Strukturierungstyp und schließlich Rillentiefe, die eine Wichtigkeit von 0.099 hat. Die Rauheit der Metallisierung hängt von den folgenden Faktoren ab: Erstens, Strukturierungstyp mit einer Wichtigkeit von 0.239, Oberflächenrauhigkeit, Laphöhe, Rillentiefe, Ablationstyp und schließlich Schoßbreite, die eine Wichtigkeit von 0.071 hat. Die Erhöhung der LDS-Reaktionen einschließlich der Lap-Dimensionen (Höhe und Breite), Oberflächenrauhigkeit und Rillentiefe führt zu einer groben Metallisierungsoberfläche. Daher ist es wichtig, eine Regulierung für den produzierten Strukturierungs-Ablationstyp vorzunehmen, um eine glatte Metallisierungsoberfläche zu gewährleisten, die für den endgültigen MID-Schritt notwendig ist. Die Wichtigkeitsfolge der LDS-Reaktionen auf die Adhäsion der Metallisierung ist wie folgt: Erstens hat der Prozentsatz an LDS-Defekten eine Bedeutung von 0.269, der Strukturtyp, des Oberflächenrauhigkeit, Rillentiefe, Rundenhöhe und schließlich des Lap-Breite, die alle 0.081 besitzen. Die Erhöhung des Randfaktors (Abmessungen) hat einen negativen Einfluss auf die Adhäsionsqualität, während die Oberflächenrauhigkeit und die Rillentiefe diese Haftfestigkeit begünstigen.

Der zweite Teil der theoretischen Arbeit ist die Modellierung, die mit ANN und RSM Ansätzen arbeitet. Die vorgeschlagenen Modelle werden verwendet, um die angenommenen Parameter mit Antworten zu korrelieren, ihre Wirkung und ihre Wechselwirkung zwischen einander zu analysieren und den Prozess zu optimieren. Die Ergebnisse der ANN- und RSM-Modelle wurden mit den experimentellen Daten verglichen. Der minimale Fehler des ANN Modell beträgt 0.927% und für den RSM Modell 1.027%, während der maximale Fehler des ANN Modell 4.376% und der des RSM Modell 5.197% beträgt. Die vorgeschlagenen Modelle ANN und RSM haben die Möglichkeit, eine breite Palette von optimalen Parametereinstellungen basierend auf gewünschten Kriterien zu liefern.

References

[1] Franke, Jörg, et al. "*Three-Dimensional Molded Interconnect Devices (3D-MID): Materials, Manufacturing, Assembly and Applications for Injection Molded Circuit Carriers*". Carl Hanser Verlag GmbH Co KG, (2014).

[2] Islam, Aminul. "*Two Component Micro Injection Moulding For Moulded Interconnect Devices*" PH.D Thesis (2008).

[3] Graeser Suzanne, *3D-MID Technology @ Cicor*. Industrialization of 3D-MID: challenges and solutions. URL www.innovdays-plasturgie.com. Access data: 01.03 2017.

[4] Khuntontong, Puttachat. "*Fabrication of polymer micro devices by ultrasonic hot embossing*. Dissertation" Aachen, (2008).

[5] Paulsen, Jason A., et al. "*Printing Conformal Electronics on 3D Structures with Aerosol Jet Technology.*" Future of Instrumentation International Workshop (FIIW), IEEE, (2012).

[6] Islam, Aminul, et al. "*Process Chains for the Manufacturing of Molded Interconnect Devices*" The International Journal of Advanced Manufacturing Technology 42.9-10 (2009): 831-841.

[7] LPKF Laser and Electronics. "*Three-Dimensional Circuits LPKF LDS: Laser Direct Structuring for 3D Molded Interconnect Devices*", Technical Information. Access data: 01.03 2017.

[8] Franke, Jörg (Hrsg.): *MID-Studie 2011*. Erlangen: Forschungsvereinigung Räumliche Elektronische Baugruppen 3-D MID, (2011).

[9] Goth, Christian and Guido, Schatz. "*Assembly Technologies and Connection Methods for 3D-MID*", http://www.harting-mitronics.ch. Access data: 01.03 2017.

[10] Heininger, Nils, Wolfgang John, and Hans-Jürgen Boßler. "*Manufacturing of Molded Interconnect Devices from Prototyping to Mass Production with Laser Direct Structuring*" International Congress MID. (2004).

[11] HARTING. "*3D-MID in Medical Technology*" [Online]. Available http://www.harting-mitronics.ch, Access data: 01.03 2017.

[12] LPKF Laser and Electronics: *LPKF Fusion3D 1100*. Technical Information, [Online]. Available in http://www.lpkf.de/produkte/mid/fusion3d-1100.htm - Access data: 01.03 2017.

[13] Feldmann, Klaus, et al. "*Innovative Impulse zur Herstellung und Optimierung räumlicher elektronischer Schaltungsträger (MID)*", Access data: 01.03 2017.

[14] Wu, Yan Jun, et al. "*Kinematic Analysis and Simulation of MID Laser Direct Structuring Equipment*." Advanced Materials Research. 590. Trans Tech Publications, (2012).

[15] Evonik Industries, Polymers & Lasers Laser Application Center, Technical Information, Germany. (2011).

[16] Goth, Christian, and Michael Roemer. "*1 External Current-free, Chemical Metallization.*" http://www.harting-mitronics.ch. Access data: 01.03 2017.

[17] Bachy, Bassim, and Franke, Jörg. "*Experimental Investigation and Optimization for the Effective Parameters in the Laser Direct Structuring Process*." Journal of Laser Micro Nanoengineering 10.2 (2015): 202.

[18] Bachy, Bassim, and Franke, Jörg. "*Modeling and Optimization of Laser Direct Structuring Process Using Artificial Neural Network and Response Surface Methodology*." International Journal of Industrial Engineering Computations 6.4 (2015): 553-564.

[19] Photonics Technical Note "*Average and Peak Power*" Available https://www.newport.com Access data: 01.03 2017.

[20] Nowakowski, Krzysztof A. "*Laser beam interaction with materials for micro scale applications*". Diss. Draper Laboratory, Cambridge, MA, (2005).

[21] Sintec Optronics Pte Ltd "*Focused Beam Diameter with Focusing Lens*" Available http://www.sintecoptronics.com/- Access data: 01.11 2016.

[22] Tzeng, Yih-fong. "*Parametric Analysis of the Pulsed Nd:YAG Laser Seam-Welding Process*" Journal of Materials Processing Technology 102.1 (2000):40-47.

[23] Teixidor, Daniel, et al. "*Modeling Pulsed Laser Micromachining of Micro Geometries Using Machine-Learning Techniques.*" Journal of Intelligent Manufacturing 26.4 (2015): 801-814.

[24] DSM LDS technology explanation. Guide for the LDS developer. Technical Information, (2008).

[25] Thawari, G., et al. "*Influence of Process Parameters During Pulsed Nd:YAG Laser Cutting of Nickel-Base Super-Alloys*." Journal of Materials Processing Technology 170.1 (2005): 229-239.

[26] Hitz, C. Breck, James J. Ewing, and Jeff Hecht. "*Introduction to Laser Technology*". John Wiley & Sons, (2012).

[27] Huske, M., et al. "*Laser Supported Activation and Additive Metallization of Thermoplastics for 3D-Mids*." Proceeding of the 3rd LANE. (2001).

[28] Kuhn, Thomas, and Franke, Jörg. "*Test Methods and Influencing Factors for the Adhesion Strength Measurement of Metallized Structures on Thermoplastic Substrates*." Electronics Packaging Technology Conference (EPTC), 2014 IEEE 16th. IEEE, (2014).

[29] Goth, Christian, et al. "*Hot Pin Pull Method–New Test Procedure for the Adhesion Measurement for 3D-MID*." Advanced Materials Research. Vol. 1038. Trans Tech Publications, (2014).

[30] Buckmüller, Peter, et al. "*Aluminium Wedge-Wedge Wire Bonding on Thermoplastic Substrates Made by LPKF-LDS® Technology*." Electronic System-Integration Technology Conference (ESTC), 2010 3rd. IEEE, (2010).

[31] Kordass, Timo, and Franke, Jörg. "*Galvanic Plating for 3D-MID Applications*." Electronics Technology (ISSE), Proceedings of the 2014 37th International Spring Seminar on. IEEE, (2014).

[32] Eberhardt, Wolfgang, Kern, Frank and Zimmermann, André. "*Laserdirektstrukturierung von Spritzgegossenen Keramischen 3D-Schaltungsträgern*" IGF Project, Stuttgart University, (2015).

[33] Kibria, G., B. Doloi, and B. Bhattacharyya. "*Experimental Analysis on Nd: YAG Laser Micro-Turning of Alumina Ceramic*." The International Journal of Advanced Manufacturing Technology 50.5-8 (2010): 643-650.

[34] Zhang, Bin, et al. "*The Quality and Reliability of Fine Circuit Lines Fabricated by the Laser Structuring Technique*." Industrial Engineering Research (2006): 10.

[35] Zhang, Bin, et al. "*Feasibility of the 248 nm Excimer Laser in the Laser Structuring of Fine Circuit Lines on Printed Circuit Board.*" The International Journal of Advanced Manufacturing Technology 33.11-12 (2007): 1149-1158.

[36] Genna, S., et al. "*An experimental study on the surface mechanisms formation during the laser milling of PMMA*." Polymer Composites 36.6 (2015): 1063-1071.

[37] Romoli, L., et al "*Layered Laser Vaporization of PMMA Manufacturing 3D Mould Cavities.*" CIRP Annals-Manufacturing Technology 56.1 (2007): 209-212.

[38] Mendonca, C. R., et al. "*Femtosecond Laser Micromachining in the Conjugated Polymer MEH–PPV.*" Applied Surface Science 254.4 (2007): 1135-1139.

[39] Raciukaitis, Gediminas, and Mindaugas Gedvilas. "*Processing of Polymers by UV Picosecond Lasers.*" Proceedings of 24 th ICALEO Conference. 2005.

[40] Spyratou, E., et al. "*UV Laser Ablation of Intraocular Lenses: SEM and AFM Microscopy Examination of the Biomaterial Surface.*" Applied Surface Science 256.8 (2010): 2539-2545.

[41] Bachy, Bassim, and Franke, Jörg. "*Simulation of Laser Structuring by Three Dimensional Heat Transfer Model.*" Microsystems, Packaging, Assembly and Circuits Technology Conference (IMPACT), 2014 9th International. IEEE, (2014).

[42] Bachy, Bassim, et al. "*Simulation and Experimental Investigation for the 2D and 3D Laser Direct Structuring Process*." The International Journal of Advanced Manufacturing Technology 89 (2016): 1591-1602.

[43] Zhang, Yiming, et al. "*Modeling and Simulation on Long Pulse Laser Drilling Processing.*" International Journal of Heat and Mass Transfer 73 (2014): 429-437.

[44] Begic-Hajdarevic, Derzija, and Izet Bijelonja. *"Experimental and Numerical Investigation of Temperature Distribution and Hole Geometry during Laser Drilling Process.*" Procedia Engineering 100 (2015): 384-393.

[45] Moncayo, Marco A., et al. "*Laser Surface Modification of Alumina: Integrated Computational and Experimental Analysis.*" Ceramics International 39.6 (2013): 6207-6213.

[46] Moncayo, Marco A., et al. "*Computational Modeling and Experimental Based Parametric Study of Multi-Track Laser Processing on Alumina*." Optics & Laser Technology 48 (2013): 570-579.

[47] Joshi, Ajit, et al. "*A Study of Temperature Distribution for Laser Assisted Machining of Ti-6Al-4V Alloy*." Procedia Engineering 97 (2014): 1466-1473.

[48] Madić, Miloš, et al. "*An Artificial Neural Network Approach for Analysis and Minimization of HAZ in CO_2 laser cutting of stainless steel*." UPB Scientific Bulletin, Series D: Mechanical Engineering 75.2 (2013): 85-96.

[49] Madić, Miloš, et al. "*ANN Modeling of Kerf Transfer in CO2 Laser Cutting and Optimization of Cutting Parameters Using Montecarlo Method."* International Journal of Industrial Engineering Computations 6.1 (2015): 33-42.

[50] Ismail, Mohd Idris Shah, Yasuhiro Okamoto, and Akira Okada. "*Neural Network Modeling For Prediction of Weld Bead Geometry in Laser Micro-welding*." Advances in Optical Technologies (2013): 1-7.

[51] Kalaiselvan, K., et al. "*Artificial Neural Network Application on Ti/Al Joint Using Laser Beam Welding–A Review*." World Academy of Science, Engineering and Technology, International Journal of Mechanical, Aerospace, Industrial, Mechatronic and Manufacturing Engineering 8.8 (2014): 1477-1481.

[52] Wang, Xiao, Hao Chen, and Huixia Liu. "*Numerical-Simulation-Driven Optimization of a Laser Transmission Welding Process under Consideration of Scattering.*" Journal of Applied Polymer Science 131.12 (2014).

[53] Maamri, Ilyes, Abderrazak El Ouafi, and Noureddine Barka. "*Prediction of 4340 Steel Hardness Profile Heat-treated by Laser Using Artificial Neural Networks and Multi Regression approaches*." International Journal of Engineering and Innovative Technology 4.6 (2014): 14-22

[54] D'Addona, Doriana M., et al. "*Prediction of Poly-Methyl-Methacrylate Laser Milling Process Characteristics Based on Neural Networks and Fuzzy Data*." Procedia CIRP 41 (2016): 981-986.

[55] Wang, Xiao, et al. "*Simulation and Optimization of Continuous Laser Transmission Welding Between PET and Titanium through FEM, RSM, GA and Experiments.*" Optics and Lasers in Engineering 51.11 (2013): 1245-1254.

[56] Liu, Wei, et al. "*Numerical Modeling and Experimental Verification of Residual Stress in Autogenous Laser Welding of High-Strength Steel*." Lasers in Manufacturing and Materials Processing 2.1 (2015): 24-42.

[57] Holman, J. P. "*Heat Transfer 10th ed*." Mcgraw Hill, (2010).

[58] Bejan, A., "*Heat Transfer*", Wiley, New York, (1993).

[59] Schramm, Rene "*Strukturierte Additive Metallisierung durch kaltaktives Atmosphärendruckplasma*" PH.D Thesis (2015).

[60] Wang, Hongze, and Yansong Zhang. "*Modeling of Heat Affected Zone Softening in Laser Welding of M1500*." ASME 2015 International Manufacturing Science and Engineering Conference. American Society of Mechanical Engineers, (2015).

[61] Priti Duggal, B.Tech." *An Experimental Study of Rim Formation in Single-Shot Femtosecond Laser Ablation of Borosilicate Glass*" (2006).

[62] Kärtner, Franz . "*IMPRS: Ultrafast Source Technologies*." Course in electrodynamics, Lectures, (2014).

[63] Begic-Hajdarevic, Derzija, and Izet Bijelonja. "*Experimental and Numerical Investigation of Temperature Distribution and Hole Geometry during Laser Drilling Process.*" Procedia Engineering, 100, (2015): 384-393.

[64] Ning, Jie, et al. "*Numerical Study of the Effect of Laser-Arc Distance on Laser Energy Coupling in Pulsed Nd:YAG Laser/TIG Hybrid Welding*." The International Journal of Advanced Manufacturing Technology (2016): 1-15.

[65] Oztekin, Ezgi ., et al. "*Sources of Variability in Fire Test Data: a Case Study on Poly (Aryl Ether Ether Ketone)(PEEK)*." Combustion and Flame 159.4 (2012): 1720-1731.

[66] Tardif, Xavier, et al. "*Experimental Study of Crystallization of Polyetheretherketone (PEEK) Over a Large Temperature Range Using a Nano-Calorimeter.*" Polymer Testing 36 (2014): 10-19.

[67] VICTREX® High Performance Peek Polymers ©Victrex plc, technical data, (2014).

[68] Parvaiz, M. Rahail, et al. "*Polyetheretherketone (PEEK) Composites Reinforced with Fly Ash and Mica*." Journal of Minerals and Materials Characterization and Engineering 9.01 (2010): 25.

[69] Cho, Won-Ik, et al. "*Numerical Study of Alloying Element Distribution in CO2 Laser–GMA Hybrid Welding.*" Computational Materials Science 49.4 (2010): 792-800.

[70] Liu, F. R., et al. "*Micro Scale 3D FEM Simulation on Thermal Evolution Within the Porous Structure in Selective Laser Sintering*." Journal of Materials Processing Technology 212.10 (2012): 2058-2065.

[71] Haque, E., and P. Hampson. "*Modelling Phase Change in a 3D Thermal Transient Analysis.*" The International Journal of Multiphysics 8.1 (2016): 49-67.

[72] Evonik Industries, VESTAMID®HTplus LDS 3031 black, Technical Information, (2014).

[73] Wangui, Esther, Bernard W. Ikua, and George N. Nyakoe. "*A Study on Influence of Beam Orientation in Engraving Using CO2 Laser.*" Journal of Sustainable Research in Engineering 1.1, (2014): 42-48.

[74] Gecys, Paulius, et al. "*Ripple Formation by Femtosecond Laser Pulses for Enhanced Absorptance of Stainless Steel*." Journal of Laser Micro Nanoengineering 10.2 (2015): 129-133.

[75] Hana Chmelíčková and Hana Šebestová. "*Pulsed Laser Welding, Nd YAG Laser*", In Tech 4 ,(2012) :41-58,

[76] Samant, Anoop. "*Laser Machining of Structural Ceramics: Computational and Experimental Analysis*." PH.D Thesis (2009).

[77] Patel, Parina, et al. "*Mechanism of Thermal Decomposition of Poly (Ether Ether Ketone)(PEEK) From a Review of Decomposition Studies*." Polymer Degradation and Stability 95.5 (2010): 709-718.

[78] Patel, Parina, et al. "*Investigation of the Thermal Decomposition and Flammability of PEEK and its Carbon and Glass-Fibre Composites*." Polymer Degradation and Stability 96.1 (2011): 12-22.

[79] Vasconcelos, Gibran da Cunha, et al. "*Evaluation of Decomposition Kinetics of Poly (Ether-Ether-Ketone) by Thermogravimetric Analysis*." Materials Research 17.1 (2014): 227-235.

[80] Naundorf, Gerhard, and Horst Wissbrock. "*A Fundamentally new Mechanism for Additive Metallization of Polymeric Substrates in Ultra-Fine Line Technology Illustrated for 3D-Mids*." Galvanotechnik(Germany) 91.9 (2000): 2449-2451.

[81] Horn, H., et al. "*Excimer Laser Pretreatment and Metallization of Polymers*." Nuclear Instruments and Methods in Physics Research Section B: Beam Interactions with Materials and Atoms 151.1 (1999): 279-284.

[82] Dirk Bäcker, LPKF-LDS™ "*Laser-Based Procedure for High Volume Production of Mids*" (2011).

[83] Dowden, John, "*The Theory of Laser Materials Processing*" heat and mass transfer in modern technology. 119. Springer Science & Business Media, 119 (2009).

[84] Koechner, Walter, and Michael Bass. "*Solid-State Lasers*"*: A Graduate Text*. Springer Science & Business Media, (2003).

[85] LPKF Laser and Electronics. “Approved *Plastics for Laser Direct Structuring With LPKF LDS Systems*" (2015).

[86] J.K. Farrer and M.M. Nowell "*EBSD Analysis of Solid-State Reactions Between Al2O3 and Cu2O*" Microscopy Society of America, (2005).

[87] KEYENCE, Color 3D Laser Microscope, VK Analyzer Plus, Reference Manual, (2008).

[88] Dunn, Peter M. "*James Lind (1716-94) of Edinburgh and the Treatment of Scurvy*." Archives of Disease in Childhood-Fetal and Neonatal Edition 76.1 (1997): F64-F65.

[89] J. Paulo Davim "*Design of Experiments in Production Engineering*", Springer, (2016).

[90] Oehlert, Gary W. "*A first course in design and analysis of experiments*". (2010).

[91] Boomer, George. "*Introduction to Experimental Design for Discrete-Choice Models*." (2000).

[92] Cukor, Goran, Zoran Jurković, and Milenko Sekulić. "*Rotatable Central Composite Design of Experiments versus Taguchi Method in the Optimization of Turning*." Metalurgija 50.1 (2011): 17-20.

[93] Viktor P. Astakhov, Vasily V. Galitsky "*Tool Life Testing in Gundrilling: an Application of the Group Method of Data Handling (GMDH)*" International Journal of Machine Tools & Manufacture 45 (2005) 509–517.

[94] Kowalski, Scott M., and Kevin J. Potcner. "*How to Recognize a Split-Plot Experiment.*" Quality progress 36.11 (2003): 60.

[95] Proust, Marcel, and A. JMP. "*Design of Experiments Guide.*" Version11, JMP, A Business Unit of SAS, AS Campus Drive, Cary, (2014).

[96] Tavares, Sergio Manuel Oliveira. "*Analysis of Surface Roughness and Models of Mechanical Contacts*". Ph. D. dissertation, (2005).

[97] JIS B 0601-2001, "*Surface Roughness by Different Processing Methods*", Technical Data ,(2001).

[98] Naglieri, Valentina, et al. "*Optimized Slurries for Spray Drying: Different Approaches to Obtain Homogeneous and Deformable Alumina-Zirconia Granules*." Materials 6.11 (2013): 5382-5397.

[99] Ratautas, K., et al. "*Laser-Induced Selective Metal Plating on PP and PC/ABS Polymers Surface.*" Molded Interconnect Devices (MID), 2016 12th International Congress. IEEE, (2016).

[100] Brinkhues, Sven, et al. "*Investigation of Adhesion Strength of Metallization on Thermoplastic and Ceramic Substrates*." Molded Interconnect Devices (MID), 2016 12th International Congress. IEEE, (2016).

[101] Kostakos, John. "*Relation Between Surface Roughness and Adhesion as Studied with AFM*. " MS thesis. University of Twente, (2013).

[102] Quinn, Gerry, and Michael J. Keough. "*Experimental Design and Data Analysis for Biologists*". Cambridge University Press, (2002).

[103] Shan, Songqing, and G. Gary Wang. "*Survey of Modeling and Optimization Strategies to Solve High-Dimensional Design Problems with Computationally-Expensive Black-Box Functions*." Structural and Multidisciplinary Optimization 41.2 (2010): 219-241.

[104] Gallina, Alberto. "*Response Surface Methodology as a Tool for Analysis of Uncertainty in Structural Dynamics*." AGH-University of Science and Technology, (2009).

[105] Astakhov, Viktor P. "*Design of Experiment Methods in Manufacturing: Basics and Practical Applications*." Statistical and Computational Techniques in Manufacturing. Springer Berlin Heidelberg, (2012): 1-54.

[106] Malek, Alaeddin. "*Application of Recurrent Neural Networks to Optimization Problems.*" Recurrent Neural Networks (X. Hu and P. Balasubramaniam, eds.), In-Tech (2008): 255-288.

[107] Benyoucef, Lyes, and Bernard Grabot,. "*Artificial Intelligence Techniques for Networked Manufacturing Enterprises Management*". Springer Science & Business Media, (2010).

[108] Sordo, Margarita. "*Introduction to Neural Networks in Healthcare*." Open Clinical Document (2002).

[109] Olden, Julian D., Michael K. Joy, and Russell G. Death. "*An Accurate Comparison of Methods for Quantifying Variable Importance in Artificial Neural Networks Using Simulated Data*." Ecological Modelling 178.3 (2004): 389-397.

[110] Khuri, André I., and Siuli Mukhopadhyay. "*Response Surface Methodology*." Wiley Interdisciplinary Reviews: Computational Statistics 2.2 (2010): 128-149.

[111] Hessainia, Zahia, et al. "*On the Prediction of Surface Roughness in the Hard Turning Based on Cutting Parameters and Tool Vibrations*." Measurement 46.5 (2013): 1671-1681.

[112] Demirel, Muhammet, and Berkant Kayan. "*Application of Response Surface Methodology and Central Composite Design for the Optimization of Textile Dye*

Degradation by Wet Air Oxidation." International Journal of Industrial Chemistry 3.1 (2012): 24.

[113] Lenth, Russell V. "*Response-Surface Methods in R, Using RSM*." Journal of Statistical Software 32.7 (2009): 1-17.

[114] Carley, Kathleen, et al. "*Response Surface Methodology"*. Carnegie Mellon University - School Of Computer Science, (2004).

[115] Demuth, Howard, and Mark Beale. "*Neural Network Toolbox*." For Use with MATLAB, R2014b. The MathWorks Inc, (2014).

[116] Newton, Isaac. "*Minitab Cookbook*". Packt Publishing Ltd, (2014).

[117] Snijders, Tom, et al. "*Multilevel Analysis: An Introduction to Basic and Advanced Multilevel Modeling", second edition* London etc. Sage Publishers, (2012).

[118] Hyndman, Rob J., and Anne B. Koehler. "*Another Look at Measures of Forecast Accuracy.*" International journal of forecasting 22.4 (2006): 679-688.

[119] Halici, Ugur. "*Artificial neural networks*." Middle East Technical University, Ankara, (2004).

[120] Czogiel, Irina, Karsten Luebke, and Claus Weihs. "*Response Surface Methodology for Optimizing Hyper Parameters*." (2006).

[121] Coello, Carlos, et al. "*Evolutionary Multi-Criterion Optimization"*. Springer, (2005).

List of Related Publications

1. Bachy, Bassim, and Franke, Jörg. "Simulation of laser structuring by three dimensional heat transfer model." *Microsystems, Packaging, Assembly and Circuits Technology Conference (IMPACT), 2014 9th International*. IEEE, 2014.
2. Bachy, Bassim, and Franke, Jörg. "Experimental investigation and optimization for the effective parameters in the laser direct structuring process." *Journal of Laser Micro Nanoengineering* 10.2 (2015): 202.
3. Bachy, Bassim, and Franke, Jörg. "Modeling and optimization of laser direct structuring process using artificial neural network and response surface methodology." *International Journal of Industrial Engineering Computations* 6.4 (2015): 553-564.
4. Bachy, Bassim, et al. "Simulation and experimental investigation for the 2D and 3D laser direct structuring process." *The International Journal of Advanced Manufacturing Technology* 89 (2016): 1591-1602.
5. Bachy, Bassim, et al.”On the Quality and the Accuracy of the Laser Direct Structuring (LDS), Experimental Investigation and Optimization” Paper submitted to Journal Optics and Lasers in Engineering, 2017.

Appendices

Table A.1: The structuring type.

Structuring Type		β	0									20									40								
		FL	0			3			5			0			3			5			0			3			5		
		H	0	50	75	0	50	75	0	50	75	0	50	75	0	50	75	0	50	75	0	50	75	0	50	75	0	50	75
p	v	f																											
1	750	60	LS	LS	RS	LS	LS	RS	N	N	N	LS	LS	RS	LS	MS	RS	LS	LS	RS	LS	LS	RS	LS	LS	RS	N	LS	RS
		100	LS	LS	RS	LS	LS	LS	N	N	N	LS	LS	RS	LS	LS	LS	LS	LS	LS	LS	LS	MS	LS	LS	RS	N	LS	LS
		140	LS	LS	RS	LS	LS	LS	N	N	N	LS	LS	RS	LS	LS	LS	N	LS	LS	LS	LS	MS	LS	LS	RS	N	LS	LS
	1500	60	LS	LS	RS	N	N	N	N	N	N	LS	LS	RS	LS	LS	LS	N	N	N	LS	LS	LS	LS	LS	LS	N	LS	LS
		100	N	LS	LS	N	N	N	N	N	N	N	N	LS	LS	LS	LS	N	N	N	N	LS	LS	LS	LS	LS	N	N	LS
		140	N	N	LS	N	N	N	N	N	N	N	N	LS	LS	LS	LS	N	N	N	N	N	N	N	N	LS	N	N	N
	2250	60	N	LS	LS	N	N	N	N	N	N	N	N	LS	LS	LS	LS	N	N	N	N	LS	LS	N	N	N	N	N	N
		100	N	N	N	N	N	N	N	N	N	N	N	N	N	N	LS	N	N	N	N	N	N	N	N	N	N	N	N
		140	N	N	N	N	N	N	N	N	N	N	N	N	N	N	LS	N	N	N	N	N	N	N	N	N	N	N	N
5	750	60	LS	RS	RS	LS	RS	RS	LS	RS	RS	MS	MS	RS	LS	RS	RS	LS	RS	RS	MS	MS	RS	LS	RS	RS	MS	RS	RS
		100	LS	RS	RS	LS	RS	RS	LS	RS	RS	LS	MS	RS	LS	RS	RS	LS	RS	RS	LS	MS	RS	LS	RS	RS	MS	MS	RS
		140	LS	RS	RS	LS	MS	RS	LS	RS	RS	LS	RS	RS	LS	MS	MS	LS	MS	RS	LS	LS	RS	LS	MS	MS	MS	LS	RS
	1500	60	MS	RS	RS	MS	RS	RS	MS	RS	RS	LS	RS	RS	LS	RS	RS	LS	RS	RS	MS	RS	RS	LS	RS	RS	MS	RS	RS
		100	MS	RS	RS	MS	RS	RS	RS	RS	RS	LS	RS	RS	LS	RS	RS	LS	RS	RS	MS	RS	RS	LS	RS	RS	MS	MS	RS
		140	MS	RS	RS	MS	MS	RS	RS	RS	RS	LS	RS	RS	LS	MS	RS	LS	MS	RS	MS	RS	RS	LS	MS	RS	MS	MS	RS
	2250	60	MS	RS	RS	MS	RS	RS	RS	RS	RS	LS	RS	RS	LS	RS	RS	LS	RS	RS	MS	RS	RS	LS	RS	RS	MS	RS	RS
		100	MS	RS	RS	MS	RS	RS	RS	RS	RS	LS	RS	RS	LS	RS	RS	LS	RS	RS	MS	RS	RS	LS	RS	RS	LS	MS	RS
		140	MS	RS	RS	MS	MS	RS	RS	RS	RS	LS	LS	RS	LS	MS	RS	LS	RS	RS	MS	LS	RS	LS	MS	RS	LS	MS	RS
9	750	60	RS	RS	RS	RS	RS	RS	MS	RS	RS	RS	RS	RS	MS	RS	RS	MS	RS	RS	MS	RS	RS	RS	RS	RS	RS	RS	RS
		100	RS	RS	RS	LS	RS	RS	LS	RS	RS	MS	MS	RS	LS	RS	RS	LS	RS	RS	MS	MS	RS	MS	RS	RS	LS	RS	RS
		140	LS	RS	RS	LS	RS	RS	LS	RS	RS	LS	MS	RS	LS	RS	RS	LS	MS	RS	LS	LS	RS	LS	RS	RS	LS	MS	RS
	1500	60	LS	RS	RS	MS	RS	RS	MS	RS	RS	MS	RS	RS	LS	RS	RS	MS	RS	RS	MS	RS	RS	MS	RS	RS	MS	RS	RS
		100	LS	RS	RS	MS	RS	RS	MS	RS	RS	MS	RS	RS	LS	RS	RS	LS	RS	RS	MS	RS	RS	MS	RS	RS	MS	RS	RS
		140	LS	RS	RS	MS	RS	RS	MS	RS	RS	MS	RS	RS	LS	RS	RS	LS	MS	RS	MS	MS	RS	MS	RS	RS	LS	MS	RS
	2250	60	MS	RS	RS	MS	RS	RS	RS	RS	RS	MS	RS	RS	LS	RS	RS	MS	RS	RS	MS	RS	RS	MS	RS	RS	MS	RS	RS
		100	MS	RS	RS	MS	RS	RS	MS	RS	RS	MS	RS	RS	LS	RS	RS	LS	RS	RS	MS	RS	RS	MS	RS	RS	MS	RS	RS
		140	MS	RS	RS	MS	RS	RS	MS	RS	RS	MS	RS	RS	LS	RS	RS	LS	RS	RS	MS	RS	RS	MS	RS	RS	MS	RS	RS

Table A.2: The ablation type.

Ablation Type		β	0									20									40								
		FL	0			3			5			0			3			5			0			3			5		
		H	0	50	75	0	50	75	0	50	75	0	50	75	0	50	75	0	50	75	0	50	75	0	50	75	0	50	75
PA	v	f																											
1	750	60	PA	PA	PA	PA	PA	PA	N	N	N	PA	PA	PA	PA	PA	PA	PA	PA	PA	PA	PA	PA	PA	PA	PA	N	PA	PA
		100	PA	PA	PA	PA	PA	PA	N	N	N	PA	PA	PA	PA	PA	PA	PA	PA	PA	PA	PA	PA	PA	PA	PA	N	PA	PA
		140	PA	PA	PA	PA	PA	PA	N	N	N	PA	PA	PA	PA	PA	PA	N	PA	PA	PA	PA	PA	PA	PA	PA	N	PA	PA
	1500	60	PA	PA	PA	N	N	N	N	N	N	PA	PA	PA	PA	PA	PA	N	N	N	PA	PA	PA	PA	PA	PA	N	PA	PA
		100	N	PA	PA	N	N	N	N	N	N	N	N	PA	PA	PA	PA	N	N	N	N	N	N	N	N	PA	N	N	PA
		140	N	N	PA	N	N	N	N	N	N	N	N	PA	PA	PA	PA	N	N	N	N	PA	PA	N	N	PA	N	N	N
	2250	60	N	PA	PA	N	N	N	N	N	N	N	N	PA	PA	PA	PA	N	N	N	N	N	N	N	N	N	N	N	N
		100	N	N	N	N	N	N	N	N	N	N	N	N	N	N	PA	N	N	N	N	N	N	N	N	N	N	N	N
		140	N	N	N	N	N	N	N	N	N	N	N	N	N	N	PA	N	N	N	N	N	N	N	N	N	N	N	N
5	750	60	MA	RA	RA	MA	RA	RA	MA	RA	RA	MA	RA	RA	MA	RA	RA	MA	RA	RA	MA	RA	RA	MA	RA	RA	MA	RA	RA
		100	MA	RA	RA	MA	RA	RA	MA	RA	RA	MA	RA	RA	MA	RA	RA	MA	RA	RA	MA	RA	RA	MA	RA	RA	MA	RA	RA
		140	MA	RA	RA	MA	RA	RA	MA	RA	RA	MA	RA	RA	MA	RA	RA	MA	RA	RA	MA	RA	RA	MA	RA	RA	MA	RA	RA
	1500	60	MA	RA	RA	MA	RA	RA	MA	RA	RA	MA	RA	RA	MA	RA	RA	MA	RA	RA	MA	RA	RA	MA	RA	RA	MA	RA	RA
		100	MA	RA	RA	MA	RA	RA	PA	RA	RA	MA	RA	RA	MA	RA	RA	PA	RA	RA	MA	RA	RA	MA	RA	RA	PA	MA	RA
		140	MA	RA	RA	MA	RA	RA	PA	RA	RA	MA	RA	RA	MA	RA	RA	PA	RA	RA	MA	RA	RA	MA	RA	RA	PA	MA	RA
	2250	60	MA	RA	RA	MA	RA	RA	PA	RA	RA	MA	RA	RA	MA	RA	RA	PA	RA	RA	MA	RA	RA	MA	RA	RA	PA	MA	RA
		100	MA	RA	RA	MA	RA	RA	PA	RA	RA	PA	RA	RA	MA	RA	RA	PA	RA	RA	PA	MA	RA	MA	RA	RA	PA	MA	MA
		140	MA	RA	RA	MA	RA	RA	PA	RA	MA	PA	MA	RA	MA	MA	RA	PA	MA	MA	PA	MA	MA	MA	MA	RA	PA	MA	MA
9	750	60	RA	RA	RA	RA	RA	RA	RA	RA	RA	RA	RA	RA	RA	RA	RA	RA	RA	RA	RA	RA	RA	RA	RA	RA	MA	RA	RA
		100	RA	RA	RA	RA	RA	RA	RA	RA	RA	RA	RA	RA	MA	RA	RA	MA	RA	RA	RA	RA	RA	MA	RA	RA	MA	RA	RA
		140	RA	RA	RA	RA	RA	RA	RA	RA	RA	RA	RA	RA	MA	RA	RA	MA	RA	RA	MA	RA	RA	MA	RA	RA	MA	RA	RA
	1500	60	MA	RA	RA	RA	RA	RA	RA	RA	RA	MA	RA	RA	MA	RA	RA	RA	RA	RA	MA	RA	RA	MA	RA	RA	MA	RA	RA
		100	MA	RA	RA	RA	RA	RA	RA	RA	RA	MA	RA	RA	MA	RA	RA	RA	RA	RA	MA	RA	RA	MA	RA	RA	MA	RA	RA
		140	MA	RA	RA	RA	RA	RA	RA	RA	RA	MA	RA	RA	MA	RA	RA	RA	RA	RA	MA	RA	RA	MA	RA	RA	MA	RA	RA
	2250	60	MA	RA	RA	MA	RA	RA	RA	RA	RA	MA	RA	RA	MA	RA	RA	RA	RA	RA	MA	RA	RA	MA	RA	RA	MA	RA	RA
		100	MA	RA	RA	MA	RA	RA	RA	RA	RA	MA	RA	RA	MA	RA	RA	RA	RA	RA	MA	RA	RA	MA	RA	RA	MA	RA	RA
		140	MA	RA	RA	MA	RA	RA	RA	RA	RA	MA	RA	RA	MA	RA	RA	RA	RA	RA	MA	RA	RA	MA	RA	RA	MA	RA	RA

Table B.1: Comparison between the Rz before and after the metallization for the structuring type MS.

Test No	β (°)	FL(mm)	H (%)	P (W)	v (m/s)	f (kHz)	Rz (µm)		Stru. Type	Abla. Type
							Before	After		
1	0	0	0	5	1.5	60	31,6	28,1	MS	MA
2	0	0	0	5	1.5	100	34,04	33,11	MS	MA
3	0	0	0	5	1.5	140	40,26	33,53	MS	MA
4	0	0	0	5	2.25	60	30,95	27,53	MS	MA
5	0	0	0	5	2.25	100	32,42	30,91	MS	MA
6	0	0	0	5	2.25	140	38,68	32,94	MS	MA
7	0	0	0	9	2.25	60	35,5	34,52	MS	MA
8	0	0	0	9	2.25	140	44,34	41,76	MS	MA
9	0	5	0	9	0.75	60	48,985	45,95	MS	RA
10	20	0	0	5	0.75	60	50,131	46,15	MS	MA
11	40	0	0	5	0.75	60	41,595	38,9	MS	MA
12	40	0	0	5	2.25	60	31,944	30,9	MS	MA
13	40	0	0	5	2.25	140	23,015	29,6	MS	MA
14	40	0	0	9	0.75	60	58,867	50,75	MS	RA
15	40	0	0	9	2.25	60	40,187	37,41	MS	MA
16	40	0	0	9	2.25	140	31,077	28,08	MS	MA
17	40	5	0	5	0.75	60	54,064	49,37	MS	MA
18	40	5	0	5	0.75	140	39,964	34,93	MS	MA
19	40	5	0	5	2.25	60	30,338	29,14	MS	PA
20	40	5	0	9	2.25	60	38,289	37,72	MS	MA
21	40	5	0	9	2.25	140	32,781	30,13	MS	MA

Table B.2: Rz before and after the metallization for the structuring type RS at P 5 W.

Test No	β (°)	FL(mm)	H (%)	P (W)	v (m/s)	f (kHz)	Rz (µm)		Stru. Type	Abla. Type
							Before	After		
1	0	0	50	5	0.75	60	39,51	37,32	RS	RA
2	0	0	75	5	0.75	60	57,57	51,43	RS	RA
3	0	0	75	5	0.75	140	51,22	50,02	RS	RA
4	0	0	75	5	2.25	60	28,01	23	RS	RA
5	0	0	75	5	2.25	140	31,23	30,7	RS	RA
6	0	5	75	5	0.75	60	36,716	34,76	RS	RA
7	0	5	75	5	0.75	140	16,417	16,4	RS	RA
8	0	5	75	5	2.25	60	24,537	23,26	RS	RA
9	40	0	75	5	0.75	60	44,14	42,32	RS	RA
10	40	0	75	5	0.75	140	36,578	29,81	RS	RA
11	40	0	75	5	2.25	60	32,458	31,56	RS	RA
12	40	0	75	5	2.25	140	27,547	26,86	RS	MA
13	40	5	75	5	0.75	60	58,587	42,16	RS	RA
14	40	5	75	5	0.75	140	35,447	34,15	RS	RA
15	40	5	75	5	2.25	60	33,421	30,55	RS	RA
16	40	5	75	5	2.25	140	27,752	21,57	RS	MA

Table B.3: Rz before and after the metallization for the structuring type RS at P 9 W.

Test No	β (°)	FL(mm)	H (%)	P (W)	v (m/s)	f (kHz)	Rz (µm)		Stru. Type	Abla. Type
							Before	After		
1	0	0	0	9	0.75	60	54,73	67,68	RS	RA
2	0	0	75	9	0.75	60	63,79	67,47	RS	RA
3	0	0	75	9	2.25	60	36,58	43	RS	RA
4	0	0	75	9	2.25	140	41,9	51,34	RS	RA
5	0	5	0	9	2.25	60	33,146	41,42	RS	RA
6	0	5	75	9	0.75	60	67,085	73,9	RS	RA
7	0	5	75	9	0.75	140	51,285	51,9	RS	RA
8	0	5	75	9	2.25	60	45,405	48,21	RS	RA
9	40	0	75	9	0.75	60	95,739	98,32	RS	RA
10	40	0	75	9	0.75	140	55,321	59,773	RS	RA
11	40	0	75	9	2.25	60	34,759	45,34	RS	RA
12	40	0	75	9	2.25	140	27,512	31,5	RS	RA
13	40	5	0	9	0.75	60	62,414	73,03	RS	MA
14	40	5	75	9	0.75	60	94,437	96,78	RS	RA
15	40	5	75	9	0.75	140	77,05	77,25	RS	RA
16	40	5	75	9	2.25	60	43,791	57,31	RS	RA
17	40	5	75	9	2.25	140	39,11	40,8	RS	RA

Table B.4: Rz before and after the metallization for the structuring type LS.

Test No	β (°)	FL(mm)	H (%)	P (W)	v (m/s)	f (kHz)	Rz (µm)		Stru. Type	Abla. Type
							Before	After		
1	0	0	0	5	0.75	60	43,1	49,72	LS	MA
2	0	0	0	5	0.75	100	48,56	53,71	LS	MA
3	0	0	0	5	0.75	140	50,71	55,56	LS	MA
4	0	0	0	9	0.75	140	85,95	87,8	LS	RA
5	0	3	0	5	0.75	60	42,127	44,9	LS	MA
6	0	5	0	5	0.75	60	34,299	37,38	LS	MA
7	0	5	0	5	0.75	140	20,853	22,7	LS	MA
8	0	5	0	9	0.75	140	38,483	40,47	LS	RA
9	20	3	0	1	0.75	60	23,94	36,11	LS	PA
10	40	0	0	9	0.75	140	41,545	56,13	LS	MA
11	40	5	0	5	2.25	140	19,294	33,48	LS	PA
12	40	5	0	9	0.75	140	35,427	38,21	LS	MA